



Structural investigation of nanoparticle superlattices by advanced X-ray scattering methods

Dissertation

zur Erlangung des Doktorgrades
an der Fakultät für Mathematik, Informatik und
Naturwissenschaften
Fachbereich Physik
der Universität Hamburg

vorgelegt von

DMITRII LAPKIN

Hamburg

2022

Gutachter der Dissertation:

Prof. Dr. Christian G. Schroer
Prof. Dr. Ivan A. Vartaniants

Zusammensetzung der Prüfungskommission:

Prof. Dr. Christian G. Schroer
Prof. Dr. Ivan A. Vartaniants
Prof. Dr. Edgar Weckert
Prof. Dr. Patrick Huber
Prof. Dr. Robin Santra

Vorsitzender der Prüfungskommission:

Prof. Dr. Robin Santra

Datum der Disputation:

16.12.2022

Vorsitzender des Fach-Promotionsausschusses PHYSIK:

Prof. Dr. Wolfgang J. Parak

Leiter des Fachbereichs PHYSIK:

Prof. Dr. Günter H. W. Sigl

Dekan der Fakultät MIN:

Prof. Dr.-Ing. Norbert Ritter

Zusammenfassung

Kolloidale Kristalle sind geordnete Anordnungen kolloidaler Partikel, die eine Überstruktur ähnlich der in klassischen Kristallen bilden. In den letzten Jahrzehnten hat die Forschung an kolloidalen Kristallen aufgrund ihrer faszinierenden strukturbezogenen Stoffeigenschaften wie Beugung von Licht im optischen Wellenlängenbereich, hohe Porosität usw. eine Blüte erlebt. Darüber hinaus finden kolloidale Kristalle häufig als Modellsystem für klassische Kristalle Verwendung, da ihre größeren Abmessungen eine leichtere Untersuchung von Strukturveränderungen ermöglicht. Mesokristalle sind eine spezielle Unterklasse von kolloidalen Kristallen, bei denen die kristallinen Nanopartikel, aus denen der kolloidale Kristall besteht, zueinander ausgerichtet sind. Solche hoch geordneten Nanokristallüberstrukturen können funktionelle kollektive Stoffeigenschaften aufweisen, die sich von denen herkömmlicher kolloidaler Kristalle und einzelner Nanopartikel unterscheiden. Diese kollektiven Stoffeigenschaften werden durch die Wechselwirkungen zwischen den Teilchen beeinflusst, die stark von den strukturellen Besonderheiten der Mesokristalle abhängen. Obwohl kolloidale Kristalle und Mesokristalle bereits viele praktische Anwendungen gefunden haben, sind die Beziehungen zwischen Struktur und Stoffeigenschaften aufgrund des Mangels an geeigneten Methoden für Strukturuntersuchungen noch immer wenig verstanden.

Diese kumulative Dissertation basiert auf sechs Publikationen und widmet sich der Entwicklung von Röntgenmethoden für die Strukturuntersuchung von kolloidalen Kristallen und Mesokristallen.

In den ersten drei Publikationen wird die Struktur von kolloidalen Kristallen und Mesokristallen durch die Analyse der gemessenen zweidimensionalen (2D) Streumuster offengelegt. Die erste Publikation befasst sich mit der strukturellen Entwicklung während des Abkühlens und Erhitzens eines thermoresponsiven kolloidalen Kristalls, der aus Gold-Poly(N-Isopropylacrylamid) Kern-Schale-Nanopartikeln besteht. Die Bragg-Peak-Analyse der in Ultra-Röntgenkleinwinkelstreuung (USAXS) Geometrie gemessenen Daten ermöglichte einen einzigartigen Einblick in die Kristallisations- und Schmelzprozesse solcher kolloidalen Kristalle. Die zweite und dritte Publikation befassen sich mit Mesokristallen, die aus anorganischen halbleitenden Bleisulfid- oder Bleihalogenid-Perowskit-Nanopartikeln bestehen, die durch organische Kupfer-Tetraaminophthalocyanin- (Cu4APc) oder Ölsäure-Liganden (OA) stabilisiert werden. Die experimentelle Geometrie ermöglichte die gleichzeitige Messung sowohl der Röntgenkleinwinkelstreuung (SAXS) der Übergitterstruktur als auch der Röntgenweitwinkelstreuung (WAXS) der Atomgitter der einzelnen Nanopartikel. Die Analyse der Bragg-Peaks, die sowohl bei kleinen als auch bei großen Winkeln an verschiedenen räumlichen Punkten der Probe beobachtet wurden, ermöglichte eine räumlich aufgelöste Strukturkartierung der Mesokristalle. Die extrahierten Parameter der Einheitszelle des Übergitters wurden mit der Winkelausrichtung der Nanopartikel innerhalb des Übergitters kombi-

niert, um die vollständige Struktur des Mesokristalls auf beiden Längenskalen zu erhalten. Die gefundenen Strukturen wurden dann mit den gemessenen funktionellen Stoffeigenschaften der Mesokristalle wie Leitfähigkeit und Photolumineszenz korreliert.

In den anderen drei Publikationen wird die Strukturinformation durch Anwendung der winkelaufgelösten-Röntgen-Kreuzkorrelationsanalyse (AXCCA) auf die gemessenen Intensitätsverteilungen im dreidimensionalen (3D) reziproken Raum extrahiert. Die vierte Publikation enthält die Details der Adaption dieser Methode für die Anwendung auf 3D-Intensitätsverteilungen anstelle der üblichen 2D-Streumuster. In dieser Arbeit wurde gezeigt, dass AXCCA zur qualitativen Strukturbestimmung in dicht gepackten kolloidalen Kristallen geeignet ist, und zwar anhand einer Beispielprobe, die aus kugelförmigen Siliziumdioxidteilchen bestand. In der fünften und sechsten Publikation wurde AXCCA erfolgreich auf die gemessenen 3D-Streuintensitätsverteilungen angewandt, um die Struktur von Mesokristallen aus Gold- und Magnetit-Nanowürfeln aufzuklären.

Die vorgeschlagenen Ansätze für Strukturuntersuchungen an kolloidalen Kristallen und Mesokristallen lassen sich auch auf andere Materialien übertragen. Die erzielten Ergebnisse zur Struktur von kolloidalen Kristallen und Mesokristallen und ihre Korrelation mit den funktionellen Eigenschaften sind neu und für die Materialwissenschaft von großem Interesse.

Abstract

Colloidal crystals are ordered arrays of colloidal particles forming a superlattice similar to that in conventional crystals. In recent decades, the research on colloidal crystals has blossomed due to their fascinating structure-related properties such as diffraction of light at optical wavelengths, high porosity, etc. Moreover, colloidal crystals are often viewed as a model system for conventional crystals since their larger dimensions allow easier tracing of changes in structure. Mesocrystals are a special subclass of colloidal crystals in which the crystalline nanoparticles constituting the crystal are mutually oriented. Such highly ordered nanocrystal superlattices can display functional collective properties distinct from those of conventional colloidal crystals and individual nanoparticles. These collective properties are conditioned by the interparticle interactions which are highly dependent on the structural features of the mesocrystals. Even though colloidal crystals and mesocrystals have already found many practical applications, the structure-property relationships are still poorly understood due to the lack of suitable methods of structural investigations.

This cumulative Thesis is based on six publications and is devoted to the development of X-ray methods for the structural study of colloidal crystals and mesocrystals.

In the first three publications, the structure of colloidal crystals and mesocrystals is revealed by analysis of the measured two-dimensional (2D) scattering patterns. The first publication addresses the structural evolution of a thermoresponsive colloidal crystal consisting of gold–poly(N-isopropylacrylamide) core–shell nanoparticles during cooling and heating. The Bragg peak analysis of the data obtained in Ultra-Small-Angle X-ray Scattering (USAXS) experimental geometry provided a unique insight into the processes of crystallization and melting of such colloidal crystals. The second and third publications deal with mesocrystals consisting of inorganic lead sulfide or lead halide perovskite semiconductive nanoparticles stabilized by organic copper tetraaminophthalocyanine (Cu4APc) or oleic acid (OA) ligands. The experimental geometry allowed the simultaneous registration of both Small-Angle X-ray Scattering (SAXS) from the superlattice structure and Wide-Angle X-ray Scattering (WAXS) from the atomic lattices of the constituting nanoparticles. Analysis of the Bragg peaks registered at both small and wide angles at different spatial points of the sample allowed spatially-resolved structural mapping of the mesocrystals. The extracted superlattice unit cell parameters were combined with the angular orientation of the nanoparticles inside the superlattice to obtain the complete structure of the mesocrystal on both length scales. The revealed structures were then correlated with the measured functional properties of the mesocrystals such as conductivity and photoluminescence.

In the other three publications, the structural information is extracted by application of Angular X-ray Cross-Correlation Analysis (AXCCA) to the measured inten-

sity distributions in three-dimensional (3D) reciprocal space. The fourth publication contains the details of adapting this method for application to 3D intensity distributions instead of common 2D scattering patterns. In this work, AXCCA was shown prospective for qualitative structure determination in close-packed colloidal crystals using an exemplary sample consisting of spherical silica particles. In the fifth and sixth publications, AXCCA was successfully applied to the measured 3D scattered intensity distributions to reveal the structure of mesocrystals composed of gold and magnetite nanocubes.

The proposed approaches to structural studies of colloidal crystals and mesocrystals can be further extended to other materials. The obtained results on the structure of colloidal crystals and mesocrystals and their correlations with the functional properties are highly novel and are of great interest to the materials science community.

Eidesstattliche Versicherung / Declaration on oath

Hiermit erkläre ich an Eides statt, dass ich die vorliegende Dissertationsschrift selbst verfasst und keine anderen als die angegebenen Quellen und Hilfsmittel benutzt habe.

I hereby declare, on oath, that I have written the present dissertation by my own and have not used other than the acknowledged resources and aids.

Ort, Datum (Place, Date)

Unterschrift (Signature)

Contents

1	Introduction	1
2	Overview	3
2.1	Interaction of X-rays with matter	3
2.1.1	Coherence	8
2.1.2	X-ray scattering at free electrons	10
2.1.2.1	Scattering at a single electron	10
2.1.2.2	Scattering at several electrons	12
2.1.3	X-ray scattering at an atom	14
2.1.4	X-ray scattering by macroscopic particles	16
2.1.4.1	Scattering at a single particle	16
2.1.4.2	Scattering at several particles	18
2.1.5	X-ray scattering from a crystal	20
2.1.5.1	Crystalline structures	20
2.1.5.2	Reciprocal lattice	23
2.1.5.3	Crystalline structure factor	25
2.1.5.4	Ewald sphere	26
2.1.5.5	Crystalline defects	28
2.1.5.6	Effect of finite crystallite size on scattering	30
2.1.5.7	Effect of crystalline lattice distortion on scattering	32
2.1.5.8	Williamson-Hall equation	33
2.1.6	X-ray scattering from a fluid	33
2.1.6.1	Radial distribution function	33
2.1.6.2	Scattering from a fluid	34
2.1.6.3	Structure factor of hard sphere fluid	36
2.1.7	Angular X-ray cross-correlation analysis	38
2.2	Modern sources of X-ray radiation	43
2.2.1	Synchrotron light sources	44
2.2.2	Free-electron lasers	51
2.3	Colloidal systems: structure and properties	55
2.3.1	Colloidal crystals	58

2.3.1.1	Structure of colloidal crystals	59
2.3.1.2	Crystallization of colloidal crystals	61
2.3.1.3	Structural investigation of colloidal crystals	62
2.3.1.4	Properties and applications of colloidal crystals	64
2.3.2	Mesocrystals	65
3	Publications	69
3.1	Structural investigation of colloidal crystals and mesocrystals by complementary small- and wide-angle X-ray scattering techniques	70
3.1.1	In situ characterization of crystallization and melting of soft, thermoresponsive microgels by small-angle X-ray scattering	72
3.1.2	Structure–transport correlation reveals anisotropic charge transport in coupled PbS nanocrystal superlattices	84
3.1.3	Spatially resolved fluorescence of caesium lead halide perovskite supercrystals reveals quasi-atomic behavior of nanocrystals	91
3.2	Angular X-ray cross-correlation analysis applied to the scattering data in 3D reciprocal space	101
3.2.1	Angular X-ray cross-correlation analysis applied to the scattering data in 3D reciprocal space from a single crystal	102
3.2.2	Exploring the 3D structure and defects of a self-assembled gold mesocrystal by coherent X-ray diffraction imaging	116
3.2.3	Morphogenesis of magnetite mesocrystals: Interplay between nanoparticle morphology and solvation shell	127
4	Summary	139
	List of publications	143
	List of abbreviations	147
	Bibliography	149
	Acknowledgments	171

Chapter 1

Introduction

Colloidal suspensions – dispersions of solid particles with sizes in the range of approximately 1 nm to 1 μm in a liquid solvent – are often viewed as analogs to atomic systems. Thermal motion makes the behavior of colloidal particles similar to the behavior of atoms and allows the formation of thermodynamically stable states. Spherical colloidal particles were found able to form colloidal crystals similar to conventional atomic crystals [1, 2]. Despite much weaker interactions between colloidal particles in comparison to those between atoms, the colloidal crystals became a model system for studying conventional crystals. They demonstrate a wide range of possible crystalline structures [3] and structural defects [4, 5] common for atomic crystals. Nonspherical colloidal particles possess a directionality of interparticle interactions and mimic atomic systems even better, although they are more difficult to synthesize. But recent advances in colloidal chemistry made it possible, and many works on colloidal crystals from nonspherical particles were published in the last years [6–8]. The directional interparticle forces cause the non-spherical particles in such colloidal crystals to align with each other. If colloidal particles have an internal crystalline structure, the mutual orientation of the particles makes their atomic lattices coherent over a large distance. Such structures constitute a separate class of colloidal crystals called mesocrystals [9]. The alignment of the atomic lattices allows quantum coupling of adjacent colloidal particles that leads to the unique properties of such mesocrystals.

The size of colloidal particles lies in the range of optical wavelengths that makes the colloidal crystals ideal candidates for applications as photonic crystals [10, 11]. Indeed, the diffraction of light in the colloidal crystals leads to the formation of photonic band gaps analogous to those for electrons in conventional crystals [12, 13]. The enormous specific surface area of colloidal crystals makes prospective their application in catalysis or as sensors [14], electrodes [15], etc. Pores between the particles in colloidal crystals can be used as a template for synthesis of highly porous materials that can be used in fuel cells [16]. The quantum coupling between adjacent particles in mesocrystals leads to emergent electronic and optical properties in such materials. They were

reported to exhibit photoconductivity [17], photoluminescence [18], thermoelectricity [19], superfluorescence [20], etc. It should be noted that all these properties of colloidal crystals and mesocrystals depend to a decisive extent on the control over their structure. Understanding structure-property correlations would greatly contribute to the wider use of colloidal crystals and mesocrystals in practical applications.

The large sizes of the colloidal particles allow structural investigation of colloidal systems by optical and electron microscopy. These methods are routinely used for structural investigation from the very discovery of colloidal crystals to the present day [1, 5, 21]. Unfortunately, both of these methods are sensitive only to a thin surface layer of the structures and place strict requirements on the experimental conditions. This makes impossible assessing the structure of bulk colloidal crystals, whose properties may differ from those in thin films or on the surface. Moreover, this fact hampers in situ studies of dynamical processes in colloids, such as self-assembly into crystals, phase transitions, etc. Another disadvantage of microscopy methods is the inability to cover simultaneously two scales of order – the colloidal and the atomic – in mesocrystals. X-rays, thanks to their large penetration depth, offer a unique opportunity to reveal the structure of bulk colloidal crystals and mesocrystals. Different techniques, such as Small-Angle X-ray Scattering (SAXS) [22, 23], Grazing-Incidence Small-Angle X-ray Scattering (GISAXS) [24, 25], Coherent Diffraction Imaging (CDI) [26] were used to characterize the order in colloidal systems. These methods supplemented by Wide-Angle X-ray Scattering (WAXS) or Grazing-Incidence Wide-Angle X-ray Scattering (GI-WAXS), sensitive to the atomic structure of the particles, allow full structural characterization of mesocrystals [27, 28]. Besides, the X-ray scattering techniques are suitable for in situ experiments [24, 25, 29]. This makes X-ray methods indispensable for the structural characterization of colloidal crystals and mesocrystals.

This cumulative Thesis is focused on the further development of advanced X-ray scattering methods for the structural investigations of colloidal crystals and mesocrystals. The Thesis is structured as follows. Chapter 2 provides a short overview of the theoretical basis, methods and samples used in this work. Section 2.1 introduces the theory of X-ray scattering and the experimental methods used in this work. Section 2.2 contains the description of modern X-ray sources, such as X-ray tubes, synchrotrons and X-ray Free-Electron Lasers (XFELs). Section 2.3 summarizes the basics of colloidal systems and mesocrystals, and their properties. Chapter 3 contains author's publications on the topic of the Thesis grouped into two sections. Section 3.1 is dedicated to structural analysis of colloidal crystals and mesocrystals by complementary SAXS and WAXS techniques. Section 3.2 is devoted to structural analysis of colloidal crystals and mesocrystals by means of Angular X-ray Cross-Correlation Analysis (AXCCA) adopted for application to 3D scattered intensity distributions. Chapter 4 provides a comprehensive summary of the results and the conclusion of this Thesis.

Chapter 2

Overview

2.1 Interaction of X-rays with matter

X-rays are electromagnetic waves with the wavelengths ranging from about 10^{-8} to 10^{-12} m. This range of the wavelengths is comparable with the length scale of interatomic distances in matter that defines the interactions of X-rays with matter. The interaction is quite weak in comparison to the radiation of longer wavelengths (i.e. visible light or radio waves) that allows deep propagation through media and objects. On the other hand, such short wavelengths provide excellent resolution suitable for studying the atomic structure of matter. This makes the X-rays an indispensable tool for the non-destructive study of the internal structure of bulk samples. In this Section, the theory of interaction of X-rays with matter is given according to [30–34].

In classical electrodynamics, X-rays, as any electromagnetic field, obey the Maxwell equations in media with free charge density ρ and free current density \mathbf{j} [30, 31]

$$\nabla \cdot \mathbf{D} = 4\pi\rho, \quad (2.1a)$$

$$\nabla \cdot \mathbf{B} = 0, \quad (2.1b)$$

$$\nabla \times \mathbf{E} = -\frac{1}{c} \frac{\partial \mathbf{B}}{\partial t}, \quad (2.1c)$$

$$\nabla \times \mathbf{H} = \frac{1}{c} \left(4\pi\mathbf{j} + \frac{\partial \mathbf{D}}{\partial t} \right), \quad (2.1d)$$

where \mathbf{D} is the electric induction field, \mathbf{E} is the electric field, \mathbf{B} is the magnetic induction field and \mathbf{H} is the magnetic field. The electric/magnetic induction fields \mathbf{D}/\mathbf{B} are connected to the electric/magnetic fields \mathbf{E}/\mathbf{H} by the constitutive relations that take into account the polarization and magnetization of the medium

$$\mathbf{D} = \varepsilon\mathbf{E}, \quad (2.2a)$$

$$\mathbf{B} = \mu\mathbf{H}, \quad (2.2b)$$

where ε and μ are the relative permittivity and the relative permeability, respectively. In general, the relative permittivity and permeability are tensors, but in the simplest case of isotropic medium they are scalar.

Applying the curl operator $\nabla \times$ to Eqs. (2.1c) and (2.1d), taking into account that $\nabla \times \nabla \times \mathbf{a} = \nabla(\nabla \cdot \mathbf{a}) - \Delta \mathbf{a}$ for any vector \mathbf{a} , and using Eqs. (2.1a) and (2.1b), one gets the following equations

$$\Delta \mathbf{E} - \frac{\varepsilon \mu}{c^2} \frac{\partial^2 \mathbf{E}}{\partial t^2} = 4\pi \nabla \rho + \frac{4\pi}{c^2} \frac{\partial \mathbf{j}}{\partial t}, \quad (2.3a)$$

$$\Delta \mathbf{H} - \frac{\varepsilon \mu}{c^2} \frac{\partial^2 \mathbf{H}}{\partial t^2} = -\frac{4\pi}{c} \nabla \times \mathbf{j}, \quad (2.3b)$$

that are called wave equations and describe an electromagnetic wave propagating with the phase velocity $v_p = c/\sqrt{\varepsilon\mu}$. In non-magnetic materials $\mu = 1$ and, due to weak interaction with matter, for X-rays $\varepsilon \approx 1$ that gives the phase velocity equal to the speed of light in vacuum $v_p = c$.

The right parts of the Eqs. (2.3) describe possible sources of electromagnetic waves: gradients in charge distribution, alternating current density and curls in current density. The alternating current density is especially important, because the current density \mathbf{j} corresponds to the movement of charges with the momentum \mathbf{p} as $\mathbf{j} = \rho e \mathbf{p}/m_e$ and hence

$$\frac{\partial \mathbf{j}}{\partial t} = -\frac{\rho e}{m_e} \frac{\partial \mathbf{p}}{\partial t}, \quad (2.4)$$

where ρ is the charge density, e is the elementary charge and m_e is the electron mass. Thus, charges moving with acceleration emit electromagnetic waves. This fact underlies the scattering and generation of X-rays that will be discussed below in this section and in Section 2.2.

In empty space without free charges and currents (i.e. $\rho \equiv 0$ and $\mathbf{j} \equiv 0$), the wave equations (2.3) take the following form

$$\Delta \mathbf{E} - \frac{\varepsilon \mu}{c^2} \frac{\partial^2 \mathbf{E}}{\partial t^2} = 0, \quad (2.5a)$$

$$\Delta \mathbf{H} - \frac{\varepsilon \mu}{c^2} \frac{\partial^2 \mathbf{H}}{\partial t^2} = 0. \quad (2.5b)$$

The general solution of these equations is a superposition of plane monochromatic waves

$$\mathbf{E}(\mathbf{r}, t) = \mathbf{E}_0 e^{i(\mathbf{k} \cdot \mathbf{r} - \omega t + \varphi_0)}, \quad (2.6a)$$

$$\mathbf{H}(\mathbf{r}, t) = \mathbf{H}_0 e^{i(\mathbf{k} \cdot \mathbf{r} - \omega t + \varphi_0)}, \quad (2.6b)$$

where \mathbf{r} is a radius-vector of a point in space, \mathbf{k} is a wave vector normal to the sur-

face of constant phase (wavefront) and φ_0 is a constant phase that can be put to zero $\varphi_0 = 0$ without any loss of generality. Inserting Eq. (2.6) into Eq. (2.5) one gets $k = \|\mathbf{k}\| = \omega/c = 2\pi/\lambda$, i.e. the spatial frequency k is directly dependent on the temporal frequency ω . Inserting Eq. (2.6) into Eqs. (2.1a) and (2.1b) one gets $\mathbf{k} \cdot \mathbf{E} = 0$ and $\mathbf{k} \cdot \mathbf{H} = 0$, respectively. From Eqs. (2.6) and (2.1d) one gets $\mathbf{H} \times \mathbf{k} = k\mathbf{E}$ from which $\|\mathbf{E}\| = \|\mathbf{H}\|$ and $\mathbf{E} \cdot \mathbf{H} = 0$. Thus, the electric \mathbf{E} and magnetic \mathbf{H} fields are perpendicular to each other and to the wave vector \mathbf{k} as shown in Fig. 2.1, i.e. the electromagnetic wave is transversal. The direction $\epsilon = \mathbf{E}_0/\|\mathbf{E}_0\|$ of the electric field at zero phase is called a polarization vector. The linearity of Eqs. (2.3) allows expansion of almost any electromagnetic wave into series of plane monochromatic waves.

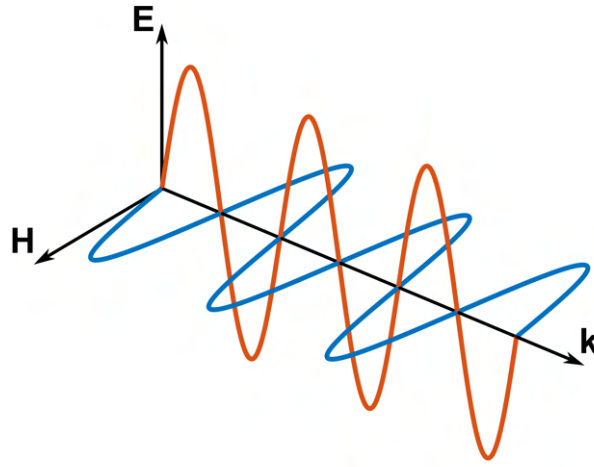


Figure 2.1: Electric \mathbf{E} and magnetic \mathbf{H} fields in a plane vertically polarized electromagnetic wave with a wavevector \mathbf{k} .

Let us multiply Eq. (2.1c) by \mathbf{H} , Eq. (2.1d) by \mathbf{E} and add them up. Then, the resulting equation can be written as follows

$$\frac{1}{c}\mathbf{E} \cdot \frac{\partial \mathbf{E}}{\partial t} + \frac{1}{c}\mathbf{H} \cdot \frac{\partial \mathbf{H}}{\partial t} = -\mathbf{H} \cdot (\nabla \times \mathbf{E}) + \mathbf{E} \cdot (\nabla \times \mathbf{H}) \quad (2.7)$$

or, given $\nabla \cdot (\mathbf{a} \times \mathbf{b}) = \mathbf{b} \cdot (\nabla \times \mathbf{a}) - \mathbf{a} \cdot (\nabla \times \mathbf{b})$ for any vectors \mathbf{a} and \mathbf{b} ,

$$\frac{\partial}{\partial t} \frac{\|\mathbf{E}\|^2 + \|\mathbf{H}\|^2}{8\pi} = -\nabla \cdot \left(\frac{c}{4\pi} \mathbf{E} \times \mathbf{H} \right). \quad (2.8)$$

The quantity

$$w = \frac{\|\mathbf{E}\|^2 + \|\mathbf{H}\|^2}{8\pi} \quad (2.9)$$

is the electromagnetic energy density and is conserved in an isolated system. Its dissipation is described by the electromagnetic energy flux, or the Poynting vector

$$\mathbf{S} = \frac{c}{4\pi} \mathbf{E} \times \mathbf{H}. \quad (2.10)$$

For a plane monochromatic wave from Eq. (2.6), given its temporal periodicity and that $\mathbf{E} = \mathbf{H} \times \mathbf{n}$, where $\mathbf{n} = \mathbf{k}/\|\mathbf{k}\|$ is the wavefront propagation direction, the time-averaged Poynting vector is equal to

$$\mathbf{S} = \frac{c}{8\pi} \|\mathbf{E}\|^2 \mathbf{n} = \frac{c}{8\pi} \|\mathbf{H}\|^2 \mathbf{n}. \quad (2.11)$$

Thus, the energy flux is collinear to the wavefront propagation direction.

The electromagnetic energy flux is the quantity that can be relatively easily measured in an experiment. Although another quantity is typically considered, the intensity $I = \|\mathbf{E}\|^2$, which is linearly proportional to the energy flux.

Modern quantum physics suggests that the electromagnetic energy (2.9) and, therefore, the electric \mathbf{E} and magnetic \mathbf{H} fields are quantized. Any change in the electromagnetic energy can happen only when a photon with the energy of $E_{ph} = \hbar\omega = h\nu$, where $\hbar = h/(2\pi)$ is the Planck constant, is emitted or absorbed. The choice between the quantum and classical descriptions is to be made based on which approach gives easier description. The photoelectric effect and related absorption of X-rays, briefly mentioned below, are typically formulated in terms of quantum mechanics. The scattering of X-rays, that is mostly addressed in this work, is easily described in terms of classical electrodynamics that we will further follow.

The first observed interaction of the X-rays with the matter was described by W. C. Röntgen in his original paper dated back to 1895 [35]. Namely, he observed attenuation of the X-rays by different tissues of a hand that allowed him to obtain a picture of the skeleton. The attenuation of light was described long before Röntgen's observation in 1729 by P. Bouguer [36] and can be described by the Beer-Lambert-Bouguer law [37]

$$dI(z) = -\mu(z)I(z)dz, \quad (2.12)$$

where the light propagates along the z -axis, $\mu(z)$ is the attenuation coefficient that for a media with N attenuating species can be expressed as $\mu(z) = \sum_{i=1}^N \sigma_i n_i(z)$, where σ_i is the attenuation cross-section of the i -th species and $n_i(z)$ is the number concentration of the i -th attenuating species. For constant attenuation coefficient $\mu(z) \equiv \mu$, the solution of Eq. (2.12) is exponential decay

$$I(z) = I_0 e^{-\mu z}, \quad (2.13)$$

where I_0 is the intensity at $z = 0$. These equations remains valid for X-ray waves as well. Distinct attenuation cross-sections of different materials allow a non-destructive study of the internal structure of the samples. The attenuation contrast is widely used in X-ray imaging techniques such as projection radiography and Computed Tomography (CT) for medical [38], industrial [39] and scientific [40] applications. The attenu-

ation happens due to two processes: absorption and scattering of the light by atoms constituting the material.

The first process, absorption, is a result of the photoelectric effect explained by Einstein in 1905 [41]. A photon of incident X-ray beam is absorbed by a core electron of an atom constituting the sample only if the photon energy is higher than the electron binding energy as shown in Fig. 2.2(a). The electron binding energies are characteristic for different chemical elements and are highly sensitive to their chemical states. It makes possible to reveal the chemical composition of the sample measuring the absorption spectrum of the sample (the corresponding technique is called X-ray Absorption Spectroscopy (XAS)) [42] or the kinetic energies of ejected electrons from the sample surface (the corresponding method is called X-ray Photoemission Spectroscopy (XPS)) [43]. At the energies close to the binding energy (so-called absorption edge), the absorption spectrum is highly sensitive to the local surrounding of the atoms that makes possible to study the local structure of the sample (the corresponding technique is called Extended X-ray Absorption Fine Structure (EXAFS) spectroscopy) [44].

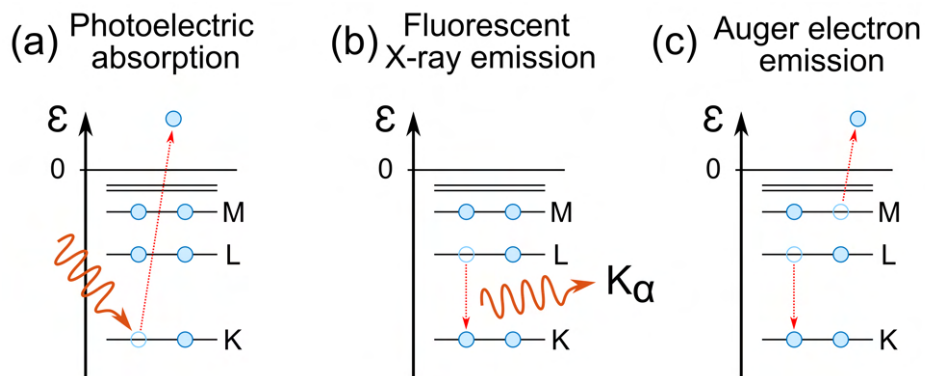


Figure 2.2: Schematic energy level diagram of an atom. Only three bottom energy levels are shown filled with electrons for clarity. (a) The photoelectric absorption process. An X-ray photon is absorbed and an electron ejected from the atom. The hole created in the inner shell can be filled by one of two distinct processes: (b) Fluorescent X-ray emission. One of the electrons in an outer shell fills the hole, creating a photon. In this example the outer electron comes either from the L shell that is referred as $K\alpha$ fluorescence. (c) Auger electron emission. One of the electrons in an outer shell fills the hole, the excess energy is transferred to another electron in the outer shell, which is ejected from the atom. Adapted from [32].

The absorption of a photon and release of a photoelectron transfer the atom into an unstable excited state that quite fast relaxes. The created hole is filled with an electron from one of the outer shells, while the difference in energy is either emitted in form of a photon as shown in Fig. 2.2(b) or transferred to another electron from outer shell that is consequently ejected from the atom as shown in Fig. 2.2(c). Both emitted photons and electrons have energies that reflect the electronic structure of the sample and are studied in X-ray Fluorescence (XRF) spectroscopy [45] and X-ray induced Auger Electron Spectroscopy (XAES) [46], respectively.

All spectroscopic techniques are widely and routinely used nowadays in materials science, but give a little information about the order of elementary units in the material. More comprehensive structural information is typically obtained by X-ray scattering methods that are described below and were mostly used in this work.

2.1.1 Coherence

In the classical electrodynamics, the electromagnetic waves are assumed to be deterministic (i.e. have a defined amplitude and phase at each moment of time). In reality, the wave generation is a stochastic process and a more correct approach to describing electromagnetic waves lies in terms of statistical optics.

The statistical properties of electromagnetic fields are commonly described in terms of correlation functions. Typically, for predictions of the results of an interference experiment, the first-order correlation function

$$\Gamma(\mathbf{r}_1, \mathbf{r}_2, \tau) = \langle E^*(\mathbf{r}_1, t)E(\mathbf{r}_2, t + \tau) \rangle, \quad (2.14)$$

and its normalized version

$$\gamma(\mathbf{r}_1, \mathbf{r}_2, \tau) = \frac{\Gamma(\mathbf{r}_1, \mathbf{r}_2, \tau)}{\sqrt{\Gamma(\mathbf{r}_1, \mathbf{r}_1, 0)\Gamma(\mathbf{r}_2, \mathbf{r}_2, 0)}}, \quad (2.15)$$

are enough.

The X-ray scattering techniques are mostly based on interference of scattered electromagnetic waves which makes the coherence one of the most important properties of the electromagnetic waves for applications. Typically, two types of coherence are considered. Temporal, or longitudinal, coherence describes the ability of a wave interfere with a delayed copy of itself, while spatial, or transversal, coherence describes the ability of a wave interfere with a spatially shifted wave.

The visibility of interference fringes is defined by the absolute value of the normalized mutual coherence function (2.15). The dependence on the spatial variables \mathbf{r}_1 and \mathbf{r}_2 defines the transverse coherence in the plane normal to the wavevector of an electromagnetic wave, while the dependence on the time variable τ - the longitudinal coherence along the wavevector. At the point $\mathbf{r}_1 = \mathbf{r}_2$ and $\tau = 0$ the coherence has the maximum value of unity, i.e. the wave is always coherent with itself in a single point. When the distance in space $\mathbf{r}_2 - \mathbf{r}_1$ or in time τ increases, the coherence decreases down to zero at some distance. For a propagating electromagnetic wave, one can define a coherent volume in all three dimensions inside of which the coherence is high enough to give constructive interference.

From the Wiener-Khinchin theorem [47, 48], the temporal dependence of the mutual coherence function (2.14) is defined by the Fourier transform of the radiation

power spectrum $S(\omega)$

$$\Gamma(\mathbf{r}, \mathbf{r}, \tau) = \frac{1}{2\pi} \int_{\mathbb{R}} S(\omega) e^{i\omega\tau} d\omega, \quad (2.16)$$

where ω is the radiation frequency. If the power spectrum has a Gaussian shape with the full-width-at-half-maximum (FWHM) $\Delta\omega$, the corresponding mutual coherence has a Gaussian temporal dependence with the FWHM $\tau_c = 8 \ln 2 / \Delta\omega$, which is called coherence time. The characteristic longitudinal coherence length along the wavevector is equal then to

$$L_l = c\tau_c = \frac{8 \ln 2 c}{\Delta\omega} = \frac{4 \ln 2}{\pi} \frac{\lambda^2}{\Delta\lambda}. \quad (2.17)$$

At modern sources, such as synchrotrons described in Section 2.2, the bandwidth $\Delta\lambda / \lambda$ is determined by a monochromator. The typical bandwidth provided by a double crystal Si(111) monochromator is $\Delta\lambda / \lambda = 1 \times 10^{-4}$ that at the photon energy of 12 keV ($\lambda \approx 1.03 \text{ \AA}$) gives the longitudinal coherence length of $L_l \approx 900 \text{ nm}$.

From the van Cittert-Zernike theorem [49, 50], the spatial dependence of the mutual coherence function (2.14) in a plane distant from an incoherent source with the intensity $I(\eta, \nu)$ can be expressed as

$$\Gamma(\Delta x, \Delta y, 0) \sim \iint_{\mathbb{R}^2} I(\eta, \nu) e^{-i\frac{2\pi}{\lambda z}(\Delta x \eta + \Delta y \nu)} d\eta d\nu, \quad (2.18)$$

where $\Delta x = x_2 - x_1$ and $\Delta y = y_2 - y_1$ are the distances along x- and y-axes between the points \mathbf{r}_1 and \mathbf{r}_2 in the observation plane, η and ν are the coordinates in the source plane, z is the distance between the source and observation planes, and λ is the radiation wavelength. Under assumption of a Gaussian-shaped source with the FWHMs a_x and a_y , the corresponding coherence lengths are

$$L_t^{x/y} = \frac{4 \ln 2}{\pi} \frac{\lambda z}{a_{x/y}}. \quad (2.19)$$

For a synchrotron source, the transverse coherence length is defined by the electron bunch size. For the typical values of the source size of $85 \times 15 \mu\text{m}^2$ (FWHM, horizontally \times vertically) [51] at the photon energy of 12 keV ($\lambda \approx 1.03 \text{ \AA}$) and the distance from the source to the sample of 100 m, the corresponding coherence lengths are about 100 μm and 600 μm , respectively.

The classical description of the X-ray scattering given below is made under assumption that the sample is fully inside the coherence volume given by the longitudinal and transverse coherence lengths. Otherwise, the interference between the X-rays scattered by distant parts of the sample is suppressed that would lead to lower contrast in the scattering patterns. For extreme cases, the scattering from different sample parts should be considered separately with the resulting scattering pattern being a sum of

the scattered intensities instead of amplitudes.

2.1.2 X-ray scattering at free electrons

2.1.2.1 Scattering at a single electron

The most simple scattering event happens as a consequence of interaction between the electromagnetic wave and an electron. In the framework of classical electrodynamics, the scattering happens elastically, that gives coherent scattered waves that can interfere with each other. Let us consider the simplest possible interaction between a plane monochromatic wave (2.6) and a free electron. The momentum \mathbf{p} of an electron at spatial point \mathbf{r}' in the incident periodic electric field $\mathbf{E}_{in}(\mathbf{r}', t)$ changes according to the second Newton's law:

$$\frac{\partial \mathbf{p}}{\partial t}(t) = -e\mathbf{E}_{in}(\mathbf{r}', t). \quad (2.20)$$

The accelerated electron will emit an outgoing electromagnetic wave with the electric field $\mathbf{E}_{out}(\mathbf{r}, t)$ that is defined by Eqs. (2.3) and (2.4):

$$\Delta \mathbf{E}_{out} - \frac{1}{c^2} \frac{\partial^2 \mathbf{E}_{out}}{\partial t^2} = -\frac{4\pi e}{c^2 m_e} \delta(\mathbf{r} - \mathbf{r}') \frac{\partial \mathbf{p}}{\partial t}(t). \quad (2.21)$$

Without loss of generality, let us put the scattering electron to the origin of coordinates (i.e. $\mathbf{r}' = 0$). Under assumptions that the electron speed \mathbf{v} is much lower than the speed of light $\|\mathbf{v}\| \ll c$ and that the emitted wave is measured in the point \mathbf{r} far away from the scatterer $\|\mathbf{r}\| \gg \lambda$, where λ is the wavelength of the wave, the solution of Eq. (2.21) can be represented as [33]

$$\mathbf{E}_{out}(\mathbf{r}, t) = -\frac{r_0}{er} \left[\frac{\partial \mathbf{p}}{\partial t} \left(t - \frac{r}{c} \right) \times \mathbf{n} \right] \times \mathbf{n}, \quad (2.22)$$

where $r_0 = e^2 / (m_e c^2) \approx 2.817 \times 10^{-15}$ m is the classical electron radius and $\mathbf{n} = \mathbf{r} / \|\mathbf{r}\|$. The corresponding emitted magnetic field, from Eq. (2.1c), is

$$\mathbf{H}_{out}(\mathbf{r}, t) = -\frac{r_0}{er} \frac{\partial \mathbf{p}}{\partial t} \left(t - \frac{r}{c} \right) \times \mathbf{n}. \quad (2.23)$$

The corresponding Poynting vector can be calculated from Eq. (2.10)

$$\mathbf{S}(\mathbf{r}, t) = \frac{cr_0^2}{4\pi e^2 r^2} \left\| \frac{\partial \mathbf{p}}{\partial t} \times \mathbf{n} \right\|^2 \mathbf{n}, \quad (2.24)$$

and the corresponding total emitted power is

$$P(t) = \int_{\Omega} \mathbf{S} \, d\sigma = \frac{2cr_0^2}{3e^2} \left\| \frac{\partial \mathbf{p}}{\partial t} \right\|^2, \quad (2.25)$$

where integration is carried out over a closed contour Ω around the emitter (the coordinate origin).

Given Eq. (2.20) for an electron in a plane monochromatic field, the equations Eqs. (2.22) and (2.23) take the following form

$$\mathbf{E}_{out}(\mathbf{r}, t) = \frac{r_0}{r} \left[\mathbf{E}_{in} \left(t - \frac{r}{c} \right) \times \mathbf{n} \right] \times \mathbf{n}, \quad (2.26a)$$

$$\mathbf{H}_{out}(\mathbf{r}, t) = \frac{r_0}{r} \mathbf{E}_{in} \left(t - \frac{r}{c} \right) \times \mathbf{n}. \quad (2.26b)$$

The wavevector \mathbf{k} of such a scattered wave is collinear with the radius-vector of the registration point $\mathbf{k} \parallel \mathbf{r}$ and has the absolute value equal to that of the incident wave $\|\mathbf{k}\| = \|\mathbf{k}_i\|$. The fact that the incident electric field is taken at retarded time $t' = t - r/c$ introduce phase difference between electromagnetic waves scattered by electrons at different spatial points.

The quantity typically measured in a scattering experiment is the differential scattering cross-section $d\sigma/d\Omega$ that is the ratio of the energy scattered to the solid angle $d\Omega$ and the incident energy. The differential scattering cross-section is proportional to the corresponding Poynting vectors (2.11) and, therefore, to the square of the electric field

$$\frac{d\sigma}{d\Omega} = r^2 \frac{\|\mathbf{S}_{out}\|}{\|\mathbf{S}_{in}\|} = r^2 \frac{\|\mathbf{E}_{out}\|^2}{\|\mathbf{E}_{in}\|^2}, \quad (2.27)$$

that, given Eq. (2.26), takes the following form

$$\frac{d\sigma}{d\Omega} = r_0^2 |\boldsymbol{\epsilon}_i \cdot \boldsymbol{\epsilon}|^2, \quad (2.28)$$

where $\boldsymbol{\epsilon}_i = \mathbf{E}_{in}/\|\mathbf{E}_{in}\|$ and $\boldsymbol{\epsilon} = \mathbf{E}_{out}/\|\mathbf{E}_{out}\|$ are polarization vectors of the incident and scattered waves, respectively. The dot product defines the dependence of the scattered intensity on the scattering angle θ , called polarization factor

$$P(\theta) = \begin{cases} 1 & \text{scattering plane perpendicular to } \boldsymbol{\epsilon}_i \\ \cos^2(\theta) & \text{scattering plane parallel to } \boldsymbol{\epsilon}_i \end{cases} \quad (2.29)$$

This factor defines the toroidal shape of the radiation pattern of a single electron shown in Fig. 2.3.

The total scattering cross-section σ_T can be obtained by integration of Eq. (2.28) over the unit sphere

$$\begin{aligned} \sigma_T &= \int_{\Omega} r_0^2 |\boldsymbol{\epsilon}_i \cdot \boldsymbol{\epsilon}|^2 d\Omega = \int_0^{2\pi} \int_{-\pi/2}^{\pi/2} r_0^2 \cos^2(\theta) \cos(\theta) d\theta d\varphi = \\ &= \frac{8\pi}{3} r_0^2 \approx 0.665 \times 10^{-28} \text{ m}^2. \end{aligned} \quad (2.30)$$

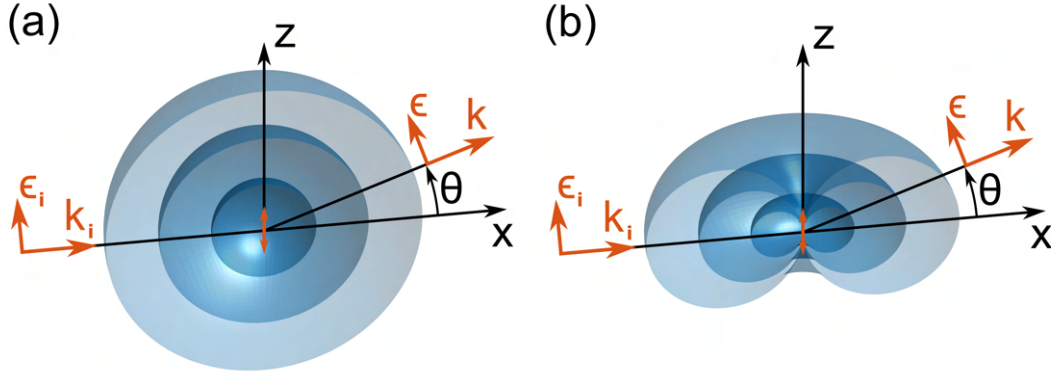


Figure 2.3: The classical description of the scattering of X-rays by an electron. The incident electromagnetic wave with the wavevector \mathbf{k}_i and the polarization vector $\boldsymbol{\epsilon}_i$ makes the electron at the coordinate origin to oscillate and emit the scattered wave with the wavevector \mathbf{k} and the polarization vector $\boldsymbol{\epsilon}$. a) Surfaces of constant phases of the scattered electromagnetic wave show the spherical wavefront. b) Surfaces of constant amplitude of electric field of the scattered electromagnetic wave show the $\cos(\theta)$ polarization factor. Adapted from [32].

This result was first obtained by J. J. Thomson [52], and is referred to as the Thomson cross-section for scattering of electromagnetic waves by a free electron. Noteworthy, both differential and total scattering cross-sections for a free electron do not depend on the incident X-ray energy. This is not valid for bounded electron in an atom, especially when the incident X-ray energy is close to the electron binding energy, as will be discussed below.

The classical electrodynamics postulate that the electromagnetic wave frequency can not change upon scattering. However, from the view of quantum physics, the incident photons can change their energy and momentum when collided with an electron. The latter process was described by Compton in the early 1920th [53, 54]. This process significantly contribute to the attenuation of incident X-rays, especially at high energies, that is used, for example, in medical applications [55, 56]. Due to their nature, the scattered X-rays in this case are incoherent and, therefore, can not give any constructive interference. Thus, they give diffuse background in scattering patterns that can not be used to extract the structural information about the sample. On the other hand, the spectrum of the inelastic-scattered X-rays provide information about the electron momentum distribution in material that is used in the technique called X-ray Compton scattering [57].

2.1.2.2 Scattering at several electrons

Let us consider now a continuous electron density distribution $\rho(\mathbf{r}')$, on which a plane X-ray wave is scattered. From the linearity of Eq. (2.21), the resulting scattered electric field is a sum of partial fields scattered by different electrons and defined by Eq. (2.22). For simplicity, let us put the coordinate origin to the center of mass of the electron distribution, as shown in Fig. 2.4. Then, the electric field $\mathbf{E}_s(\mathbf{r}, t)$ scattered by

an electron at the spatial point \mathbf{r}_s can be represented as

$$\mathbf{E}_s(\mathbf{r}, t) = \frac{r_0}{r} \epsilon \|\mathbf{E}_{in}\| \exp \left[i \mathbf{k}_i \cdot \mathbf{r}_s - i \omega \left(t - \frac{\|\mathbf{r} - \mathbf{r}_s\|}{c} \right) \right], \quad (2.31)$$

where \mathbf{k}_i and \mathbf{k} are wavevectors of the incident and scattered waves, respectively.

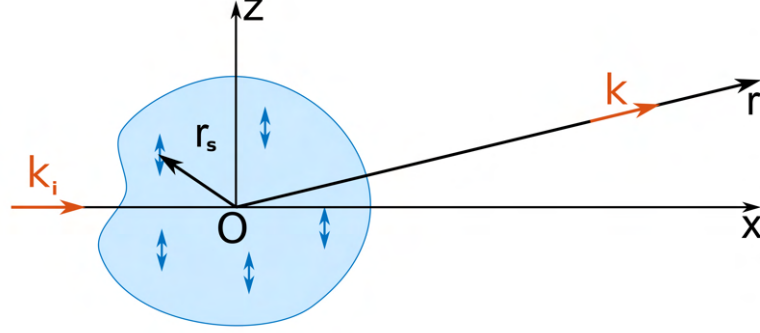


Figure 2.4: A scheme of scattering from an electron density distribution. The incident electromagnetic wave with the wavevector \mathbf{k}_i is scattered by an electron at the spatial point \mathbf{r}_s in the direction of radius-vector \mathbf{r} with the wavevector \mathbf{k} . Not in scale, $\|\mathbf{r}\| \gg \|\mathbf{r}_s\|$.

Given $\|\mathbf{r}\| \gg \|\mathbf{r}_s\|$, one can approximate $\|\mathbf{r} - \mathbf{r}_s\| \approx r - \mathbf{r} \cdot \mathbf{r}_s / r$ and $\mathbf{r} / r = \mathbf{k} / k$. Inserting these to Eq. (2.31), one gets

$$\mathbf{E}_s(\mathbf{r}, t) = \frac{r_0}{r} \epsilon \|\mathbf{E}_{in}\| \exp \left[i (\mathbf{k}_i - \mathbf{k}) \cdot \mathbf{r}_s - i \omega \left(t - \frac{r}{c} \right) \right], \quad (2.32)$$

where the last phase term $i \omega (t - r/c)$ is the same for any scattering electron and can be neglected. Typically, one introduces a new vector $\mathbf{q} = \mathbf{k} - \mathbf{k}_i$ that is known as the momentum transfer or scattering vector. For several discrete free electrons, the resulting electric field will be equal to

$$\mathbf{E}(\mathbf{q}) = \frac{r_0}{r} \epsilon \|\mathbf{E}_{in}\| \sum_{s=1}^N e^{-i \mathbf{q} \cdot \mathbf{r}_s}, \quad (2.33)$$

and, for a continuous electron density $\rho(\mathbf{r}')$ – to

$$\mathbf{E}(\mathbf{q}) = \frac{r_0}{r} \epsilon \|\mathbf{E}_{in}\| \int_V \rho(\mathbf{r}') e^{-i \mathbf{q} \cdot \mathbf{r}'} d\mathbf{r}'. \quad (2.34)$$

From Eq. (2.27), the corresponding differential scattering cross-sections are then

$$\frac{d\sigma}{d\Omega}(\mathbf{q}) = r_0^2 |\epsilon_i \cdot \epsilon|^2 \left| \sum_{s=1}^N e^{-i \mathbf{q} \cdot \mathbf{r}_s} \right|^2, \quad (2.35a)$$

$$\frac{d\sigma}{d\Omega}(\mathbf{q}) = r_0^2 |\epsilon_i \cdot \epsilon|^2 \left| \int_{\mathbb{R}^3} \rho(\mathbf{r}') e^{-i \mathbf{q} \cdot \mathbf{r}'} d\mathbf{r}' \right|^2, \quad (2.35b)$$

that give more complex angular dependence of the scattered intensity from the sample.

In practice, people measure the quantity that is proportional to those differential cross-sections – the dimensionless scattered intensity

$$I(\mathbf{q}) = \left| \int_{\mathbb{R}^3} \rho(\mathbf{r}) e^{-i\mathbf{q}\cdot\mathbf{r}} d\mathbf{r} \right|^2 \propto |\mathcal{F}[\rho(\mathbf{r})]|^2, \quad (2.36)$$

where \mathcal{F} denotes a three-dimensional Fourier transform from real space into so-called reciprocal space [58]. The direct \mathcal{F} and inverse \mathcal{F}^{-1} Fourier transforms for an arbitrary function are defined as

$$\mathcal{F}[f(\mathbf{r})] = \frac{1}{(2\pi)^3} \int_{\mathbb{R}^3} f(\mathbf{r}) e^{-i\mathbf{q}\cdot\mathbf{r}} d\mathbf{r}, \quad (2.37a)$$

$$\mathcal{F}^{-1}[g(\mathbf{q})] = \int_{\mathbb{R}^3} g(\mathbf{q}) e^{i\mathbf{q}\cdot\mathbf{r}} d\mathbf{q}. \quad (2.37b)$$

In the considerations above, we neglected the secondary and subsequent scattering of already scattered waves due to the low probability of such events. Such approach is called the kinematic theory of diffraction. In some cases, for example, for thick crystalline samples, the secondary scattering plays a significant role in the interaction of incident wave with the sample, and it cannot be omitted. The full theory taking into account these effects is called the dynamical theory of diffraction. However, in this Thesis, we remain within the framework of the kinematic theory of diffraction, which is sufficient to describe the results of the considered experiments.

2.1.3 X-ray scattering at an atom

The main difference between free electrons and an electron in an atom is the binding energy in the latter case. The binding energy of the electrons on the most outer shells is much lower than that of X-rays, but the inner shells (K, L and, sometimes, M) have the binding energies in the range of X-ray wave energies. When an X-ray wave illuminates an atom, the electrons on the outer shells behave almost as free ones, while the scattering on the electrons with the binding energy higher than the incident X-ray energy is suppressed. In the limit, when the incident X-ray energy is higher than all binding energies of the atom and all electron behave as free ones, the scattering is fully described by the so-called atomic form-factor

$$f^0(\mathbf{q}) = \int_{\mathbb{R}^3} \rho(\mathbf{r}) e^{-i\mathbf{q}\cdot\mathbf{r}} d\mathbf{r}, \quad (2.38)$$

where $\rho(\mathbf{r})$ is the electron density distribution in the atom. The atomic form-factor at $\|\mathbf{q}\| \rightarrow 0$ approaches $f^0(0) \rightarrow Z$, where Z is the number of electrons in the atom. At large scattering vectors $\|\mathbf{q}\| \rightarrow \infty$ different electrons scatter with random phases and, thus, $f^0(\infty) \rightarrow 0$.

To describe scattering at lower X-ray energies, when the inner electrons are bound, one introduces the dispersion corrections $f'(h\nu)$ and $f''(h\nu)$ as follows

$$f(\mathbf{q}, h\nu) = f^0(\mathbf{q}) + f'(h\nu) + if''(h\nu), \quad (2.39)$$

where the first additional term describes the suppressed scattering and the second – the absorption by the atom. Both factors are highly dependent on the incident energy near the absorption edge of the particular chemical element that is used in some techniques, for example, in Anomalous X-ray Scattering (AXRS) [59] and spectroscopic methods described above. In practice, the atomic form-factors of most chemical elements and important ions are calculated and represented in the form of analytical approximation

$$f^0(q) = \sum_{i=1}^4 a_i \exp \left[-b_i \left(\frac{q}{4\pi} \right)^2 \right] + c, \quad (2.40)$$

where a_i , b_i and c are the parameters tabulated in, for example, International Tables for Crystallography [60]. Examples of the atomic form-factors for different elements are shown in Fig. 2.5.

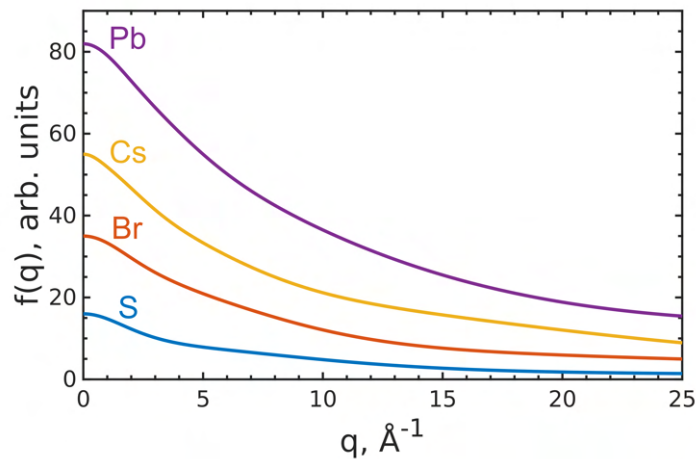


Figure 2.5: Atomic form-factor $f^0(q)$ for different elements: lead Pb, caesium Cs, bromine Br and sulfur S. Plotted according to Eq. (2.40) using the constants from [60].

2.1.4 X-ray scattering by macroscopic particles

2.1.4.1 Scattering at a single particle

Let us consider scattering of a plane X-ray wave on a macroscopic particle consisting of the same atoms. The electronic density, which defines the resulting scattering intensity according to Eq. (2.36), can be represented as

$$\rho(\mathbf{r}) = \rho_{el}(\mathbf{r}) * [\rho_{at}(\mathbf{r})s_p(\mathbf{r})] , \quad (2.41)$$

where $\rho_{el}(\mathbf{r})$ is the electron density in a single atom, $\rho_{at}(\mathbf{r})$ is the density of atoms in the particle, $s_p(\mathbf{r})$ is the shape function of the particle, which is equal to unity inside the particle and to zero everywhere outside, and $f(\mathbf{r}) * g(\mathbf{r})$ denotes the convolution operator $f(\mathbf{r}) * g(\mathbf{r}) = \int f(\mathbf{r}')g(\mathbf{r} - \mathbf{r}') d\mathbf{r}'$. According to the Convolution theorem [58],

$$\mathcal{F}[f(\mathbf{r}) * g(\mathbf{r})] = \mathcal{F}[f(\mathbf{r})] \mathcal{F}[g(\mathbf{r})] \quad (2.42)$$

and vice versa

$$\mathcal{F}[f(\mathbf{r})g(\mathbf{r})] = \mathcal{F}[f(\mathbf{r})] * \mathcal{F}[g(\mathbf{r})] . \quad (2.43)$$

Then, the scattered intensity corresponding to the electron density (2.41) can be represented in the following form

$$\begin{aligned} I(\mathbf{q}) &= \left| \int_{\mathbb{R}^3} \rho_{el}(\mathbf{r})e^{-i\mathbf{q}\cdot\mathbf{r}} d\mathbf{r} \right|^2 \left| \left[\int_{\mathbb{R}^3} \rho_{at}(\mathbf{r})e^{-i\mathbf{q}\cdot\mathbf{r}} d\mathbf{r} \right] * \left[\int_{\mathbb{R}^3} s_p(\mathbf{r})e^{-i\mathbf{q}\cdot\mathbf{r}} d\mathbf{r} \right] \right|^2 = \\ &= V_p^2 |f(\mathbf{q})|^2 \left| \left[\int_{\mathbb{R}^3} \rho_{at}(\mathbf{r})e^{-i\mathbf{q}\cdot\mathbf{r}} d\mathbf{r} \right] * F(\mathbf{q}) \right|^2 , \end{aligned} \quad (2.44)$$

where $f(\mathbf{q})$ is the atomic form-factor (2.39), V_p is the particle volume and

$$F_p(\mathbf{q}) = \frac{1}{V_p} \int_{\mathbb{R}^3} s_p(\mathbf{r})e^{-i\mathbf{q}\cdot\mathbf{r}} d\mathbf{r} \quad (2.45)$$

is the particle form-factor amplitude.

The atomic density in a macroscopic particle has two distinct characteristic length scales: one on the scale of inter-atomic distance and one on the macroscopic level. Then, we can decompose the atomic density $\rho_{at}(\mathbf{r}) = \overline{\rho_{at}} + \delta\rho_{at}(\mathbf{r})$ into the mean atomic density $\overline{\rho_{at}}$ and a deviation $\delta\rho_{at}(\mathbf{r})$, which describes the atomic structure of the macro-

scopic sample. Then, the scattered intensity takes the form

$$I(\mathbf{q}) = V_p^2 |f(\mathbf{q})|^2 \left| \overline{\rho_{at}} F_p(\mathbf{q}) + \left[\int_{\mathbb{R}^3} \delta\rho_{at}(\mathbf{r}) e^{-i\mathbf{q}\cdot\mathbf{r}} d\mathbf{r} \right] * F_p(\mathbf{q}) \right|^2, \quad (2.46)$$

where the first term corresponds to the macroscopic structure, while the second – to the atomic short-range structure of the sample. Due to different length scales, these two terms contribute into the sum at different q -values. The first term contributes into the scattered intensity at low q -values, while the second – mostly at high q -values. The scattering from the internal structure will be discussed below, in this section we consider only the scattering from macroscopic objects and will omit the second term. The scattering intensity from macroscopic objects is known as SAXS, because low q -values correspond to small scattering angles. The SAXS intensity is defined then by

$$I_{SAXS}(\mathbf{q}) = \overline{\rho_{at}}^2 V_p^2 |f(\mathbf{q})|^2 P_p(\mathbf{q}), \quad (2.47)$$

where $P_p(\mathbf{q}) = |F_p(\mathbf{q})|^2$ is the particle form-factor.

For a particle with arbitrary shape, the form-factor can be calculated only numerically, but for particles with simple geometrical shapes it can be represented in an analytical form.

Let us first consider a spherical particle with the radius R , then the form-factor amplitude (2.45) is isotropic, depends only on the absolute value of the scattering vector $q = \|\mathbf{q}\|$, and can be calculated as

$$\begin{aligned} F_p(q) &= \frac{1}{V_p} \int_0^R \int_0^\pi \int_0^{2\pi} e^{-iqr \cos\theta} r^2 \sin\theta d\varphi d\theta dr = \frac{4\pi}{V} \int_0^R \frac{\sin(qr)}{qr} r^2 dr = \\ &= 3 \frac{\sin(qR) - qR \cos(qR)}{(qR)^3} = 3j_1(qR), \end{aligned} \quad (2.48)$$

where $j_1(x)$ is the spherical Bessel function of the first kind.

For a cubic particle with the edge length $a = 2R$ oriented along the coordinate axes, the form-factor amplitude (2.45) can be calculated as follows

$$\begin{aligned} F_p(\mathbf{q}) &= \frac{1}{V_p} \int_{-R}^R \int_{-R}^R \int_{-R}^R e^{-i(q_x x + q_y y + q_z z)} dx dy dz = \\ &= \frac{1}{2R} \int_{-R}^R e^{iq_x x} dx \frac{1}{2R} \int_{-R}^R e^{iq_y y} dy \frac{1}{2R} \int_{-R}^R e^{iq_z z} dz = \\ &= \frac{\sin(q_x R)}{q_x R} \frac{\sin(q_y R)}{q_y R} \frac{\sin(q_z R)}{q_z R}, \end{aligned} \quad (2.49)$$

In contrast to the spherical form-factor (2.48), the cubic form-factor is highly anisotropic that allows determination of the cube angular orientation from two-dimensional (2D) scattering patterns. For both spherical (2.48) and cubic (2.49) form-factors, their scaling is inversely proportional to the particle size. Examples of spherical and cubic form-factors for different sizes of the particles are shown in Fig. 2.6.

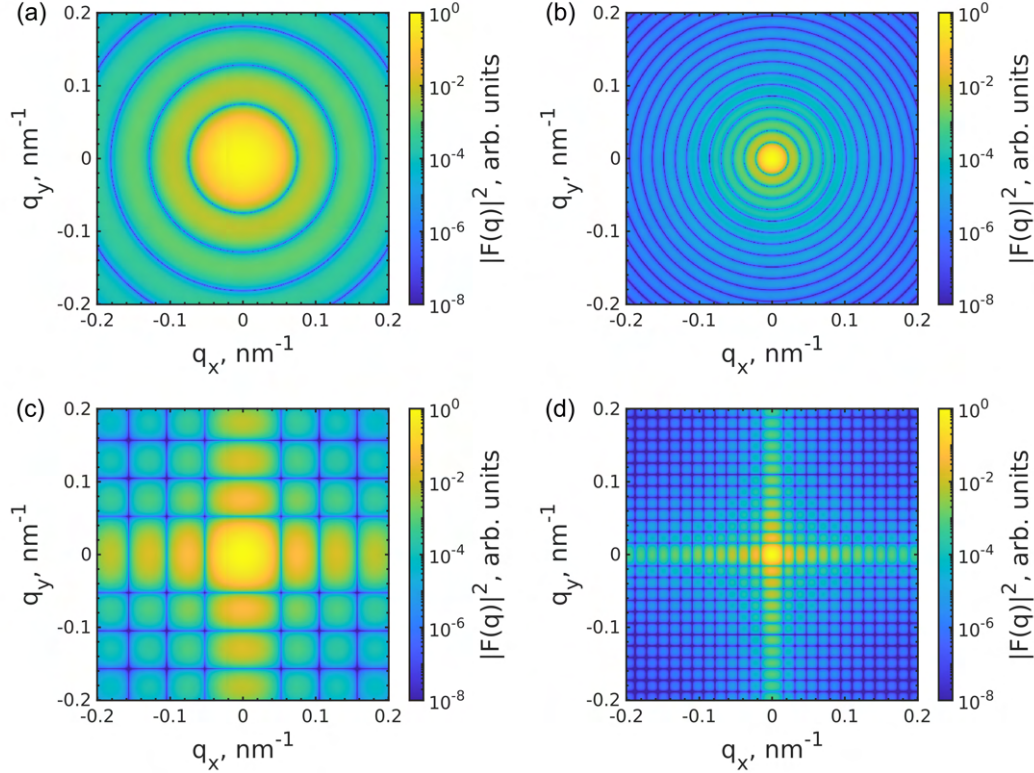


Figure 2.6: Cuts $q_z = 0$ through the form-factor $P_p(\mathbf{q}) = |F_p(\mathbf{q})|^2$ for (a,b) spheres with the radii $R = 60$ nm (a) and $R = 200$ nm (b), and (c,d) cubes with the edge lengths $a = 2R = 120$ nm (a) and $a = 2R = 400$ nm (b).

2.1.4.2 Scattering at several particles

The intensity scattered by one particle is typically too low to be properly measured. To obtain enough statistics one measures scattering from a system containing many identical particles. Then, the electronic density in such a system is defined by modified Eq. (2.41) as

$$\rho(\mathbf{r}) = \rho_{el}(\mathbf{r}) * [\rho_{at}(\mathbf{r})s_p(\mathbf{r})] * [\rho_p(\mathbf{r})s_{smpl}(\mathbf{r})] , \quad (2.50)$$

where $\rho_p(\mathbf{r})$ is the particle density in the sample and $s_{smpl}(\mathbf{r})$ is the shape function of the sample (probe). We note, that since the macroscopic particles are classical objects, at each moment their positions can be described by delta-functions and the particle density is defined by a Fourier series as in Eq. (2.35a) instead of continuous Fourier

transform. Then, the corresponding scattered intensity can be represented as

$$I_{SAXS}(\mathbf{q}) = \overline{\rho_{at}}^2 V_p^2 |f(\mathbf{q})|^2 P_p(\mathbf{q}) \left| \sum_{s=1}^{N_p} e^{i\mathbf{q}\cdot\mathbf{r}_s} * \int_{\mathbb{R}^3} s_{smp}(\mathbf{r}) e^{i\mathbf{q}\cdot\mathbf{r}} d\mathbf{r} \right|^2, \quad (2.51)$$

where N_p is the number of particles in the sample, \mathbf{r}_s are the coordinates of the particles, and the integral including the shape function approaches a delta-function $\int s_{smp}(\mathbf{r}) \exp(i\mathbf{q}\cdot\mathbf{r}) d\mathbf{r} \rightarrow \delta(\mathbf{q})$ when the sample/probe size is big enough. Then, Eq. (2.51) takes the following form

$$I_{SAXS}(\mathbf{q}) = \overline{\rho_{at}}^2 V_p^2 |f(\mathbf{q})|^2 P_p(\mathbf{q}) S(\mathbf{q}), \quad (2.52)$$

where $S(\mathbf{q})$ is the structure factor

$$S(\mathbf{q}) = \left| \sum_{s=1}^{N_p} e^{-i\mathbf{q}\cdot\mathbf{r}_s} \right|^2 = \sum_{s=1}^{N_p} e^{i\mathbf{q}\cdot\mathbf{r}_s} \sum_{s'=1}^{N_p} e^{-i\mathbf{q}\cdot\mathbf{r}_{s'}} = \sum_{s=1}^{N_p} \sum_{s'=1}^{N_p} e^{i\mathbf{q}\cdot(\mathbf{r}_s - \mathbf{r}_{s'})} \quad (2.53)$$

that defines the contribution of interference between the X-rays scattered by different particles in the system into the scattered intensity. It will be discussed in details below in subsections 2.1.5 and 2.1.6 for the crystalline and short-range orders of the particles.

Let us consider that the distance between the particles is much larger than the characteristic size of the particles themselves and is random for each pair of the particles (for example, in a very dilute dispersion of the particles). Then, the structure factor (2.53) can be represented as follows

$$\begin{aligned} S(\mathbf{q}) &= \sum_{s=1}^{N_p} \sum_{s'=1}^{N_p} e^{i\mathbf{q}\cdot(\mathbf{r}_s - \mathbf{r}_{s'})} = \sum_{s=s'=1}^{N_p} e^{i\mathbf{q}\cdot(\mathbf{r}_s - \mathbf{r}_{s'})} + \sum_{s=1}^{N_p} \sum_{s' \neq s}^{N_p} e^{i\mathbf{q}\cdot(\mathbf{r}_s - \mathbf{r}_{s'})} = \\ &= N_p + \sum_{s=1}^{N_p} \sum_{s' \neq s}^{N_p} e^{i\mathbf{q}\cdot(\mathbf{r}_s - \mathbf{r}_{s'})} \rightarrow N_p \end{aligned} \quad (2.54)$$

because the interference terms are of high frequency and are all random and, thus, do not give any constructive interference. Other cases of the structure factor calculations, when the interference terms can not be omitted, are given below.

Then, the scattered intensity from a dilute dispersion of particles is simply

$$I_{SAXS}(\mathbf{q}) = N_p \overline{\rho_{at}}^2 V_p^2 |f(\mathbf{q})|^2 P_p(\mathbf{q}) \quad (2.55)$$

that gives enhancement in N_p times in comparison to the scattering from one particle that notably improve the statistics. One should note that in diluted samples the particles are typically angularly disordered and the measured intensity (form-factor) is averaged over all possible orientations.

In practice, the synthesized particles rarely have the same size. Typically, they are polydisperse and their sizes/shapes can be described by a distribution of some parameters with the probability density $D(\mathbf{p})$, where \mathbf{p} is the vector of parameters $\mathbf{p} = (p_1, p_2, \dots, p_n)$. Then, the resulting scattered intensity is averaged over the distribution

$$I_{SAXS}(\mathbf{q}) = N_p |f(\mathbf{q})|^2 \int_{\mathbb{R}^n} D(\mathbf{p}) \overline{\rho_{at}}(\mathbf{p})^2 V_p(\mathbf{p})^2 P_p(\mathbf{q}, \mathbf{p}) d\mathbf{p}, \quad (2.56)$$

that gives possibility to fit the parameters \mathbf{p} to the measured scattered intensities.

Study of SAXS is widely applied in the technique of the same name - SAXS [61] that is especially useful to study nanoparticles [62] and biological macromolecules [63].

2.1.5 X-ray scattering from a crystal

2.1.5.1 Crystalline structures

Let us consider a crystal – an ordered periodic arrangement of constituents (atoms, ions, molecules, or macroscopic particles) with long-range order that is characterized by high anisotropy and symmetries. The basis for the symmetries is the spatial periodicity – the fact that the structure is invariant to translations [64]. This fact can be formalized if one introduces translation basis $\langle \mathbf{a}_1, \mathbf{a}_2, \mathbf{a}_3 \rangle$ composed of vectors \mathbf{a}_i that are possible translations in three different non-coplanar directions. Then, any translation can be represented as

$$\mathbf{a}_{n_1 n_2 n_3} = n_1 \mathbf{a}_1 + n_2 \mathbf{a}_2 + n_3 \mathbf{a}_3, \quad n_1, n_2, n_3 \in \mathbb{Z}. \quad (2.57)$$

Basically, the number of possible basis is unlimited, as soon as any linear combination $\mathbf{a}'_j = \sum_{i=1}^3 \alpha_{ij} \mathbf{a}_i$ can be chosen as a lattice basis as well, but there are some conventions discussed below.

If one choose one of the lattice constituents (a lattice point) and take all possible translations from this node, he will get a crystalline lattice. The parallelepiped built up on the vectors $\langle \mathbf{a}_1, \mathbf{a}_2, \mathbf{a}_3 \rangle$ taken from one of the lattice point is called a unit cell. The whole crystalline lattice is composed by all possible translations of such parallelepipeds. Typically, the unit cells are described in terms of the unit cell parameters that are lengths of the edges $a = \|\mathbf{a}_1\|$, $b = \|\mathbf{a}_2\|$, $c = \|\mathbf{a}_3\|$ and angles between the edges: α between \mathbf{a}_2 and \mathbf{a}_3 , β between \mathbf{a}_1 and \mathbf{a}_3 and γ between \mathbf{a}_1 and \mathbf{a}_2 (see Fig. 2.7).

By a convention, there are two fundamental types of unit cells and corresponding basis. The unit cell with the smallest possible volume is called primitive unit cell. The unit cell with the smallest possible volume that have the same symmetries as the whole lattice (including rotational, mirror etc.) is called a conventional unit cell. The possible rotational and mirror symmetries give 14 types of the unit cells that are called

the Bravais lattices that are shown in Fig. 2.7. The primitive unit cells contain only one lattice point per unit cell, while the non-primitive conventional ones (centered) contain more than one lattice point per cell. The unit cell parameters corresponding to these Bravais lattices are summarized in Table 2.1.

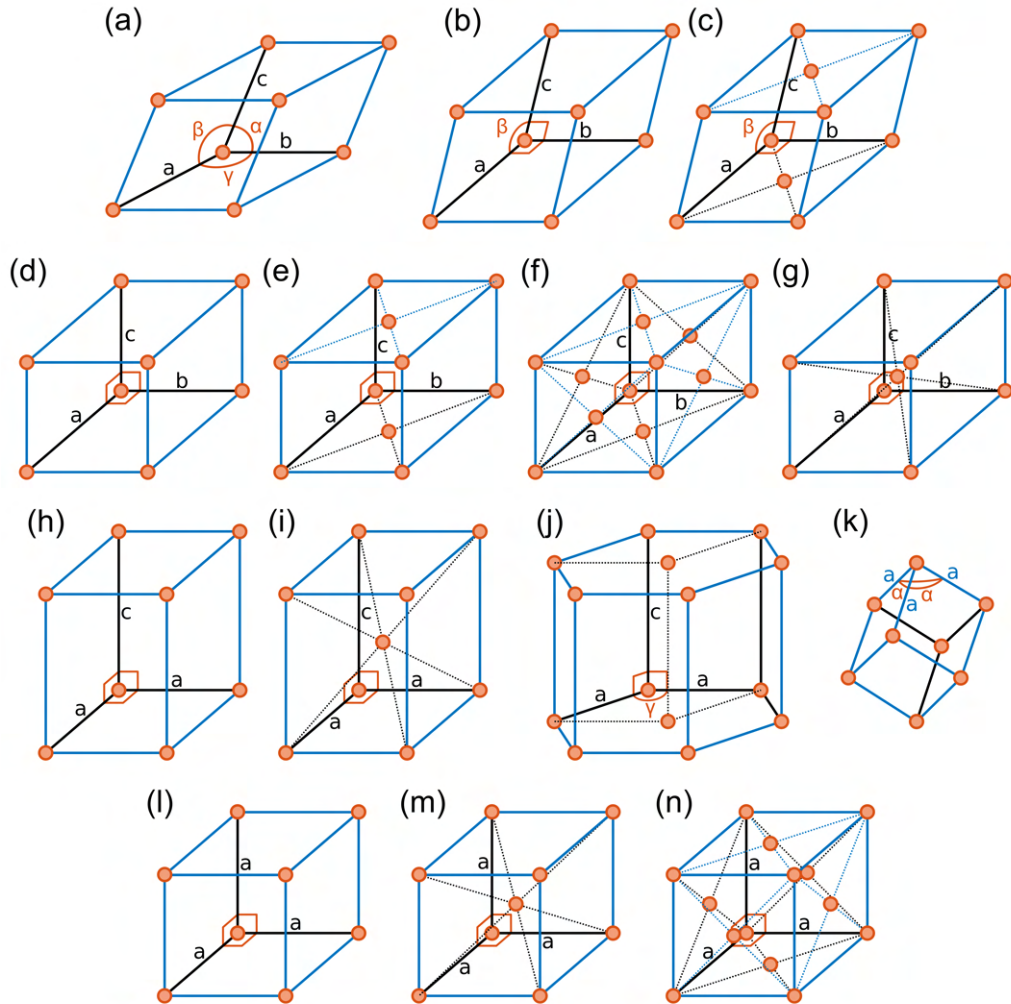


Figure 2.7: Sketches of 14 Bravais lattices: triclinic (a); monoclinic primitive (b) and base-centered (c); orthorhombic primitive (d), base-centered (e), face-centered (f) and body-centered (g); tetragonal primitive (h) and body-centered (i); hexagonal (j); rhombohedral (k); cubic primitive (l), body-centered (m) and face-centered (n). Adapted from [64].

The full description of possible symmetries of the crystalline lattices is given in terms of space groups [65]. The Bravais lattices represent only 14 out of 230 space groups, but usually they are enough to describe quite complex structures, including those studied in this work.

For atomic crystals the main factor defining the crystal structure is the symmetry of the chemical bonds of the atoms constituting the crystal. For crystals consisting of macroscopic particles (so-called colloidal crystals discussed in details in Section 2.3), the symmetry is mostly defined by the particle shape. One of the important parameters in this case is the packing density $\eta = N_p V_p / V_{uc}$, where N_p is the number of particles

Table 2.1: Unit cell parameters corresponding to the Bravais lattices

Lattice	Edge lengths	Angles
Triclinic	$a \neq b \neq c$	$\alpha \neq \beta \neq \gamma$
Monoclinic	$a \neq b \neq c$	$\alpha = \gamma = 90^\circ, \beta \neq 90^\circ$
Orthorhombic	$a \neq b \neq c$	$\alpha = \beta = \gamma = 90^\circ$
Tetragonal	$a = b \neq c$	$\alpha = \beta = \gamma = 90^\circ$
Hexagonal	$a = b \neq c$	$\alpha = \gamma = 90^\circ, \gamma = 120^\circ$
Rhombohedral	$a = b = c$	$\alpha = \beta = \gamma$
Cubic	$a = b = c$	$\alpha = \beta = \gamma = 90^\circ$

per unit cell, V_p is the volume of the particles and V_{uc} is the volume of the unit cell. Typically, the particles tend to maximize the packing density and form so-called close-packed structures.

Let us consider packing of spherical particles with radius R into different lattices. Obviously, the closest packing for a certain lattice is provided when the nearest-neighbour distance d_{NN} is equal to $2R$. A single simple cubic unit cell contains one sphere and provides the nearest-neighbour distance equal to the unit cell parameter $d_{NN} = a$ that gives a packing density of $\eta_{sc} = (4/3)\pi R^3 / (2R)^3 = \pi/6 \approx 0.52$. A single body-centered cubic (bcc) lattice contains two spheres and provides the nearest-neighbour distance equal to the half of the cube diagonal $d_{NN} = a\sqrt{3}/2$ that gives a packing density of $\eta_{bcc} = 2(4/3)\pi R^3 / (4R/\sqrt{3})^3 = \pi\sqrt{3}/8 \approx 0.68$. A single face-centered cubic (fcc) unit cell contains four spheres and provides the nearest-neighbour distance equal to the half of the square facet diagonal $d_{NN} = a\sqrt{2}/2$ that gives a packing density of $\eta_{fcc} = 4(4/3)\pi R^3 / (2\sqrt{2}R)^3 = \pi\sqrt{2}/6 \approx 0.74$. The sketches of these structures are shown in Fig. 2.8(a-c).

The value for the fcc lattice is the highest theoretically possible for spherical particles [66]. Noteworthy, this is not the only crystalline structure that provides the highest packing density. Another one is so-called hcp structure providing the same packing density of $\eta_{hcp} = \pi\sqrt{2}/6 \approx 0.74$. Both fcc and hcp structures consist of hexagonal layers, which are the closest possible 2D arrangement of spheres, that are stacked together, but the stacking sequences are different. Two possible sequences in respect to the reference layer (denoted as A) are shown in Fig. 2.8(d,e). The ...ABC... sequence corresponds to the fcc structure, where the hexagonal 2D layer represent (111) planes, while the ...ABAB... sequence corresponds to the hcp structure, where the hexagonal 2D layers represent (001) planes. The negligible difference in energy between fcc and hcp stacking motifs [67] makes the close-packed structures prone to irregularities in the stacking sequence that are called stacking faults and represent a class of plane defects described below.

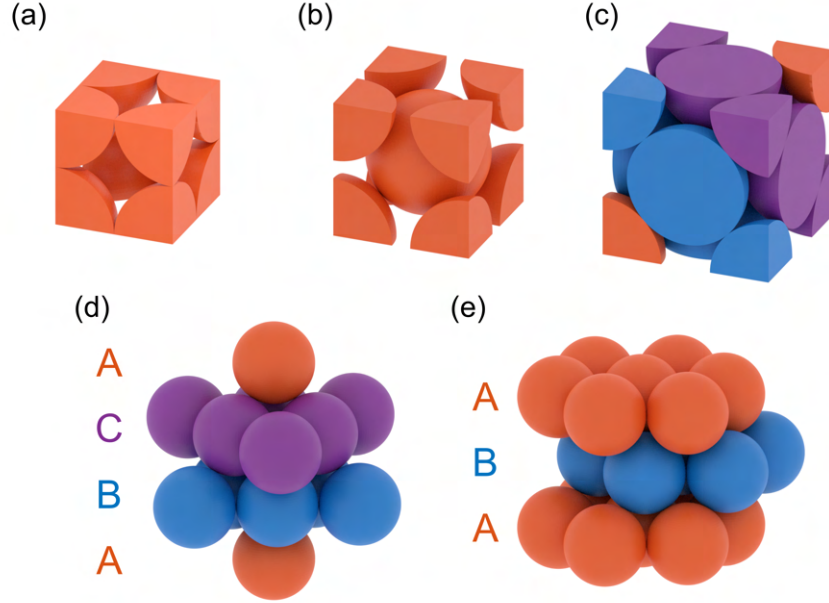


Figure 2.8: (a,b,c) Packing of spheres of equal radius into different cubic unit cells: simple cubic (a), bcc (b) and fcc (c). (d,e) Close-packed structures for spheres: fcc (a) and hexagonal close-packed (hcp) (b). The colours of the corresponding 2D layers in panels (c) and (d) are identical.

2.1.5.2 Reciprocal lattice

Let us turn now to scattering from such crystalline structures. The electron density in the crystalline material can be described as

$$\rho(\mathbf{r}) = \left[\sum_{n_1, n_2, n_3 = -\infty}^{\infty} \sum_{s=1}^{N_{uc}} [\rho_s(\mathbf{r}) * \delta(\mathbf{r} - \mathbf{a}_{n_1 n_2 n_3} - \mathbf{a}'_s)] \right] s_{\text{smp}}(\mathbf{r}), \quad (2.58)$$

where $\rho_s(\mathbf{r})$ is the electron density of the constituents in the s -th lattice point, \mathbf{a}'_s is the radius-vector of the s -th particle out of N_{uc} inside each unit cell (the basis), $\mathbf{a}_{n_1 n_2 n_3}$ is a lattice vector (2.57), and $s_{\text{smp}}(\mathbf{r})$ is the shape function of the whole area (sample) illuminated with the incident X-ray beam. Then, the scattered intensity according to Eq. (2.36) and given Eqs. (2.42) and (2.43) takes the following form

$$I(\mathbf{q}) = \left| \left[\sum_{n_1, n_2, n_3 = -\infty}^{\infty} \sum_{s=1}^{N_{uc}} e^{-i\mathbf{q} \cdot (\mathbf{a}_{n_1 n_2 n_3} + \mathbf{a}'_s)} \int_{\mathbb{R}^3} \rho_s(\mathbf{r}) e^{-i\mathbf{q} \cdot \mathbf{r}} d\mathbf{r} \right] * \int_{\mathbb{R}^3} s_{\text{smp}}(\mathbf{r}) e^{-i\mathbf{q} \cdot \mathbf{r}} d\mathbf{r} \right|^2, \quad (2.59)$$

where the first integral is proportional to the form-factor amplitude $F_s(\mathbf{q})$ of the constituent in the s -th lattice point, either atoms (2.38) or particles (2.45), etc., and the second integral is the form-factor amplitude of the sample itself. For simplicity, let us assume at this stage that the sample is much bigger than the lattice basis vectors and the sample form-factor is equal to a delta-function $\int s_{\text{smp}}(\mathbf{r}) \exp(i\mathbf{q} \cdot \mathbf{r}) d\mathbf{r} \rightarrow \delta(\mathbf{q})$.

Then, Eq. (2.59) takes the following form

$$\begin{aligned}
I(\mathbf{q}) &= \left| \sum_{n_1, n_2, n_3 = -\infty}^{\infty} \sum_{s=1}^{N_{uc}} F_s(\mathbf{q}) e^{-i\mathbf{q} \cdot (\mathbf{a}_{n_1 n_2 n_3} + \mathbf{a}'_s)} \right|^2 = \\
&= \left| \sum_{s=1}^{N_{uc}} F_s(\mathbf{q}) e^{i\mathbf{q} \cdot \mathbf{a}'_s} \right|^2 \left| \sum_{n_1, n_2, n_3 = -\infty}^{\infty} e^{i\mathbf{q} \cdot \mathbf{a}_{n_1 n_2 n_3}} \right|^2,
\end{aligned} \tag{2.60}$$

where the first sum is called unit cell structure factor, while the second is lattice structure factor. In the second sum, the terms have the absolute value of unity and equally distributed phases on the unit circle that give zero after the summation in any case except of

$$\mathbf{q} \cdot \mathbf{a}_{n_1 n_2 n_3} = 2\pi m, \quad m \in \mathbb{Z}, \tag{2.61}$$

for any n_1, n_2 and n_3 , when the sum is infinite.

This condition is called Laue condition and can be represented in the following form

$$\mathbf{q} = \mathbf{g}_{hkl} = h\mathbf{b}_1 + k\mathbf{b}_2 + l\mathbf{b}_3, \quad h, k, l \in \mathbb{Z}, \tag{2.62}$$

where \mathbf{g}_{hkl} is a vector of a so-called reciprocal lattice built up on the reciprocal basis vectors

$$\mathbf{b}_1 = 2\pi \frac{\mathbf{a}_2 \times \mathbf{a}_3}{\mathbf{a}_1 \cdot [\mathbf{a}_2 \times \mathbf{a}_3]}, \quad \mathbf{b}_2 = 2\pi \frac{\mathbf{a}_3 \times \mathbf{a}_1}{\mathbf{a}_1 \cdot [\mathbf{a}_2 \times \mathbf{a}_3]} \quad \text{and} \quad \mathbf{b}_3 = 2\pi \frac{\mathbf{a}_1 \times \mathbf{a}_2}{\mathbf{a}_1 \cdot [\mathbf{a}_2 \times \mathbf{a}_3]}. \tag{2.63}$$

From these explicit definitions of \mathbf{b}_j ; it follows that

$$\mathbf{a}_i \cdot \mathbf{b}_j = \begin{cases} 2\pi & i = j \\ 0 & i \neq j \end{cases} \tag{2.64}$$

i.e. \mathbf{b}_1 is perpendicular to the plane built up on the vectors \mathbf{a}_2 and \mathbf{a}_3 and so on. Examples of the reciprocal lattices for certain lattices in real space are shown in Fig. 2.9.

In general form, the condition (2.61) together with Eq. (2.62) define a set of parallel planes

$$\frac{1}{2\pi} \mathbf{g}_{hkl} \cdot \mathbf{a}_{n_1 n_2 n_3} = hn_1 + kn_2 + ln_3 = m, \quad h, k, l, m \in \mathbb{Z}, \tag{2.65}$$

for every fixed h, k, l and changing m . The numbers h, k and l are typically selected to be coprime (mutually prime), otherwise both sides of Eq. (2.65) can be divided by the corresponding common divider and brought to the same form. A set of such numbers is called Miller indices. Each set of the Miller indices define a set of planes that intersect the axes along $\mathbf{a}_1, \mathbf{a}_2$ and \mathbf{a}_3 at $ma_1/h, ma_2/k$ and ma_3/l , respectively. These planes are normal to \mathbf{g}_{hkl} vector. A single plane or a set of planes are typically referred to as (hkl) .

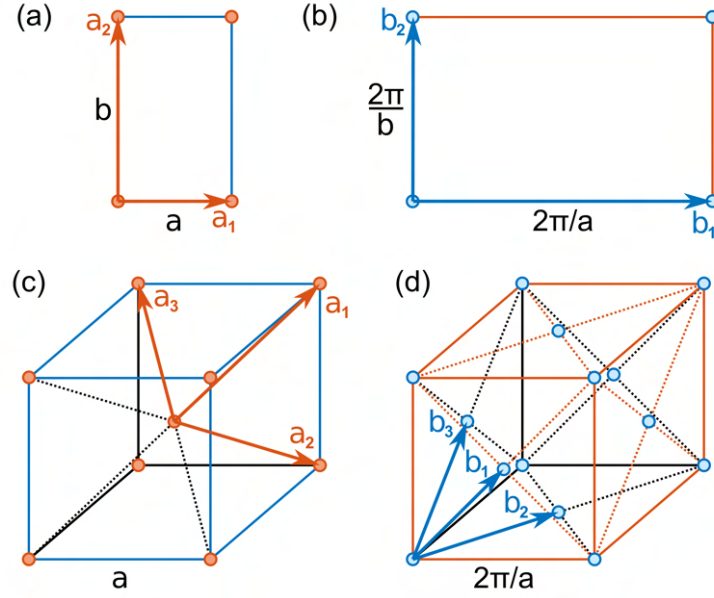


Figure 2.9: Real space lattices: 2D orthorhombic (a) and three-dimensional (3D) bcc (b) with corresponding basis vectors \mathbf{a}_1 , \mathbf{a}_2 and \mathbf{a}_3 . And corresponding to them reciprocal lattices: 2D orthorhombic (c) and 3D fcc (d) with the corresponding basis vectors \mathbf{b}_1 , \mathbf{b}_2 and \mathbf{b}_3 . Adapted from [32].

The distance between two consequent planes from one set is

$$d_{hkl} = \frac{2\pi}{\|\mathbf{g}_{hkl}\|} = \frac{2\pi}{\|h\mathbf{b}_1 + k\mathbf{b}_2 + l\mathbf{b}_3\|}. \quad (2.66)$$

The reciprocal lattice is a convenient tool for interpretation of the scattering experiments with crystalline samples, as discussed below.

2.1.5.3 Crystalline structure factor

As was discussed, the second sum in Eq. (2.60) is not zero only when the condition (2.62) is satisfied. In such a case, the sum can be represented as [32]

$$\left| \sum_{n_1, n_2, n_3 = -\infty}^{\infty} e^{-i\mathbf{q} \cdot \mathbf{a}_{n_1 n_2 n_3}} \right|^2 = N \frac{(2\pi)^3}{V_{uc}} \sum_{h, k, l = -\infty}^{\infty} \delta(\mathbf{q} - \mathbf{g}_{hkl}), \quad (2.67)$$

where N is the number of illuminated unit cells, and V_{uc} is the unit cell volume. Though we assume the lattice to be infinite, the number of illuminated unit cells is limited to N . Otherwise, the scattered intensity in the Bragg peaks tends to infinity. Then, Eq. (2.60) takes the following form

$$I(\mathbf{q}) = N \frac{(2\pi)^3}{V_{uc}} \sum_{h, k, l = -\infty}^{\infty} |F_{hkl}|^2 \delta(\mathbf{q} - \mathbf{g}_{hkl}), \quad (2.68)$$

where F_{hkl} is the unit cell structure factor amplitude at \mathbf{g}_{hkl}

$$F_{hkl} = F_{uc}(\mathbf{g}_{hkl}) = \sum_{s=1}^{N_{uc}} F_s(\mathbf{g}_{hkl}) e^{-i\mathbf{g}_{hkl} \cdot \mathbf{a}'_s}, \quad (2.69)$$

where the summation is done over the N_{uc} particles inside a unit cell. The scattered intensity (2.68) represents narrow intensity spikes at $\mathbf{q} = \mathbf{g}_{hkl}$, which are known as the Bragg peaks. A Bragg peak corresponding to the vector of reciprocal lattice \mathbf{g}_{hkl} is typically referred to as hkl reflection from the (hkl) set of crystallographic planes.

Let us consider two examples of non-primitive unit cells especially relevant for this work: bcc and fcc ones. The lattice basis vectors for a cubic lattice can be defined as $\mathbf{a}_1 = [a00], \mathbf{a}_2 = [0a0], \mathbf{a}_3 = [00a]$, where a is the edge length of the cubic unit cell.

The bcc unit cell contains two lattice points with relative coordinates $\mathbf{a}'_1 = 0$ and $\mathbf{a}'_2 = \frac{1}{2}\mathbf{a}_1 + \frac{1}{2}\mathbf{a}_2 + \frac{1}{2}\mathbf{a}_3$. If all lattice points are occupied by the same constituents (i.e. the form-factors $F_s(\mathbf{q})$ are identical), the corresponding unit cell structure factor amplitude is

$$F_{hkl}^{bcc} = F(\mathbf{g}_{hkl}) \left[1 + e^{-i\pi(h+k+l)} \right] = \begin{cases} 2F_s(\mathbf{g}_{hkl}) & h+k+l \text{ is even} \\ 0 & \text{otherwise} \end{cases} \quad (2.70)$$

An fcc unit cell contains four lattice points with relative coordinates $\mathbf{a}'_1 = 0, \mathbf{a}'_2 = \frac{1}{2}\mathbf{a}_1 + \frac{1}{2}\mathbf{a}_2, \mathbf{a}'_3 = \frac{1}{2}\mathbf{a}_1 + \frac{1}{2}\mathbf{a}_3$ and $\mathbf{a}'_4 = \frac{1}{2}\mathbf{a}_2 + \frac{1}{2}\mathbf{a}_3$. The corresponding unit cell structure factor amplitude is

$$F_{hkl}^{fcc} = F(\mathbf{g}_{hkl}) \left[1 + e^{-i\pi(h+k)} + e^{-i\pi(h+l)} + e^{-i\pi(k+l)} \right] = \begin{cases} 4F_s(\mathbf{g}_{hkl}) & h, k, l \text{ are all even or all odd} \\ 0 & \text{otherwise} \end{cases} \quad (2.71)$$

As can be seen from Eqs. (2.70) and (2.71), the unit cell structure factor for some indices hkl is equal to zero. The corresponding Bragg peaks do not appear in the measured intensities and are called forbidden.

In practice, if one measure the intensities of many Bragg peaks, it is possible to recover the structure of the crystalline lattice calculating the inter-planar distances (2.66) and recover the unit cell structures from the unit cell structure factor (2.69). This is the basis of one of the most widely used application of the X-ray scattering – X-ray crystallography [68, 69].

2.1.5.4 Ewald sphere

A useful way to visualize the Laue conditions (2.62) of the Bragg peak observation is provided by the Ewald sphere construction. Let us first consider the case of

monochromatic incident beam. The wavevector \mathbf{k}_i of the incident beam connects an arbitrary point A with the origin O of the reciprocal lattice of the sample, as shown in Fig. 2.10(a). All possible scattered vectors \mathbf{k} , if plotted starting at the point A , form a sphere with the radius $k = \|\mathbf{k}\| = \|\mathbf{k}_i\|$, called the Ewald sphere. From the definition of the momentum transfer vector $\mathbf{q} = \mathbf{k} - \mathbf{k}_i$ and, therefore, to fulfill the condition (2.62), a reciprocal lattice point should lay on the circle. This can be achieved by rotation of the sample that corresponds to rotation of the reciprocal lattice around the origin O . In Fig. 2.10(a), we show an example, when the Laue condition is fulfilled for the 220 reflection of a simple cubic lattice.

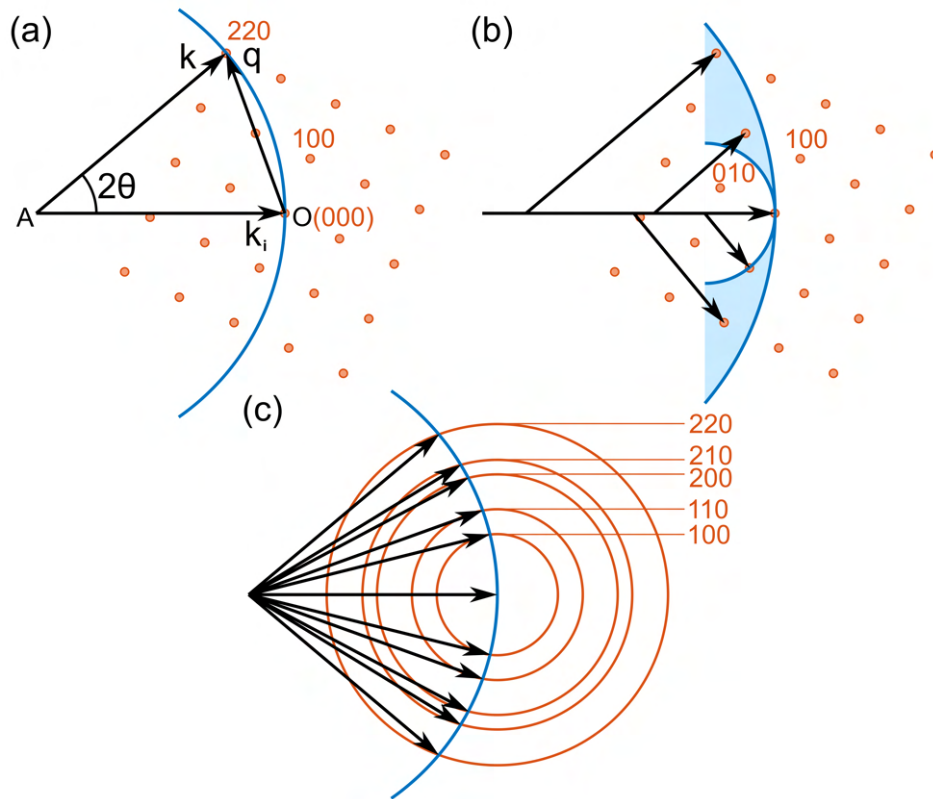


Figure 2.10: Construction of the Ewald sphere. The incident wave with the wavevector \mathbf{k}_i is scattered with the wavevector \mathbf{k} when a reciprocal lattice point intersects the Ewald sphere of the radius $k = \|\mathbf{k}_i\| = \|\mathbf{k}\|$. (a) In the case of monocrystalline diffraction with monochromatic X-rays. Only a single 220 point of the reciprocal lattice intersects the Ewald sphere and gives a reflection at the angle of 2θ . (b) In the case of monocrystalline diffraction with a "white" X-ray beam. A few reciprocal lattice points intersect the Ewald spheres corresponding to different X-ray energies (k -values) and give reflections at different angles 2θ . (c) A case of polycrystalline diffraction with monochromatic X-rays. Angularly averaged reciprocal lattice points give spheres in reciprocal space. Intersections of the spheres with the Ewald sphere give Debye-Scherrer rings corresponding to all allowed reflections at different angles 2θ .

Obviously, at each angular position of the sample, only a few reflections (typically only one) can be observed simultaneously. There are different possibilities to measure more reflections to extract the relevant structural information. The first possible approach is called single-crystal X-ray diffraction and involves collecting scattered intensities at different angular positions of a single crystalline sample. The second

approach utilizes a so-called "white beam" - polychromatic X-rays with energies in a broad range. One can build up the Ewald sphere for each energy from the range that are different in their radii as shown in Fig. 2.10(b). Then, the Laue condition will be fulfilled for reciprocal lattice points that are in the area between the extreme spheres. This approach allows measuring many reflections from a single crystalline sample simultaneously, but complicates the analysis of measured scattered intensities. The third approach is to measure scattered intensities from a powder sample that consists of many similar crystallites with different orientations. In this case, the reciprocal lattice, being angularly averaged, becomes concentric spheres with the radii corresponding to all allowed reflections, as shown in Fig. 2.10(c). The intersections of these spheres with the Ewald sphere form the so-called Debye-Scherrer rings that are measured in powder diffraction.

2.1.5.5 Crystalline defects

In the previous subsections, ideal crystalline structures, which can be described by strictly periodic electron density distributions, were considered. In practice, crystals typically possess irregularities of different types that are formed spontaneously or introduced intentionally during the growth process. The most common irregularities can be classified into a few types.

The first type are point defects that affect the positions of a single atom and a few neighbours of this atom as shown in Fig. 2.11(a). If a lattice node is not occupied by an atom/particle, it is called a vacancy. The vacancy can possibly lead to relaxation of the nearest neighbours positions towards the empty node that leads to tensile strain of the lattice. In contrast, an additional atom/particle can be present at the positions in between the regular lattice nodes. Such atom/particle is called an interstitial atom/particle and leads to relaxation of the nearest neighbours positions outwards the empty node that also leads to tensile strain of the lattice. If a lattice contains, among the nominal atom/particle types, atoms/particles of other types in the regular lattice nodes, they are called impurities. Due to different radius or shape they also can lead to tensile strain in the lattice. All these defects lead to change in the structure factor (2.69) of certain affected unit cells that could lead to appearance of forbidden reflections. The lattice strain conditioned by the point defect leads to change in the scattered intensity as discussed in Subsection 2.1.5.7.

The second type of lattice irregularities are line defects that affect the position of atoms in the vicinity of one column of atoms/particles (the column represent atoms localized along a crystallographic direction) as shown in Fig. 2.11(b,c). Such defects

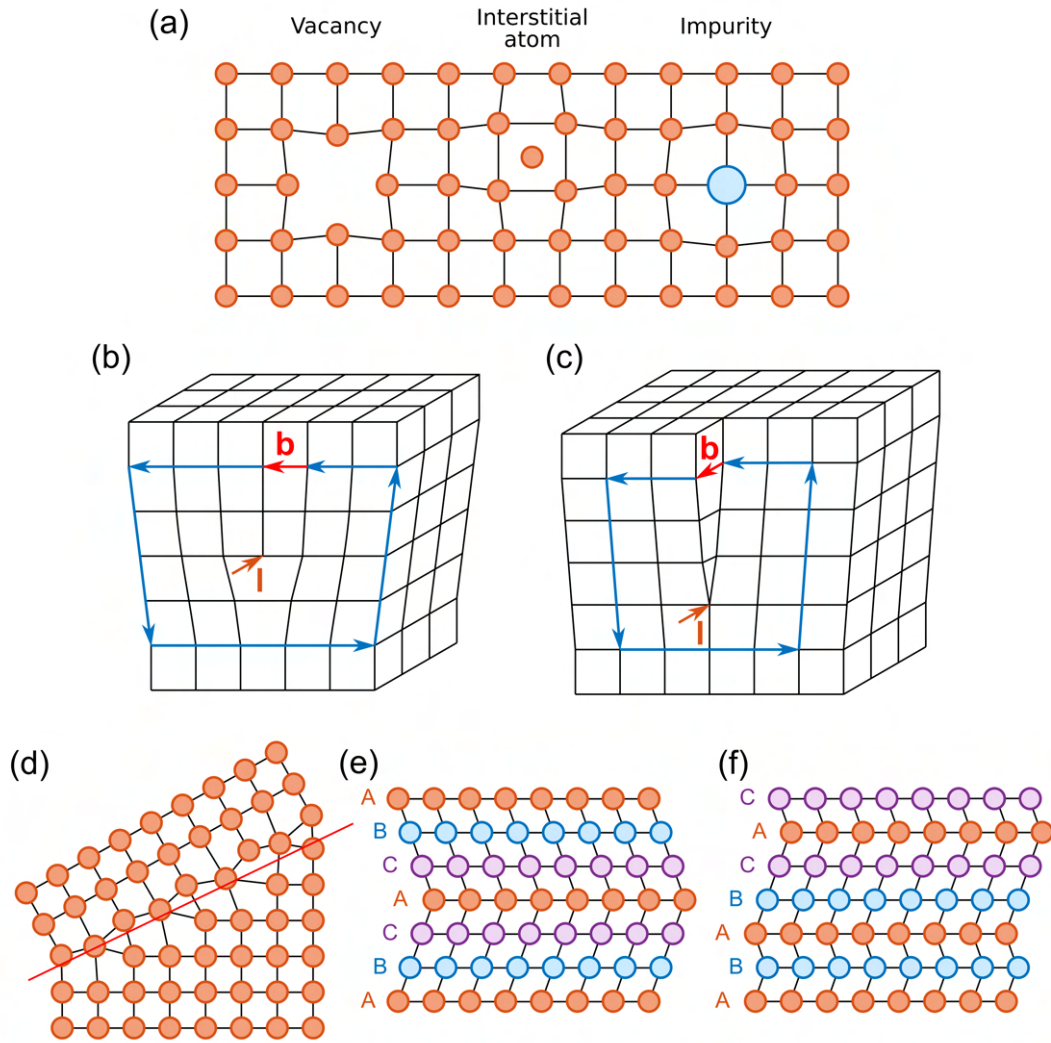


Figure 2.11: Different types of defects in crystals. (a) Point defects: a vacancy, an interstitial atom and an impurity. (b,c) Line defects: an edge dislocation (b) and a screw dislocation (c). \mathbf{l} is the guide vector of the dislocations line, \mathbf{b} is the Burgers vector corresponding to the dislocation. (d,e,f) Plane defects: a grain boundary in a cubic lattice (a), a twinning boundary in an fcc lattice (b) and an random hexagonal closed-packed (rhcp) stacking sequence with several stacking faults (c).

are called dislocations and are typically described by means of the Burgers vector

$$\mathbf{b} = - \oint_{\Gamma} d\mathbf{u}, \quad (2.72)$$

where Γ is a closed contour around the dislocation line and $d\mathbf{u}$ is elementary displacement of the atoms at each point of the contour. An edge dislocation is formed when a plane of atoms/particles abruptly terminates inside the crystal as shown in Fig. 2.11(b). The Burgers vector in this case is normal to the dislocation line. A screw dislocation is formed when a single quadrant of a crystal in respect to a column of atoms/particles is slipped along the dislocation line by one or a few interplane distances as shown in

Fig. 2.11(c). In this case, the Burgers vector is collinear with the dislocation line. In practice, the dislocations have a mixed origin and are characterized by the angle between the corresponding Burgers vector and the dislocation line. Relaxation of the positions of atoms/particles around the dislocation line in this case leads to tensile strain that affect the scattered intensity as discussed in Subsection 2.1.5.7.

The third type of lattice irregularities are plane defects that affect the positions of atoms in the vicinity of one plane of atoms/particles. A common plane defect in bulk materials is a grain boundary, when the crystallographic orientation of the crystal changes across a plane as shown in Fig. 2.11(d). It can be formed during the independent growth of two crystalline grains starting from different nucleation centers. The X-ray scattering from different grains can be considered separately; the resulting scattered intensity will consist of the sets of Bragg peaks originating from all the crystalline grains inside the sample. The grain boundary itself will contribute to the scattered intensity in form of so-called Crystal Truncation Rods (CTRs) [70] that is the Fourier transform of the boundary plane as described in Subsection 2.1.5.6. A special case of the grain boundaries is a twinning boundary, when the crystallographic orientation of the grains is mirrored across the boundary plane as shown in Fig. 2.11(e). Another type of plane defects – stacking faults – is typical for close-packed structures (fcc and hcp). As it was mentioned above, the energy difference between these stacking motifs of hexagonal 2D planes is very low that makes them prone to irregularities. Any irregularity in the stacking motive is called a stacking fault. When the stacking of the hexagonal planes is completely random as shown in Fig. 2.11(f), the structure is called rhcp [71]. Each of the stacking faults basically represents a grain boundary and produce a CTR. As soon as all these grain boundaries are parallel to each other, the CTRs interfere with each other that results in a complex intensity modulation along the CTR that is typically called a Bragg rod. The intensity modulation depends on the specific stacking sequence of the sample [4].

2.1.5.6 Effect of finite crystallite size on scattering

Let us consider now the effect of finite crystallite size on scattering from a crystal. The finite size of the sample can be taken into account by introducing the proper shape function $s_{smp}(\mathbf{r})$ in Eq. (2.59). Then, the scattered intensity (2.68) modifies to

$$\begin{aligned}
 I(\mathbf{q}) &= N_{uc} \frac{(2\pi)^3}{V_{uc}} \left| \sum_{h,k,l=-\infty}^{\infty} F_{hkl} F_{smp}(\mathbf{q} - \mathbf{g}_{hkl}) \right|^2 \approx \\
 &\approx N_{uc} \frac{(2\pi)^3}{V_{uc}} \sum_{h,k,l=-\infty}^{\infty} |F_{hkl}|^2 |F_{smp}(\mathbf{q} - \mathbf{g}_{hkl})|^2,
 \end{aligned} \tag{2.73}$$

where $F_{smp}(\mathbf{q})$ is the sample form-factor amplitude that can be calculated as it was discussed in Subsection 2.1.4. The most intense central peak of the sample form-factor can be approximated for most of the shapes with great precision by a Gaussian function. Here we assume that the sample is isotropic (spherical), then the form-factor can be approximated as

$$|F_{smp}(\mathbf{q})|^2 \approx \exp\left(-\frac{\|\mathbf{q}\|^2}{2\sigma^2}\right), \quad (2.74)$$

where $w_s = 2\sqrt{2\ln 2}\sigma$ is the FWHM of the Bragg peak. A comparison of the spherical form-factor and its approximation by the Gaussian function is shown in Fig. 2.12.

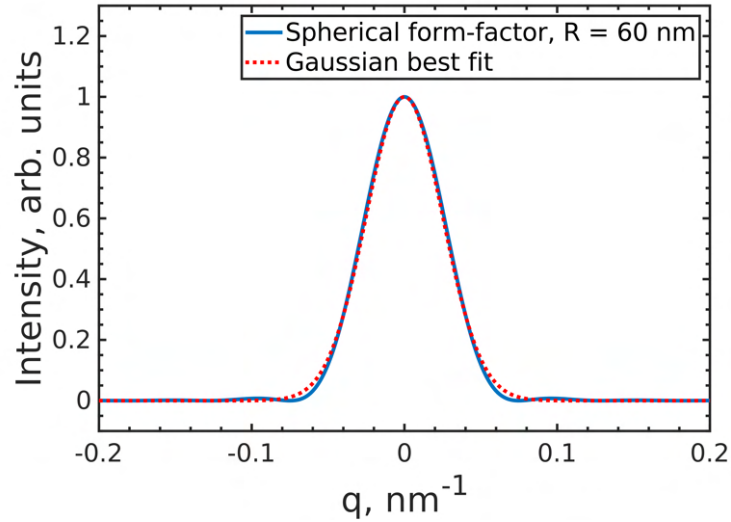


Figure 2.12: Spherical form-factor for a sphere with the radius $R = 60$ nm (blue solid line), and a corresponding best fit with the Gaussian function (2.74) (red dotted line).

Therefore, the Bragg peaks from finite sample are not δ -like anymore, but have finite size. The dependence of the FWHM w_s on the sample size (radius) R is called the Scherrer equation

$$w_s = \frac{\pi K}{R}, \quad (2.75)$$

where K is so-called Scherrer constant of the order of unity, which is dimensionless and depends on the shape of the sample [72].

The equation (2.73) is obtained under assumption that the whole sample is illuminated coherently and all parts of the sample scatter coherently. In practice, this assumption is rarely justified. The transverse coherence length of the incident beam can be smaller than a bulk sample. The sample can consist of domains with different structures that scatter incoherently. Then, the Scherrer's equation (2.75) gives an estimation of the mean size of coherently scattering domains in the sample.

2.1.5.7 Effect of crystalline lattice distortion on scattering

Now, let us consider how the lattice distortion affects the scattered intensity. One possible deformation is so-called macrostrain, i.e. the compression/elongation is homogeneous throughout the whole sample. It would simply lead to change in the lattice parameters and, therefore, in the reciprocal lattice parameters that would imply changes in the Bragg peak positions. Another, more complicated case is so-called microstrain, when the lattice point displacement is different in distinct areas of the sample. Then, the lattice point positions in the lattice sum (2.67) would include a displacement field $\mathbf{u}_{n_1 n_2 n_3}$, which is usually assumed to be normally distributed with $\langle \mathbf{u} \rangle = 0$. Then, the final scattered intensity takes the following form

$$I(\mathbf{q}) = |F_{uc}(\mathbf{q})|^2 \left| \sum_{n_1, n_2, n_3 = -\infty}^{\infty} e^{i\mathbf{q} \cdot \mathbf{a}_{n_1 n_2 n_3}} \sum_{n_1, n_2, n_3 = -\infty}^{\infty} e^{i\mathbf{q} \cdot \mathbf{u}_{n_1 n_2 n_3}} \right|^2, \quad (2.76)$$

where $F_{uc}(\mathbf{q})$ is the unit cell structure factor amplitude (2.69).

An approximation for calculation of this sum can be made if we assume that the sample has a mosaic structure, i.e. consist of many domains with different lattice parameters. Let us consider that the interplane distance d_{hkl} in the direction $[hkl]$ is normally distributed with the probability density function

$$f(d_{hkl}) = \frac{1}{\sqrt{2\pi\sigma_{d_{hkl}}^2}} \exp \left[-\frac{(d_{hkl} - d'_{hkl})^2}{2\sigma_{d_{hkl}}^2} \right], \quad (2.77)$$

where d'_{hkl} is the mean interplanar distance and $\sigma_{d_{hkl}}$ is the standard deviation. The distortion is typically characterized by the fraction $\varepsilon_{hkl} = 2\sqrt{2 \ln 2} \sigma_{d_{hkl}} / d'_{hkl}$ that is called root-mean-square microstrain in the direction $[hkl]$. For small strain values $\varepsilon_{hkl} \ll 1$, the corresponding probability distribution for the momentum transfer vector modulus $\|\mathbf{g}_{hkl}\| = 2\pi/d_{hkl}$ is

$$\begin{aligned} f(\|\mathbf{g}_{hkl}\|) &= \sqrt{\frac{2\pi}{\sigma_{d_{hkl}}^2 \|\mathbf{g}_{hkl}\|^4}} \exp \left[-\frac{\left(\frac{2\pi}{\|\mathbf{g}_{hkl}\|} - \frac{2\pi}{\|\mathbf{g}'_{hkl}\|} \right)^2}{2\sigma_{d_{hkl}}^2} \right] \approx \\ &\approx \sqrt{\frac{2\pi}{\sigma_{d_{hkl}}^2 \|\mathbf{g}'_{hkl}\|^4}} \exp \left(-\frac{2\pi^2 \|\Delta\mathbf{g}_{hkl}\|^2}{\sigma_{d_{hkl}}^2 \|\mathbf{g}'_{hkl}\|^4} \right), \end{aligned} \quad (2.78)$$

where $\|\mathbf{g}'_{hkl}\| = 2\pi/d'_{hkl}$ is the mean momentum transfer vector corresponding to the mean interplane distance d'_{hkl} and $\Delta\mathbf{g}_{hkl} = \mathbf{g}_{hkl} - \mathbf{g}'_{hkl}$ is the deviation of the momentum transfer vector \mathbf{g}_{hkl} in the direction collinear with this vector.

One can assume that areas of the sample with different interplane distances scatter incoherently. Then, the scattered intensity from such a sample is averaged over this

distribution and the total scattered intensity is defined by a convolution of Eqs. (2.68) and (2.78)

$$I(\mathbf{q}) = (2\pi)^3 \frac{V}{V_{uc}^2} \sum_{h,k,l=-\infty}^{\infty} |F_{hkl}|^2 \frac{1}{\sqrt{2\pi\sigma_{hkl}^2}} \exp \left[-\frac{\|\mathbf{q} - \mathbf{g}'_{hkl}\|^2}{2\sigma_{hkl}^2} \right], \quad (2.79)$$

where $\sigma_{hkl} = \sigma_{d_{hkl}} \|\mathbf{g}'_{hkl}\|^2 / (2\pi) = \varepsilon_{hkl} \|\mathbf{g}'_{hkl}\| / (2\sqrt{2 \ln 2})$. Thus, the Bragg peaks become broadened with a Gaussian profiles with the FWHM w_d that is dependent on the strain along the crystallographic axis $[hkl]$ corresponding to the certain Bragg peak

$$w_d = \varepsilon_{hkl} \|\mathbf{g}_{hkl}\|. \quad (2.80)$$

More correct approach based on the assumption that different areas of the sample scatter coherently is described by A.R. Stokes and A.J.C. Wilson [73]. The resulting scattered intensity in this case have the same Gaussian shape (2.79), but the FWHM (2.80) is $2\sqrt{2\pi}$ times larger.

2.1.5.8 Williamson-Hall equation

If one take into account both factors of broadening – the finite size of the sample and microstrains present in the sample, the resulting intensity is the convolution of two Gaussian profiles from Eqs. (2.74) and (2.78) and the intensity distribution from an ideal crystal (2.68). The resulting FWHM w_{hkl} of the Bragg peak with the indexes hkl is defined then by the Williamson-Hall equation [74]:

$$w_{hkl}^2 = w_s^2 + w_d^2 = \left(\frac{\pi K}{R} \right)^2 + (\varepsilon_{hkl} \|\mathbf{g}_{hkl}\|)^2. \quad (2.81)$$

Using this equation, it is possible to extract the mean strain value in the sample and the mean size of coherently-scattering domains, which in special cases is equal to the mean crystallite size.

2.1.6 X-ray scattering from a fluid

2.1.6.1 Radial distribution function

While crystalline materials are characterized by the long-range order, amorphous solids and fluids have only short-range local order that is different for every constituent (particle). The correct description of such systems is possible by means of statistical physics. The radial distribution function $g(r)$ reflects the mean variation of the particle density as a function of distance r from a reference particle. If ρ is the mean number density of particles in the system, and $N(r)$ is the number of particles in a thin spherical

layer between r and $r + dr$, then

$$\rho g(r) = \frac{N(r)}{4\pi r^2 dr}. \quad (2.82)$$

If the particle density in real space is defined by $\rho(\mathbf{r})$, the radial distribution function can be expressed as [75]

$$\rho g(\mathbf{r}) = 1 + \frac{1}{N} \langle \delta\rho(\mathbf{r}) * \delta\rho(-\mathbf{r}) \rangle - \delta(\mathbf{r}), \quad (2.83)$$

where $\delta\rho$ is the deviation from the mean particle density, N is the total number of particles in the system and the averaging is performed over the ensemble (different realizations of the system).

For a perfect crystalline material, the radial distribution function represents a set of narrow peaks. In contrast, for a fluid or amorphous material, the radial distribution function represent several broad oscillations that quite fast tend to unity, as r increases, due to disorder, as shown in Fig. 2.13.

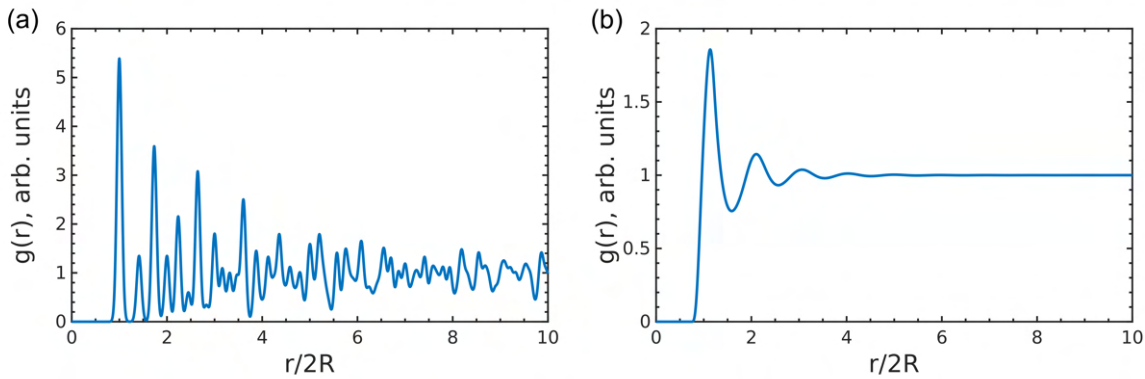


Figure 2.13: Examples of radial distribution functions $g(r)$ for an fcc crystal (a) and fluid (b), both consisting of hard spheres with radius R .

2.1.6.2 Scattering from a fluid

The electronic density in a fluid/amorphous atomic system can be represented as

$$\rho(\mathbf{r}) = \rho_{el}(\mathbf{r}) * \rho_{at}(\mathbf{r}) s_{smpl}(\mathbf{r}), \quad (2.84)$$

where $\rho_{el}(\mathbf{r})$ is the electron density in atoms constituting the sample, $\rho_{at}(\mathbf{r})$ is the density of the atoms in the sample, and $s_{smpl}(\mathbf{r})$ is the shape function of the sample/probe. Then, the scattered intensity according to Eq. (2.36) and given Eqs. (2.42) and (2.43)

takes the following form

$$I(\mathbf{q}) = \left| \int_{\mathbb{R}^3} \rho_{el}(\mathbf{r}) e^{-i\mathbf{q}\cdot\mathbf{r}} d\mathbf{r} \right|^2 \left| \int_{\mathbb{R}^3} \rho_{at}(\mathbf{r}) e^{-i\mathbf{q}\cdot\mathbf{r}} d\mathbf{r} * \int_{\mathbb{R}^3} s_{smp}(\mathbf{r}) e^{-i\mathbf{q}\cdot\mathbf{r}} d\mathbf{r} \right|^2, \quad (2.85)$$

which is almost identical with Eq. (2.44). The first integral is the atomic form-factor amplitude $f(\mathbf{q})$ from Eq. (2.38), and the integral including the shape function approaches a delta-function $\int s_{smp}(\mathbf{r}) \exp(i\mathbf{q}\cdot\mathbf{r}) d\mathbf{r} \rightarrow \delta(\mathbf{q})$ when the sample/probe size is big enough. Then, Eq. (2.85) takes the following form

$$I(\mathbf{q}) = |f(\mathbf{q})|^2 \left| \int_{\mathbb{R}^3} \rho_{at}(\mathbf{r}) e^{-i\mathbf{q}\cdot\mathbf{r}} d\mathbf{r} \right|^2 = |f(\mathbf{q})|^2 \left| \overline{\rho_{at}} \delta(\mathbf{q}) + \int_{\mathbb{R}^3} \delta\rho_{at}(\mathbf{r}) e^{-i\mathbf{q}\cdot\mathbf{r}} d\mathbf{r} \right|^2. \quad (2.86)$$

The term with the delta-function contributes only to the small-angle scattering and was discussed in the Subsection 2.1.4. Here, we are interested only in the second term, which contributes at much higher angles. Then, the scattered intensity can be represented as

$$\begin{aligned} I(\mathbf{q}) &= |f(\mathbf{q})|^2 \int_{\mathbb{R}^3} \int_{\mathbb{R}^3} \delta\rho_{at}(\mathbf{r}) \delta\rho_{at}(\mathbf{r}') e^{-i\mathbf{q}\cdot(\mathbf{r}-\mathbf{r}')} d\mathbf{r} d\mathbf{r}' = \\ &= |f(\mathbf{q})|^2 \int_{\mathbb{R}^3} \delta\rho_{at}(\mathbf{r}) * \delta\rho_{at}(-\mathbf{r}) e^{-i\mathbf{q}\cdot\mathbf{r}} d\mathbf{r}. \end{aligned} \quad (2.87)$$

And, using Eq. (2.83), one finally gets

$$I(\mathbf{q}) = N_{at} |f(\mathbf{q})|^2 \left[1 + \overline{\rho_{at}} \int_{\mathbb{R}^3} [g(\mathbf{r}) - 1] e^{-i\mathbf{q}\cdot\mathbf{r}} d\mathbf{r} \right]. \quad (2.88)$$

One can introduce fluid structure factor

$$S(\mathbf{q}) = 1 + \overline{\rho_{at}} \int_{\mathbb{R}^3} [g(\mathbf{r}) - 1] e^{i\mathbf{q}\cdot\mathbf{r}} d\mathbf{r}, \quad (2.89)$$

which for an isotropic fluids/amorphous can be averaged over the angles. Thus, it depends only on the absolute value of the transfer vector q :

$$S(q) = 1 + 4\pi\overline{\rho_{at}} \int_{\mathbb{R}^3} [g(r) - 1] \frac{\sin(qr)}{qr} r^2 dr. \quad (2.90)$$

Then, the scattered intensity from an atomic fluid/amorphous sample can be rep-

resented as

$$I(q) = N_{at} |f(q)|^2 S(q), \quad (2.91)$$

where N_{at} is the number of atoms constituting the sample, $f(q)$ is the atomic form-factor (2.38) and $S(q)$ is the fluid structure factor (2.90).

The scattered intensity from a fluid/amorphous sample consisting of macroscopic particles can be obtained from the SAXS intensity for the particles (2.52) using the fluid structure factor (2.90) calculated for the particle density $\rho_p(\mathbf{r})$.

2.1.6.3 Structure factor of hard sphere fluid

The radial distribution function $g(r)$ is defined by the interactions between particles in the system. A useful approach to take into account these interactions was proposed by L.S. Ornstein and F. Zernike [76]. The total correlation function $h(r) = g(r) - 1$ can be expressed by the Ornstein-Zernike integral equation as

$$h(|\mathbf{r}_1 - \mathbf{r}_2|) = c(|\mathbf{r}_1 - \mathbf{r}_2|) + \bar{\rho}_p \int_{\mathbb{R}^3} c(|\mathbf{r}_1 - \mathbf{r}_3|) h(|\mathbf{r}_3 - \mathbf{r}_2|) d\mathbf{r}_3, \quad (2.92)$$

where $c(|\mathbf{r}_1 - \mathbf{r}_2|)$ is the direct correlation function describing correlations between particles at spatial points \mathbf{r}_1 and \mathbf{r}_2 , which is defined only by the inter-particle potential, and $\bar{\rho}_p$ is the mean particle density in the system. This equation states that the total correlation function between two particles is the sum of their direct correlations and indirect correlations propagated via all other particles in the system. The Fourier transform of this equation gives

$$H(q) = C(q) + \bar{\rho}_p H(q) C(q), \quad (2.93)$$

where $H(q) = \mathcal{F}[h(r)]$ and $C(q) = \mathcal{F}[c(r)]$ are the Fourier transforms of the total and direct correlations functions, respectively. Then, the fluid structure factor (2.90) can be represented as

$$S(q) = 1 + \bar{\rho}_p H(q) = \frac{1}{1 - \bar{\rho}_p C(q)}. \quad (2.94)$$

A useful approximation for the direct correlation function was proposed by J.K. Percus and G.J. Yevick [77]

$$c(r) = \left[e^{-\frac{U(r)}{k_B T}} - 1 \right] e^{\frac{U(r)}{k_B T}} g(r), \quad (2.95)$$

where $U(r)$ is the inter-particle potential, k_B is the Boltzmann constant, and T is the absolute temperature.

One of a few analytical solutions for this equation was obtained by M.S. Wertheim

for a system of hard spheres [78]. For such a system, the inter-particle potential is

$$U(r) = \begin{cases} \infty & \text{for } r < 2R \\ 0 & \text{for } r \geq 2R \end{cases}, \quad (2.96)$$

where R is the hard sphere radius. This potential formalize the fact that the spheres do not interact and can not interpenetrate into each other. The direct correlation function in this case takes the following form

$$c(r) = - \left[\alpha + \beta \frac{r}{2R} + \gamma \left(\frac{r}{2R} \right)^3 \right], \quad (2.97)$$

where

$$\alpha = \frac{(1 + 2\eta)^2}{(1 - \eta)^4}, \quad \beta = -\frac{3\eta(2 + \eta)^2}{2(1 - \eta)^4}, \quad \gamma = \frac{(1 + 2\eta)^2}{2(1 - \eta)^4}, \quad (2.98)$$

and $\eta = 4\pi R^3 \bar{\rho}_p / 3$ is the volume fraction of the particles.

The Fourier transform of this direct correlation function is readily evaluated [79] to finally give the structure factor

$$S(q) = \frac{1}{1 + 24\eta \frac{G(2qR)}{2qR}}, \quad (2.99)$$

where

$$G(x) = \frac{\alpha}{x^2} (\sin(x) - x \cos(x)) + \frac{\beta}{x^3} \left(2x \sin(x) + (2 - x^2) \cos(x) - 2 \right) + \frac{\gamma}{x^5} \left(-x^4 \sin(x) + 4(3x^2 - 6) \cos(x) + 4(x^3 - 6x) \sin(x) + 24 \right). \quad (2.100)$$

This structure factor depends on two parameters: hard sphere radius R and the volume fraction of the particles η . Examples of the hard sphere structure factor for different radii R and volume fractions η are shown in Fig. 2.14.

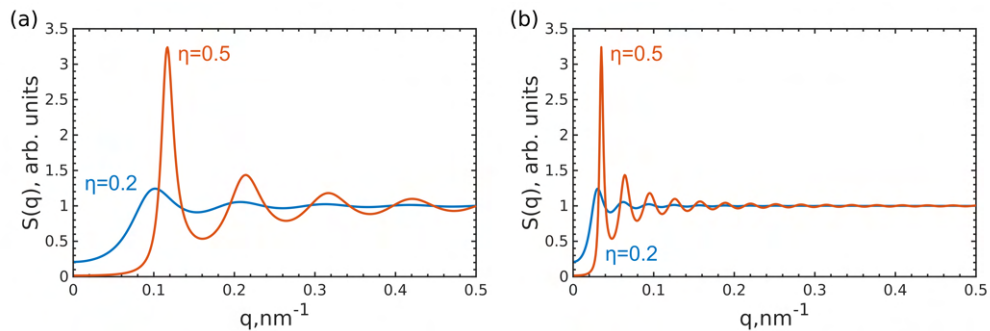


Figure 2.14: Structure-factor of hard sphere fluid in the Percus-Yevick approximation for the sphere radius $R = 60$ nm (a) and $R = 200$ nm (b) with the volume fractions $\eta = 0.2$ and 0.5 .

Despite primitiveness of the model, it is widely used to fit the scattering patterns from systems with complex inter-particle potentials, such as polymers [79], liquid metals [80], metal glasses [81], microemulsions [82] etc. Other models, for which analytical structure factor can be calculated, are sticky hard spheres [83] and screened Coulomb potential [84].

2.1.7 Angular X-ray cross-correlation analysis

Sometimes, the structural information can not be deduced directly from a scattering pattern because it is hidden behind different experimental features. One of possibilities to extract such hidden structural information is AXCCA. To study the correlations between intensities measured at different points on a 2D detector, one can consider a two-point Cross-Correlation Function (CCF) defined as follows

$$C(q_1, q_2, \Delta) = \langle \tilde{I}(q_1, \varphi) \tilde{I}(q_2, \varphi + \Delta) \rangle_\varphi, \quad (2.101)$$

where $\tilde{I}(q, \varphi)$ is the normalized intensity measured on an arc with the radius q in respect to the direct beam position and φ is an azimuthal coordinate along the arc, Δ is a relative angle between two points and $\langle \dots \rangle_\varphi$ denotes averaging over the angle φ . The variables used in this definition are shown in Fig. 2.15(a).

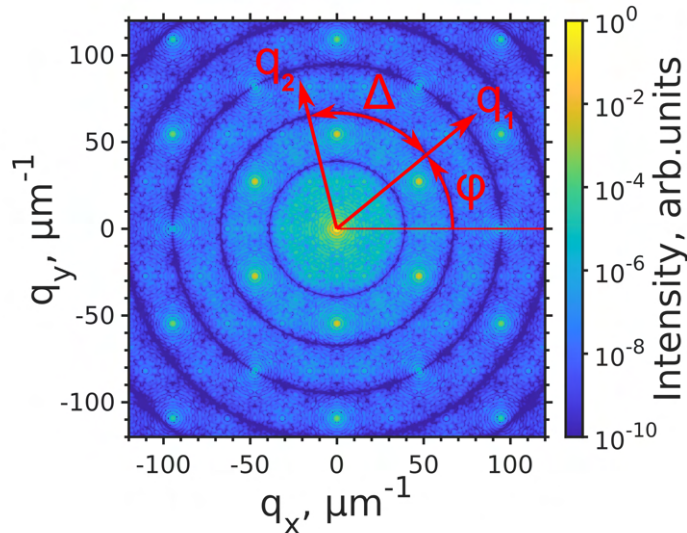


Figure 2.15: Definition of a cross-correlation function. Intensities taken at two different points q_1 and q_2 separated by the angle Δ contribute to the CCF at this angle Δ .

The measured intensity $I(q, \varphi)$ can be normalized to its mean value $\langle I(q, \varphi) \rangle_\varphi$ in

different ways

$$\tilde{I}(q, \varphi) = I(q, \varphi) - \langle I(q, \varphi) \rangle_{\varphi}, \quad (2.102a)$$

$$\tilde{I}(q, \varphi) = I(q, \varphi) / \langle I(q, \varphi) \rangle_{\varphi}, \quad (2.102b)$$

$$\tilde{I}(q, \varphi) = [I(q, \varphi) - \langle I(q, \varphi) \rangle_{\varphi}] / \langle I(q, \varphi) \rangle_{\varphi}. \quad (2.102c)$$

All three corrections give qualitatively same resulting CCF, although vertically shifted when the mean intensity value is subtracted as in Eq. (2.102a), and vertically scaled when divided by the mean intensity value as in Eq. (2.102b). The characteristic features present in the CCF do not depend on the normalization in an ideal case. In reality, noise and other experimental features such as detector gaps and bad detector calibration lead to differences in the CCFs obtained for differently normalized measured intensities which should be treated with caution [85].

The resulting CCF is a function of one angular variable Δ , while the q -values q_1 and q_2 are parameters. This function has higher values when the intensities scattered at a certain relative angle Δ are correlated and lower – when they are uncorrelated or anticorrelated. The CCF has many interesting properties that provide additional structural information about the sample under study.

The averaging over the absolute azimuthal angles in Eq. (2.101) leads to the fact that the CCF does not depend on the angular orientation of the scattering pattern in the plane normal to the incident beam. If we consider a system consisting of a few randomly oriented identical particles, a scattering pattern contains features that can be attributed solely to different particles and to the interference between them. The CCF calculated for such a pattern contain two types of correlations: between the features that belong to a single particle and between the features that belong to different particles. As soon as the CCF does not depend on the angular orientation, the positions of the first type of correlations are constant, while the correlations of the second type depend on the relative orientation of the particles in the sample, which is random. If one average CCFs over many realization of the same system but in different random orientations, the random inter-particle correlations are eliminated and only the systematic intra-particle correlations that describe the inner-particle structure are kept and enhanced. It was mathematically proven in 2D case [86] that an ensemble averaged CCF converges to a single-particle CCF

$$\langle C(q_1, q_2, \Delta) \rangle_M \rightarrow C_1(q_1, q_2, \Delta) \text{ as } M \rightarrow \infty, \quad (2.103)$$

where $C(q_1, q_2, \Delta)$ is a CCF calculated for a scattering pattern from a system containing a few randomly oriented identical particles, $\langle \dots \rangle_M$ denotes ensemble averaging over M diffraction patterns collected from a system of the same particles but in different random angular orientations, and $C_1(q_1, q_2, \Delta)$ is a CCF calculated for a scattering pa-

tern from a single particle. Such ensemble averaging can be done either spatially (by collecting scattering patterns from different areas of the sample) or temporary (when particles in a dispersion are randomized due to thermal motion). Such averaging allows enhancement of the characteristic signal and is often used in applications.

In many applications, it is convenient to analyse the Fourier expansion of the CCF instead of the CCF itself. Indeed, as soon as the scattered intensities are periodic functions of the azimuthal angle φ with the period of 2π , the CCFs are periodic functions with the same period. Therefore, they can be expanded into the Fourier series:

$$\tilde{I}(q, \varphi) = \sum_{n=-\infty}^{\infty} \tilde{I}^n(q) e^{in\varphi}, \quad (2.104a)$$

$$C(q_1, q_2, \Delta) = \sum_{n=-\infty}^{\infty} C^n(q_1, q_2) e^{in\Delta}, \quad (2.104b)$$

where

$$\tilde{I}^n(q) = \frac{1}{2\pi} \int_{-\pi}^{\pi} \tilde{I}(q, \varphi) e^{-in\varphi} d\varphi, \quad (2.105a)$$

$$C^n(q_1, q_2) = \frac{1}{2\pi} \int_{-\pi}^{\pi} C(q_1, q_2, \Delta) e^{-in\Delta} d\Delta, \quad (2.105b)$$

are the n -th Fourier coefficients of the intensity $\tilde{I}(q, \varphi)$ and CCF $C(q_1, q_2, \Delta)$, respectively. From the convolution theorem (2.42), the Fourier coefficients are related as

$$C^n(q_1, q_2) = \tilde{I}^{n*}(q_1) \tilde{I}^n(q_2), \quad (2.106)$$

where $*$ denotes the complex conjugation. This relations can be used for both calculation of the CCF from the experimentally measured intensities and extraction of the single-particle scattered intensities from an ensemble-averaged CCFs. An n -fold symmetry in the diffraction pattern would give all n -fold components in the CCF Fourier spectrum, when others would be suppressed. This fact can be used to reveal the symmetries in disordered or weakly oriented samples.

This approach was first proposed by Z. Kam in his pioneering works [87, 88] for reconstruction of a single-particle scattering pattern from many patterns measured from a system of disordered identical particles. At that time it did not get further development due to a lack of suitable instrumentation. However, since the more recent work by Wochner et al. [89], AXCCA has experienced somewhat of a renaissance due to advances in instrumentation and computing power. Novel X-ray sources with their outstanding properties, namely high brightness and coherence and a possibility of tight focusing, described in Section 2.2 brought it back into view. The initial idea of

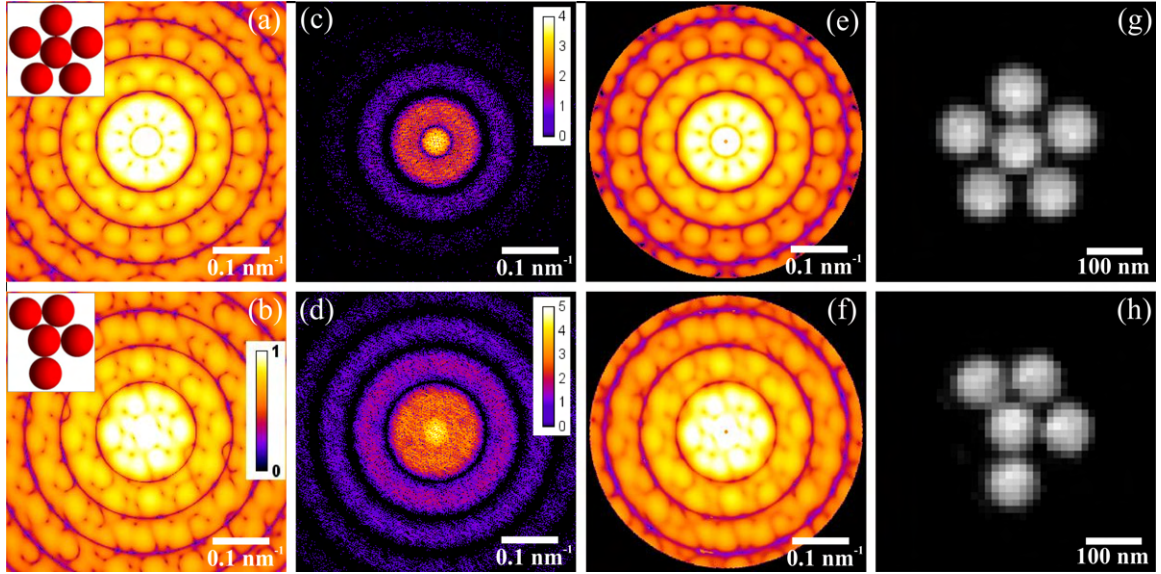


Figure 2.16: Recovery of a single-particle scattering pattern by AXCCA. (a, b) Scattering patterns (logarithmic scale) simulated for a single pentagonal cluster (a) and an asymmetric cluster (b) (clusters are shown in the insets). (c, d) Scattering patterns from a disordered system consisting of $N = 10$ clusters in random position and orientation. (e, f) Scattering patterns corresponding to a single pentagonal (e) and asymmetric (f) clusters recovered from $M = 10^5$ diffraction patterns of the form (c) and (d), respectively. (g, h) Structure of a single cluster reconstructed by an iterative phase retrieval algorithm using the diffraction patterns shown in (e) and (f). Adapted from [86].

a single-particle scattering pattern recovery was comprehensively developed in theoretical works [86, 90–94]. This single-particle scattering pattern can be further used for reconstruction of the electron density in the particle by iterative phase retrieval algorithms as was demonstrated for 2D [95, 96] and 3D [97, 98] particles. An example of such application of AXCCA is shown in Fig. 2.16.

Ability to detect symmetries present in scattering patterns with AXCCA was reported to be used for studying of different disordered or weakly ordered materials. A. Clark et al. [99] reported on the local structure of a colloidal glass revealed from the angular correlations in optical laser scattering patterns. P. Wochner et al. [89] used AXCCA to reveal the local structure of a colloidal glass from X-ray scattering patterns. The local structure of atomic glasses was revealed from the angular correlations in the electron scattering patterns [100–102]. It was also used to reveal orientational ordering in a dispersion of nanorods [103], distortions in oxygen clusters [104]. Time-resolved AXCCA allowed revealing structural dynamics in photoactive metal complexes upon laser excitation [105]. Application to the scattering data from liquid crystals was reported to reveal the structural evolution during the hexatic-smectic phase transition [106, 107], as shown in Fig. 2.17, including reconstruction of the 2D pair-distribution function [108].

AXCCA was also found useful to study crystalline materials with long-range order. The analysis of correlations in scattering patterns provide more structural information

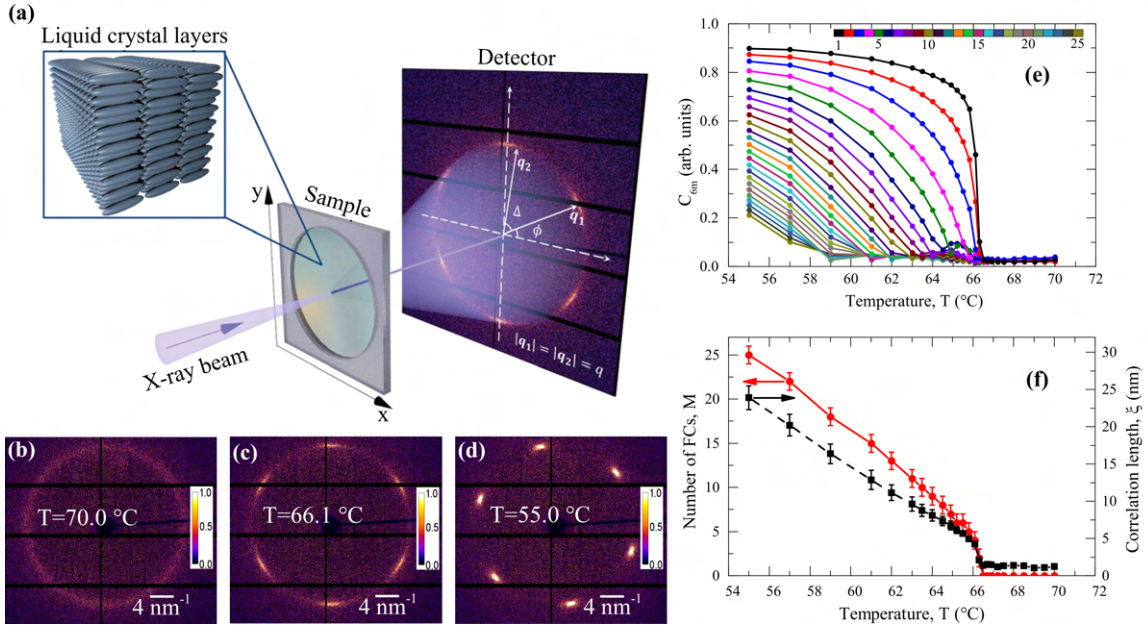


Figure 2.17: Study of the smectic-hexatic transition in a liquid crystal by AXCCA. (a) Scheme of the experimental setup. A focused X-ray beam is incoming perpendicular to the surface of a freely suspended liquid crystal film. The diffraction pattern in transmission geometry is measured by a 2D detector positioned behind the sample. (b–d) Diffraction patterns from a liquid crystal film in the smectic (b) and hexatic phase (c, d). (e) Temperature dependence of the square roots of the 6-fold Fourier coefficients $\sqrt{C_{6m}}$ of the CCF $C(q, q, \Delta)$ calculated for $q = 14.16\text{ nm}^{-1}$ corresponding to the maximum of the Bragg peaks in (b–d). (f) Temperature dependence of the total number of visible six-fold FCs M and positional correlation length ζ . Adapted from [106].

than a conventional radial intensity profile analysis. For example, crystalline structures and defects in the structure of silver and gold nanoparticles in solution [109, 110] and free-flying Xenon clusters [111] were revealed by this technique. It also allowed refining the structure of colloidal crystals [112–115] and mesocrystals [28, 116], including the determination of the angular orientation of the nanoparticles constituting the mesocrystal [28] and the details of attachment of organic ligands to the nanoparticles [116].

2.2 Modern sources of X-ray radiation

W. C. Röntgen discovered X-rays [35] while experimenting with the Crookes tube – an electrical discharge tube invented by W. Crookes in the 1870s [117]. The tube was the first vacuum tube with the vacuum high enough to allow electrons to travel from cathode to anode without collision with the residual gas molecules inside the tube. At that time, there were intensive studies with these tubes on properties of so-called cathode rays, which were later called electrons [118]. In turn, Röntgen noticed that, besides cathode rays, there are rays of another nature emitted from the anode. These rays, which he was unable to attenuate or refract, were called X-rays.

The X-rays in such a tube (that were designed specially for X-ray emission just in a few months after Röntgen's discovery) are generated by two main mechanisms. The first one is breaking radiation (or "Bremsstrahlung") due to deceleration of flying electrons inside the anode. The decelerated electrons, as any accelerated charged particles according to Eqs. (2.3) and (2.4), emit X-rays with continuous spectrum. When the kinetic energy of the flying electron is higher than the binding energy of the inner shell electrons of the atoms in the anode, the atomic electron can be removed from the atom in a collision with the flying one. The created in such an event hole will be filled by an electron from one of the outer shells. In the most used materials, a hole in the K -shell is filled with an electron from the L -shell. The difference in energy between these shells is compensated by emitting a photon with the energy characteristic for a certain material of the anode. Due to the fine structure of the electronic levels, the spectrum of this X-ray fluorescence is represented by two sharp peaks $K_{\alpha 1}$ and $K_{\alpha 2}$. For some material also K_{β} peaks are present that correspond to transitions from the M -shell to the K -shell. An example of resulting spectrum of an X-ray tube is shown in Fig. 2.18. Typically, only quasi-monochromatic radiation from one of the peaks is used, while other energies are filtered out.

The main disadvantages of the X-ray tubes are very low coherence and low power density of the useful emitted X-rays. The last property is crucial for many applications, because the interaction between the X-rays and matter is weak as was shown in Section 2.1. This ensures not only deep penetration into the sample, but also a low scattered intensity. Therefore, experiments on small or weakly-scattering samples require high incident flux.

One of the main characteristics of the X-rays sources is therefore the spectral photon flux equal to the number of photons emitted per second within the relative bandwidth of 0.1%:

$$F(\lambda) = \frac{\text{photons/s}}{(0.1\% \text{ bandwidth})}, \quad (2.107)$$

where λ is the wavelength of the emitted X-rays. In practice, the X-rays are typically collimated into narrow beams. In order to take into account the geometry of the beam,

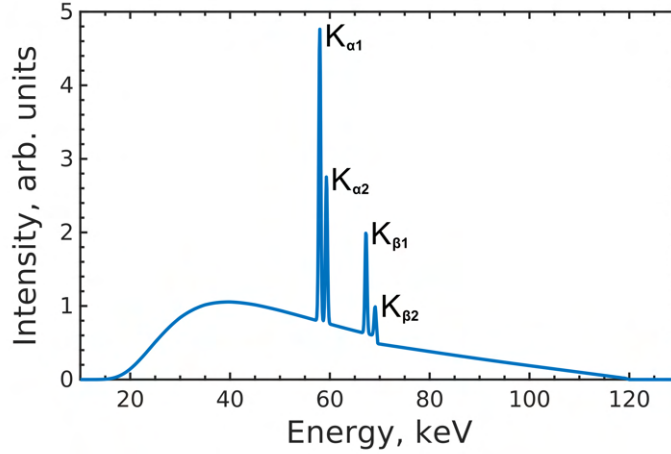


Figure 2.18: Spectrum of an X-ray tube with a tungsten anode at the accelerating voltage of 120 kV. Adapted from [119].

another measure, called brilliance $B(\lambda)$, is more widely used:

$$B(\lambda) = \frac{F(\lambda)}{4\pi^2 \varepsilon_x \varepsilon_y}, \quad (2.108)$$

where $\varepsilon_{x/y}$ is called emittance and comprises the size $\sigma_{x/y}$ and divergence $\sigma'_{x/y}$ of the X-ray source in the x/y -directions, respectively: $\varepsilon_{x/y} = \sigma_{x/y} \sigma'_{x/y}$.

The development of the X-ray tubes during the 20th century increased their brilliance by a few orders of magnitude (see Fig. 2.19). The main limiting factor here was cooling of the anode bombarded by electrons that was overcome by different inventions such as rotating anode, liquid metal anode etc. In the 1960s, an alternative X-ray generation method – synchrotron radiation – came into scientific use. It gave rise to dedicated synchrotron light sources and, later, XFELs, described below, which provide much higher brilliance and better coherence than X-ray tubes. Despite this fact, X-ray tubes remain the most widely used X-ray sources due to their compactness and commercial availability.

2.2.1 Synchrotron light sources

The first theoretical considerations of the radiation emitted by a relativistic charged particle moving in a circular path were made by A. Liénard in 1898 [121]. It became of great interest three decades later, when the first large-scale particle accelerators started to be built. When the maximum achieved energy of the particle became high enough (~ 100 MeV), the radiation losses of the particles became so high that they could not be ignored anymore. The corresponding theory of radiation was developed by many groups at that time [122–124]. This radiation was first observed by H. C. Pollock and R. V. Langmuir [125] in 1947 at a 70 MeV synchrotron at the General Electric Research

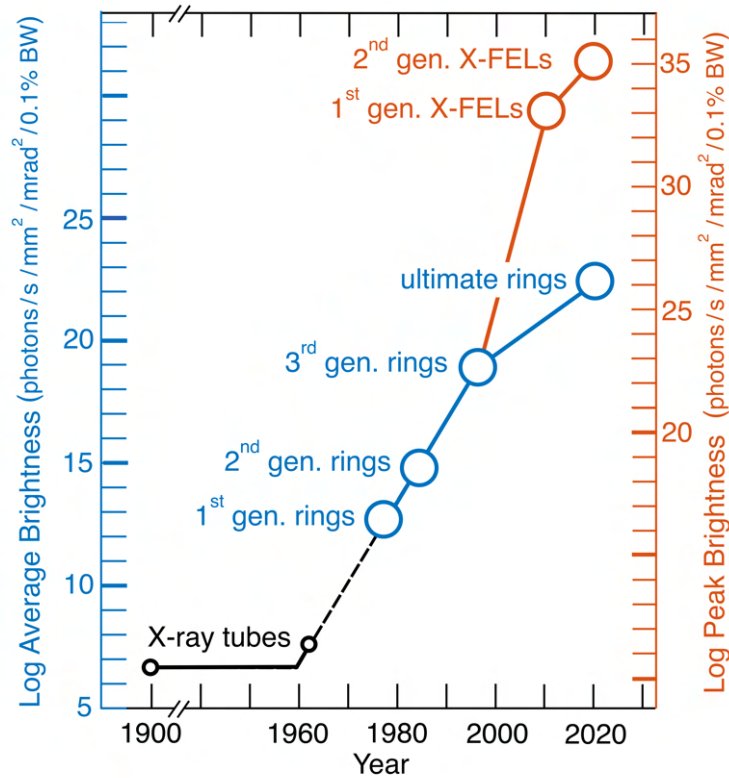


Figure 2.19: Historical evolution of the average brightness of X-ray tubes and storage rings (blue) and peak brightness of XFELs (orange). Adapted from [120].

Laboratory in Schenectady, New York (USA). After that, the radiation was named synchrotron radiation. This finding was followed by comprehensive studies of the synchrotron radiation properties [126–129]. All these studies were conducted at the particle accelerators dedicated to high-energy physics, and the synchrotron radiation was considered as a parasitic effect. Such sources belong to the so-called first generation of synchrotron radiation sources. The first dedicated storage ring based synchrotron radiation facility Tantalus was opened in 1968 at the Synchrotron Radiation Center (SRC) in Stoughton, Wisconsin (USA). This marked the transition to the second generation of sources whose main purpose was to produce X-rays.

In the storage rings, electrons accelerated to sub-light speeds (ultra-relativistic) are kept on a circular trajectory by a special periodic arrangement of magnets called a magnet lattice. This lattice consists of bending magnets and corrections magnets (quadrupoles, sextupoles and octupoles) to keep the electron beam in orbit, focus it, and correct chromatic aberrations. In the bending magnets, the electrons are subjected to centripetal acceleration and, as any accelerated charged particle, emit electromagnetic waves according to Eqs. (2.3) and (2.4). The main difference between the synchrotron radiation and the deceleration radiation (Bremsstrahlung) discussed above is that the latter one is produced when a charged particle is accelerated in the direction collinear to its velocity, while the former one – when the acceleration is normal to the

particle velocity.

The equations for dipole radiation in Subsection 2.1.2 were obtained under the assumption of a non-relativistic electron with the speed $v \ll c$ and can not be directly applied to an ultra-relativistic ($v \approx c$) electron. On the other hand, one can choose a coordinate frame where the electron is at rest at a certain moment of time. The results obtained in this system then can be converted into the laboratory system by the Lorentz transformation. The details are given elsewhere [31, 130], here only the most important results are summarized.

Let us consider an electron moving with the ultra-relativistic speed \mathbf{v} , which lays in the horizontal plane, in a constant vertical magnetic field \mathbf{H} . It will undergo acceleration by the Lorentz force and, according to the second Newton's law:

$$\frac{\partial \mathbf{p}}{\partial t}(t) = -\frac{e}{m_e c} \mathbf{v} \times \mathbf{H}, \quad (2.109)$$

where $\mathbf{p} = m_e \mathbf{v} / \sqrt{1 - \beta^2}$ is the relativistic momentum and $\beta = \|\mathbf{v}\|/c$. The electron in such a field moves along a circular path with the radius $R = \mathcal{E} / (e\|\mathbf{H}\|)$, where \mathcal{E} is the electron energy which is conserved in a magnetic field.

The total emitted power from Eq. (2.25) combined with Eq. (2.109) and given the energy $\mathcal{E} \approx cp$ for an ultra-relativistic electron takes the following form:

$$P = \frac{2}{3} r_0^2 \left(\frac{\mathcal{E}}{m_e c^2} \right)^2 \|\mathbf{H}\|^2 c = \frac{2e^2 c}{3(m_e c^2)^4} \frac{\mathcal{E}^4}{R^2}, \quad (2.110)$$

The dependence of the radiated energy on the electron energy to the fourth power caused the late discovery of the synchrotron radiation. At the energies lower than ~ 100 MeV, the radiation is negligible and could not be detected. On the other hand, at high energies these energy losses should be compensated by acceleration of the electrons. At energies higher than ~ 100 GeV, the losses are so high that their compensation becomes unfeasible.

From Eq. (2.22) and the fact that the electron acceleration in a bending magnet is in the horizontal plane (2.109), it follows that the emitted X-rays are horizontally polarized, if observed in the storage ring plane. This fact has to be taken into account when planning an experiment to make better use of the polarization factor (2.29). If the X-rays are observed at low angles above or below the storage ring plane, the polarization becomes circular that can be used in experiments requiring this type of polarization.

The angular distribution of the emitted power in the moving frame is given by Eq. (2.24) and depends only on the angle θ' between the radius-vector and the velocity

vector. After the Lorentz transformation, it takes the following form:

$$\mathbf{S}(\mathbf{r}) = \frac{r_0^2}{4\pi} \left(\frac{\mathcal{E}}{m_e c^2} \right)^2 \|\mathbf{H}\|^2 c \frac{(1 - \beta^2)^2}{(1 - \beta \cos(\theta))^3} \times \left[\cos(\varphi)^2 + \sin(\varphi)^2 \left(\frac{\cos(\theta) - \beta}{1 - \beta \cos(\theta)} \right)^2 \right] \frac{\mathbf{r}}{r}, \quad (2.111)$$

where θ is the angle between the radius-vector and the velocity vector and φ is the angle between the radius-vector and the horizontal plane. In the ultra-relativistic limit, $\beta \approx 1$, $\gamma^2 = 1/(2(1 - \beta))$ and, therefore, $1 - \beta \cos(\theta) \approx (1 - \beta)(1 + \gamma^2 \theta^2)$. The main factor defining the angular dependence of the emitted power in Eq. (2.111) is then

$$\frac{(1 - \beta^2)^2}{(1 - \beta \cos(\theta))^3} \approx \frac{8\gamma^2}{(1 + \gamma^2 \theta^2)^3}. \quad (2.112)$$

that describes a Lorentzian-type shape with the FWHM $\Delta\theta \approx 1/\gamma$. Thus, due to the Lorentz transformation, the emitted radiation from an ultra-relativistic electron is concentrated in a very narrow cone in the direction of the electron velocity (tangent to the trajectory) as shown in Fig. 2.20.

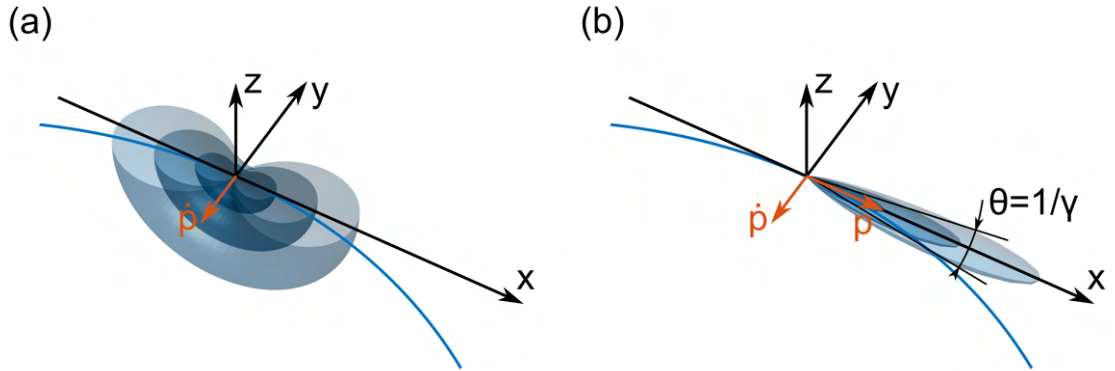


Figure 2.20: Constant intensity isosurfaces of the synchrotron radiation from an electron moving in a vertical magnetic field: in the coordinate system moving with the electron (a) and in the laboratory coordinate system (b).

Nowadays, the most of synchrotron radiation sources operate at energies of about 3 or 6 GeV ($\gamma \approx 6 \times 10^3$ or 12×10^3 , respectively) that gives the beam opening angles of about $\Delta\theta \approx 0.17$ or 0.08 mrad, respectively. Such tight natural focusing is one of the keys for the outstanding brightness of the synchrotron radiation sources. Moreover, in reality the electrons in storage rings travel in bunches that gives summation of the emitted intensities and provides the intensity scaling as $I \sim N_e$, where N_e is the number of electrons in a bunch. The typical bunch charge is about $q \sim 1$ nC that gives the number of electrons $N_e \sim 10^{10}$. On the other hand, the velocity distribution of electrons in the bunch leads to increased emittance and, therefore, lower brilliance.

Due to the small beam opening angle, an observer at a certain point outside the trajectory see the emitted radiation in short pulses when his position is inside the cone. The length Δt of the pulse can be estimated from a simple geometric consideration. The observer see first the radiation when an electron is at angle $\psi = -1/\gamma$ in respect to an axis perpendicular to the direction of observation. And the radiation continues until the electron reaches angle $\psi = 1/\gamma$. The length of the radiation pulse is then the difference in time of flight between the electron and emitted photons:

$$\Delta t = t_e - t_\gamma = \frac{2R\psi}{c\beta} - \frac{2R \sin(\psi)}{c} \approx \frac{2R}{c} \left(\frac{1}{\beta\gamma} - \frac{1}{\gamma} + \frac{1}{6\gamma^3} \right) \approx \frac{4R}{3c\gamma^3}. \quad (2.113)$$

For a typical bending magnet with $R = 50$ m installed at 6 GeV storage ring, the pulse length is $\Delta t \approx 0.1$ as. But, as was mentioned before, the electrons in storage rings travel in bunches, therefore the real pulse length is defined by the bunch length and is typically in the range of a few tens of picoseconds [51].

The spectrum of the synchrotron radiation is given by the Fourier transform of the short pulses emitted by one electron. The detailed calculations are rather complicated and can be found elsewhere [130, 131]. The characteristic frequencies (energies) can be estimated as

$$\omega_{typ} = \frac{2\pi}{\Delta t} \approx \frac{3\pi c\gamma^3}{2R}, \quad (2.114)$$

where Δt is the pulse length (2.113). The Fourier components with the frequencies above this value will undergo destructive interference and the emitted intensity will drop down. More accurate calculation give the critical frequency of $\omega_c = \omega_{typ}/\pi$ that divides the spectrum into two parts of equal power. For a typical bending magnet with $R = 20$ m installed at 6 GeV storage ring, the critical energy corresponding to the critical frequency is $\mathcal{E}_c \approx 24$ keV. A typical spectrum from a bending magnet is shown in Fig. 2.21.

The high brilliance, tight natural focusing, and the broad energy spectrum of synchrotron radiation made it of great importance for many applications already in the 1970s. However, further increase of brilliance was almost impossible due to physical constraints: the limited available magnetic fields, the instability of bunches with high charge and the high radiation energy losses at higher electron energies. In the next third generation of synchrotron radiation sources, the radiation was generated by so-called insertion devices in the straight sections of the storage rings, while the bending magnets served only to switch the electron bunches from one straight section to another.

Such insertion devices consist of a number of short magnet poles with alternating polarity as shown in Fig. 2.22. The magnetic field in the middle of the gap has only the

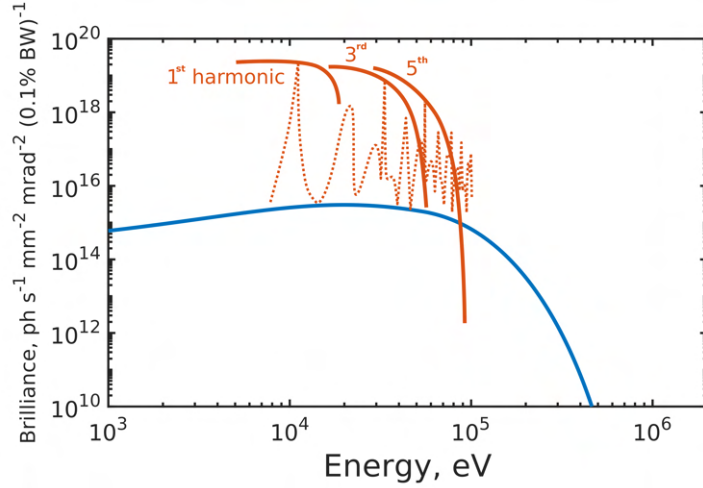


Figure 2.21: Examples of the radiation spectrum from a bending magnet (blue) and an undulator (orange). The dotted line for the undulator shows the spectrum for a fixed distance g between the magnets, the solid lines – the intensities of the 1st, 3rd and 5th harmonics for different distances g . Adapted from [132].

vertical component

$$H_z = \frac{H_0}{\cosh(\pi g / \lambda_u)} \sin(2\pi x / \lambda_u), \quad (2.115)$$

where H_0 is the nominal magnetic field of the magnets, g is the vertical distance between the magnets and λ_u is the period of the magnetic structures.

The trajectory in such a field is defined by the Lorentz force (2.109) that under assumption of $v_y \ll c$ and $v_x = \beta c = \text{const}$ gives

$$\frac{\partial^2 y}{\partial x^2}(s) = -\frac{eH_0}{m_e \gamma \beta c \cosh(\pi g / \lambda_u)} \sin(2\pi x / \lambda_u), \quad (2.116)$$

and the corresponding maximal horizontal angle in respect to the orbit is

$$\left| \frac{\partial y}{\partial x} \left(\frac{n\lambda_u}{2} \right) \right| = \frac{\lambda_u e H_0}{2\pi m_e \gamma \beta c \cosh(\pi g / \lambda_u)} = \frac{K}{\gamma}, \quad (2.117)$$

where $K = \lambda_u e H_0 / (2\pi m_e \beta c \cosh(\pi g / \lambda_u))$ is called the undulator parameter. If $K \leq 1$, the maximum angle of the particle trajectory is smaller than the natural opening angle of the radiation $\Delta\theta = 1/\gamma$ and such insertion device is called undulator. If $K > 1$, the maximum transverse speed of the electron oscillations is so high that a longitudinal Lorentz force comes into play and the assumption $v_x = \beta c = \text{const}$, under which the harmonic movement (2.116) was obtained, is not valid anymore. In this case, the insertion device is called wiggler.

Let us consider now the spectrum of an undulator. As it was mentioned above, in an undulator the electron trajectory is described by Eq. (2.116) that implies harmonic oscillations of the electron with the frequency $\omega_u = 2\pi\beta c / \lambda_u$ in the laboratory frame.

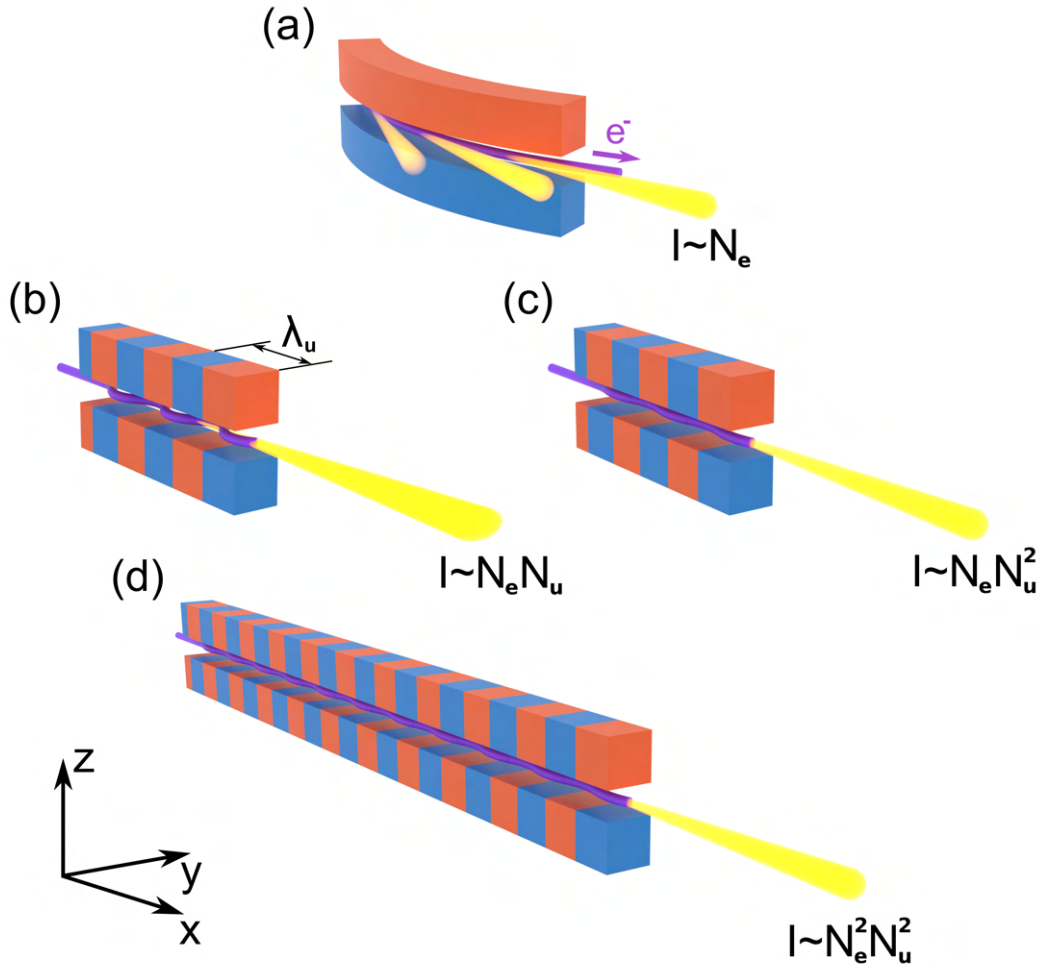


Figure 2.22: Different sources of synchrotron radiation: (a) bending magnet, (b) wiggler, (c) undulator and (d) free-electron laser. The bending magnet consist of two poles with different polarity. The insertion devices (wiggler and undulator) and the free-electron laser consist of periodic magnetic structures with the period λ_u .

In the frame that moves with the mean electron speed βc , due to the Lorentz transformation, the electron oscillates with the frequency of $\gamma\omega_u$ and, according to Eq. (2.22), emits an electromagnetic wave of the same frequency. After transformation back into the laboratory frame, due to the Lorentz transformation and taking into account the Doppler shift, the emitted electromagnetic wave has the frequency

$$\omega_1 = \frac{\omega_u}{1 - \beta \cos(\theta)} \approx \frac{4\pi\gamma^2 c}{\lambda_u(1 + \gamma^2\theta^2)}, \quad (2.118)$$

where θ is the polar angle of the radiation propagation vector in respect to the undulator axis. More accurate calculations, when the longitudinal Lorentz force is taken into account, gives an additional term in the denominator:

$$\omega_n \approx \frac{4n\pi\gamma^2 c}{\lambda_u \left(1 + \frac{1}{2}K^2 + \gamma^2\theta^2\right)}, \quad (2.119)$$

where n is the number of harmonic. A typical spectrum of the radiation from an undulator is shown in Fig. 2.21.

Since the X-rays are generated in an undulator by the same electron during harmonic oscillations, the emitted waves in different periods of the undulator are coherent. Therefore, the emitted intensity scales as $I \sim N_e N_u^2$, where N_u is the number of undulator periods (typically, $N_u \sim 50$), and the opening angle of the radiation decreases as $\Delta\theta \sim 1/(\gamma\sqrt{N_u})$. In a wiggler, the electron movement is not harmonic and the emitted waves are not coherent. Therefore, the intensity scales as $I \sim N_e N_u$, and the opening angle stays the same as for one electron $\Delta\theta \sim 1/\gamma$. This fact gave the gain in brilliance of other five orders of magnitude for the third generation of the synchrotron radiation sources in comparison to the second one as shown in Fig. 2.19.

Nowadays, the third generation of synchrotron radiation sources with the insertion devices de facto became a standard worldwide. The existing facilities include PETRA III (Hamburg, Germany), SPring-8 (Sayo, Japan), APS (Chicago, Illinois, USA), NSLS-II (Upton, New York, USA), Diamond (Didcot, Oxfordshire, UK), SLS (Viligen, Switzerland) etc. The high brilliance of these sources led to a significant reduction in the time required for measurements and made it possible to study various processes in situ. It also allowed one to measure weakly scattering samples such as highly dilute solutions, small crystals, thin films, biomolecules, etc. The relatively high coherence of modern synchrotron sources has led to the development of coherent X-ray scattering methods such as CDI [133], X-ray ptychography [134] and X-ray Photon Correlation Spectroscopy (XPCS) [135, 136], etc. Due to the coherence, it is also possible to tightly focus the X-ray beam for nanoprobe experiments [137].

Further development of the synchrotron radiation sources aims to decrease the electron bunch emittance down to that of the photon beam. This would lead to further improvement in the brilliance and, especially, in the provided coherent flux. The sources with such properties are called diffraction-limited sources and are typically attributed to the fourth generation. The reduced emittance in such machines is achieved by exploiting a more complex magnet lattice called multibend achromat (MBA). The MBA concept [138] involves increasing the number of bending magnets and reducing the bending angle of each magnet, and increasing the number of correcting magnets. Examples of the sources using this technology are currently operating ESRF-EBS (Grenoble, France), MAX IV (Lund, Sweden), Sirius (Campinas, Brazil) and planned upgrades PETRA IV (Hamburg, Germany), APS-U (Chicago, Illinois, USA), SLS-2 (Viligen, Switzerland), etc.

2.2.2 Free-electron lasers

In the 1960s, novel sources of coherent radiation – masers and, later, lasers – became of a great interest due to the unique properties of the generated radiation such

as high intensity and coherence [139]. The principle of operation of such devices is to amplify the radiation by stimulated emission from a gain medium interacting with the radiation in an optical cavity. The main disadvantage of the mechanism was the fact that the laser properties were limited by the electronic structure of the gain medium. The fixed energy of electron transitions in atomic or molecular gain media made impossible to easily tune the wavelength of radiation produced by lasers.

In 1971, John M. J. Madey proposed to use electrons passing an undulator as the gain medium [140]. A practical realization of a maser consisting of an undulator placed in an optical cavity was demonstrated by his group in 1977 [141]. It was called a Free-Electron Laser (FEL) due to the fact that the electrons in the undulator were not bound to any atoms or molecules. In 1980, A. M. Kondratenko and E. L. Saldin demonstrated that if an undulator is long enough, the initial random field of spontaneous radiation in the undulator may be amplified and finally become fully coherent interacting with the electrons (so-called Self-Amplified Spontaneous Emission (SASE)) [142]. A several realization of the FELs using SASE mechanism producing radiation in visible and Ultraviolet (UV) ranges were demonstrated in the early 2000s [143–145]. The absence of the need for an optical cavity for the operation of such a laser basically removed the limitation on the minimum wavelength and made it possible to build a FEL producing X-rays. But the accelerators that time were not able to provide the electron beam stability required for perfect overlap between the electron beam and the emitted photon beam inside the undulator, that is required for successful interaction between them. The progress in accelerators made it possible to first achieve the extreme ultraviolet radiation with the wavelength of 32 nm at FLASH (Hamburg, Germany) in 2005 [146]. The first FEL operating in the soft and hard X-ray ranges (an XFEL) – Linac Coherent Light Source (LCLS) – was commissioned at the SLAC National Accelerator Laboratory (Stanford, California, USA) in 2010 [147].

The theory of FELs is comprehensively developed and can be found elsewhere [148]. Here, only the basics of the interaction between an electron in an undulator and an electromagnetic wave is given. Let us consider an electron moving in two periodical vertical magnetic fields: one from the undulator poles (2.115) and one from an electromagnetic wave with the frequency $\omega_1 = 4\pi\gamma^2c/(1 + K^2/2)$ resonant for the undulator:

$$H_{L,z}(t) = H_L \sin(\omega_1 t + \psi), \quad (2.120)$$

The horizontal Lorentz force from the electromagnetic wave is then

$$F_y(t) = -e\beta c H_L \sin(\omega_1 t + \psi). \quad (2.121)$$

Over a period T , this force transfer to the electron the following amount of energy:

$$\Delta\mathcal{E} = \int_0^T F(t) dy = \int_0^T F(t) \frac{\partial y}{\partial t} dt, \quad (2.122)$$

where $\partial y/\partial t$ is the transverse speed of the electron. For the electron in an undulator magnetic field, the horizontal speed from Eq. (2.116) is equal to $\partial y/\partial t = \beta c(K/\gamma) \cos(\omega_1 t)$, where K is the undulator parameter of the particular undulator. Then Eq. (2.122) takes the following form:

$$\begin{aligned} \Delta\mathcal{E} &= -e\beta^2 c^2 H_L \frac{K}{\gamma} \int_0^T \sin(\omega_1 t + \psi) \cos(\omega_1 t) dt = \\ &= -e\beta^2 c^2 H_L \frac{K}{\gamma} \frac{\pi}{\omega_1} \sin(\psi) \sim -\sin(\psi). \end{aligned} \quad (2.123)$$

Due to ultra-relativistic speed, about the same amount of energy is transferred from the electric field of the electromagnetic wave. Thus, an electron gains the energy of $\Delta\mathcal{E} \sim -\sin(\psi)$, where ψ is the phase difference between the initial electromagnetic wave and the wave emitted by this particular electron. Therefore, the electron is either accelerated or decelerated to bring the waves emitted by this electron in phase with the initial wave. This leads to formation of so-called microbunches inside each electron bunch with the distance between them equal to the resonant wavelength $\lambda_1 = \lambda_u(1 + K^2/2)/(2\gamma^2)$. The process of the microbunch formation is gradual and during the process the intensity grows up exponentially as $I \sim I_0 \exp(x/L_g)$, where L_g is the characteristic gain length. After some time the microbunches are fully formed and the emitted intensity saturates. The process of the bunch formation is shown schematically in Fig. 2.23. The gain length L_g for X-ray wavelength reaches several tens of meters that requires long undulators. All electrons from the same microbunch emit waves in phase, i.e. coherently, that leads to the saturated intensity scaling as $I \sim N_e^2 N_u^2$. The peak brilliance of XFELs is, therefore, about 10 orders of magnitude higher than that of synchrotrons (see Fig. 2.19). The small length of the microbunches allowed to reach the X-ray pulse length of a few tens of femtoseconds [146, 147].

The ultimate brilliance, coherence, and extremely short pulses of X-rays generated by XFELs made them perfect instruments for exciting applications. The extremely intense and short pulses from XFELs opened the way for the so-called diffraction-before-destruction approach. The intensity of a single pulse is high enough to produce a reasonable scattered signal from a single biomolecule or particle, while the short pulse length allows this signal to be measured before the sample is destroyed by radiation damage. This approach found an application in such techniques as Single-Particle Imaging (SPI) [149] and Serial Femtosecond Crystallography (SFX) [150]. The ultra-

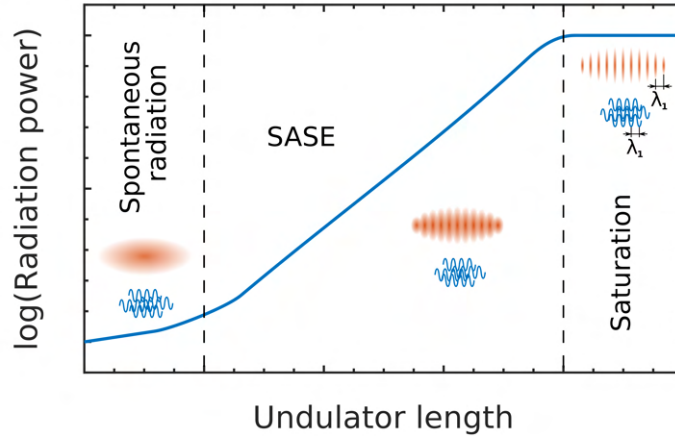


Figure 2.23: Evolution of the power radiated by an electron bunch passing an undulator. The macroscopic electron bunch turns into microbunches due to interaction with the radiation. The distance between the microbunches is equal to the first undulator harmonic wavelength λ_1 . Adapted from [32].

short XFEL pulses also find an application in pump-probe experiments, when the sample is first pumped with a conventional laser and then probed by the X-rays [151]. This kind of experiment is used to study ultrafast processes on atomic level, such as phase transitions, ionisation, etc.

However, extreme complexity of the instrumentation and, consequently, high costs of construction, maintenance and operation limited the spread of XFELs to a few scientific centers around the world. Examples of operating XFELs include LCLS (Stanford, California, USA), EuXFEL (Schenefeld, Germany), SwissFEL (Villigen, Switzerland), SACLA (Kouto, Japan), and PAL-XFEL (Pohang, Korea).

2.3 Colloidal systems: structure and properties

Colloidal systems are disperse systems consisting of insoluble particles with at least one of the dimensions in the range of 1 nm to 1 μm suspended throughout a continuous dispersion medium [152, 153]. The particles and the medium should differ in composition or phase. The three states of matter (gaseous, liquid and solid) give 9 different possible combinations listed in Table 2.2. In this work we are particularly interested in colloidal solutions, or sols, that consist of solid particles dispersed in liquid solvent. This Section is partially based on Refs. [21, 152, 153].

Table 2.2: Classification of dispersions by the nature of medium/phase

		Dispersed phase		
		Gaseous	Liquid	Solid
Dispersion medium	Gaseous	Do not exist	Liquid aerosol	Solid aerosol
	Liquid	Foam	Emulsion	Sol
	Solid	Solid foam	Gel	Solid sol

The colloidal systems are widely spread in nature. The examples of emulsions include such vital materials as milk and biological membranes formed by fat molecule agglomerates (micelles) in aqueous media. The common examples of sols are blood, inks, paints, mud, etc. The first artificial colloids – namely, colloidal gold – were first used in the late Roman Empire for ruby glass production [154]. But the mechanism, which yielded the colour, remained unknown until Michael Faraday did a systematic study of colloidal gold in 1857 [155]. The term “colloid” was introduced later by Michael Graham in 1861 to describe materials that diffuse slowly through a porous membrane [156], but later this class expanded to the modern one. Nowadays, the colloidal particles can be prepared from various materials including metals [157–160], inorganic [161–164] and organic [165] semiconductors, polymers [166–168] etc. Recent developments in particle fabrication allow producing colloidal particles of different shapes such as spheres [163, 166], cubes [160–162, 165, 168], prisms [158], plates [159, 164], dumbbells [167], etc.

The considered size range is rather arbitrary. It has the lower boundary of 1 nm to distinct the colloids from true solutions of molecules or atoms. Although, some macromolecules have bigger size and, therefore, solutions of macromolecules (for example, polymers) are sometimes considered as colloids. The upper boundary is based on the kinetics and properties of the particles in such a system. Particles smaller than 1 μm typically have the energy of thermal (Brownian) motion comparable to the potential energy of gravity that prevent their sedimentation. Also, for such particles, the number of surface atoms is higher or comparable to the number of volume atoms (not located on the particle surface) that defines their unique properties.

The high surface energy makes colloidal particles prone to aggregation. To suppress such aggregation, there are two main mechanisms: electrostatic stabilization and steric stabilization. Electrostatic stabilization is based on electrostatic repulsion between charged particles as shown in Fig. 2.24(a). The charged particle surface interacts with the counterions in the solvent forming so-called electrical double layer. The interactions of such charged particles with the formed electrical double-layer is defined by the so-called ζ -potential. The full description of such interactions are given in the framework of the Derjaguin-Landau-Verwey-Overbeek (DLVO) theory [169, 170]. Steric stabilization is based on preventing particles to get close mechanically by covering them by a layer of molecules (often polymers) as shown in Fig. 2.24(b). Typically, both mechanisms coexist simultaneously and the stabilization is electrosteric.

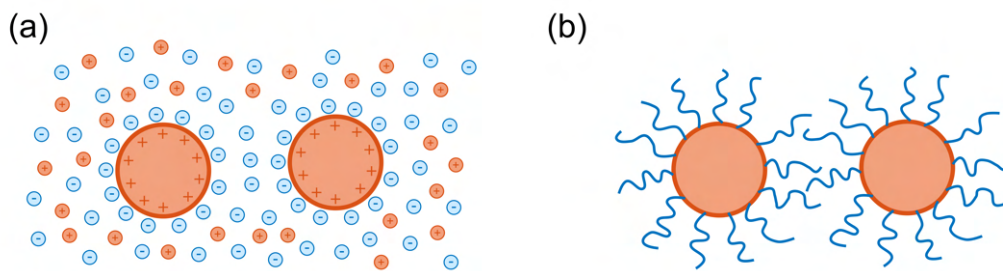


Figure 2.24: Stabilization of colloidal solutions: (a) electrostatic and (b) steric.

Colloidal particles are often viewed as large atoms with tailorable size, shape and interactions. Both colloidal particles and atoms experience strong thermal motions, which enable them to form thermally equilibrated phases. In contrast, the colloidal particles are much larger and, therefore, move slower that allow the tracing of their movement directly by means of microscopy. This makes colloidal systems excellent model systems to study phase transitions. The phase behaviour of conventional materials is defined by the temperature, and an analog to the temperature for colloidal crystals is the volume fraction η that can be tuned in different ways. When the volume fraction is high enough (the exact value vary dependent on the shape of the colloidal particles and interactions between them), the colloidal system crystallizes or turns into an amorphous (glassy) state. The resulting crystalline phase is called colloidal crystal and has many prospective for applications properties discussed in Subsection 2.3.1.

As already mentioned, the relatively big particles and slow movement of colloids makes possible studying them by optical [171–174] or electronic [175–178] microscopy. Unfortunately, these methods have major disadvantages. The optical microscopy have a limited resolution and, therefore, applicable only for colloids containing large particles as exemplified in Fig. 2.25(a-f). The electronic microscopy typically works in vacuum conditions that makes hard study of colloids in solutions, where the dynamics is present, although possible in special cells [175, 178] as shown in Fig. 2.25(g-k). Moreover, both methods allow visualizing only thin films or surface of the sample, where

kinetics can be sufficiently different from the bulk colloids.

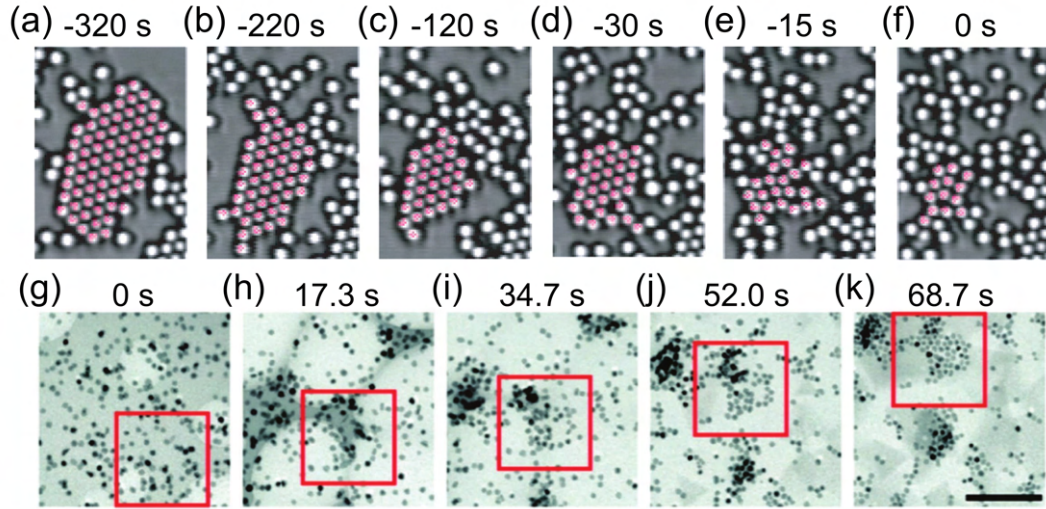


Figure 2.25: Examples of phase transitions in colloids studied by microscopy. (a-f) Melting of a crystallite of 700 nm-radius polystyrene spheres. Images were obtained using an inverted optical microscope ($63\times$ magnification). The purple dots indicate particles identified by the cluster algorithm. Adapted from [173]. (g-k) Crystallization in a colloid of Pt nanoparticles with 7.3 nm average diameter studied by transmission electron microscopy (TEM) during solvent evaporation. The red box highlights a forming crystallite. The bar is 100 nm. Adapted from [176].

A powerful tool to study the dynamics of bulk colloids is Dynamic Light Scattering (DLS), where changes in temporal correlations of scattered laser light are associated with the Brownian motion of the colloidal particles in the gravitational potential [179, 180]. The temporal correlations are quantified by the second-order correlation function

$$g^{(2)}(\tau) = \frac{\langle I(t)I(t+\tau) \rangle}{\langle I(t) \rangle^2}, \quad (2.124)$$

where $I(t)$ is the measured intensity at time t , τ is the time delay, and $\langle \dots \rangle$ denotes time average. For photon counts obeying Gaussian statistics, the second-order correlation function $g^{(2)}(\tau)$ can be easily converted into the first-order correlation function $g^{(1)}(\tau)$ as $g^{(1)}(\tau) = \sqrt{g^{(2)}(\tau) - 1}$. The time dependence of this function reflects the diffusion characteristic times and diffusion coefficients that can be interpreted to extract the particle size distribution as shown in Fig. 2.26(a,b). If the measurements are done in additional external electric field, the ζ -potential of the colloidal particles can be extracted [181, 182]. The theoretical basis of the method assume that only single light scattering events happen in the system under study. Thus, the method is limited only to very dilute samples, where this assumption is fulfilled. Unfortunately, it makes impossible to study phase transitions, which typically happen at sufficiently large concentrations (volume fractions). The further development of the method is XPCS based on the same principle, but utilizing X-rays instead of laser light [135, 136]. The smaller

scattering cross-section and higher penetration depth of X-rays in comparison to the visible light allowed to study dynamics of colloids including phase-transitions such as crystallization and glass transition [183–185] as shown in Fig. 2.26(c).

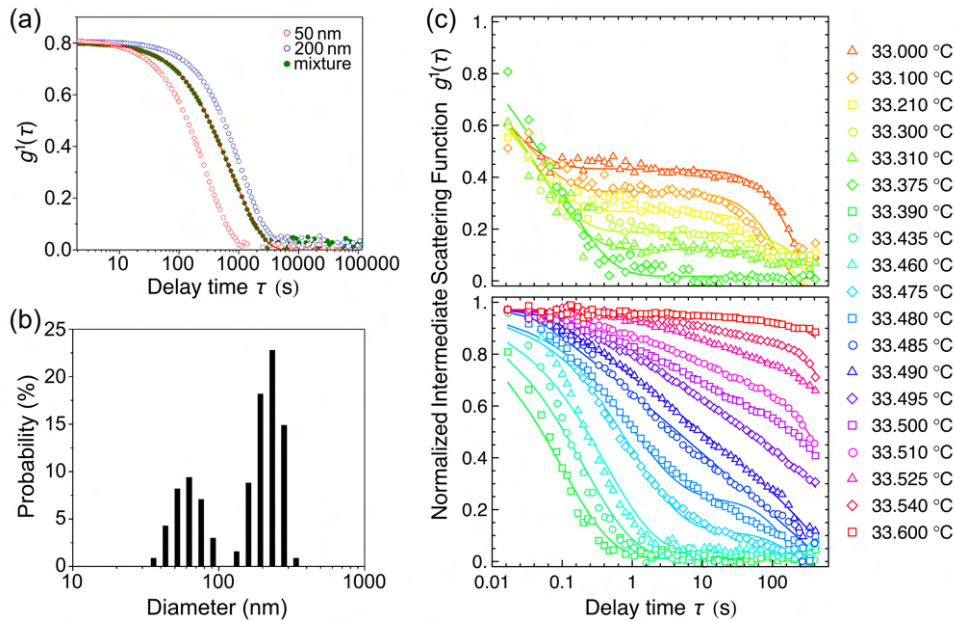


Figure 2.26: (a,b) Example of DLS analysis of spherical polystyrene colloidal particles of average sizes 50 nm, 200 nm, and their mixture in water: the correlation function $g^{(1)}(\tau)$ (a) and the extracted size distribution (b). Adapted from [182]. (c) Example of XPCS analysis of 195 nm-radius silica spheres at a volume fraction of $\phi = 0.52$ in water-lutadine mixture at different temperatures bear the glass transition. The correlation function $g^{(1)}(\tau)$ is calculated at $q = 0.012 \text{ nm}^{-1}$. Adapted from [184].

An insight on the structure of bulk colloids give the X-ray scattering methods. The form-factor of the colloidal particles in diluted sols can be extracted by means of SAXS described in Subsection 2.1.4. It allows determining the shape and size distribution of colloidal particles [186–190]. The interference between X-rays scattered by different colloidal particles in more dense colloids gives rise to the structure factor that, depending on the structure of the colloid, can be fluid/amorphous as described in Subsection 2.1.6 or crystalline as described in Subsection 2.1.5. It allows to study the structural evolution during the phase transitions.

2.3.1 Colloidal crystals

The first natural colloidal crystal was observed by Wendell Stanley in 1935 when experimenting with dispersions of purified tobacco mosaic virus (TBMV) [191]. The identity of shape and size of the virus copies made them possible to form a structure with long-range order. Progress in colloid chemistry at that time led to the possibility of synthesizing artificial monodisperse particles able to form the long-range order structures. The first artificial colloidal crystal was observed in the 1950s on an example of charged spherical latex particles [1, 2].

2.3.1.1 Structure of colloidal crystals

The crystallization in colloidal systems was also predicted in 1950s theoretically [192] and by computer simulations [193, 194]. It was shown that a system of uncharged hard spheres behave as a fluid at low volume fractions η , consist of coexisting fluid and crystal phases between $\eta_f = 0.494$ and $\eta_s = 0.545$, and is fully crystalline above the latter [195]. The phase behaviour very similar to the predicted one was shown in 1980s for a systems of sterically stabilized uncharged spherical silica [196] and poly(methyl methacrylate) (PMMA) [197] particles. Such hard spherical particles form close-packed hexagonal 2D layers which further assemble into fcc, hcp or rhcp 3D close-packed structures [3, 4, 22, 23, 198–202] described in Subsection 2.1.5.

Soft spheres demonstrate a richer phase behaviour including fcc, bcc, simple hexagonal, body-centered tetragonal and body-centered orthorombic lattices [203–205]. Such soft particles can be synthesized by grafting long polymers on the particle surface, reducing the crosslinker density in polymer particles [206], or enhancing the electrostatic interaction for charged particles [203, 204, 207].

The thermodynamically stable crystalline structure for colloidal hard cubes is a simple cubic lattice that theoretically allows packing with the highest possible volume fraction of $\eta = 1$ [208]. In practice, the colloidal cubes have not only sharp edges [6], but more frequently rounded ones [160, 209, 210]. The rounded edged cubes are a special case of so-called superball shape mathematically described as

$$\left|\frac{x}{a}\right|^m + \left|\frac{y}{a}\right|^m + \left|\frac{z}{a}\right|^m \leq 1, \quad (2.125)$$

where the shape parameter m defines the transition from a sphere ($m = 2$) to a cube ($m \rightarrow \infty$) and a is a half the edge length (a radius) as shown in Fig. 2.27. The phase behaviour of such superballs for intermediate values of m was predicted theoretically and by simulations [208, 211, 212].

It was shown that the crystalline lattice changes from an fcc lattice for $m = 2$ to a simple cubic lattice for $m \rightarrow \infty$. The optimal densest packing for superballs with $2 < m < 2.308$ is so-called C_0 -lattice defined by the lattice vectors

$$\begin{aligned} \mathbf{a}_1 &= a \left(2^{1-1/m}, 2^{1-1/m}, 0 \right), \\ \mathbf{a}_2 &= a \left(0, 0, 2 \right), \\ \mathbf{a}_3 &= a \left(-2s, 2s + 2^{1-1/m}, 1 \right), \end{aligned} \quad (2.126)$$

where s is the smallest positive root of the equation $(s + 2^{-1/m})^m + s^m + 2^{-m} - 1 = 0$. The optimal densest packing for superballs with $m > 2.308$ is so-called C_1 -lattice

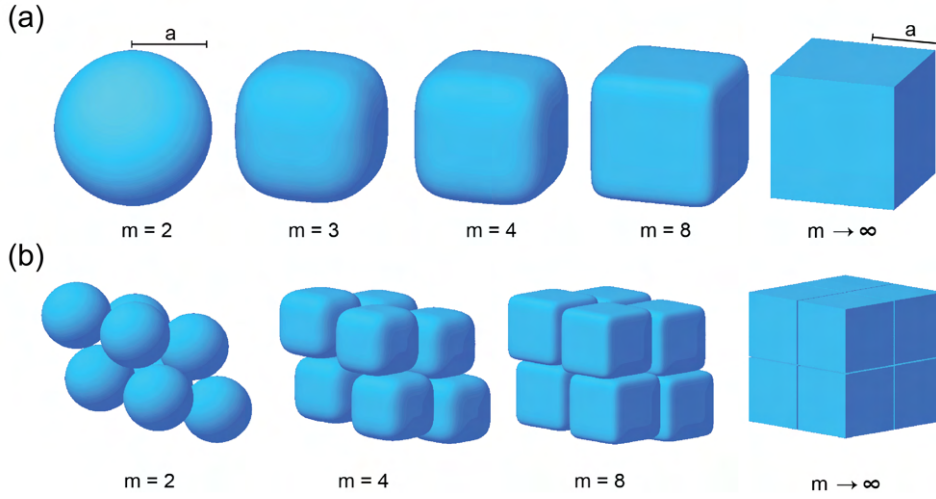


Figure 2.27: (a) Shape of superballs with different values of the shape parameter m . (b) Optimal C_1 -lattices for superballs with different values of the shape parameter m . Adapted from [21].

defined by the lattice vectors

$$\begin{aligned}
 \mathbf{a}_1 &= a \left(2^{1-1/m}, 2^{1-1/m}, 0 \right), \\
 \mathbf{a}_2 &= a \left(2^{1-1/m}, 0, 2^{1-1/m} \right), \\
 \mathbf{a}_3 &= a \left(2s + 2^{1-1/m}, -2s, -2s \right),
 \end{aligned} \tag{2.127}$$

where s is the smallest positive root of the equation $(s + 2^{-1/m})^m + 2s^m - 1 = 0$. These structures for different values m are shown in Fig. 2.27. Despite the fact that these two lattices are optimal at different values of m , they both exist for any $m > 1$. The highest packing density is provided by tight contact between the corners and facets of adjacent particles that are all oriented the same way. At lower volume fractions η than ones corresponding to the close-packed crystals, the particles form slightly deformed C_0 and C_1 structures. At even lower η , the stable structures for $2 < m < 6$ were found to be plastic fcc crystals, i.e. the cubes lose their isoorientation and can freely rotate at the lattice nodes. These structures were observed experimentally for palladium nanocubes in a ligand-rich solution [209], copper nanocubes [160] and silica superballs [213].

The colloidal particles with more complex shapes were shown to form different crystalline structures by simulations. Truncated tetrahedra were shown to form diamond, β -tin, high-pressure lithium, and bcc structures depending on the truncation degree [214]. For truncated cubes such structures as distorted simple cubic, body-centered tetragonal and Minkowski lattice are expected [215]. Some of these structures were observed experimentally [216, 217]. Colloidal crystals consisting of particles with more exotic shapes, such as dumbbells [7, 218, 219], octapods [8], rods [220], etc. were reported.

2.3.1.2 Crystallization of colloidal crystals

To form a colloidal crystal, the volume fraction η of colloidal particles should exceed a certain threshold value. In practice, one needs to increase the particle concentration in a sol to obtain a colloidal crystal. There are several ways of colloidal crystal synthesis, but the most widespread methods are sedimentation by gravity and solvent evaporation.

The concentration profile in the gravitational field is defined by the Boltzmann distribution [64]

$$n(z) = n(0)e^{-\frac{\Delta\rho Vgz}{kT}}, \quad (2.128)$$

where $n(z)$ is the number concentration at the height z from the solution bottom ($z = 0$), $\Delta\rho = \rho_{particle} - \rho_{solvent}$ is the difference between the particle and solvent densities, V is the particle volume, g is the gravity acceleration, k is the Boltzmann constant and T is the absolute temperature. For example, for spherical gold particles in aqueous solution with $\Delta\rho \approx 18 \text{ g cm}^{-3}$ and the radius of $\sim 100 \text{ nm}$, the characteristic height is $kT/(\Delta\rho Vg) \approx 5 \text{ mm}$. Therefore, the volume fraction at the solution bottom can be higher than the crystallization threshold. In such a case, the colloidal particles can crystallize at the bottom of the solution [221, 222] as shown in Fig. 2.28(a). In contrast, for soft spherical polymer particles in organic solvent with $\Delta\rho \approx 0.3 \text{ g cm}^{-3}$ and the same radius of $\sim 100 \text{ nm}$, the characteristic height is $kT/(\Delta\rho Vg) \approx 30 \text{ cm}$. The concentration in a vessel of a conventional size is almost constant, and the sedimentation in gravity is impossible. In this case one can consider centrifugation, where the characteristic length is defined by the effective acceleration $g' = \omega^2 R$, where ω is the revolution frequency and R is the centrifuge radius. The effective acceleration in a centrifuge can reach a few tens of gravity acceleration g that makes possible to sediment even particles with low density [223].

The particle concentration in a sol increases naturally with evaporation of the solvent. This mechanism underlies many methods for the preparation of colloidal crystals. The simplest method is drop-casting, when a drop of sol is left undisturbed on a substrate. After evaporation of the solvent, islands of a colloidal crystal remain on the substrate. Unfortunately, it is quite hard to obtain crystals of high quality this way. To improve the crystal quality, different modifications of this method are used, including spin-coating [224, 225] or vertical deposition [226, 227]. The latter method uses capillary forces and convection in the meniscus of a colloidal suspension on a substrate. The capillary force brings the particles closer effectively increasing the volume fraction, while convection brings more particles with the solvent flow to the growing front as shown in Fig. 2.28(b).

Recent advances in colloidal chemistry made possible fabrication of tunable colloids, volume fraction η of which can be changed by external stimuli. One of the most

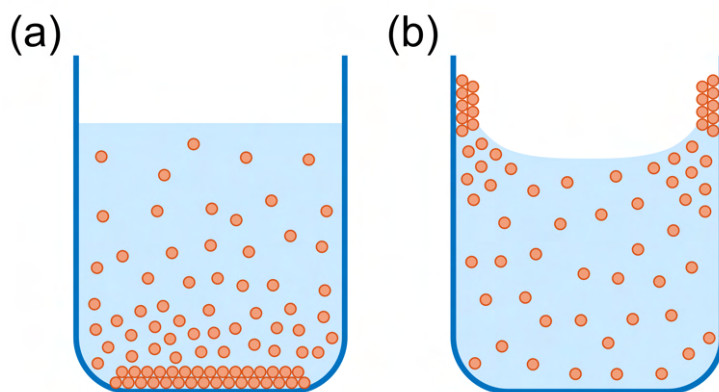


Figure 2.28: (a) Sketch of the sedimentation of a colloid. The gravity creates a concentration gradient according to Eq. (2.128) that leads to crystallization at the vessel bottom. (b) Sketch of a vertical deposition process. The capillary forces create a meniscus with elevated concentration of colloidal particles that leads to crystallization on the vessel walls. Not in scale. Adapted from [21].

common example are poly(*N*-isopropylacrylamide) (PNIPAM) spheres with temperature-dependent size [228–232]. PNIPAM is a polymer which has a Lower Critical Solution Temperature (LCST) in water of $\sim 32^\circ\text{C}$ [228], below which the polymer is water-soluble and insoluble above. The polymer network below LCST has high water content, which is released upon heating, leading to the collapse of the polymer network to about 10 times smaller volume. The phase transition is called Volume Phase Transition (VPT). At high concentrations of colloidal PNIPAM particles, the volume fraction of the particles ϕ can be easily tuned by changing the temperature in a narrow range that allows the direct control of crystallization.

2.3.1.3 Structural investigation of colloidal crystals

The structural evolution during the self-assembly in sedimentation or vertical deposition processes is hard to study due to unsuitable conditions for the use of microscopy. The most convenient techniques to trace how the structure evolves in these conditions are the X-ray methods. A single colloidal crystallite at the beginning of the crystallization process is too small to give scattering strong enough for detection. A huge footprint of the incident beam at grazing-incidence angle in GISAXS technique allows simultaneous illumination of many crystallites on the substrate that sufficiently enhances the scattered signal. Therefore, GISAXS allows time-resolved measurements of the self-assembly process starting from a monolayer of colloidal particles [233–236] to bulk films [24, 25, 237–239] on solid [24, 25, 233–235, 238] as well as liquid [236, 237, 239] substrates. When the thickness of the formed colloidal crystals is large enough, SAXS experiments in transmission geometry are also possible [29, 240–243] as shown in Fig. 2.29. Typically, for spherical colloidal particles, close-packed structures are formed initially, and only the unit cell parameters evolve during the consequent aging [24,

236, 240]. In some cases, especially for anisotropic colloidal particle, a sequence of a few intermediate crystalline phases is observed [24, 25, 29, 238, 242].

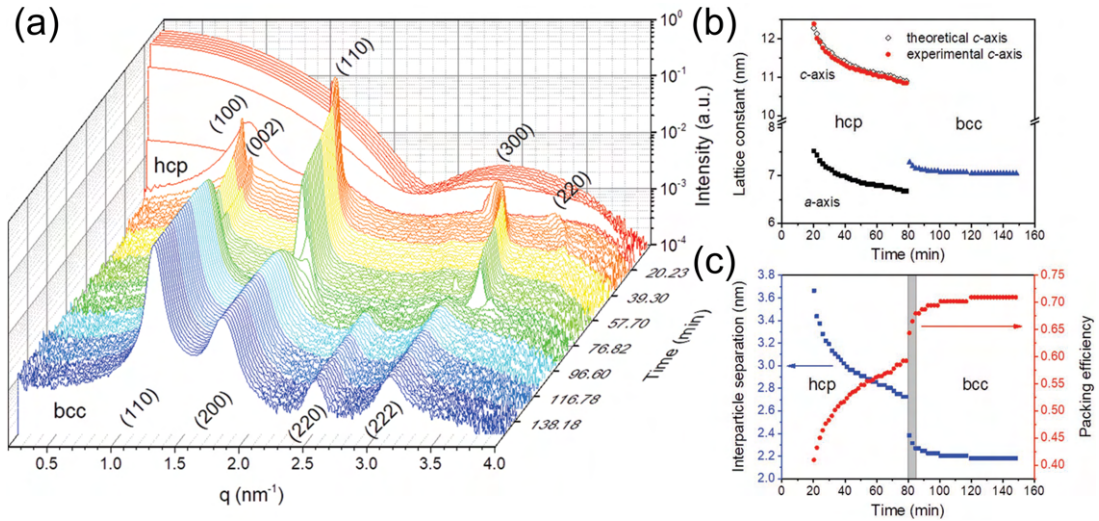


Figure 2.29: In situ SAXS study of structural evolution of a colloidal crystal consisting of lead sulfide nanoparticles with the size of about 2 nm during evaporation of heptane solvent. (a) Averaged time-resolved intensity profiles measured every 2 min. At ~ 20 min the first Bragg peaks attributed to an hcp lattice appear in the scattered intensity. Transition of hcp into bcc superlattice occurs at ~ 80 min. (b) Time dependence of lattice constants for both hcp and bcc superlattices. (c) Interparticle separation and filling fraction of soft nanocrystals as a function of time during the observed crystal structure evolution. The gray region depicts the coexistence of both hcp and bcc phases with the predominant bcc superlattice. Adapted from [29].

The tunable colloids enable the driving a phase transition quasi-statically and cycling through the transition multiple times for better statistics. The PNIPAM itself has low optical and X-ray scattering contrasts and, therefore, is typically modified by other molecules or particles. The use of fluorescent dyes makes possible the optical investigation of phase transitions in PNIPAM-based colloidal crystals [21, 230–232]. To increase the X-ray scattering contrast, one typically uses metal-PNIPAM core-shell particles [244, 245]. It allowed revealing the phase diagram of PNIPAM colloids [244, 245] and time-resolved investigations of their melting [230–232]. Using a mixture of the thermo-responsive PNIPAM particles with non-thermo-responsive particles, it was shown possible to induce point defects in colloidal crystals [21].

Dried colloidal crystals, either free-standing or on a substrate, allow application of a wider range of techniques to study their structure. The electron microscopy is applied routinely from the discovery of artificial colloidal crystals [1, 2]. In addition to revealing the structure, this method allows investigation of structural defects [5]. An example of microphotos of colloidal crystals obtained by electron microscopy is shown in Fig. 2.30(a-d). Unfortunately, the electron microscopy is sensitive only to the sample surface. The X-ray methods allow probing the structure of bulk colloidal crystals. The coexistence of different stacking motifs in hard sphere colloidal crystals was confirmed by presence of the Bragg rods in the scattered intensity [4, 23, 199, 200,

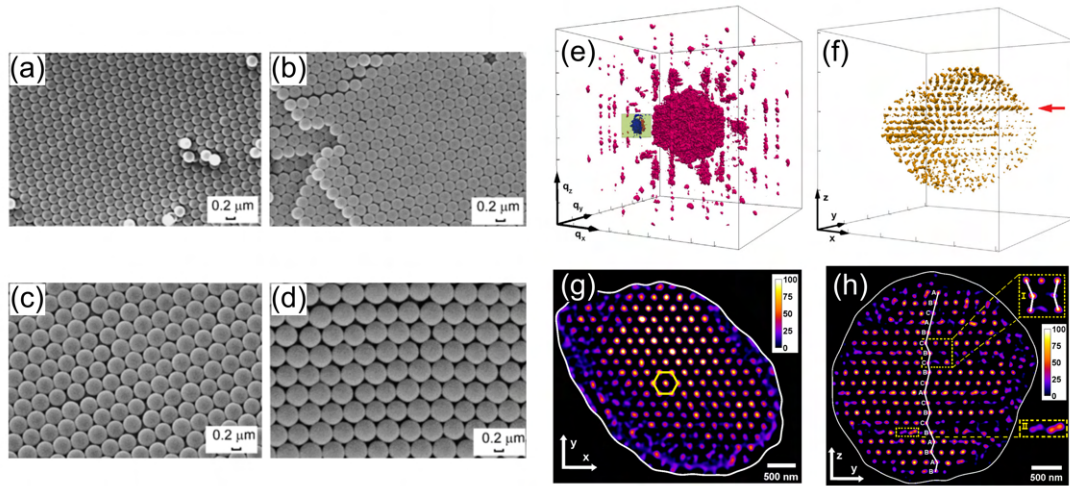


Figure 2.30: (a-d) Scanning electron microphotos of colloidal crystals consisting of polystyrene spheres with different diameters: 200 nm (a), 280 nm (b), 450 nm (c) and 560 nm (d). Adapted from [246]. (e-h) Results of Coherent Diffractions Imaging of a colloidal crystal grain consisting of silica spheres with the diameter of 230 nm. (e) Measured scattered X-ray intensity distribution in 3D reciprocal space. Length of the coordinate arrows correspond to $50 \mu\text{m}^{-1}$. (f) Reconstructed electron density distribution in 3D real space. The red arrow marks the crystalline plane shown as a 2D slice in (g). Length of the coordinate arrows correspond to $1 \mu\text{m}$. (g) 2D slice through the horizontal plane indicated in (f). (h) Projection of the reconstructed electron density on the [100] crystallographic direction of the hexagonal lattice. Each layer is marked by the letter corresponding to the stacking sequence in an hcp/fcc lattice. The insets show examples of in-plane defects. Adapted from [26].

[202]. By means of X-ray diffraction such structures were found prone to line defects [22, 201]. Comprehensive information about the particle positions in colloidal crystals is provided by CDI [26, 247] as shown in Fig. 2.30(e-h). Colloidal crystal domains of different orientations were revealed by ptychography [248]. In a colloidal crystal composed of polymer particles, it is possible to study in situ the structural evolution upon heating, when the polymer particles melt [249–251].

2.3.1.4 Properties and applications of colloidal crystals

The size of colloidal particles is comparable with the wavelength of visible light that defines their optical properties. The periodic packing of colloidal particles in colloidal crystals causes Bragg diffraction of visible light, and thus generates structural colours and photonic band gaps [13, 252]. Electromagnetic waves with energies within these band gaps are prohibited from propagating through the colloidal crystals [10, 12]. This makes evident an analogy between a photon in a colloidal crystal and an electron in a periodical potential of a conventional crystal. Thus, the colloidal crystals demonstrating such properties are typically called photonic crystals [11, 13]. Thermoresponsive colloidal particles allows tuning the structure of colloidal crystals or make them switchable that makes them interesting for applications as tunable photonic crystals [253]. The colloidal photonic crystals find applications in photonic crystal lasers, where

they, combined with a fluorescent compound, serve as the gain medium [254, 255].

Colloidal crystals can be used as templates for synthesis of 3D ordered macroporous materials. Liquid or gaseous precursors can react in the voids of a colloidal crystal forming a solid between the colloidal particles. The templates can subsequently be removed to acquire the macroporous network, in which the spherical voids are highly ordered, periodic and interconnected [256, 257]. The obtained macroporous products, often called inverse opals, do not only have the special 3D porous structure, but also maintain the optical properties of colloidal crystals. They found applications as photonic crystals [257], sensors [14], electrodes [15], catalysts [258], etc. [259]

Thanks to the developed surface, many colloidal crystals show superhydrophobic properties [260, 261], which can be used for antifogging coatings.

2.3.2 Mesocrystals

As discussed above, anisotropic colloidal particles can form crystalline structures, where all the particles are isooriented. If the particles in such colloidal crystal are crystalline, it implies long-range order not only at the macroscopic level, but also at the atomic level of the atomic crystalline lattices. H. Cölfen and M. Antonietti introduced the term "mesocrystal" to describe such systems with crystallographic order on two scales: atomic and colloidal [9], as shown in Fig. 2.31. Along with this designation, the terms "supercrystal" [262, 263], "supracrystal" [264, 265] and "nanocrystal superlattice" [25, 233, 239] are used. The mutual alignment of the nanocrystals inside a mesocrystal is not always perfect. To describe the degree of alignment, the term "mesocrystallinity" is sometimes used by analogy with the term "crystallinity" [266]. However, it is hard to quantify the "mesocrystallinity", and there is no definition as to which degree of misalignment is still tolerable to call a structure a mesocrystal.

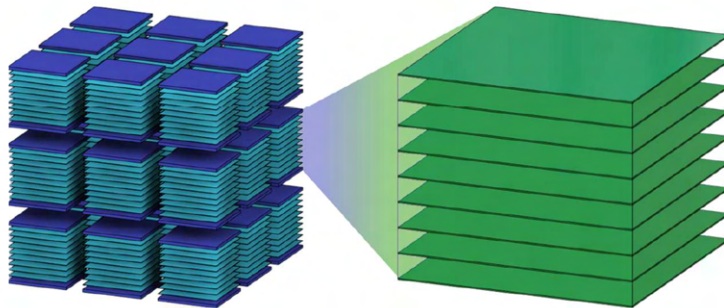


Figure 2.31: Sketch of a mesocrystal consisting of nanocrystals. The atomic lattice (AL) planes of all nanocrystals are perfectly aligned. Only one family of planes is shown for clarity. Adapted from [267].

The directional forces between faceted, single crystalline nanoparticles compared to the isotropic forces of spherical particles result in the alignment of nanoparticles

with respect to their atomic lattices (ALs). A crucial role for the inter-particle interactions play the organic ligands stabilizing the particles. A thick shell of long molecules on a particle surface can inhibit the directionality of the inter-particle forces with formation of a colloidal crystal with randomly oriented nanocrystals. Simulations show a complicated phase behaviour of mesocrystals dependent on the thickness and hardness of the ligand shells [268]. An interesting feature of mesocrystals is possibility to substitute initial ligands by other ones by so-called ligand exchange procedure [269, 270] that leads to even more complicated phase behaviour. Different superlattice structures are reported, including simple cubic [271], fcc [262, 272–274], bcc [25, 27, 275, 276] and bct [25, 28, 277] ones. The nanocrystals can take a single [25, 27, 28, 271, 275–277] or a few [262, 272, 274] defined mutual orientations aligned with the superlattice crystallographic axes.

Two structural scales of mesocrystals complicate their structural investigations. Study of the superlattice (SL) and the AL of the nanocrystal requires combination of different techniques. As discussed above, the electron microscopy is a useful technique to study the SL structure of colloidal crystals. Recent development of High Resolution Transmission Electron Microscopy (HRTEM) made possible resolving the atomic structure of nanocrystals [272]. Unfortunately, the sample thickness and the field of view in HRTEM are limited to single nanocrystals that makes impossible study of bulk mesocrystals. Nevertheless, it is possible to probe the ALs of many nanocrystals in a mesocrystal by electron diffraction complementary to a common electron microscopy. Therefore, a combination of electron microscopy and electron diffraction is widely used to assess both structural scales in mesocrystals [271–273, 275] as shown in Fig. 2.32.

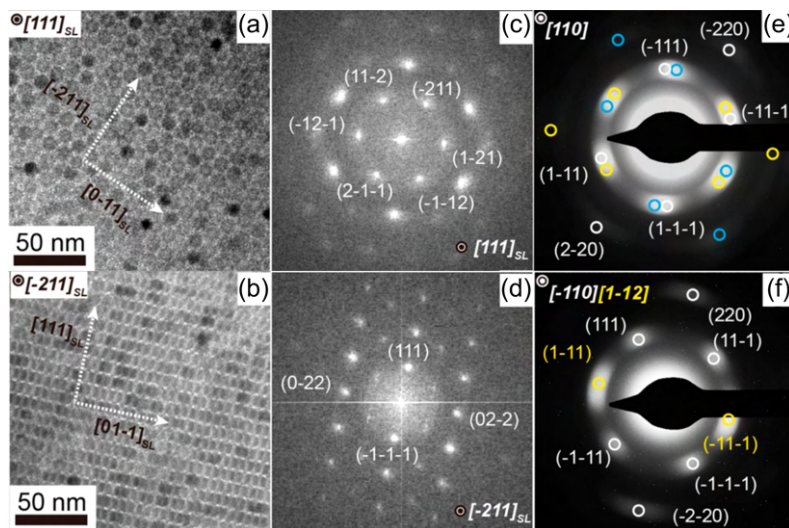


Figure 2.32: (a,b) Transmission Electron Microscopy (TEM) images of SLs formed by Si nanocrystals with cuboctahedral shape. The SLs have fcc structure with various orientations with (a) $(111)_{SL}$ and (b) $(\bar{2}\bar{1}1)_{SL}$ planes parallel to the substrate. (c,d) Fast Fourier Transforms of the images in (a,b), respectively. (e,f) Electron diffraction patterns taken from $\sim 1 \mu\text{m}^2$ area of SL shown in (a,b), respectively. The Bragg peaks are from the AL of the nanocrystals. Adapted from [273].

In X-ray scattering, simultaneous registration of SAXS from the SL and WAXS from the ALs is also complicated. A couple of detectors can be used for simultaneous measurement of the scattered intensities at small and wide angles [25]. Or, measurements of SAXS and WAXS can be done consequently with different distances between a single detector and the sample and/or at different wavelength [27, 277]. In case of availability of a large enough detector, a simultaneous detection of both SAXS and WAXS is possible [28, 262, 274] as shown in Fig. 2.33. In many cases this complications prevent complementary study of both levels of order and mesocrystals are treated as conventional colloidal crystals only by means of SAXS [24, 29, 238, 239, 242].

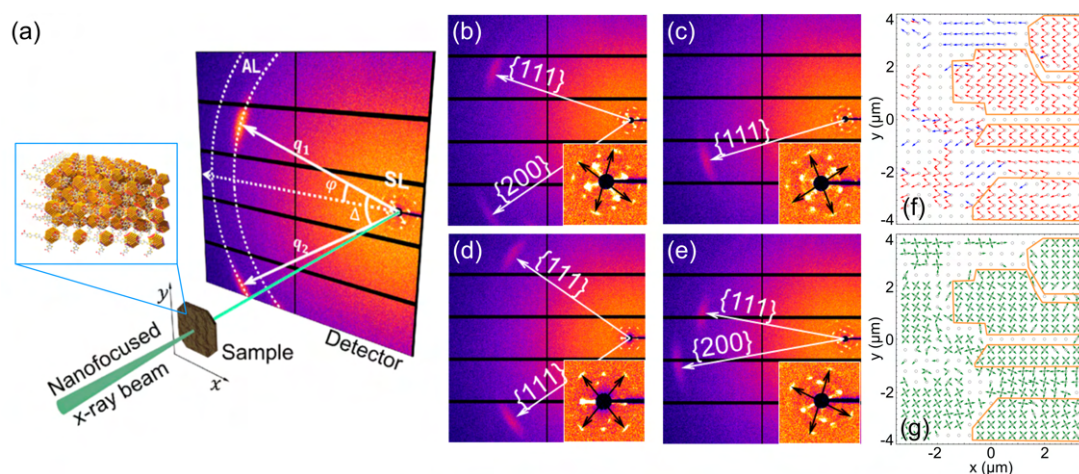


Figure 2.33: (a) Scheme of an X-ray diffraction experiment where both SAXS from the superlattice and WAXS from the atomic lattice of the nanoparticles are measured by a single 2D detector. (b-e) Examples of measured diffraction patterns from a mesocrystal consisting of PbS nanocrystals. Diffraction patterns measured at different positions of the sample. One can see SAXS scattering from the SL and WAXS Bragg peaks, corresponding to 111_{AL} and 200_{AL} reflections of the PbS AL. The insets display enlarged SAXS regions with the scattering signal from the SL. (f,g) Spatially resolved maps of angular positions of the diffraction peaks. (f) Angular positions of the 111_{AL} Bragg peaks are shown by red arrows, and angular positions of 200_{AL} Bragg peaks – by blue arrows. (g) Angular positions of the SL diffraction peaks shown with black arrows in (a-d) are shown by green arrows. Domains are indicated by orange lines. Adapted from [28].

Application of X-ray methods makes possible in situ studies of structure evolution during solvent evaporation from a mesocrystal. Thus, a transition from fcc to bcc structure via an intermediate bct stages was detected by in situ GISAXS/GIWAXS [25] as shown in Fig. 2.34. The phase transition of the SL was accompanied by a change in the orientation of the nanocrystals. Mesocrystals were found prone to defects that results in diffuse scattered intensity in SAXS regime [27]. A spatially-resolved combined SAXS/WAXS allowed a comprehensive study of defects and grain boundaries in a mesocrystal [274]. A structural evolution of a mesocrystal upon ligand exchange was studied by means of GISAXS/GIWAXS [270]. The SL was found to contract upon replacement of the ligands by shorter ones, while the nanocrystals became more disordered. Interestingly, the mutual orientation of the nanocrystals in particular mesocrystal-

tals is so fine that interference of the X-rays scattered from the ALs of the adjacent nanocrystals was reported [267, 278].

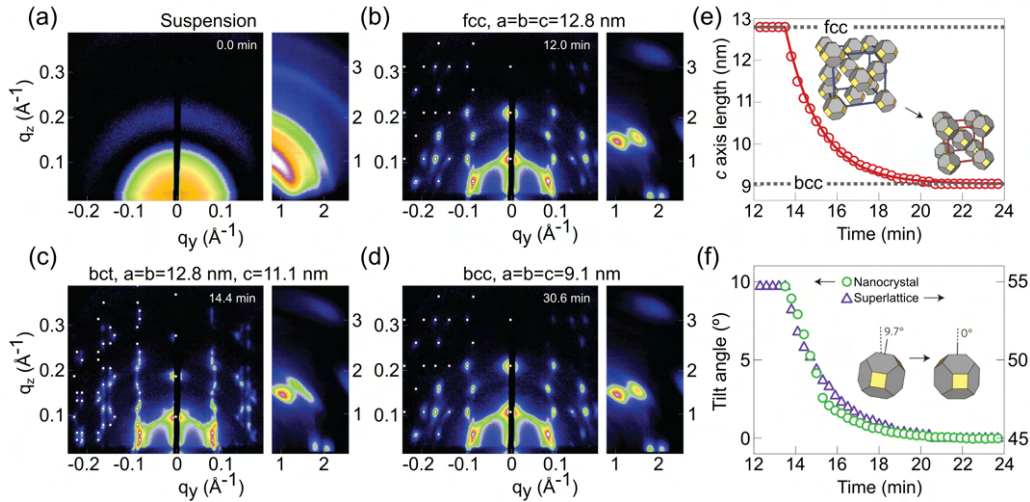


Figure 2.34: (a-d) Temporal evolution of GISAXS (square panels) and GIWAXS (vertical panels) patterns during the in situ measurement of PbS nanocrystal self-assembly. The GISAXS patterns show the transition from a colloidal suspension to an fcc SL to a bcc SL via contraction of the c axis. The white circles on the left halves of the GISAXS patterns are the predicted scattering locations for the SL parameters indicated above each image. (e) Temporal evolution of the c axis length extracted from the GISAXS pattern in (a-d). (f) Temporal evolution of the $[100]_{SL}$ and $[100]_{AL}$ axes tilt in respect to the substrate. Adapted from [25].

The long-range order of nanocrystals in a mesocrystal leads to electrostatic and quantum interaction between them. The electronic structure of a mesocrystal sufficiently differs from that of a single nanocrystal. Especially significant are the differences for semiconductor nanocrystals, where discrete energy levels split into minibands when coupled in a mesocrystal [279, 280]. Such quantum coupling of nanocrystals in a SL were observed for semiconductor [281] and metal [282] nanocrystals. By changing the size of nanocrystals, interparticle distances, and energy barrier height, one can engineer the minibands in such mesocrystals and fine-tune electronic and optical properties of such nanostructures, providing exciting possibilities for optimization of electronic, photovoltaic, and thermoelectric devices. This explains the interest in mesocrystals composed from semiconductor nanocrystals. The use of lead sulfide [262, 269, 270, 272, 274, 277], lead selenide [276, 277], cadmium selenide [17, 18, 281], caesium lead halide perovskite [20, 267, 271, 278], etc. nanocrystals was reported.

The directional interactions between faceted nanocrystals and possibility of covalent bonding by organic ligands lead to outstanding mechanical properties of mesocrystals. The drastic improvement in hardness and elastic modulus in an ordered mesocrystal in comparison to a conventional colloidal crystals was shown for iron oxide nanoparticles [263, 275]. The mechanisms of deformation in such mesocrystals were found essentially the same as in atomic crystalline lattices [5].

Chapter 3

Publications

This Chapter is based on six papers with significant personal contributions from the Author. All six papers are devoted to the study of colloidal crystals and mesocrystals using novel X-ray methods. However, the papers can be separated into two groups according to the particular methods used for the structural analysis of the samples.

Section 3.1 includes three papers on studies of colloidal crystals and mesocrystals by means of Ultra-Small-Angle X-ray Scattering (USAXS), complementary SAXS/WAXS and AXCCA. The obtained results on the crystallization and melting of colloidal crystals, structures and defects in mesocrystals, and correlations with their electronic properties are of high interest to the materials science community. The developed experimental X-ray techniques and the proposed approaches for data analysis contribute to the methodology of further possible structural studies of colloidal crystals and mesocrystals.

Section 3.2 includes three papers on the development of Angular X-ray Cross-Correlation Analysis in application to the measured scattered X-ray intensities in 3D reciprocal space. The correlations between the intensities scattered at different angles provide additional information beyond that extracted from the radial intensity distribution profile. This technique allows revealing different crystalline structures with higher precision as well as revealing the defects present in the sample. The developed technique complements a number of techniques available for investigation of 3D X-ray scattered intensity distributions. The results of the application of the technique to colloidal crystals and mesocrystals are of high interest to the materials science community.

3.1 Structural investigation of colloidal crystals and mesocrystals by complementary small- and wide-angle X-ray scattering techniques

The first paper is focused on the study of structural evolution during crystallization and melting of colloidal crystals consisting of gold-PNIPAM core-shell nanoparticles. We performed an in-situ X-ray experiment when the structural evolution during cooling and heating was traced by means of USAXS. Analysing the form-factor of the core-shell particles and the structure factor of the colloid we found that the crystallization-melting cycle is not fully reversible due to defect formation in the SL structure.

In this work, I personally participated in the X-ray experiment and took the leading part in the data analysis, including the core-shell form-factor fitting, the fluid structure factor fitting with the Perkus-Yevick hard sphere model, and the Bragg peak fitting. Parts of the data analysis were performed by Nastasia Mukharamova and Svetlana Dubinina. The main part of the manuscript was written by me after a discussion of the obtained results with other co-authors and with the contributions of other co-authors.

The Supplementary Materials for this paper can be found at: <https://doi.org/10.1039/d1sm01537k>

The second paper is focused on the correlational study of electrical conductivity and structure of mesocrystalline microchannels consisting of lead sulfide PbS nanocrystals functionalized with copper 4,4',4'',4'''-tetraaminophthalocyanine (Cu4APc). The mesocrystalline microchannels were formed on a Kapton substrate with preliminary deposited gold electrodes that allowed transport measurements. After the transport measurements, we performed an X-ray scattering experiment to study the structure of the same microchannels. Analyzing the diffraction patterns we found two distinct SL structures present: bcc and hcp characterized by different interparticle distance. Comparing the obtained structure with the measured conductivity values we found a strong correlation that can be explained by the hopping transport mechanism strongly dependent on the interparticle distance.

In this work, I personally participated in the X-ray experiment and took the leading part in the X-ray data analysis, including the Bragg peak fitting and AXCCA of the intensities measured in SAXS and WAXS regions. Parts of the data analysis were performed by Nastasia Mukharamova. Andre Maier prepared the samples and performed Atomic Force Microscopy (AFM) and Scanning Electron Microscopy (SEM) measurements. The part of the manuscript on the X-ray experiment results was written by me with the contributions of other co-authors.

The Supplementary Materials for this paper can be found at: <https://doi.org/>

The third paper is focused on correlational study of fluorescence and structure of mesocrystals consisting of lead halide perovskite nanocrystals stabilized with oleic acid (OA) and oleylamine (OAm). We found that the fluorescence spectra and lifetime are different at various spatial points within a single mesocrystal. We performed an X-rays experiment and found that the SL structure also differs from the average one on the local level. We believe that the changes in the fluorescent properties are conditioned by the structural defects.

In this work, I personally participated in the X-ray experiment and took the leading part in the X-ray data analysis, including the Bragg peak fitting in SAXS and WAXS regions. Christopher Kirsch prepared the samples and conducted optical absorption and fluorescence measurements in solution. Jonas Hiller carried out confocal fluorescence (-lifetime) measurements. The part of the manuscript on the X-ray experiment results was written by me with the contributions from other co-authors.

The Supplementary Materials for this paper can be found at: <https://doi.org/10.1038/s41467-022-28486-3>


 Cite this: *Soft Matter*, 2022, 18, 1591

In situ characterization of crystallization and melting of soft, thermoresponsive microgels by small-angle X-ray scattering†

 Dmitry Lapkin,^a Nastasia Mukharamova,^a Dameli Assalauova,^a Svetlana Dubinina,^{ab} Jens Stellhorn,^{ac} Fabian Westermeier,^a Sergey Lazarev,^{ad} Michael Sprung,^a Matthias Karg,^e Ivan A. Vartanyants^{id}*^{af} and Janne-Mieke Meijer^{id}*^g

Depending on the volume fraction and interparticle interactions, colloidal suspensions can form different phases, ranging from fluids, crystals, and glasses to gels. For soft microgels that are made from thermoresponsive polymers, the volume fraction can be tuned by temperature, making them excellent systems to experimentally study phase transitions in dense colloidal suspensions. However, investigations of phase transitions at high particle concentration and across the volume phase transition temperature in particular, are challenging due to the deformability and possibility for interpenetration between microgels. Here, we investigate the dense phases of composite core–shell microgels that have a small gold core and a thermoresponsive microgel shell. Employing Ultra Small-Angle X-ray Scattering, we make use of the strong scattering signal from the gold cores with respect to the almost negligible signal from the shells. By changing the temperature we study the freezing and melting transitions of the system *in situ*. Using Bragg peak analysis and the Williamson–Hall method, we characterize the phase transitions in detail. We show that the system crystallizes into an *rhcp* structure with different degrees of in-plane and out-of-plane stacking disorder that increase upon particle swelling. We further find that the melting process is distinctly different, where the system separates into two different crystal phases with different melting temperatures and interparticle interactions.

 Received 27th October 2021,
 Accepted 16th December 2021

DOI: 10.1039/d1sm01537k

rsc.li/soft-matter-journal

1. Introduction

Microgels feature an internal gel-like structure that can be highly swollen by solvent rendering them soft and deformable.^{1,2} With their typical dimensions in the submicrometer range, microgels resemble many physical properties of classical colloids, while also behaviour common for macromolecules and surfactants is observed.^{2–4} In addition, the microgel network can be finely tuned, for instance their softness can be modified through the degree of chemical cross-linking,^{5–7} while a response to external stimuli, such as temperature, pH, or concentration gradients, can be reached by altering the chemical composition.^{1,2,8} These complex interactions and their tunability render microgels as the ideal model system to study soft colloidal interactions and phase behaviour. In this role microgels have been used to study important fundamental phenomena, such as phase transitions, defect formation, as well as the glass transition or jamming in dense soft particle systems.^{9–21} In particular, studies from the last few years addressed the microgel structure in densely packed systems, revealing that microgels at sufficiently high particle densities can experience different phenomena such as interpenetration^{22–24} and/or deswelling.^{22,25–29}

^a Deutsches Elektronen-Synchrotron DESY, Notkestraße 85, 22607 Hamburg, Germany

^b Moscow Institute of Physics and Technology (State University), Institutskiy Per. 9, 141701 Dolgoprudny, Moscow Region, Russia

^c Department of Applied Chemistry, Graduate School of Advanced Science and Engineering, Hiroshima University, 1-4-1 Kagamiyama, Higashihiroshima 739-8527, Japan

^d National Research Tomsk Polytechnic University (TPU), Lenin Avenue 30, 634050 Tomsk, Russia

^e Heinrich-Heine-Universität Düsseldorf, Universitätsstraße 1, D-40225 Düsseldorf, Germany

^f National Research Nuclear University MEPhI (Moscow Engineering Physics Institute), Kashirskoe shosse 31, 115409 Moscow, Russia.

E-mail: ivan.vartanyants@desy.de

^g Department of Applied Physics and Institute for Complex Molecular Systems, Eindhoven University of Technology, Groene Loper 19, 5612 AP Eindhoven, The Netherlands. E-mail: j.m.meijer@tue.nl

† Electronic supplementary information (ESI) available: Details on the core–shell particle characterization, analysis of the scattering from a dilute sample, analysis of the fluid structure factor of the dense sample, and details on the Bragg peaks fitting are presented. See DOI: 10.1039/d1sm01537k



When microgels are prepared from poly-*N*-isopropylacrylamide (PNIPAM), the size and volume fraction of microgels can be controlled *in situ* by temperature variations.³⁰ This makes PNIPAM microgels of particular interest for *in situ* investigations of phase transitions, such as crystallization and melting.^{10,15,17} The temperature behaviour is related to the lower critical solution temperature (LCST) of PNIPAM in water below which polymer-solvent interactions are favoured. Above the LCST polymer-polymer interactions dominate leading to chain collapse into globules and results in the pronounced volume phase transition (VPT) behaviour. Below the VPT temperature (VPTT) PNIPAM microgels are highly swollen by water and thus possess large volumes. Surpassing the VPTT a strong deswelling is observed due to the expulsion of water and the microgel volume can decrease by almost 90%.^{30–32} During shrinkage a transition from soft repulsive to short-range attractive particle interactions is also observed for particles with weak to no electrostatic stabilization.^{34,35} In contrast, a change from soft repulsive to less soft, electrostatic interactions is observed for microgels that possess more ionic groups.^{30,32}

Importantly, the temperature responsive phase behaviour of PNIPAM microgels is still not completely understood. In particular, this is the case for high particle concentrations close to and above the VPTT where the exact particle interactions and their internal degrees of freedom become relevant. In a recent study by Bergman *et al.*³³ it was highlighted that upon approaching the VPTT the microgel interaction potential can be best described by a multi-Hertzian model, taking into account repulsion from the higher cross-linked cores. One of the main reasons why the temperature response of PNIPAM microgels is hard to address, is the fact that upon close contact the microgels start to overlap and cannot be resolved individually. This explains why most optical (fluorescent) microscopy studies have focused on dilute systems³⁴ or crystalline systems in which the periodic order helps to resolve particle centers^{10,15,17} and only intensive experimental optimization such as specific fluorescent labelling and super-resolution methods provide enough resolution to resolve the microgels in dense states.²² Also, for scattering methods using *e.g.* neutrons or X-rays the microgels possess very little contrast and thus long measurement times are required. In addition, it has been shown that the microgel form factor significantly differs from the dilute, non-interacting state,²⁷ rendering the analysis of the structure factor of the dense state difficult.

The use of core-shell (CS) particles can circumvent several of these problems, as the cores can be labelled such that these can be easily detected, for instance with fluorescent dyes or high contrast materials, and thereby can provide information on the particle centre distributions.^{35–38} Combined with the development of *in situ* techniques, their availability opens up the possibility to perform time-resolved studies during temperature-induced phase transitions, such as crystallization and melting, which is still not fully understood.³⁹ For *in situ* studies using the great resolution in space and time of small-angle X-ray scattering (SAXS), CS microgels with high electron density cores are desired. Ideally suited for this purpose are CS microgels with small, monodisperse gold nanoparticle cores

that are accessible *via* seeded precipitation polymerization.^{40,41} These particles are also of interest for several optical applications because gold nanoparticles feature localized surface plasmon resonances (LSPR) while the microgel shells can be used to control inter-particle spacing and assembled structures.^{42,43} Periodic 2D lattices of these CS microgels were found to sustain surface lattice resonances (SLRs) as the result of plasmonic/diffractive coupling that arises when the inter-particle spacing is close to the LSPR.^{44,45} The self-assembly into 3D crystals has been studied by UV-VIS spectroscopy and small-angle neutron scattering (SANS),⁴⁶ but structural changes induced by temperature were not explored yet.

Here, we investigate the phase behaviour of dilute and dense suspensions of Au-PNIPAM CS microgels with Ultra-Small Angle X-ray Scattering (USAXS). The gold core provides high X-ray scattering contrast while the particle interactions are governed by the microgel shell which makes this combination uniquely suited for *in situ* investigations. We explore the phase transitions between crystalline and fluid-like states in response to both cooling and heating with a temperature rate of 0.1 °C min⁻¹. We investigate the exact details of the processes using our recently developed Bragg peak analysis⁴⁷ and identify the crystal structure and structural changes during crystallization and melting. This allows us to identify the freezing and melting point but also reveals unexpected interparticle behaviour. In addition, we find that upon melting the system behaves differently compared to crystallization, showing the separation into three different crystallites consisting of two phases with distinctly different melting behaviour. Our results show that the combination of the CS microgels with USAXS opens up the possibility for detailed investigations of soft PNIPAM microgel phase behaviour upon changes in temperature and provides new fundamental insight into the nature of the phase transitions, also important for their application as functional materials.

2. Experimental section

2.1. Sample preparation

Temperature-sensitive CS microgels consisting of gold nanoparticle cores and chemically cross-linked microgel shells (PNIPAM) were synthesized following established protocols.^{40,45} The obtained CS particles were found to contain an Au core of the radius $R_{\text{core}} = 29.1 \pm 4.2$ nm and to have a hydrodynamic radius R_h , in the swollen state of $R_h(20\text{ °C}) = 228.9$ nm and in the collapsed state of $R_h(50\text{ °C}) = 151.1$ nm. The VPTT was determined to be at approximately 32.2 °C (see for details ESI,† Section S1 and Fig. S1). Two different dispersions of Au-PNIPAM particles with different concentrations, 0.5 wt% and 12 wt%, were prepared in deionized water (>18.2 MΩ cm at 25 °C) and kept at these conditions by adding ~5 mg of ion exchange resin. The 12 wt% dispersion showed upon visual inspection optical Bragg reflections at $T = 20\text{ °C}$ and their absence at $T = 50\text{ °C}$ indicating a phase transition. The effective volume fraction ϕ_{eff} of the samples at different temperatures was estimated from the CS particle volume *via* R_h and the free



volume based on interparticle spacing in the fully crystalline state of the 12 wt% sample at $T = 38\text{ }^{\circ}\text{C}$ assuming an face-centered cubic (fcc) packing. We find at $T = 20\text{ }^{\circ}\text{C}$ for the 12 wt% dispersion $\phi_{\text{eff}} = 0.60$ and for the 0.5 wt% dispersion $\phi_{\text{eff}} = 0.025$ (see for details ESI[†], Section S2). The dispersions ($\sim 20\text{ }\mu\text{L}$) were placed into flat capillaries ($4 \times 0.2 \times 50\text{ mm}^3$, internal dimensions, Vitrocom) by employing a reduced pressure method. For the 12 wt% sample the dispersion was heated to $T = 50.0\text{ }^{\circ}\text{C}$ prior to filling the capillary to reduce the dispersion viscosity. To prevent water evaporation during the experiment the open ends of the capillaries were flame sealed.

2.2. USAXS experiment

Ultra-small angle X-ray scattering was performed at the Coherence Applications Beamline P10 of the PETRA III synchrotron radiation facility at DESY, Hamburg. An X-ray beam with the photon energy $E = 8.539\text{ keV}$ (wavelength $\lambda = 0.145\text{ nm}$) was cut down to the size of $\sim 50 \times 50\text{ }\mu\text{m}^2$ on the sample by a slits system. A 2D detector EIGER X 4M (Dectris AG) with 2070×2167 pixels and a pixel size of $75 \times 75\text{ }\mu\text{m}^2$ was positioned 21.3 m behind the sample in USAXS geometry (Fig. 1). To avoid air absorption, an evacuated flight tube was placed between the sample and detector. The exposure time was selected to be 0.1 s to minimize radiation damage during the experiment. The sample capillaries were mounted in a copper sample holder which provided a uniform temperature distribution along the capillary. The holder had two small windows with a diameter of $1 \times 4\text{ mm}^2$ to allow X-rays to pass through the sample (see Fig. S2, ESI[†]). Heating and cooling of the sample was performed by a Peltier element and circulating water bath. The temperature was measured by a thermocouple, which was in contact with the copper frame. A temperature controller adjusted the Peltier element to maintain a certain temperature with $0.001\text{ }^{\circ}\text{C}$ stability. Measurements were performed in the temperature range between $20.0\text{ }^{\circ}\text{C}$ and $50.0\text{ }^{\circ}\text{C}$.

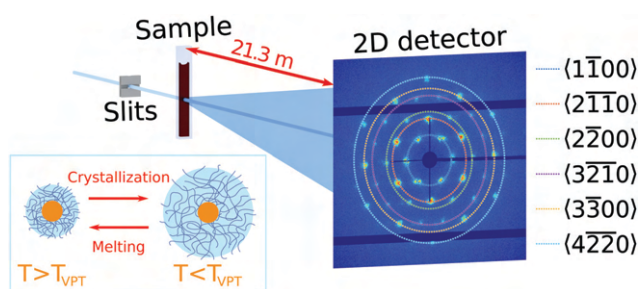


Fig. 1 Scheme of the USAXS setup at the Coherence Applications Beamline P10 at PETRA III synchrotron storage ring. The beam was shaped with $50 \times 50\text{ }\mu\text{m}^2$ slits before passing through the sample. The core-shell microgel dispersions were sealed in the glass capillaries. The scattering pattern was detected by an EIGER X 4M detector positioned 21.3 m behind the sample. Diffraction pattern shown in this figure was collected at $T = 35\text{ }^{\circ}\text{C}$. Families of Bragg peaks are indicated in the caption. For the crystalline sample this results in distinct Bragg peaks in the 2D USAXS pattern that are assigned to a random hexagonal close-packed (rhcp) crystal structure oriented along the [0001] axis. The inset on the bottom left shows a schematic representation of the swelling/deswelling behaviour of the PNIPAM shell of the CS microgels upon cooling/heating, resulting in a phase transition from a fluid to a crystal phase and vice versa.

3. Results

3.1. Core-shell particle and phase characterization

We first investigated the general properties of the CS microgels in the dilute state with 0.5 wt% and $\phi_{\text{eff}}(20\text{ }^{\circ}\text{C}) = 0.025$ between $T = 25.0\text{ }^{\circ}\text{C}$ and $T = 50.0\text{ }^{\circ}\text{C}$. Examples of the 2D USAXS patterns measured in the fully collapsed state ($T = 40.0\text{ }^{\circ}\text{C}$) and just slightly above the VPTT ($T = 35.0\text{ }^{\circ}\text{C}$) are shown in Fig. 2a and b. The scattered intensity $I(q)$ is a product of the form factor $P_{\text{cs}}(q)$ of the CS particles and the structure factor $S(q)$ of the superlattice, $I(q) \propto P_{\text{cs}}(q)S(q)$. At this low volume fraction interference between scattering from different particles is negligible (*i.e.* $S(q) \approx 1$) and the resulting scattering represents solely the $P_{\text{cs}}(q)$ of the CS microgels. The radially averaged intensity profiles are shown in Fig. 2c (see also ESI[†], Fig. S3a and b). First of all, we note the large difference in scattering contrast between the gold core and the polymer shell that leads to two distinct features in the $P_{\text{cs}}(q)$, with a first minimum around $q \sim 30\text{ }\mu\text{m}^{-1}$ and a second minimum at $q \sim 160\text{ }\mu\text{m}^{-1}$, respectively. To extract the CS characteristics, the profiles were fitted with a core-shell model in which we accounted for the particle polydispersity by using a Gaussian size distribution (see ESI[†], Section S4 for details of the fitting). The fitting was performed for each temperature and the evolution of the extracted parameters is shown in Fig. S4 (ESI[†]). The core scattering contrast was fixed at $\Delta\rho_{\text{core}} = 4326\text{ nm}^{-3}$ and the core radius was found to be $R_{\text{core}} = 25.8 \pm 4.6\text{ nm}$ for all temperatures. This Au-core size agrees well with $R_{\text{core}} = 29.1 \pm 4.2\text{ nm}$ measured by TEM. In addition, the fits also confirm the size change of the PNIPAM shell with increasing temperature. We find that the total shell radius R_{shell} decreases from $R_{\text{shell}}(25\text{ }^{\circ}\text{C}) = 192 \pm 31\text{ nm}$ to $R_{\text{shell}}(50\text{ }^{\circ}\text{C}) = 162 \pm 22\text{ nm}$, while the shell scattering contrast $\Delta\rho_{\text{shell}}$ increases from $\Delta\rho_{\text{shell}}(25\text{ }^{\circ}\text{C}) = 16\text{ nm}^{-3}$ up to $\Delta\rho_{\text{shell}}(50\text{ }^{\circ}\text{C}) = 25\text{ nm}^{-3}$, confirming the collapse of the PNIPAM shell. This change in size agrees well with the observed change in the hydrodynamic radius R_{h} from $R_{\text{h}}(25\text{ }^{\circ}\text{C}) = 220.8\text{ nm}$ to $R_{\text{h}}(50\text{ }^{\circ}\text{C}) = 151.1\text{ nm}$. The discrepancy between R_{shell} and R_{h} is typically observed for microgels and can be explained by a fuzzy-sphere structure with lower cross-linking density and dangling ends in the outer region of the shell.⁹ Here, this detail is ignored in the $P_{\text{cs}}(q)$ fit where a homogeneous density is assumed leading to a smaller R_{shell} .

Next, we investigated the high concentration sample with $\phi_{\text{eff}}(20\text{ }^{\circ}\text{C}) = 0.60$ that showed a crystal to fluid phase transition between $T = 20.0\text{ }^{\circ}\text{C}$ to $T = 50.0\text{ }^{\circ}\text{C}$, as evident from the appearance of optical Bragg reflections upon cooling. Examples of the 2D USAXS patterns in the collapsed state at $T = 40.0\text{ }^{\circ}\text{C}$ and close to the VPTT at $T = 35.0\text{ }^{\circ}\text{C}$ are shown in Fig. 2d and e, together with the radial averaged profiles shown in Fig. 2f. We assume the USAXS signal is dominated by scattering from the Au cores due to two reasons: the higher scattering contrast of the Au cores and the decrease in the contrast between the shells due to the dense packing of the CS microgels at high ϕ_{eff} . Therefore, we attribute the main contribution to $I(q)$, and hence $S(q)$, to be originating from the Au cores. At $T = 40.0\text{ }^{\circ}\text{C}$, the 2D-USAXS pattern shows broad isotropic rings characteristic for



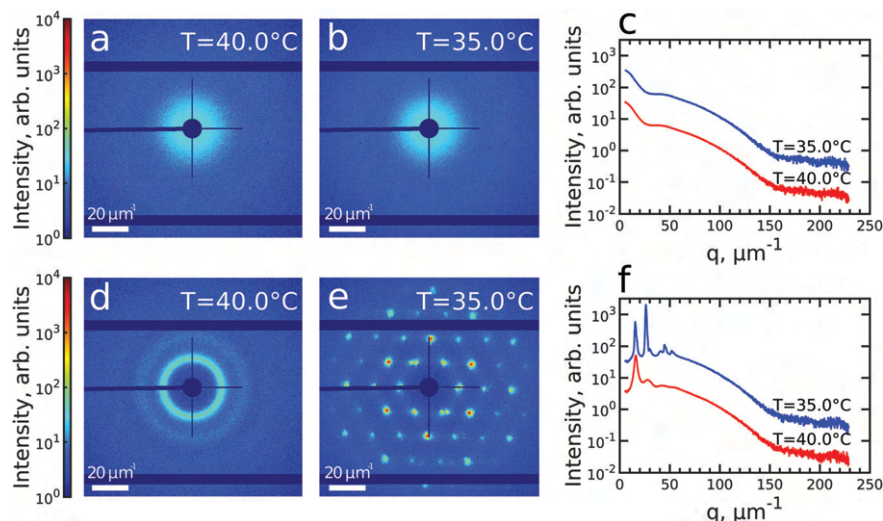


Fig. 2 (a and b) Typical 2D-USAXS patterns of the dilute colloidal sample with 0.5 wt% at $T = 40.0\text{ }^{\circ}\text{C}$ (a) and $T = 35.0\text{ }^{\circ}\text{C}$ (b). (c) The corresponding radially averaged profiles of the scattered intensity. (d and e) Typical 2D-USAXS patterns of the densely packed colloidal sample with 12 wt% at $T = 40.0\text{ }^{\circ}\text{C}$ (d) and $T = 35.0\text{ }^{\circ}\text{C}$ (e). (f) The corresponding radially averaged profiles of the scattered intensity. In (c) and (f) the profiles of scattered intensity are offset by an order of magnitude for clarity.

scattering from a disordered fluid phase. At $T = 35.0\text{ }^{\circ}\text{C}$, the 2D-USAXS pattern shows six prominent orders of narrow Bragg peaks originating from the CS microgels that have organized into a crystal lattice. The six-fold symmetry of the Bragg peaks can be attributed to a random hexagonal close-packed (*rhcp*) crystal lattice as indicated in Fig. 1 and will be discussed in detail below.

3.2. *In situ* characterization of crystallization

To investigate the crystallization process of the CS microgel system, the phase transition from fluid to crystalline state was

followed *in situ* with USAXS by applying continuous cooling around the temperature where the phase transition was observed. For this, the sample was first heated to $T = 50\text{ }^{\circ}\text{C}$ to allow the system to equilibrate in a fluid state, followed by a cooling step to $T = 40\text{ }^{\circ}\text{C}$ where the CS microgels already swell resulting in $\phi_{\text{eff}}(40\text{ }^{\circ}\text{C}) = 0.21$ based on the R_h but remain in a fluid-like state. Next, the system was continuously cooled with a rate of $0.1\text{ }^{\circ}\text{C min}^{-1}$ and diffraction patterns were collected every 30 s from $T = 39.0\text{ }^{\circ}\text{C}$ to $T = 35.0\text{ }^{\circ}\text{C}$ giving a temperature resolution of $0.05\text{ }^{\circ}\text{C}$. At each temperature, radially averaged $I(q)$

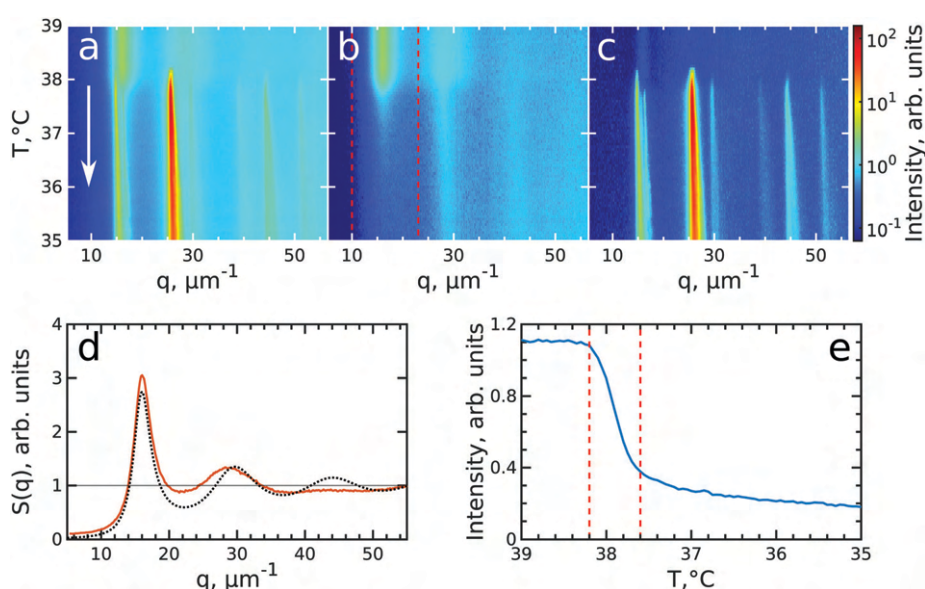


Fig. 3 Evolution of crystallization of CS system at $\phi_{\text{eff}}(20\text{ }^{\circ}\text{C}) = 0.60$ during cooling. The radially averaged intensity plots for different temperatures are stacked together in 2D maps as a function of scattering vector q and temperature T for (a) full structure factor $S(q)$, (b) fluid structure factor $S_{\text{iso}}(q)$ (the intensity between the Bragg peaks), (c) crystal structure factor $S_{\text{ktal}}(q)$ (containing only the Bragg peaks). The white arrow in (a) indicates the direction of the experiment. (d) Fluid structure factor $S_{\text{iso}}(q)$ at $T = 39.0\text{ }^{\circ}\text{C}$ (red line) and the best Percus–Yevick hard sphere structure factor fit (black dotted line). (e) Integrated $S_{\text{iso}}(q)$ near the first fluid ring (in the range of $q = 10\text{--}23\text{ }^{\mu\text{m}^{-1}}$ as indicated by the red dashed lines in panel (b)). The vertical red dashed lines indicate the temperature range of active crystallization.



profiles of the diffraction patterns were extracted. From these profiles, $S(q)$ can be obtained by dividing the measured intensity $I(q)$ by the fitted form factor $P_{cs}(q)$ from the dilute sample at each temperature step as $S(q) \propto I(q)/P_{cs}(q)$. The evolution of $S(q)$ as a function of temperature during the full cooling process is shown as an intensity map in Fig. 3a. At high temperatures ($T > 38^\circ\text{C}$, top part of Fig. 3a), $S(q)$ contains only broad features that can be attributed to the scattering from the isotropic fluid. At $T = 38.2^\circ\text{C}$ the first sharp Bragg peaks start to appear, indicating the onset of crystallization. The size change of the PNIPAM shell at this particle concentration (12 wt%) leads to a significant change in particle volume fraction from $\phi_{\text{eff}}(40^\circ\text{C}) = 0.21$ to $\phi_{\text{eff}}(35^\circ\text{C}) = 0.30$ in between these two temperatures ϕ_{eff} thus exceeds the freezing volume fraction ϕ_f , i.e. $\phi_{\text{eff}} > \phi_f$, and results in the crystallization of the CS particles.

To follow the transitions of the fluid and crystalline phases separately, we extracted the isotropic structure factor $S_{\text{iso}}(q)$ by taking the average intensity on a ring at a q -value between the Bragg peaks and the crystal structure factor via $S_{\text{xtal}}(q) = S(q) - S_{\text{iso}}(q)$, which contains highly anisotropic features caused by the Bragg peaks of the crystalline phase. Fig. 3b and c show the distinctly different evolution of $S_{\text{iso}}(q)$ and $S_{\text{xtal}}(q)$ for the full temperature range, respectively. At high temperatures ($T > 38.2^\circ\text{C}$) $S_{\text{iso}}(q)$ shows only the fluid features that almost completely disappear upon crystallization of the sample ($T < 37.6^\circ\text{C}$). At $T < 37^\circ\text{C}$ the small remaining intensity in $S_{\text{iso}}(q)$ comes only from the tails of the Bragg peaks. In contrast, at high temperatures ($T > 38.2^\circ\text{C}$) $S_{\text{xtal}}(q)$ shows very small traces of the first maximum of the fluid structure factor, while at $T = 38.2^\circ\text{C}$ the appearance of the first Bragg peaks occurs that are followed by the appearance of higher order peaks between $T = 38.2$ – 38.0°C which upon further cooling, continue to increase in intensity. We extracted the exact state of the fluid and the phase transition temperature from $S_{\text{iso}}(q)$. Fig. 3d shows $S_{\text{iso}}(q)$ at $T = 39.0^\circ\text{C}$ where a broad first maximum from the fluid phase can be seen. We fitted the $S_{\text{iso}}(q)$ with the Percus–Yevick hard sphere model $S_{\text{PY}}(q)$ (see ESI,† Section S5 for details of the fitting).⁴⁸ The best fit for $S_{\text{iso}}(q)$ with a hard sphere radius of $R_{\text{PY}} = 216 \pm 1$ nm and a volume fraction of $\phi_{\text{PY}} = 0.47 \pm 0.03$ is also shown in Fig. 3d. The obtained R_{PY} is larger than the CS size of $R_{\text{h}}(39^\circ\text{C}) = 162.7$ nm and can be explained by the charged characteristics of our microgels with a zeta-potential of $\zeta \approx -30$ mV that dominates the particle interactions in the collapsed state (see for details Fig. S1, ESI†). The surface charges result in long-range electrostatic repulsion between the CS particles under the deionized conditions that leads to a Debye length of $\kappa^{-1} \sim 100$ nm. The high volume fraction $\phi_{\text{PY}} = 0.47$ indicates the system is indeed showing signatures of a fluid close to the hard sphere freezing volume fraction $\phi_{\text{f-HS}} = 0.494$. From the fluid structure factor intensity $S_{\text{iso}}(q)$ the onset and end of the full crystallization process were determined. Fig. 3e shows the integrated value of $S_{\text{iso}}(q)$ around the first maximum in the range of 10 – $23 \mu\text{m}^{-1}$ (red dashed lines in Fig. 3b). The intensity remains constant up to $T = 38.2^\circ\text{C}$ and then starts to drop significantly, which coincides with the appearance of the Bragg peaks in $S_{\text{xtal}}(q)$. Clearly, this

temperature is the starting point for crystallization of the sample and at this point $\phi_{\text{eff}} = \phi_f = 0.23$, as a result of the small increase of the CS particle size ($R_{\text{h}}(38^\circ\text{C}) = 165.8$ nm). The major drop in intensity occurs between $T = 38.2$ – 37.6°C and indicates the crystallization of the major part of the system during this small temperature and time window (0.6°C , 6 min), which we will refer to as the ‘active crystallization’ regime. We note that further cooling still leads to a small decrease in the $S_{\text{iso}}(q)$ intensity which can be caused by crystallization of residual amounts of the fluid phase as well as potential annealing of crystalline defects that would decrease the intensity of the Bragg peak tails (further discussed below).

To investigate the crystallization process in more detail, we performed Bragg peak analysis on the peaks visible in the 2D USAXS patterns.⁴⁷ There are six prominent orders of Bragg peaks present in $S_{\text{xtal}}(q)$ at $q/q_1 = 1, \sqrt{3}, 2, \sqrt{7}, 3, 2\sqrt{3}$ with respect to the first order peak at $q_1 \approx 15 \mu\text{m}^{-1}$. These Bragg peaks indicate the presence of a single crystal domain with an *rhcp* structure aligned with its hexagonal close-packed planes parallel to the capillary walls and, hence, perpendicular to the X-ray beam. The *rhcp* structure is typically found for colloidal spheres, as the spheres pack into close packed hexagonal planes while the stacking sequence of the planes is random, leading to alternating *fcc* and hexagonal close-packed (*hcp*) crystal structures.^{14,49–52} The Bragg peaks can be identified as the hexagonal close packed $1\bar{1}00$, $2\bar{1}\bar{1}0$, $2\bar{2}00$, $3\bar{2}\bar{1}0$, $3\bar{3}00$ and $4\bar{2}\bar{2}0$ families, respectively (see Fig. 1). We do note that there are two additional peaks of lower intensity next to the $1\bar{1}00$ peaks in the pattern. We believe that these peaks originate from another crystal grain and were therefore excluded from the further analysis.

The Bragg peak analysis was done by fitting the peaks with a 2D Gaussian function (see ESI,† Section S6 for details). Each diffraction pattern was interpolated into a polar (q, φ)-coordinate frame and divided by the corresponding single particle form-factor. Each Bragg peak was fitted separately with a 2D Gaussian function in the polar coordinates. The following fitting parameters were extracted: the peak intensity, the q -position of the center of the peak, and the full widths at half maximum (FWHMs) in radial and azimuthal directions. Finally, the obtained values were averaged for each Bragg peak family with the error bars representing the standard deviation within each family.

The evolution of the integrated Bragg peak intensities for each Bragg peak family over the full investigated temperature range is shown in Fig. 4a. The first peaks to appear are the brightest $2\bar{1}\bar{1}0$ family peaks at $T = 38.25^\circ\text{C}$, confirming again that at this temperature the crystallization starts. Upon further cooling, higher order Bragg peaks appear, with the last set of peaks belonging to the $3\bar{2}\bar{1}0$ family, which also possesses the lowest intensity, at $T = 38.05^\circ\text{C}$. The intensity of all peaks rapidly increases from the moment they appear until the intensity increase significantly slows down for temperatures approaching $T = 37.6^\circ\text{C}$. Further cooling only leads to a minor rise off all intensities. The appearance and the rise in intensity of the peaks up to $T = 37.6^\circ\text{C}$, indicates the growth of a crystal nuclei from the fluid and the increasing long-range order of the crystal grain.



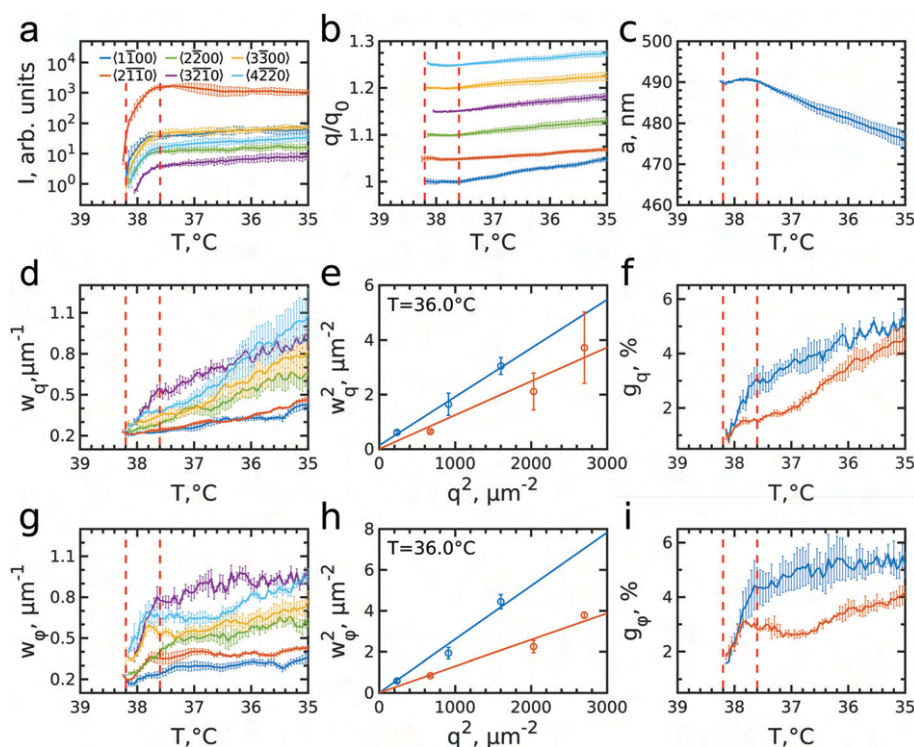


Fig. 4 Evolution of the Bragg peaks and crystal parameters during cooling. In all panels the vertical red dashed lines indicate the temperature range of active crystallization. (a) Integrated intensity, (b) q -position of the peaks in respect to the first registered q -value of the peak, q_0 (plots are offset by 0.05 for clarity). The error bars are standard deviations between the peaks of the same family. (c) Evolution of the lattice parameter, a , averaged over all observed Bragg peaks. (d and g) The size of the Bragg peaks (FWHM) in radial (d) and azimuthal (g) directions. The error bars are standard deviations between the peaks of the same family. (e and h) Examples of the Williamson–Hall plots for FWHMs of the subpeaks in radial (e) and azimuthal (h) directions at $T = 36.0$ °C. Points are experimental values for the stacking-dependent (blue) and stacking-independent (red) peaks and straight lines are the best fit for each group. (f and i) Evolution of the radial (f) and angular (i) lattice distortions extracted by the Williamson–Hall method from the stacking-dependent (blue) and stacking-independent (red) peaks.

The evolution of the peaks position with respect to the initial q -values, q_0 , is shown in Fig. 4b. During the initial rapid crystallization, the peak positions stay quite stable or even slightly decrease. However, after $T = 37.6$ °C, when most of the sample has crystallized, all Bragg peaks start moving towards higher q -values, indicating that the lattice spacing decreases. Surprisingly, the increase rate varies for different Bragg peak families. For the most intense $2\bar{1}\bar{1}0$ peaks, the q -value increases only by $\sim 2\%$ from the start of crystallization to the final temperature $T = 35.0$ °C, while that of the $1\bar{1}00$ peak increases up to $\sim 5\%$. All other Bragg peaks move with rates between these two extrema, although $2\bar{2}00$ and $3\bar{2}\bar{1}0$ are closer to the rate of $1\bar{1}00$, and $3\bar{3}00$ and $4\bar{2}\bar{2}0$ are closer to $2\bar{1}\bar{1}0$. Interestingly, these two groups of peaks have different origins. In reciprocal space the stacking disorder of the planes in the $rhcp$ structure leads to the appearance of stacking-dependent Bragg rods along the direction normal to the close packed planes, which in this case is parallel to the X-ray beam. Here, the $1\bar{1}00$, $2\bar{2}00$ and $3\bar{2}\bar{1}0$ can be identified as stacking-dependent peaks, while the $2\bar{1}\bar{1}0$, $3\bar{3}00$ and $4\bar{2}\bar{2}0$ are stacking-independent peaks. The difference in their q -value evolution seems to indicate that there are differences in how the crystal grows and how the defect structure develops in the in- and out-of-plane direction of the crystal grain.

From the peak positions of all Bragg peaks, we can calculate the average hcp unit cell parameter a as shown in Fig. 4c. During the active crystallization a is almost constant, only increasing slightly from $a = 489 \pm 1$ nm to $a = 491 \pm 1$ nm. However, further cooling leads to a decrease to $a = 476 \pm 5$ nm. The interparticle spacing upon crystallization is larger than $2R_p(38$ °C) = 331.7 nm and its decrease with further cooling is contradictory to the swelling of the PNIPAM shells to $2R_p(35$ °C) = 362.3 nm (see ESI,† Fig. S1c). Both discrepancies seem to be caused by the electrostatic interactions between the CS particles that, as mentioned above, lead to long-range interparticle interactions and hence an earlier onset of crystallization. It has been shown for ionic microgels that at a fixed temperature an increase in number density (and thus ϕ_{eff}) results in a decrease in interparticle spacing.^{11,53} Moreover, at high enough particle concentration the overlap of the counterion clouds can even lead to deswelling of the microgels.²⁵ However, in our case the situation might be even more complex as we find apparent microgel charge changes in dependence on the swelling state as evidenced by the different zeta potentials, *i.e.* $\zeta(38$ °C) = -25.6 mV and $\zeta(35$ °C) = -18.5 mV (see for details Fig. S1, ESI†). We do note that these values were obtained in the dilute system and thus might not reflect the dense system case. Clearly, the decrease in interparticle spacing upon cooling is the result of a complex



change in interparticle interactions of the microgels, and remains a topic that is still not fully understood.^{2,33}

We can further extract information about the distortions caused by strain in the crystal lattice by performing Williamson–Hall analysis of the Bragg peaks.⁵⁴ For this we determined the FWHM of each Bragg peak w_q and w_ϕ in radial and azimuthal direction, respectively. Fig. 4d and g show w_q and w_ϕ averaged for each Bragg peak family for the full temperature range. While each family has different absolute values their overall trends of w_q and w_ϕ are quite similar. There is, however, a clear difference between the trends in w_q and w_ϕ . While w_q continuously grows throughout the whole cooling process indicating continuously growing strain in the crystal lattice, w_ϕ only increases during the active crystallization between $T = 38.2$ – 37.6 °C and then remains constant showing that after crystallization the strain in this directions does not evolve. Next, we used the Williamson–Hall equation⁵⁵

$$w_{q,\phi}^2(q) = g_{q,\phi}^2 q^2 + \left(\frac{2\pi}{L_{q,\phi}}\right)^2, \quad (1)$$

where $w_{q,\phi}(q)$ is the FWHM of a Bragg peak at position q , $g_{q,\phi}$ the lattice distortion and $L_{q,\phi}$ the size of coherently scattering domains; subscripts q and ϕ denote radial and azimuthal directions, respectively. Fig. 4e and h show w_q^2 and w_ϕ^2 as a function of q^2 for all Bragg peak families at $T = 36.0$ °C where the sample has fully crystallized. In contrast to the prediction of the Williamson–Hall equation, the points of the different Bragg peak families do not fall on a single straight line but separate again into stacking-dependent peaks ($1\bar{1}00$, $2\bar{2}00$ and $3\bar{2}\bar{1}0$) and stacking-independent ones ($2\bar{1}\bar{1}0$, $3\bar{3}00$ and $4\bar{2}\bar{2}0$). This separation agrees well with previously observed differences in the FWHMs of stacking-dependent and stacking-independent Bragg peaks for a similar colloidal system with *rhcp* packing.⁵⁰ The difference in the FWHMs is caused by the presence of additional in-plane stacking disorder, which means that the hexagonal planes consist of islands with different lateral positions with characteristic line defects in between them leading to a lower degree of order in these in-plane directions.⁴⁹ In addition, for soft colloidal crystals different types of defects consisting of combined in-plane and out-of-plane stacking disorder, *i.e.* partial dislocations, have been observed and would lead to a similar effect.⁵⁶ Therefore, we fitted the stacking-dependent and stacking-independent Bragg peaks separately and extracted the lattice distortions g_q and g_ϕ over the full temperature range, as shown in Fig. 4f and i.

We find that in the radial direction, the lattice distortions for both stacking types are initially the same with $g_q \approx 1\%$, indicating the initial crystal grain experiences little strain. As the active crystallization proceeds, the distortions start to increase with a higher rate for the stacking-dependent peaks than for the stacking-independent Bragg peaks. Upon further cooling to $T = 35.0$ °C, the radial distortions reached values of $g_q \approx 5.5\%$ and $g_q \approx 4.5\%$ for stacking-dependent and stacking-independent peaks, respectively. This larger distortion for the stacking-dependent peaks is expected since the in-plane stacking disorder leads to effectively smaller crystal domains.

The continuous character of the increased distortion seems to be related to the continuous swelling of the CS microgels and accompanying softer interparticle interactions, similar to the decrease in interparticle spacing observed from the Bragg peak positions. The swelling leads to increasing strain in the crystals and thus will lead to larger distortions within the crystal planes.⁵⁶

In the azimuthal direction, the crystallization is characterized by a fast rise of the angular distortion g_ϕ in the active crystallization regime from 1.5% to 4% for stacking-dependent and from 1.5% to 3% for stacking-independent peaks, respectively (see Fig. 4i). This behaviour can be explained by the misorientation of the outsides of the growing crystal with respect to the nuclei orientation during the active crystallization stage. After the active crystallization, the distortions only increase slightly during further cooling reaching values of $g_\phi \approx 5\%$ and 4% , respectively. Clearly, once the full scattering volume has crystallized, the additional strain from the particle swelling does not lead to strong reorientation of the crystal planes.

3.3. *In situ* characterization of melting

After having analysed the crystallization process in detail, we now turn to the melting process induced by slowly heating the crystalline sample. We note that after the cooling measurement the sample was cooled further to $T = 20$ °C and equilibrated for 5 min. Next, the melting was followed from $T = 35.0$ °C to $T = 43.0$ °C with the same rate of 0.1 °C min^{-1} and at the same sample position as at the end of cooling. During the heating process, we observed that the intensity of the 6-fold Bragg peaks decreased and that the shape of the peaks changed.

Again, we identify the onset of melting by investigating the structure factors shown in Fig. 5. The evolution of $S(q)$, $S_{\text{iso}}(q)$ and $S_{\text{xtal}}(q)$ is shown in Fig. 5a–c. Fig. 5d shows the $S_{\text{iso}}(q)$ of the fluid state at $T = 43.0$ °C together with the best fit with the Percus-Yevick $S_{\text{PY}}(q)$ for a fluid with $\phi_{\text{PY}} = 0.42 \pm 0.01$ and $R_{\text{PY}} = 209 \pm 4$ nm. These PY values again agree with a collapsed PNIPAM shell state but are slightly larger than $R_{\text{h}}(43$ °C) = 155.5 nm, again attributed to electrostatic repulsions between the particles. Fig. 5e shows integrated $S_{\text{iso}}(q)$ in the range of $q = 10$ – 23 μm^{-1} as indicated by the red dashed lines in Fig. 5(b). The transition from a crystal to a liquid can be observed clearly by the appearance of the fluid peak in $S_{\text{iso}}(q)$ and the disappearance of the Bragg peaks in $S_{\text{xtal}}(q)$. In the temperature range of $T = 37.0$ – 38.2 °C a strong rise in the intensity of $S_{\text{iso}}(q)$ occurs that coincides with the most significant drop in the Bragg peak intensities, indicating the onset and subsequent melting of a main part of the crystalline phase. The lower $T = 37.0$ °C for the start of melting shows that the melting transition occurs at the higher volume fraction $\phi_{\text{eff}} = 0.24$ than the freezing transition. With further heating, $S_{\text{iso}}(q)$ intensity only increases gradually, indicating that a large part of the sample still remains crystalline. This is also seen in the $S_{\text{xtal}}(q)$ peaks that decrease in intensity, but remain present up to $T \approx 41.0$ °C. Finally, at $T = 41.8$ °C the Bragg peak intensity decreases and the peaks completely disappear at $T = 42.3$ °C while the liquid structure factor $S_{\text{iso}}(q)$ reaches its maximum intensity, indicating the full



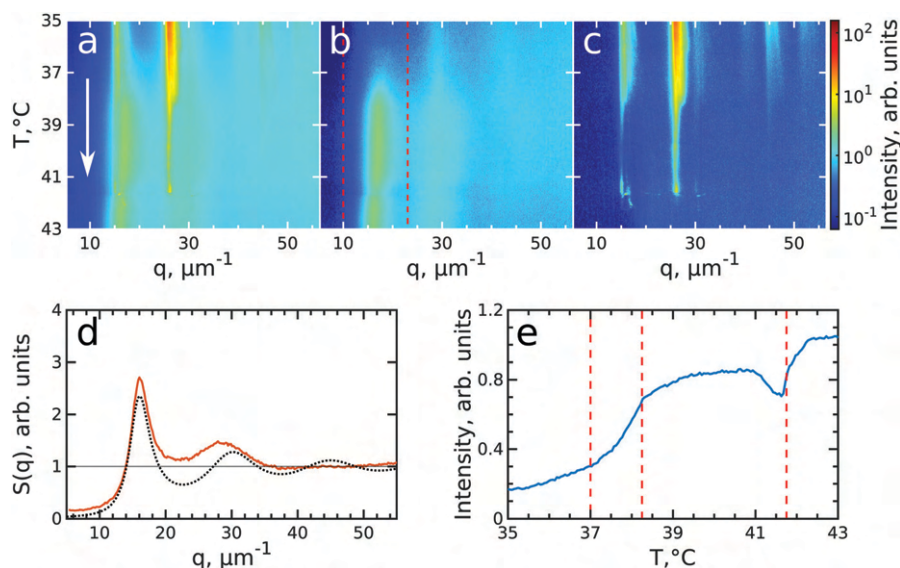


Fig. 5 Evolution of melting of CS system with $\phi_{\text{eff}}(20\text{ }^{\circ}\text{C}) = 0.60$ during heating from $T = 35\text{ }^{\circ}\text{C}$ to $T = 43\text{ }^{\circ}\text{C}$. The radially averaged intensity plots for different temperatures are stacked together in 2D maps for (a) full structure factor $S(q)$, (b) fluid structure factor $S_{\text{iso}}(q)$ (the intensity between the Bragg peaks), (c) crystal structure factor $S_{\text{xtal}}(q)$ (containing only the Bragg peaks). The white arrow in (a) indicates the direction of the experiment. Note the reverse temperature scale compared to Fig. 3. (d) Measured $S_{\text{iso}}(q)$ at final temperature $T = 43.0\text{ }^{\circ}\text{C}$ (red line) and the best fit by the Percus-Yevick hard sphere structure factor (black dotted line). (e) Integrated $S_{\text{iso}}(q)$ near the first fluid ring (in the range of $q = 10\text{--}23\text{ }\mu\text{m}^{-1}$ indicated by the red dashed lines in panel (b)). The first two vertical red dashed lines indicate the temperature range of active melting and the last the final stage of melting.

sample has returned to a fluid state. Interestingly, in $S_{\text{xtal}}(q)$ the Bragg peaks appear much sharper between $T = 38.2\text{ }^{\circ}\text{C}$ and $T = 41\text{ }^{\circ}\text{C}$, which is counterintuitive for a “normal” crystal melting. Typically melting is associated with an increase in lattice distortion and a decrease in the range of structural order that would lead to broadening of the Bragg peaks. After a more careful analysis, we found that the previously single crystal Bragg peak splits into distinctly different sets of Bragg peaks upon melting and that these peaks show different behaviour. We note that for $T > 42\text{ }^{\circ}\text{C}$ suddenly different Bragg peaks appear in

$S_{\text{xtal}}(q)$ which coincides with a drop in $S_{\text{iso}}(q)$. We believe this moment indicates the moment the crystal grain fully breaks up and rotates or possibly another crystallite drifts into the X-ray beam.

To get insight into the unexpected behaviour of the sample during melting, we examined the 2D USAXS patterns in more detail. Fig. 6a–d shows the patterns at different temperatures and Fig. 6e–h shows magnified parts around one of the peaks from the brightest $2\bar{1}\bar{1}0$ family. It can be clearly seen that the Bragg peak splits into three subpeaks already at the start of the

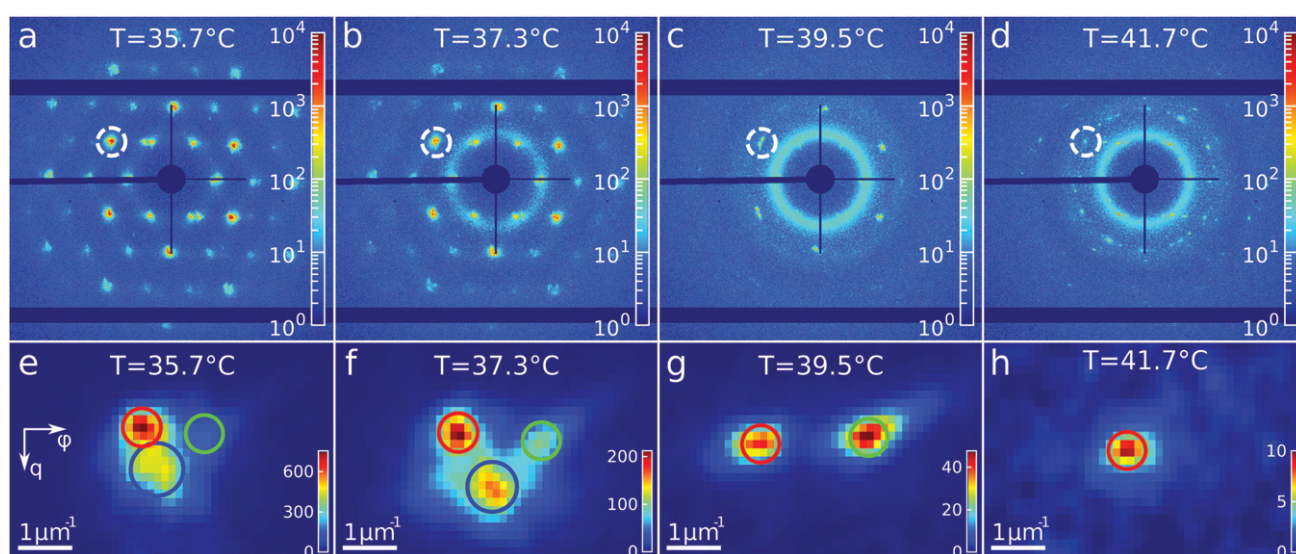


Fig. 6 Evolution of the Bragg peaks during heating. (a–d) Examples of the 2D-USAXS patterns collected during heating at different temperatures. (e–h) Areas of the diffraction patterns showing these subpeaks of the Bragg peak, indicated in (a–d) by the dashed circle, at different temperatures.



measurement at $T = 35.7$ °C. Their appearance implies that during melting the previously single crystalline structure separates into three crystallites surrounded by a fluid phase, which can be explained by the onset of melting at defects and grain boundaries position.¹⁰ The subpeaks corresponding to these crystallites are denoted “blue”, “red” and “green” as indicated by the circles in Fig. 6e–h. We performed Bragg peak analysis of these three subpeaks and the evolution of the average extracted peak intensity, q -position and ϕ -position that are shown in Fig. 7. From the different parameters, it is clear that the “blue” crystallite behaves differently compared to the “green” and “red” crystallites. First, the “blue” peak has a higher intensity than the other two (Fig. 7a). Second, although heating up to $T = 37$ °C results in a decrease in the intensities of all three peaks, further heating results in a rapid decrease and disappearing at $T = 38.2$ °C of the “blue” subpeak, while the “red” and “green” subpeaks keep decreasing in intensity and only fully disappear at $T = 41.8$ °C. We note that we can exclude sedimentation of the crystallites at this stage of the heating process as the effective volume fraction $\phi_{\text{eff}} > \phi_{\text{f}}$. Third, the “green” and “red” subpeaks move apart from each other in azimuthal direction by about four degrees while the blue subpeaks do not move (Fig. 7b). Finally, during heating the q -position of the “blue” peak increases significantly while those of the red and green subpeaks stay relatively constant (Fig. 7c). From this analysis, it is clear that the “blue” crystallite comprises the bulk of the system since it shows the reverse behaviour with full melting at the same temperature as where bulk crystallization started. Therefore, the behaviour of this “blue” crystallite is driven by the CS particle size change and corresponding change in the effective volume fraction ϕ_{eff} . For the “green” and “red” crystallites we conclude that these comprise a small part of the scattering volume and since these

crystallites remain present after melting of the bulk of the system, it can explain the occurrence of drift and orientational changes of the crystallites.

Next, we calculated the average unit cell parameter for the crystallites from the average values of all orders of each subpeak (Fig. 7d). The subpeaks corresponding to the same crystallite in each Bragg peak family were identified thanks to their similar behaviour in radial and azimuthal directions. The extracted parameters of the separate Bragg peak analysis are shown in the ESI,[†] in Fig. S7–S10, where we note that the $3\bar{2}10$ family was excluded due to its low intensity. For the “blue” crystallite we find the lattice parameter value $a = 475 \pm 5$ nm at $T = 35$ °C that decreases to $a = 468 \pm 5$ nm just before melting at $T = 37$ °C. This initial lattice spacing corresponds to the end value of the crystallization process and the decrease in lattice spacing agrees with the collapsing of the CS size. For the “green” and “red” crystallites we find $a = 489 \pm 3$ nm at $T = 35$ °C, which is 14 nm larger than at the end of crystallization. In addition, for the “red” crystallite a continuously decreases to $a = 480 \pm 3$ nm at $T = 38.2$ °C and then stays constant up to melting, while for the “green” a decrease occurs to $a = 482 \pm 3$ nm at $T = 38.2$ °C after which it increases again up to $a = 492 \pm 4$ nm, exceeding thus the initial value. This behaviour of the “green” and “red” crystallite is surprising as it is not in-line with the expected collapse of the PNIPAM shell.

Based on the separation into three crystallites and their distinct differences in behaviour, we conclude that in the CS system two different states are present during melting. Based on the USAXS patterns alone it is difficult to determine the exact location of the crystals but we speculate that the distinction comes from the bulk crystal and two wall crystallites. Our reasoning is that since the “blue” crystallite shows the expected melting behaviour compared to the system upon crystallization, this crystallite comprises the bulk of the system and the melting transition is driven by the change in CS size and the corresponding change in ϕ_{eff} . The similarities in behaviour of the “green” and “red” crystallites indicate that these crystals might be two crystalline domains formed on the capillary walls, as observed in other charged particle systems.⁵⁷ A temperature gradient close to the walls induced by the short cooling to $T = 20$ °C of the sample before the heating measurement will lead to increased swelling of the CS microgel shell ($R_{\text{h}}(20$ °C) = 228.9 nm) and could explain the larger lattice spacing in these crystals close to the wall. In addition, the swelling would lead to entanglement of the outer chains of the PNIPAM shell, and thus lead to an early separation into two states, while also explaining the delayed melting of the crystallites even below ϕ_{f} . However, real space investigations, such as polarization microscopy,^{38,57} will be needed to confirm this melting process.

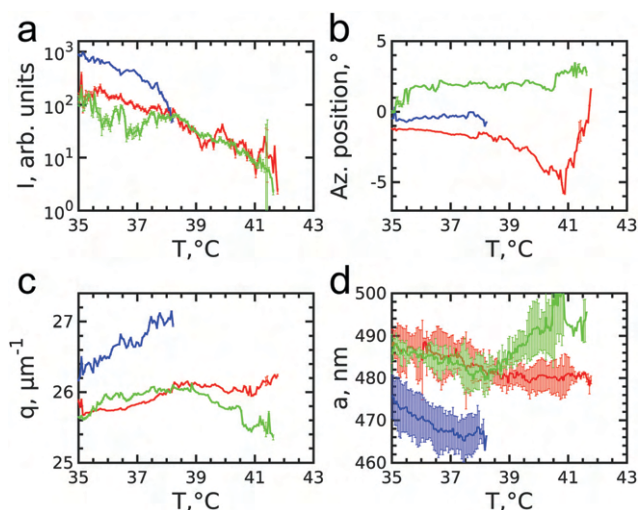


Fig. 7 Evolution of the extracted parameters of the subpeaks of the Bragg peak during melting: (a) integrated intensities, (b) azimuthal positions and (c) q -values. (d) Evolution of the lattice parameters for each superlattice crystallite. The lattice parameters are averaged over 5 orders of each subpeak.

4. Discussion

A schematic representation of the full phase behaviour observed in the dense CS particle system upon cooling and



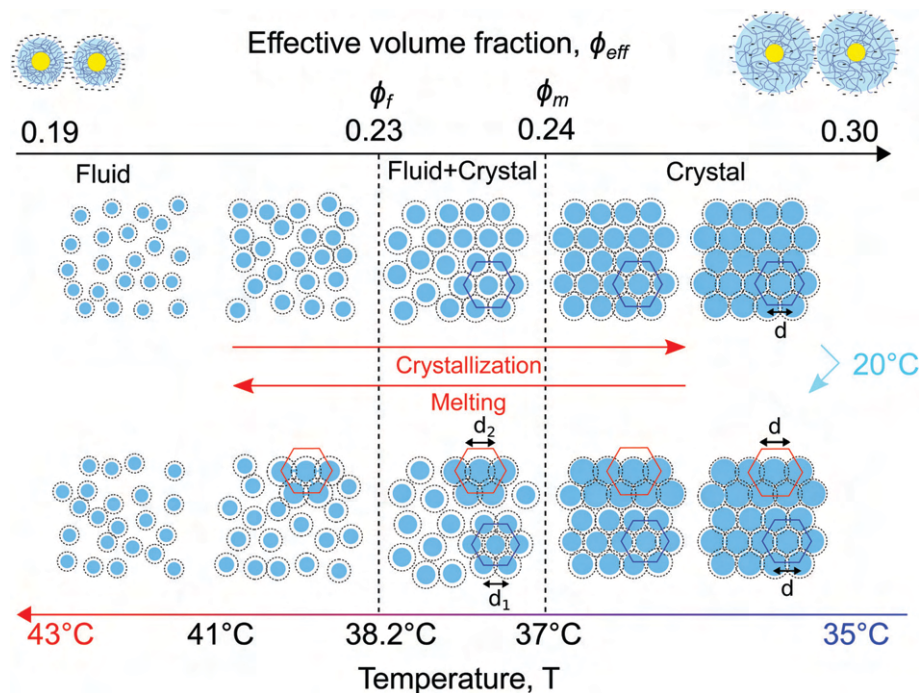


Fig. 8 Schematic representation of the observed *in situ* phase transitions from a fluid to a crystal and vice versa in the gold–PNIPAM CS system. Due to the swelling and collapsing of the PNIPAM shell in response to cooling and heating the CS microgel size and subsequently the effective volume fraction ϕ_{eff} in the system changes driving the phase transitions.

heating with a temperature ramp of $0.1\text{ }^{\circ}\text{C min}^{-1}$ is presented in Fig. 8. At high temperatures $T > 39\text{ }^{\circ}\text{C}$ the system is in a fluid state with the effective volume fraction $\phi_{\text{eff}} < \phi_f$. Upon cooling the charged CS particles start to swell and at $T = 38.2\text{ }^{\circ}\text{C}$ the effective volume fraction ϕ_{eff} increases and becomes higher than the freezing point, thus $\phi_{\text{eff}} > \phi_f$, causing the formation of a crystal nucleus that subsequently grows from the fluid. Upon a further decrease in temperature $T < 37.8\text{ }^{\circ}\text{C}$, the particle swelling increases further, thus increasing ϕ_{eff} and due to their charged and soft nature the inter-particle spacing decreases. Upon cooling the system to $T = 20\text{ }^{\circ}\text{C}$ for 5 min the CS particles close to the capillary wall swell even more and the dangling ends in the outer microgel periphery can interpenetrate. Subsequently, by heating the system again, the microgel collapse lowering the effective volume fraction. At this stage the system starts to separate into two distinct crystal states, the bulk crystal and the wall crystals. Below the melting point, $\phi_{\text{eff}} < \phi_m$, the bulk of the system starts to melt and form a fluid phase, while the wall crystals respond much slower due to possible entanglement of the outer polymer chains of the microgels. Finally, only by heating to $T > 41.5\text{ }^{\circ}\text{C}$ the full system disperses again and a fluid phase is obtained.

5. Conclusions

We have investigated the *in situ* crystallization and melting of CS microgels that contain high contrast Au cores and thermoresponsive PNIPAM shells using SAXS. The phase transitions were induced either by cooling or by heating with rates of $0.1\text{ }^{\circ}\text{C min}^{-1}$ in a densely packed suspension. We have

found that the Au core contribution dominates the scattered intensity due to their high electron density and provides sharp contrast between the CS form factor $P_{\text{cs}}(q)$ and structure factor $S(q)$, while the temperature response of the PNIPAM shell can still be monitored. We further found that the behaviour of the microgel system upon crystallization and melting is quite different and rather complex. Upon cooling, due to the increase in CS size, the dense fluid readily crystallizes into a single crystalline structure. By performing Bragg peak analysis, we revealed that an *rhcp* crystal structure is formed and that in-plane and out-of-plane stacking disorder occurs which develop differently during crystallization. Upon heating, the crystalline sample melts but we find that the crystal separates into different, smaller crystallites that undergo two different melting processes. We attribute these differences to the presence of two different crystalline phases after crystallization, a bulk crystal phase and crystal phases formed close to the capillary walls.

The combination of CS microgels containing Au cores and PNIPAM shells with SAXS and Bragg peak analysis employed in the current study provides a means to investigate the bulk behaviour of microgel systems upon temperature changes that have been limited so far due to the low scattering contrast of pure microgel particles. Our investigations therefore open up ways to address how the bulk system response ties in with the local microgel response for different particle concentrations as well as the influence of different cooling and heating rates. Such investigations can address fundamental questions regarding crystallization, melting, jamming and the glass transition, while at the same time these can provide crucial insights for potential



applications of such microgels as (multi-)functional materials in various fields.

Author contributions

J. M. M., M. K. and I. A. V. conceptualized the research. J. M. M. and M. K. performed sample preparation. D. L., D. A., J. S., F. W., S. L., M. S., M. K., I. A. V. and J. M. M. performed synchrotron experiments and data acquisition. D. L., N. M and S. D. performed data analysis. D. L., N. M., S. L., M. K., I. A. V. and J. M. M. interpreted results and wrote the manuscript. All authors read and agreed on the final text of the paper.

Conflicts of interest

There are no conflicts of interest to declare.

Acknowledgements

We acknowledge DESY (Hamburg, Germany), a member of the Helmholtz Association HGF, for the provision of experimental facilities. Parts of this research were carried out at PETRA III synchrotron facility and we would like to thank all the beamline staff for assistance in using Coherence Application beamline P10. We would like to thank Andrei Petukhov for valuable discussions. We further acknowledge Astrid Rauh for the particle synthesis, Max Schelling for the DLS measurements and Sanam Foroutanparsa for the TEM images. J. M. M. acknowledges financial support from the Netherlands Organization for Scientific Research (NWO) (016.Veni.192.119). M. K. acknowledges the German Research Foundation (DFG) for funding under grant KA3880/6-1. D. L., N. M., D. A., S. L. and I. A. V. acknowledge the Helmholtz Associations Initiative Networking Fund (Grant No. HRSF-0002) and the Russian Science Foundation (Grant No. 18-41-06001). I. A. V. acknowledges the financial support of the Russian Federation represented by the Ministry of Science and Higher Education of the Russian Federation (Agreement No. 075-15-2021-1352). S. L. acknowledges Competitiveness Enhancement Program Grant of Tomsk Polytechnic University and the Governmental program "Science", project No. FSWW-2020-0014.

References

- M. Karg, A. Pich, T. Hellweg, T. Hoare, L. A. Lyon, J. J. Crassous, D. Suzuki, R. A. Gumerov, S. Schneider, I. I. Potemkin and W. Richtering, *Langmuir*, 2019, **35**, 6231–6255, DOI: 10.1021/acs.langmuir.8b04304.
- F. Scheffold, *Nat. Commun.*, 2020, **11**, 4315, DOI: 10.1038/s41467-020-17774-5.
- F. A. Plamper and W. Richtering, *Acc. Chem. Res.*, 2017, **50**, 131–140, DOI: 10.1021/acs.accounts.6b00544.
- L. A. Lyon and A. Fernandez-Nieves, *Annu. Rev. Phys. Chem.*, 2012, **63**, 25–43, DOI: 10.1146/annurev-physchem-032511-143735.
- D. Vlassopoulos and M. Cloitre, *Curr. Opin. Colloid In.*, 2014, **19**, 561–574, DOI: 10.1016/j.cocis.2014.09.007.
- B. Sierra-Martin and A. Fernandez-Nieves, *Soft Matter*, 2012, **8**, 4141–4150, DOI: 10.1039/C2SM06973C.
- A. Fernández-Barbero, A. Fernández-Nieves, I. Grillo and E. López-Cabarcos, *Phys. Rev. E: Stat., Nonlinear, Soft Matter Phys.*, 2002, **66**, 051803, DOI: 10.1103/PhysRevE.66.051803.
- T. Hoare and R. Pelton, *J. Phys. Chem. B*, 2007, **111**, 11895–11906, DOI: 10.1021/jp072360f.
- M. Stieger, J. S. Pedersen, P. Lindner and W. Richtering, *Langmuir*, 2004, **20**, 7283–7292, DOI: 10.1021/la049518x.
- A. M. Alsayed, M. F. Islam, J. Zhang, P. J. Collings and A. G. Yodh, *Science*, 2005, **309**, 1207–1210, DOI: 10.1126/science.1112399.
- U. Gasser and A. Fernandez-Nieves, *Phys. Rev. E: Stat., Nonlinear, Soft Matter Phys.*, 2010, **81**, 052401, DOI: 10.1103/PhysRevE.81.052401.
- Z. Wang, F. Wang, Y. Peng, Z. Zheng and Y. Han, *Science*, 2012, **338**, 87–90, DOI: 10.1126/science.1224763.
- J. Mattsson, H. M. Wyss, A. Fernandez-Nieves, K. Miyazaki, Z. Hu, D. R. Reichman and D. A. Weitz, *Nature*, 2009, **462**, 83–86, DOI: 10.1038/nature08457.
- J. Brijitta, B. V. R. Tata, R. G. Joshi and T. Kaliyappan, *J. Chem. Phys.*, 2009, **131**, 074904, DOI: 10.1063/1.3210765.
- L. Frenzel, M. Dartsch, G. M. Balaguer, F. Westermeier, G. Grübel and F. Lehmkuhler, *Phys. Rev. E*, 2021, **104**, L012602, DOI: 10.1103/PhysRevE.104.L012602.
- T. Hellweg, C. D. Dewhurst, E. Brückner, K. Kratz and W. Eimer, *Colloid Polym. Sci.*, 2000, **278**, 972–978, DOI: 10.1007/s0039600000350.
- L. A. Lyon, J. D. Debord, S. B. Debord, C. D. Jones, J. G. McGrath and M. J. Serpe, *J. Phys. Chem. B*, 2004, **108**, 19099–19108, DOI: 10.1021/jp048486j.
- Z. Meng, J. K. Cho, S. Debord, V. Breedveld and L. A. Lyon, *J. Phys. Chem. B*, 2007, **111**, 6992–6997, DOI: 10.1021/jp073122n.
- G. Huang and Z. Hu, *Macromolecules*, 2007, **40**, 3749–3756, DOI: 10.1021/ma070253d.
- K. Geisel, W. Richtering and L. Isa, *Soft Matter*, 2014, **10**, 7968–7976, DOI: 10.1039/C4SM01166J.
- A. N. St. John, V. Breedveld and L. A. Lyon, *J. Phys. Chem. B*, 2007, **111**, 7796–7801, DOI: 10.1021/jp071630r.
- G. M. Conley, P. Aebischer, S. Nöjd, P. Schurtenberger and F. Scheffold, *Sci. Adv.*, 2017, **3**, e1700969, DOI: 10.1126/sciadv.1700969.
- G. M. Conley, C. Zhang, P. Aebischer, J. L. Harden and F. Scheffold, *Nat. Commun.*, 2019, **10**, 2436, DOI: 10.1038/s41467-019-10181-5.
- P. S. Mohanty, S. Nöjd, K. van Gruijthuijsen, J. J. Crassous, M. Obiols-Rabasa, R. Schweins, A. Stradner and P. Schurtenberger, *Sci. Rep.*, 2017, **7**, 1487, DOI: 10.1038/s41598-017-01471-3.
- A. Scotti, U. Gasser, E. S. Herman, M. Pelaez-Fernandez, J. Han, A. Menzel, L. A. Lyon and A. Fernández-Nieves, *Proc. Natl. Acad. Sci. U. S. A.*, 2016, **113**, 5576–5581, DOI: 10.1073/pnas.1516011113.



- 26 I. Bouhid de Aguiar, T. van de Laar, M. Meireles, A. Bouchoux, J. Sprakel and K. Schroën, *Sci. Rep.*, 2017, **7**, 10223, DOI: 10.1038/s41598-017-10788-y.
- 27 U. Gasser, J. S. Hyatt, J.-J. Lieter-Santos, E. S. Herman, L. A. Lyon and A. Fernandez-Nieves, *J. Chem. Phys.*, 2014, **141**, 034901, DOI: 10.1063/1.4885444.
- 28 S. V. Nikolov, A. Fernandez-Nieves and A. Alexeev, *Proc. Natl. Acad. Sci. U. S. A.*, 2020, **117**, 27096–27103, DOI: 10.1073/pnas.2008076117.
- 29 S. Nöjd, P. Holmqvist, N. Boon, M. Obiols-Rabasa, P. S. Mohanty, R. Schweins and P. Schurtenberger, *Soft Matter*, 2018, **14**, 4150–4159, DOI: 10.1039/C8SM00390D.
- 30 R. Pelton, *Adv. Colloid Interface*, 2000, **85**, 1–33, DOI: 10.1016/S0001-8686(99)00023-8.
- 31 M. Karg, T. Hellweg and P. Mulvaney, *Adv. Funct. Mater.*, 2011, **21**, 4668–4676, DOI: 10.1002/adfm.201101115.
- 32 R. Pelton, *J. Colloid Interface Sci.*, 2010, **348**, 673–674, DOI: 10.1016/j.jcis.2010.05.034.
- 33 M. J. Bergman, N. Gnan, M. Obiols-Rabasa, J.-M. Meijer, L. Rovigatti, E. Zaccarelli and P. Schurtenberger, *Nat. Commun.*, 2018, **9**, 5039, DOI: 10.1038/s41467-018-07332-5.
- 34 A. Zaccone, J. J. Crassous, B. Béri and M. Ballauff, *Phys. Rev. Lett.*, 2011, **107**, 168303, DOI: 10.1103/PhysRevLett.107.168303.
- 35 N. Dingenouts, C. Norhausen and M. Ballauff, *Macromolecules*, 1998, **31**, 8912–8917, DOI: 10.1021/ma980985t.
- 36 R. Higler, J. Appel and J. Sprakel, *Soft Matter*, 2013, **9**, 5372–5379, DOI: 10.1039/C3SM50471A.
- 37 M. Karg, S. Wellert, I. Pastoriza-Santos, A. Lapp, L. M. Liz-Marzán and T. Hellweg, *Phys. Chem. Chem. Phys.*, 2008, **10**, 6708–6716, DOI: 10.1039/B802676A.
- 38 J. Crassous, M. Siebenbürger and M. Ballauff, *J. Chem. Phys.*, 2006, **125**, 204906, DOI: 10.1063/1.2374886.
- 39 F. Wang, D. Zhou and Y. Han, *Adv. Funct. Mater.*, 2016, **26**, 8903–8919, DOI: 10.1002/adfm.201603077.
- 40 A. Rauh, T. Honold and M. Karg, *Colloid Polym. Sci.*, 2016, **294**, 37–47, DOI: 10.1007/s00396-015-3782-6.
- 41 M. Karg, S. Jaber, T. Hellweg and P. Mulvaney, *Langmuir*, 2011, **27**, 820–827, DOI: 10.1021/la1039249.
- 42 K. Volk, J. P. S. Fitzgerald, M. Retsch and M. Karg, *Adv. Mater.*, 2015, **27**, 7332–7337, DOI: 10.1002/adma.201503672.
- 43 M. Karg, *Macromol. Chem. Phys.*, 2016, **217**, 242–255, DOI: 10.1002/macp.201500334.
- 44 K. Volk, J. P. S. Fitzgerald, P. Ruckdeschel, M. Retsch, T. A. F. König and M. Karg, *Adv. Opt. Mater.*, 2017, **5**, 1600971, DOI: 10.1002/adom.201600971.
- 45 E. Ponomareva, K. Volk, P. Mulvaney and M. Karg, *Langmuir*, 2020, **36**, 13601–13612, DOI: 10.1021/acs.langmuir.0c02430.
- 46 A. Rauh, N. Carl, R. Schweins and M. Karg, *Langmuir*, 2018, **34**, 854–867, DOI: 10.1021/acs.langmuir.7b01595.
- 47 E. A. Sulyanova, A. Shabalin, A. V. Zozulya, J.-M. Meijer, D. Dzhigaev, O. Gorobtsov, R. P. Kurta, S. Lazarev, U. Lorenz, A. Singer, O. Yefanov, I. Zaluzhnyy, I. Besedin, M. Sprung, A. V. Petukhov and I. A. Vartanyants, *Langmuir*, 2015, **31**, 5274–5283, DOI: 10.1021/la504652z.
- 48 J. S. Pedersen, *Adv. Colloid Interfac*, 1997, **70**, 171–210, DOI: 10.1016/S0001-8686(97)00312-6.
- 49 J.-M. Meijer, V. W. A. de Villeneuve and A. V. Petukhov, *Langmuir*, 2007, **23**, 3554–3560, DOI: 10.1021/la062966f.
- 50 J.-M. Meijer, A. Shabalin, R. Dronyak, O. M. Yefanov, A. Singer, R. P. Kurta, U. Lorenz, O. Gorobstov, D. Dzhigaev, J. Gulden, D. V. Byelov, A. V. Zozulya, M. Sprung, I. A. Vartanyants and A. V. Petukhov, *J. Appl. Crystallogr.*, 2014, **47**, 1199–1204, DOI: 10.1107/S1600576714010346.
- 51 A. V. Petukhov, I. P. Dolbnya, D. G. A. L. Aarts, G. J. Vroege and H. N. W. Lekkerkerker, *Phys. Rev. Lett.*, 2003, **90**, 028304, DOI: 10.1103/PhysRevLett.90.028304.
- 52 S. Lazarev, I. Besedin, A. V. Zozulya, J.-M. Meijer, D. Dzhigaev, O. Y. Gorobtsov, R. P. Kurta, M. Rose, A. G. Shabalin, E. A. Sulyanova, I. A. Zaluzhnyy, A. P. Menushenkov, M. Sprung, A. V. Petukhov and I. A. Vartanyants, *Small*, 2018, **14**, 1702575, DOI: 10.1002/smll.201702575.
- 53 D. Gottwald, C. N. Likos, G. Kahl and H. Löwen, *Phys. Rev. Lett.*, 2004, **92**, 068301, DOI: 10.1103/PhysRevLett.92.068301.
- 54 G. K. Williamson and W. H. Hall, *Acta Metall. Mater.*, 1953, **1**, 22–31, DOI: 10.1016/0001-6160(53)90006-6.
- 55 M. A. Moram and M. E. Vickers, *Rep. Prog. Phys.*, 2009, **72**, 036502, DOI: 10.1088/0034-4885/72/3/036502.
- 56 J. Hillhorst and A. V. Petukhov, *Phys. Rev. Lett.*, 2011, **107**, 095501, DOI: 10.1103/PhysRevLett.107.095501.
- 57 T. Palberg, M. R. Maaroufi, A. Stipp and H. J. Schöpe, *J. Chem. Phys.*, 2012, **137**(9), 094906, DOI: 10.1063/1.4749261.



Structure–Transport Correlation Reveals Anisotropic Charge Transport in Coupled PbS Nanocrystal Superlattices

Andre Maier, Dmitry Lapkin, Nastasia Mukharamova, Philipp Frech, Dameli Assalauova, Alexandr Ignatenko, Ruslan Khubbutdinov, Sergey Lazarev, Michael Sprung, Florian Laible, Ronny Löffler, Nicolas Previdi, Annika Bräuer, Thomas Günkel, Monika Fleischer, Frank Schreiber, Ivan A. Vartanyants,* and Marcus Scheele*

The assembly of colloidal semiconductive nanocrystals into highly ordered superlattices predicts novel structure-related properties by design. However, those structure–property relationships, such as charge transport depending on the structure or even directions of the superlattice, have remained unrevealed so far. Here, electric transport measurements and X-ray nanodiffraction are performed on self-assembled lead sulfide nanocrystal superlattices to investigate direction-dependent charge carrier transport in microscopic domains of these materials. By angular X-ray cross-correlation analysis, the structure and orientation of individual superlattices is determined, which are directly correlated with the electronic properties of the same microdomains. By that, strong evidence for the effect of superlattice crystallinity on the electric conductivity is found. Further, anisotropic charge transport in highly ordered monocrystalline domains is revealed, which is attributed to the dominant effect of shortest interparticle distance. This implies that transport anisotropy should be a general feature of weakly coupled nanocrystal superlattices.

Semiconductive nanocrystals (NCs) can be self-assembled into ordered superlattices (SLs) to create artificial solids with emerging collective properties.^[1–3] Computational studies have predicted that properties such as electronic coupling or charge transport are determined not only by the individual NCs but also by the degree of their organization and structure.^[4–7] However, experimental proof for a correlation between structure

and charge transport in NC SLs is still pending. Previous experimental research on NC SLs has either focused solely on the process of self-organization and structural order^[8–13] or, in separate studies, on charge transport, and electronic properties.^[14–19] In order to reveal potential transport anisotropy, a correlated investigation of charge transport and structural order on the same NC SL is required. This allows addressing a variety of fundamental questions. Are the electronic properties of NC SLs influenced by the SL type and orientation? Do polycrystalline and monocrystalline SLs differ in conductivity? What is the degree of transport anisotropy in NC SLs?

Here, we address these questions by a direct correlation of the structural and electronic properties of SLs composed of electronically coupled lead sulfide (PbS)

NCs. We perform X-ray nanodiffraction and apply angular X-ray cross-correlation analysis (AXCCA)^[8,20,21] to characterize the structure of the SLs, which are correlated with electric transport measurements of the same microdomains. By that, we reveal anisotropic charge transport in highly ordered monocrystalline hexagonal-close-packed (hcp) PbS NC SLs and find strong evidence for the effect of SL crystallinity on charge transport.

A. Maier, P. Frech, N. Previdi, Dr. M. Scheele
Institute of Physical and Theoretical Chemistry
University of Tuebingen
Auf der Morgenstelle 18, Tuebingen 72076, Germany
E-mail: marcus.scheele@uni-tuebingen.de

A. Maier, Dr. F. Laible, Dr. R. Löffler, A. Bräuer, Prof. M. Fleischer,
Prof. F. Schreiber, Dr. M. Scheele
Center for Light-Matter Interaction, Sensors & Analytics LISA+
University of Tuebingen
Auf der Morgenstelle 15, Tuebingen 72076, Germany

 The ORCID identification number(s) for the author(s) of this article can be found under <https://doi.org/10.1002/adma.202002254>.

© 2020 The Authors. Published by WILEY-VCH Verlag GmbH & Co. KGaA, Weinheim. This is an open access article under the terms of the Creative Commons Attribution-NonCommercial License, which permits use, distribution and reproduction in any medium, provided the original work is properly cited and is not used for commercial purposes.

DOI: 10.1002/adma.202002254

D. Lapkin, N. Mukharamova, D. Assalauova, Dr. A. Ignatenko,
R. Khubbutdinov, Dr. S. Lazarev, Dr. M. Sprung, Prof. I. A. Vartanyants
Deutsches Elektronen-Synchrotron DESY
Notkestraße 85, Hamburg 22607, Germany
E-mail: ivan.vartanyants@desy.de

R. Khubbutdinov, Prof. I. A. Vartanyants
National Research Nuclear University MEPhI
(Moscow Engineering Physics Institute)
Kashirskoe shosse 31, Moscow 115409, Russia

Dr. F. Laible, A. Bräuer, T. Günkel, Prof. M. Fleischer, Prof. F. Schreiber
Institute of Applied Physics
University of Tuebingen
Auf der Morgenstelle 10, Tuebingen 72076, Germany

Dr. S. Lazarev
National Research Tomsk Polytechnic University (TPU)
pr. Lenina 30, Tomsk 634050, Russia

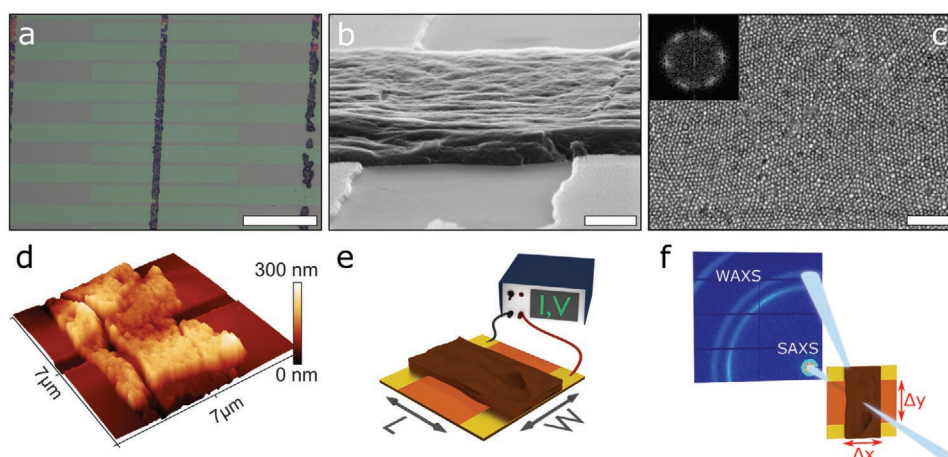


Figure 1. Microchannels of PbS NC SLs for conductivity and X-ray nanodiffraction measurements. a) Optical microscopy image of an orthogonal PbS NC stripe connecting adjacent electrodes to form individually addressable microchannels. Scale bar: 40 μm . b) SEM image in sideview (85° from normal) of a typical microchannel consisting of a ≈ 200 nm thick PbS NC SL stripe across two Au electrodes. Scale bar: 300 nm. c) High-resolution SEM image showing self-assembled PbS NCs within a microchannel with near-range order, as indicated by the fast Fourier transform (inset). Scale bar: 100 nm. d) AFM image of a microchannel on a Kapton substrate. e, f) Schematics of a SL domain on a Kapton device forming a microchannel with length $L \approx 1 \mu\text{m}$ and width $W \approx 4 \mu\text{m}$ to characterize the electronic properties (e) as well as the structural properties with X-ray nanodiffraction by means of SAXS and WAXS (f). Spatial mapping is performed along Δx and Δy directions.

As a model system we use oleic acid (OA) capped PbS NCs with a diameter of 5.8 ± 0.5 nm, which are self-assembled and functionalized with the organic π -system Cu-4,4',4'',4'''-tetraaminophthalocyanine (Cu4APc) at the liquid–air interface (details in Figures S1 and S2, Supporting Information).^[22] This results in long-range ordered and highly conductive SLs, since the rigid and relatively long ligands reduce the energy barrier for charge transport without deteriorating structural order, as it was shown previously.^[23,24] Hence, the hybrid system of PbS NCs and Cu4APc is an ideal compromise between increased electronic coupling and long-range ordered SLs, which was a fundamental prerequisite for this study. By means of soft-lithographic micro-contact printing,^[25] we transfer stripes of PbS NC-Cu4APc SLs with a width (W) of roughly $4 \mu\text{m}$ onto trenches of $\approx 1 \mu\text{m}$ length (L) between two gold contacts on X-ray transparent Kapton and Si/SiO_x substrates. This defines individually addressable microchannels with $L \approx 1 \mu\text{m}$, $W \approx 4 \mu\text{m}$, and thickness h (Figure 1a–e). Since this area is comparable to the typical grain size of PbS NC SLs,^[21] these microchannels enable transport measurements in single-crystalline PbS SLs.

In Figure 2, we display the charge transport characteristics of the microchannels as well as its dependence on the thickness of the SL and the probed area. The conductivity σ is calculated as $\sigma = (G \cdot L)/(W \cdot h)$ for all individual microchannels from two-point probe conductance (G) measurements (Figures 1e and 2a). Within the approximately two hundred individual microchannels measured, we observe electric conductivities in a wide range of values (10^{-6} – 10^{-3} S m⁻¹) (Figure 2b). This distribution correlates with the thickness of the SL (Figure 2c), which also varies by two orders of magnitude over the large number of microchannels analyzed here. The correlation is non-linear with a maximum in σ for thicknesses from 70 nm to 200 nm. Using Si/SiO_x as substrate, we performed field-effect transistor measurements of the PbS NC-Cu4APc SLs, revealing p-type behavior, which agrees with our previous study (Figure S3,

Supporting Information).^[23] The microchannels show hole-mobilities up to $\mu \approx 10^{-4}$ cm² V⁻¹ s⁻¹. Based on these transport properties and previous reports on the importance of mid-gap states in PbS NC materials, we believe that transport in the present material occurs predominantly via hopping through trap states close to the valence eigenstate (the 1S_h state).^[5,26,27]

We tested the effect of domain boundaries within the SL on electric transport on the same substrates measuring the geometry-normalized conductance of PbS NC SLs over large active channel areas of $\approx 10^4 \mu\text{m}^2$ (Figure S4, Supporting Information). As shown in Figure 2d, electric transport in this case is approximately two orders of magnitude less efficient than within the microchannels of $\approx 4 \mu\text{m}^2$, indicating the advantageous effect of the near single-crystalline channels present in the latter case (see below).

Further investigations of structural properties of the same microchannels on Kapton substrates using X-ray nanodiffraction in correlation with conductivity measurements are the focus of this study (Figure 1e,f, Figure S5, Supporting Information). We determined the structural details of all microchannels by X-ray nanodiffraction (Experimental Section and Figures S6–S9, Supporting Information). Using a nanofocused X-ray beam, we collected diffraction patterns at different positions in each channel (Figure 1f). Two typical small-angle X-ray scattering (SAXS) and wide-angle X-ray scattering (WAXS) diffraction patterns from representative microchannels, averaged over all positions within these channels, are shown in Figure 3a,g,b,h. For some of the microchannels we observe several orders of Bragg peaks in SAXS attributed to monocrystalline SLs (Figure 3a), whereas the rest of the channels demonstrate continuous Debye–Scherrer rings with low intensity modulations corresponding to polycrystalline SLs (Figure 3g). From the angular-averaged profiles, shown in Figure 3c,i, we revealed two dominant SL structures: a monocrystalline, random hexagonal-close-packed (rhcp) lattice mainly oriented along the [0001]_{SL}, and a polycrystalline,

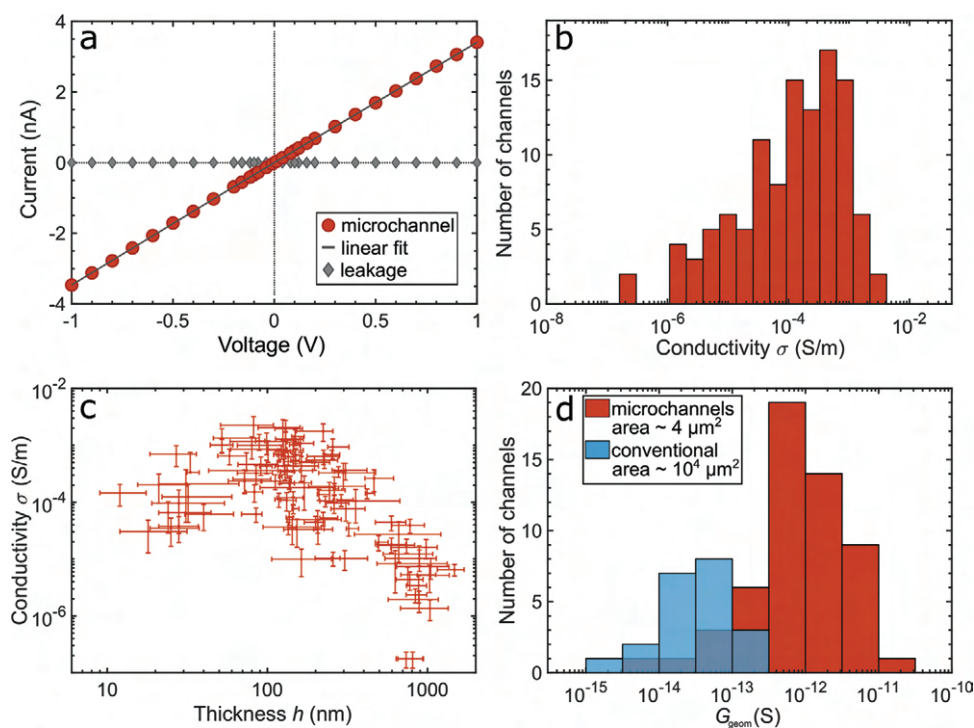


Figure 2. Electrical transport measurements of SL microchannels. a) Typical I - V curve of a PbS NC SL within a microchannel showing Ohmic behavior (red). The leak current through the dielectric substrate is negligible (gray). b) Distribution of the electric conductivities of 200 individual microchannels. c) Conductivity of the microchannels as a function of PbS NC SL thickness. The error bars represent the standard deviation of conductivity and the range of thickness determined by AFM, respectively. d) Distribution of geometry-normalized conductance of conventional large area and microchannels, probing effective areas of $\approx 10^4 \mu\text{m}^2$ (blue) and $\approx 4 \mu\text{m}^2$ (red), respectively. Measured conductance values are normalized to the channel geometry (L/W). The dark blue color corresponds to the overlap of the distributions.

body-centered-cubic (bcc) lattice primarily oriented along the $[110]_{\text{SL}}$ (scanning electron microscopy (SEM) images given in Figure S13, Supporting Information). From the peak positions in SAXS, we estimated the unit cell parameters (a_{rhcp} and a_{bcc}) for each channel and corresponding nearest-neighbor distances (NNDs), which are $d_{\text{NN}} = a_{\text{rhcp}}$ for rhcp and $d_{\text{NN}} = (\sqrt{3}/2) \cdot a_{\text{bcc}}$ for bcc, respectively. The averaged NNDs for all rhcp and bcc channels are 7.8 ± 0.4 nm and 6.9 ± 0.2 nm, respectively. In WAXS (Figure 3b,h), we observe parts of three Debye-Scherrer rings corresponding to $\{111\}_{\text{AL}}$, $\{200\}_{\text{AL}}$, $\{220\}_{\text{AL}}$ reflections of the PbS atomic lattice (AL). From the single WAXS pattern analysis we found different degrees of angular disorder of NCs: roughly 24° for rhcp and 16° for bcc channels (Figure S9, Supporting Information).

To study the relative orientation of the NCs inside the SL, we applied AXCCA,^[20] which is based on the analysis of the cross-correlation functions (CCFs), to the measured scattering data (Figures S10–S12, Supporting Information). We evaluated the CCFs for the SL and AL peaks for both rhcp and bcc structures. We found that in the rhcp monocrystalline channels (Figure 3d) the $[111]_{\text{AL}}$ and $[110]_{\text{AL}}$ directions of the NCs are collinear to the $[0001]_{\text{SL}}$ and $[2110]_{\text{SL}}$ directions, respectively (Figure 3f). In bcc polycrystalline channels (Figure 3j), all corresponding SL and AL directions are aligned (e.g., $\langle 100 \rangle_{\text{SL}}$ and $\langle 100 \rangle_{\text{AL}}$), as shown in Figure 3l. The similarity between the experimental CCFs and simulated CCFs for these structures confirms the obtained angular orientation of the NCs in the SL (Figure 3d,e and Figure 3j,k, respectively).

Upon correlating the X-ray with the electric transport measurements, we found that microchannels containing the polycrystalline bcc SLs exhibit higher conductivity than monocrystalline rhcp SLs over the entire range of thicknesses (Figure 4a). This can in part be understood in terms of the shorter NND which exponentially increases the hopping probability (Figure 4b).^[4,15] The microchannels exhibit strong characteristic Raman signals for Cu4APc (750 cm^{-1} and $1050\text{--}1650 \text{ cm}^{-1}$, Figure 4c,d), which vanish for probing areas outside the microchannels, verifying the specific functionalization of the NCs with the organic π -system (Figure S14, Supporting Information). We used the intensity of the two characteristic Raman bands to compare the relative density of Cu4APc molecules within different SLs. We found that polycrystalline bcc SLs with the smaller NND exhibit generally stronger Raman signals from Cu4APc than monocrystalline rhcp SLs with larger NND (Figure 4c,d and Figure S14, Supporting Information). This means that in monocrystalline rhcp SLs fewer native OA molecules have been exchanged by Cu4APc, resulting in larger interparticle distances, which adversely affects conductivity. From Figure 4b one can identify several cases of monocrystalline rhcp SLs having conductivities as high as those of polycrystalline bcc SLs ($\sigma \approx 10^{-4}\text{--}10^{-3} \text{ S m}^{-1}$), although the NND is much larger. We consider this as supporting evidence that the degree of SL crystallinity (poly versus mono) has a significant effect on the conductivity, which, in the present example, compensates the effect of the much larger interparticle distance. The SLs with

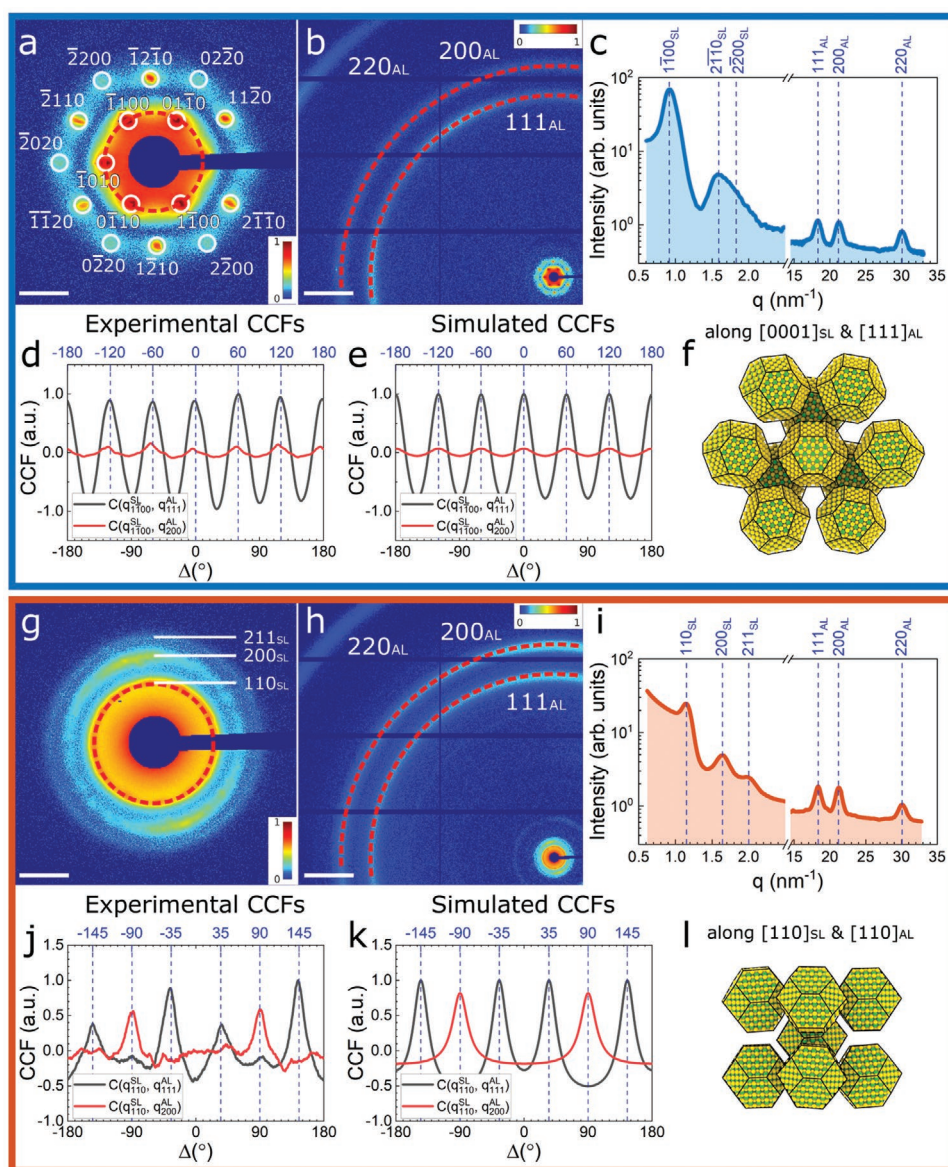


Figure 3. Structural investigation of the SL structures. a,b,g,h) Exemplary SAXS (a,g) and WAXS (b,h) patterns averaged over one microchannel for two typical cases: a,b) a monocrystalline rhcp SL oriented along $[0001]_{SL}$ and g,h) a polycrystalline bcc SL oriented along $[110]_{SL}$. c,i) Azimuthally averaged intensity profiles of SAXS ($q < 2.5 \text{ nm}^{-1}$) and WAXS ($q > 15 \text{ nm}^{-1}$) signals of the two SL types. d,j) Averaged CCFs for the two SLs, calculated for the first SAXS peaks ($\langle 1\bar{1}00 \rangle_{SL}$ in the rhcp case (d) and $\langle 110 \rangle_{SL}$ in the bcc case (j)) and the $\langle 111 \rangle_{AL}$ or $\langle 200 \rangle_{AL}$ WAXS peaks. e,k) Simulated CCFs for the two models shown in (f,l). f,l) Schematic drawing of the proposed SL structures: f) $[0001]_{SL}$ -oriented rhcp SL of PbS NCs, where the NCs are aligned as indicated and l) $[110]_{SL}$ -oriented bcc SL of PbS NCs, where all the corresponding SL and AL directions are aligned. For clarity, ligand spheres are omitted. Scale bars in (a,g) and (b,h) correspond to 1 nm^{-1} and 5 nm^{-1} , respectively.

smaller interparticle distance exhibit stronger Raman signals from Cu4APc compared to larger SLs (Figure S14, Supporting Information), corroborating a correlation between interparticle distance and ligand exchange. In fact, the smallest lattice parameter of $\approx 6.8 \text{ nm}$ in Figure 4b corresponds to an interparticle distance of $\approx 1 \text{ nm}$, which is approximately the length of one Cu4APc molecule or the minimal width of a fully exchanged ligand sphere. In contrast, residual OA leads to greater interparticle distances due to steric interactions of adjacent OA shells,^[28] explaining the spread of the NNDs (Figure 4b and Figure S8, Supporting Information). The occurrence of the

two SL types (rhcp and bcc) found here may be related to the previously observed hcp–bcc transition for OA-capped PbS NC SLs upon tailored solvent evaporation.^[29] Similarly, our polycrystalline bcc SLs are assembled from PbS NCs dispersed in hexane, whereas hexane-octane mixtures resulted in monocrystalline rhcp SLs. This invokes different solvent evaporation rates, which may lead to distinct SL unit cells.^[13,28]

From the single WAXS pattern analysis (Figure S9, Supporting Information) we found that NCs are aligned in the superlattice with different degrees of angular disorder: roughly 16° for bcc channels and 24° for rhcp channels. We believe that the NCs

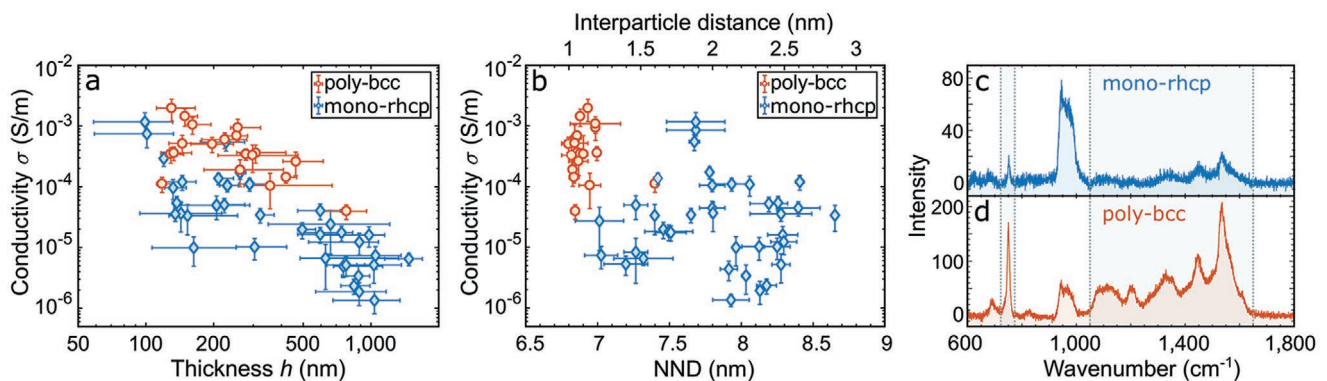


Figure 4. Parameters for structure–transport correlations. a,b) Conductivity of individual microchannels as a function of SL thickness (a) and NND (b). The SL type is indicated by the color code. c,d) Typical Raman spectra of a monocrystalline rhcp (c) and a polycrystalline bcc (d) SL, featuring characteristic Cu4APc signals at 750 cm^{-1} and $1050\text{--}1650\text{ cm}^{-1}$ (highlighted regions). The signal at $\approx 950\text{ cm}^{-1}$ originates from the Si/SiO_x substrate.

are oriented in the superlattice due to facet-specific ligand–ligand interactions. The functionalization of NCs with shorter Cu4APc ligands leads to the formation of a superlattice with higher symmetry, such as bcc, in which the NCs are highly aligned.^[30] In contrast, a large spherical ligand shell leads to a close-packed structure with a lower degree of NCs orientation, such as rhcp.

In view of the non-monotonic correlation between conductivity and SL thickness, we note that very thin NC films exhibit holes/microcracks, which are reduced with increasing thickness.^[31] In contrast, the conductivity in thick films may be affected by a fringing electric field. The electric field is not homogeneous along the sample normal, and current flows mainly in the bottom

layers close to the contacts. However, the conductivity is calculated over the entire channel where the full height is used.

We now turn to the key novelty of this work, the transport anisotropy, that is, the influence of the SL orientation with respect to the electric field on the electric conductivity. For this, it is mandatory to account for the effect of SL thickness, incomplete ligand exchange and crystallinity, and only compare SLs which are very similar in this regard. In doing so, we found strong evidence for a favored angular direction of charge carrier hopping, indicating anisotropic charge transport within the SL. **Figure 5a,d** displays exemplary SAXS patterns averaged over each microchannel of two monocrystalline rhcp SLs with identical

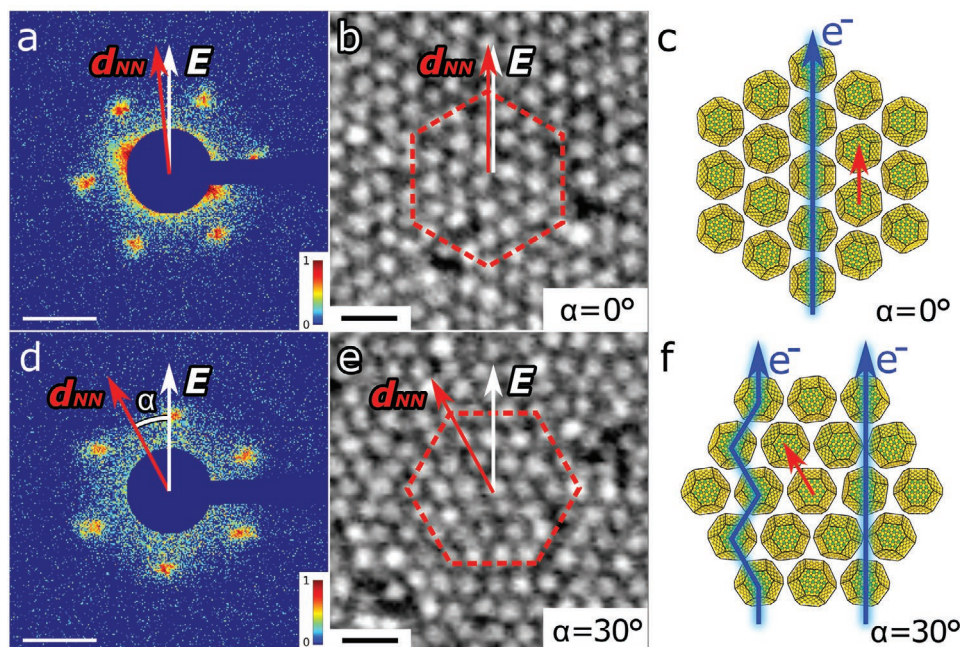


Figure 5. Anisotropic charge transport in monocrystalline NC SLs. a,d) Exemplary averaged SAXS diffraction patterns of comparable monocrystalline rhcp microchannels, oriented along $[0001]_{\text{SL}}$. The azimuthal orientation is defined by the relative angle α between the electric field vector E and the nearest-neighbor direction d_{NN} . SLs with low values of α feature 40–50% higher conductivities than their counterparts with large α . Scale bar: 1 nm^{-1} . b,e) Corresponding real-space SEM images of the SL oriented along $(0001)_{\text{SL}}$ with $\alpha = 0^\circ$ and 30° . The hexagon indicates the orientation of the SL. d_{NN} points along the alignment of the NCs (nearest neighbors). For $\alpha = 0^\circ$, the vector d_{NN} is parallel to E , resulting in enhanced conductivity. Scale bar: 15 nm . c,f) Schematic of the rhcp SL and the favored hopping path for $\alpha = 0^\circ$ (blue arrow) along the d_{NN} direction (red arrow) (c); for an in-plane offset ($\alpha = 30^\circ$), the larger hopping distance or the zig-zag path are detrimental to charge transport (f). Ligand spheres of NCs are omitted for clarity.

structure, that is, lattice parameter and thickness (Figure S15a, Supporting Information). They differ only in terms of the azimuthal orientation with respect to the applied electric field. We define the azimuthal angle α between the electric field vector E (which is oriented vertically due to horizontal electrode edges) and the nearest-neighbor direction d_{NN} (one of the $\langle 2\bar{1}10 \rangle_{\text{SL}}$ directions pointing to the nearest-neighbors). The angle α can vary from 0° to 30° for the sixfold in-plane symmetry. For $\alpha = 0^\circ$, the d_{NN} direction is oriented parallel to the vector of electric field E , whereas for $\alpha = 30^\circ$, the angular (in-plane) offset between the vectors E and d_{NN} is maximized. Our key result is that for any two otherwise comparable channels, we observe higher conductivity for the respective channels with lower angle α . The two extremes ($\alpha = 0^\circ$ and $\alpha = 30^\circ$) are shown in the corresponding real-space SEM images of the $(0001)_{\text{SL}}$ plane of two rhcp SLs in Figure 5b,e. The difference in conductivity between two otherwise identical SLs is 40–50%. A statistical investigation of other microchannels with monocrystalline rhcp SLs reveals similar α -dependent conductivity differences (Figure S15, Supporting Information). This correlation between σ and α indicates anisotropic charge transport, for which the direction of nearest neighbors is assumed to be the most efficient for transport.

In contrast to atomic crystals with transport anisotropy, which exhibit strong electronic coupling and ballistic transport (e.g., black phosphorus), the NC SLs studied here are in the weak coupling regime. This implies temperature-activated hopping as the predominant charge transport mechanism and invokes a strong dependence on the hopping distance.^[4,15] Our results suggest that charge transport is most efficient if the applied electric field is iso-oriented with the nearest-neighbor direction d_{NN} in the SL plane, since this leads to the shortest hopping distance (Figure 5c). Any other orientation (Figure 5f) results either in a larger hopping distance (straight arrow) or a deviation from the direction of the electric field together with an increased number of required jumps for electrons to travel the same distance (zig-zag path), which is detrimental to charge transport. This implies that transport anisotropy should be a general feature of weakly coupled, monocrystalline NC SLs, originating from the dominant effect of the shortest interparticle distance. Accordingly, one could predict the favored direction of charge transport within different SL types, such as simple cubic, face-centered cubic (fcc), or bcc, being the $\langle 100 \rangle$, $\langle 110 \rangle$, or $\langle 111 \rangle$ SL directions, respectively. A similar charge transport anisotropy was computationally predicted for bcc and fcc SLs.^[6] Further, we note that the orientational order of the NCs observed here might be an additional source for anisotropic charge transport as different coupling strengths have been predicted along particular AL directions.^[5,6] In the present case, the most efficient transport occurs if the $[110]_{\text{AL}}$ direction of all NCs is iso-oriented with the electric field.

A high degree of control provided over the SL type and orientation would enable the exploitation of such transport anisotropy also with more complex NC assemblies (e.g., binary NC SLs^[32] or honeycomb structures^[33]) for application in functional electronic devices with tailored transport anisotropy. Furthermore, these results constitute an important step toward the understanding of the intrinsic properties and fundamental limits of these fascinating new NC-based systems.

Experimental Section

Superlattice Microchannel Fabrication: Oleic-acid-stabilized PbS NCs were synthesized according to Weidman et al.^[34] and dispersed in hexane/octane (ratio of 4:1 and 1:0, $c = 4 \mu\text{mol L}^{-1}$). Sizing-curves to UV–vis absorption spectra and SEM investigation yield a particle size of $5.8 \pm 0.5 \text{ nm}$ (Figure S1, Supporting Information).^[35] The NCs were self-assembled at the liquid-air interface according to Dong et al.^[22] and ligand exchanged with the organic π -system Cu-4,4',4'',4'''-tetraaminophthalocyanine. For microcontact printing, a micropatterned PDMS stamp was inked with the SL film and stamped onto devices with pre-patterned Au electrodes (Kapton membranes of $125 \mu\text{m}$ thickness or Si/SiO_x wafer with 200 nm SiO_x). Individual microchannels consisting of an electrode pair and a connecting SL stripe were obtained with $L \approx 1 \mu\text{m}$ and $W \approx 4 \mu\text{m}$. The preparation was performed in a nitrogen glovebox.

Transport Measurements: All devices were measured at room temperature in a nitrogen flushed probe station (Lake Shore, CRX-6.5K). Individual electrode pairs were contacted and analyzed by a source-meter-unit (Keithley, 2636B).

X-Ray Nanodiffraction: Nanodiffraction measurements were performed at Coherence beamline P10 of the PETRA III synchrotron source at DESY. An X-ray beam with $\lambda = 0.898 \text{ nm}$ ($E = 13.8 \text{ keV}$) was focused down to a spot size of $\approx 400 \times 400 \text{ nm}^2$ (FWHM) at the GINIX nanodiffraction endstation.^[36] The 2D detector EIGER X4M (Dectris) with 2070×2167 pixels and a pixel size of $75 \times 75 \mu\text{m}^2$ was positioned 370 mm downstream from the sample and $\approx 9 \text{ cm}$ off-center to allow simultaneous detection of SAXS and WAXS signals. Diffraction mapping of individual microchannels was performed, collecting 100–200 diffraction patterns on a raster grid in Δx and Δy direction with 250 nm step size and an acquisition of 0.5 s . From averaged diffraction patterns for every channel, the SL structure was deduced and from azimuthally-averaged radial profiles the SAXS peak positions were extracted. AXCCA was applied and two-point cross-correlation functions (CCFs) for all channels were calculated, according to Equation (1)

$$C(q_{\text{SL}}, q_{\text{AL}}, \Delta) = \langle \bar{I}(q_{\text{SL}}, \varphi) \bar{I}(q_{\text{AL}}, \varphi + \Delta) \rangle_{\varphi} \quad (1)$$

where $\bar{I}(q_{\text{SL}}, \varphi) = I(q_{\text{SL}}, \varphi) - \langle I(q_{\text{SL}}, \varphi) \rangle_{\varphi}$ and $I(q_{\text{SL}}, \varphi)$ is an intensity value taken at the point (q_{SL}, φ) which are polar coordinates in the detector plane.^[8,20,21] $\langle \dots \rangle_{\varphi}$ denotes averaging over all azimuthal φ angles. q_{SL} correspond to SAXS peaks and q_{AL} to WAXS peaks.

Microchannel Characterization: SEM imaging was conducted with a HITACHI model SU8030 at 30 kV and atomic force microscopy (AFM) investigations with a Bruker MultiMode 8-HR in contact mode and Raman spectroscopy with a confocal Raman spectrometer LabRAM HR800 (Horiba Jobin-Yvon) at $\lambda = 632.8 \text{ nm}$ (He-Ne-laser).

Details on materials, the self-assembly and fabrication processes, X-ray nanodiffraction and AXCCA are given in the Supporting Information.

Supporting Information

Supporting Information is available from the Wiley Online Library or from the author.

Acknowledgements

This project has been funded by the DFG under Grant SCHE1905/3-2 and INST 37/829-1 FUGG, the latter for SEM measurements using a Hitachi SU 8030. Further funding was provided by the Helmholtz Associations Initiative Networking Fund and the Russian Science Foundation grant HRSF-0002/18-41-06001, and the Tomsk Polytechnic University Competitiveness Enhancement Program grant (project number VIU-MNOL NK-214/2018). The authors acknowledge support and discussions with E. Weckert. T. Salditt's group is acknowledged for providing nanofocusing instrument (GINIX) support at the P10 beamline. The

construction and operation of the GINIX setup is funded by the Georg-August Universität Göttingen and BMBF Verbundforschung "Struktur der Materie", projects 05KS7MGA, 05K10MGA, and 05K13MGA.

Conflict of Interest

The authors declare no conflict of interest.

Keywords

charge transport, nanocrystals, nanodiffraction, self-assembly, superlattices

Received: April 1, 2020

Revised: June 17, 2020

Published online: July 28, 2020

- [1] C. B. Murray, C. R. Kagan, M. G. Bawendi, *Science* **1995**, 270, 1335.
 [2] A. P. Alivisatos, *Science* **1996**, 271, 933.
 [3] C. R. Kagan, C. B. Murray, *Nat. Nanotechnol.* **2015**, 10, 1013.
 [4] F. Remacle, R. D. Levine, *ChemPhysChem* **2001**, 2, 20.
 [5] N. Yazdani, S. Andermatt, M. Yarema, V. Farto, M. H. Bani-Hashemian, S. Volk, W. M. M. Lin, O. Yarema, M. Luisier, V. Wood, *Nat. Commun.* **2020**, 11, 2852.
 [6] A. P. Kaushik, B. Lukose, P. Clancy, *ACS Nano* **2014**, 8, 2302.
 [7] P. Liljeroth, K. Overgaard, A. Urbieto, B. Grandidier, S. G. Hickey, D. Vanmaekelbergh, *Phys. Rev. Lett.* **2006**, 97, 096803.
 [8] I. A. Zaluzhnyy, R. P. Kurta, A. André, O. Y. Gorobtsov, M. Rose, P. Skopintsev, I. Besedin, A. V. Zozulya, M. Sprung, F. Schreiber, I. A. Vartanyants, M. Scheele, *Nano Lett.* **2017**, 17, 3511.
 [9] J. J. Geuchies, C. van Overbeek, W. H. Evers, B. Goris, A. de Backer, A. P. Gantapara, F. T. Rabouw, J. Hilhorst, J. L. Peters, O. Konovalov, A. V. Petukhov, M. Dijkstra, L. D. A. Siebbeles, S. van Aert, S. Bals, D. Vanmaekelbergh, *Nat. Mater.* **2016**, 15, 1248.
 [10] K. Whitham, D.-M. Smilgies, T. Hanrath, *Chem. Mater.* **2018**, 30, 54.
 [11] M. C. Weidman, D.-M. Smilgies, W. A. Tisdale, *Nat. Mater.* **2016**, 15, 775.
 [12] J. Novák, R. Banerjee, A. Kornowski, M. Jankowski, A. André, H. Weller, F. Schreiber, M. Scheele, *ACS Appl. Mater. Interfaces* **2016**, 8, 22526.
 [13] T. Hanrath, J. J. Choi, D.-M. Smilgies, *ACS Nano* **2009**, 3, 2975.
 [14] D. V. Talapin, C. B. Murray, *Science* **2005**, 310, 86.
 [15] Y. Liu, M. Gibbs, J. Puthusseri, S. Gaik, R. Ihly, H. W. Hillhouse, M. Law, *Nano Lett.* **2010**, 10, 1960.
 [16] S. J. Oh, N. E. Berry, J.-H. Choi, E. A. Gaulding, T. Paik, S.-H. Hong, C. B. Murray, C. R. Kagan, *ACS Nano* **2013**, 7, 2413.
 [17] W. H. Evers, J. M. Schins, M. Aerts, A. Kulkarni, P. Capiod, M. Berthe, B. Grandidier, C. Delerue, H. S. J. van der Zant, C. van Overbeek, J. L. Peters, D. Vanmaekelbergh, L. D. A. Siebbeles, *Nat. Commun.* **2015**, 6, 8195.
 [18] K. Whitham, J. Yang, B. H. Savitzky, L. F. Kourkoutis, F. Wise, T. Hanrath, *Nat. Mater.* **2016**, 15, 557.
 [19] D. M. Balazs, B. M. Matysiak, J. Momand, A. G. Shulga, M. Ibáñez, M. V. Kovalenko, B. J. Kooi, M. A. Loi, *Adv. Mater.* **2018**, 30, 1802265.
 [20] I. A. Zaluzhnyy, R. P. Kurta, M. Scheele, F. Schreiber, B. I. Ostrovskii, I. A. Vartanyants, *Materials* **2019**, 12, 3464.
 [21] N. Mukharamova, D. Lapkin, I. A. Zaluzhnyy, A. André, S. Lazarev, Y. Y. Kim, M. Sprung, R. P. Kurta, F. Schreiber, I. A. Vartanyants, M. Scheele, *Small* **2019**, 15, 1904954.
 [22] A. Dong, Y. Jiao, D. J. Milliron, *ACS Nano* **2013**, 7, 10978.
 [23] A. André, C. Theurer, J. Lauth, S. Maiti, M. Hodas, M. Samadi Khoshkoo, S. Kinge, A. J. Meixner, F. Schreiber, L. D. A. Siebbeles, K. Braun, M. Scheele, *Chem. Commun.* **2017**, 53, 1700.
 [24] S. Maiti, S. Maiti, A. Maier, J. Hagenlocher, A. Chumakov, F. Schreiber, M. Scheele, *J. Phys. Chem. C* **2019**, 123, 1519.
 [25] D. Qin, Y. Xia, G. M. Whitesides, *Nat. Protoc.* **2010**, 5, 491.
 [26] P. Nagpal, V. I. Klimov, *Nat. Commun.* **2011**, 2, 486.
 [27] Y. Zhang, D. Zhrebetskyy, N. D. Bronstein, S. Barja, L. Lichtenstein, A. P. Alivisatos, L.-W. Wang, M. Salmeron, *ACS Nano* **2015**, 9, 10445.
 [28] M. C. Weidman, Q. Nguyen, D.-M. Smilgies, W. A. Tisdale, *Chem. Mater.* **2018**, 30, 807.
 [29] I. Lokteva, M. Koof, M. Walther, G. Grübel, F. Lehmkuhler, *Small* **2019**, 15, 1900438.
 [30] J. J. Choi, C. R. Bealing, K. Bian, K. J. Hughes, W. Zhang, D.-M. Smilgies, R. G. Hennig, J. R. Engstrom, T. Hanrath, *J. Am. Chem. Soc.* **2011**, 133, 3131.
 [31] S. Shaw, B. Yuan, X. Tian, K. J. Miller, B. M. Cote, J. L. Colaux, A. Migliori, M. G. Panthani, L. Cademartiri, *Adv. Mater.* **2016**, 28, 8892.
 [32] E. V. Shevchenko, D. V. Talapin, N. A. Kotov, S. O'Brien, C. B. Murray, *Nature* **2006**, 439, 55.
 [33] M. P. Boneschanscher, W. H. Evers, J. J. Geuchies, T. Altantzis, B. Goris, F. T. Rabouw, S. A. P. van Rossum, H. S. J. van der Zant, L. D. A. Siebbeles, G. van Tendeloo, I. Swart, J. Hilhorst, A. V. Petukhov, S. Bals, D. Vanmaekelbergh, *Science* **2014**, 344, 1377.
 [34] M. C. Weidman, M. E. Beck, R. S. Hoffman, F. Prins, W. A. Tisdale, *ACS Nano* **2014**, 8, 6363.
 [35] I. Moreels, K. Lambert, D. Smeets, D. de Muyenck, T. Nollet, J. C. Martins, F. Vanhaecke, A. Vantomme, C. Delerue, G. Allan, Z. Hens, *ACS Nano* **2009**, 3, 3023.
 [36] S. Kalbfleisch, H. Neubauer, S. P. Krüger, M. Bartels, M. Osterhoff, D. D. Mai, K. Giewekemeyer, B. Hartmann, M. Sprung, T. Salditt, I. McNulty, C. Eyberger, B. Lai, *AIP Conf. Proc.* **2011**, 1365, 96.

Spatially resolved fluorescence of caesium lead halide perovskite supercrystals reveals quasi-atomic behavior of nanocrystals

Dmitry Lapkin ^{1,7}, Christopher Kirsch^{2,7}, Jonas Hiller ^{2,7}, Denis Andrienko ³, Dameli Assalauova¹, Kai Braun², Jerome Carnis ¹, Young Yong Kim ¹, Mukunda Mandal³, Andre Maier^{2,4}, Alfred J. Meixner ^{2,4}, Nastasia Mukharamova¹, Marcus Scheele ^{2,4}✉, Frank Schreiber ^{4,5}, Michael Sprung¹, Jan Wahl², Sophia Westendorf², Ivan A. Zaluzhnyy⁵ & Ivan A. Vartanyants ^{1,6}✉

We correlate spatially resolved fluorescence (-lifetime) measurements with X-ray nanodiffraction to reveal surface defects in supercrystals of self-assembled cesium lead halide perovskite nanocrystals and study their effect on the fluorescence properties. Upon comparison with density functional modeling, we show that a loss in structural coherence, an increasing atomic misalignment between adjacent nanocrystals, and growing compressive strain near the surface of the supercrystal are responsible for the observed fluorescence blueshift and decreased fluorescence lifetimes. Such surface defect-related optical properties extend the frequently assumed analogy between atoms and nanocrystals as so-called quasi-atoms. Our results emphasize the importance of minimizing strain during the self-assembly of perovskite nanocrystals into supercrystals for lighting application such as superfluorescent emitters.

¹Deutsches Elektronen-Synchrotron DESY, Notkestraße 85, 22607 Hamburg, Germany. ²Institut für Physikalische und Theoretische Chemie, Universität Tübingen, Auf der Morgenstelle 18, 72076 Tübingen, Germany. ³Max Planck Institute for Polymer Research, Ackermannweg 10, 55128 Mainz, Germany. ⁴Center for Light-Matter Interaction, Sensors & Analytics LISA+, Universität Tübingen, Auf der Morgenstelle 15, 72076 Tübingen, Germany. ⁵Institut für Angewandte Physik, Universität Tübingen, Auf der Morgenstelle 10, 72076 Tübingen, Germany. ⁶National Research Nuclear University MEPhI (Moscow Engineering Physics Institute), Kashirskoe shosse 31, 115409 Moscow, Russia. ⁷These authors contributed equally: Dmitry Lapkin, Christopher Kirsch, Jonas Hiller. ✉email: marcus.scheele@uni-tuebingen.de; ivan.vartanyants@desy.de

Advances in the self-assembly of colloidal nanocrystals (NCs) from solution into three-dimensional arrays with long-range order have enabled the design of microscopic “supercrystals” that approach the structural precision of atomic single crystals¹. The individual NCs, which are the building blocks of a supercrystal, are often regarded as “artificial atoms”, and hence analogies between atomic crystals and such supercrystals have been made^{2,3}. NC supercrystals are susceptible to doping⁴, and they can exhibit exceptional mechanical properties⁵, quasicrystal formation², enhanced electronic coupling⁶, and engineered phonon modes⁷. In view of the recent progress in exploiting the massive structural coherence in NC supercrystals to generate collective optoelectronic properties^{8–10}, a critical question remains whether this artificial atom analogy can be extended towards the optical properties of NC supercrystals. Due to surface dangling bonds and surface reconstruction, even the purest and most carefully prepared atomic crystals are not structurally perfect^{11,12}. For atomic crystals, such surface defects strongly affect the fluorescence spectra, lifetime, and quantum yield^{13–17}. For supercrystals, this is much less understood.

In this work, we show that in close analogy to atomic crystals^{18,19}, CsPbBr₂Cl and CsPbBr₃ NC supercrystals exhibit structural distortions near their surfaces which significantly alter their fluorescence properties. This finding is of high relevance for the application of these materials as tunable, bright emitters with superfluorescent behavior^{8–10}. Superfluorescence is a key property for the design of spectrally ultra-pure laser sources²⁰ or highly efficient light-harvesting systems²¹. Recent quantum chemical simulations have suggested that structural disorder in CsPbBr₃ supercrystals and its effect on the thermal decoherence plays a pivotal role in the efficiency of the superfluorescence²². Previous structural investigations of ensembles of CsPbBr₃ supercrystals by grazing-incidence small angle X-ray scattering (SAXS) indicated a primitive unit cell with slight tetragonal distortion²³, and wide-angle X-ray scattering (WAXS) showed a high degree of structural coherence²⁴. Electron microscopy of individual supercrystals revealed a frequent occurrence of local defects in the supercrystals, such as isolated NC vacancies²⁵. Confocal fluorescence microscopy of individual CsPbBr₃ supercrystals displayed spatial variations in the fluorescence peak wavelength and intensity, indicating that local structural inhomogeneities may substantially affect the fluorescence properties of the entire supercrystal²⁶. Our approach is based on simultaneous WAXS and SAXS measurements with a nano-focused beam to probe the structural defects and crystallographic orientation of the supercrystal and the constituting NCs on a local level with dimensions of ~3 μm and 7–9 nm, respectively^{27–29}. By correlation with diffraction-limited confocal fluorescence microscopy and modeling with density functional theory (DFT) we present proof that compressive strain, a loss of structural coherence and an increasing atomic misalignment between adjacent nanocrystals at the edges of CsPbBr₂Cl NC supercrystals are responsible for a blueshifted emission and decrease of the fluorescence lifetimes.

Results

We study self-assembled CsPbBr₂Cl and CsPbBr₃ NC supercrystals on glass substrates (see “Methods” for details on synthesis and self-assembly of NCs). Spatially resolved photoluminescence spectra of the NC supercrystals under 405 nm excitation in a confocal laser scanning microscope with a step size of 250 nm and 100 nm, respectively, are shown in Fig. 1. When approaching an edge of the supercrystal, we find a continuous blueshift of the emission peak wavelength. This blueshift is strongest for relatively small (few μm edge length) and highly faceted supercrystals, where it reaches up to 20 meV for CsPbBr₂Cl. We observe the

same blueshifting behavior for supercrystals composed of CsPbBr₃ NCs, although to a lesser extent (up to 12 meV).

In Fig. 2, we display fluorescence lifetime images of self-assembled CsPbBr₂Cl and CsPbBr₃ supercrystals measured on glass substrates with a lateral resolution of 200 nm under 405 nm excitation. For both supercrystal compositions, we obtain good fits of the experimental time-resolved fluorescence by pixel-by-pixel monoexponential reconvolution using an instrument response function acquired on a clean glass coverslip (Supplementary Figs. 2, 3). In the case of supercrystals composed of CsPbBr₂Cl NCs, we measure typical fluorescence lifetimes (τ) around 2.1 ns in the center which decrease by approximately 20% when scanning from the center of a supercrystal towards its edges. Supercrystals composed of CsPbBr₃ NCs exhibit typical lifetime values around 1.5 ns in the center, which shorten by approximately 30% when approaching the edges. We note that this holds true only for freshly prepared NC supercrystals. After several days of exposure to air, the trend in the spatially resolved τ -values is reversed in that such aged supercrystals exhibit longer lifetimes at the edges. However, the overall blueshift of the fluorescence peak wavelength towards the edges is preserved.

To correlate the fluorescence data with the structure of the supercrystals, we carry out X-ray synchrotron measurements by SAXS and WAXS at PETRA III facility (Hamburg, Germany) (see Fig. 3a and “Methods” for details). Using a 400 × 400 nm² X-ray beam, we perform a spatially resolved scan of a typical CsPbBr₂Cl NC supercrystal on a Kapton substrate. While the results presented here are for one typical supercrystal, examples of more supercrystals are provided in the Supplementary information (Supplementary Note 7). First, all individual patterns are integrated to obtain the average structure. The averaged background-corrected WAXS and SAXS diffraction patterns are shown in Fig. 3b, c, correspondingly. The signal in the WAXS region contains three orders of Bragg peaks from the atomic lattice (Fig. 3b), and the SAXS region (shown enlarged in Fig. 3c) displays several orders of Bragg peak from the supercrystal. A real-space map of the scan based on the integrated SAXS intensity at $q < 2 \text{ nm}^{-1}$ is shown in Fig. 3d. The map represents a square area of high intensity corresponding to a single supercrystal. For comparison, we display a scanning electron micrograph of a similar supercrystal (see the inset in Fig. 3a and Supplementary Fig. 8) from which we determine an average NC diameter of $7.3 \pm 0.4 \text{ nm}$ and an interparticle distance of $2.5 \pm 0.5 \text{ nm}$. For strongly faceted supercrystals, the NC diameter is rather uniform over the whole crystal. For less faceted supercrystals, occasional ensembles of smaller NCs are found in the vicinity of the edges. However, the spatial extent of such smaller NC populations is always limited to ~200 nm (see Supplementary Note 3).

The average diffraction pattern in the WAXS region (see Fig. 3b) contains four prominent Bragg peaks, originating from the atomic lattice (AL) of the NCs. Their radial positions at $q = 10.93 \text{ nm}^{-1}$, 15.44 nm^{-1} , and 21.90 nm^{-1} (see Supplementary Fig. 10) can be attributed to a cubic AL. We note that although a cubic phase for CsPbBr₂Cl has been reported^{30,31}, the most stable phase at room temperature is expected to be orthorhombic. Due to the small NC size and the resulting broadening of the Bragg peaks, it is impossible to distinguish between these two very similar structures. Thus, we use a pseudocubic notation to index the WAXS peaks: 110 and 002 orthorhombic peaks correspond to 100_{AL} pseudocubic peak, 112 and 200 – to 110_{AL}, and 220, 004 – to 200_{AL} peaks. The present peaks and their azimuthal positions indicate a primary orientation of the NCs along the [001]_{AL} axis with respect to the incident beam. We find the unit cell parameter to be $a_{\text{AL}} = 0.575 \pm 0.003 \text{ nm}$, which is in good agreement with previously reported values for CsPbBr₂Cl³². From the peak broadening, we extract the NC size

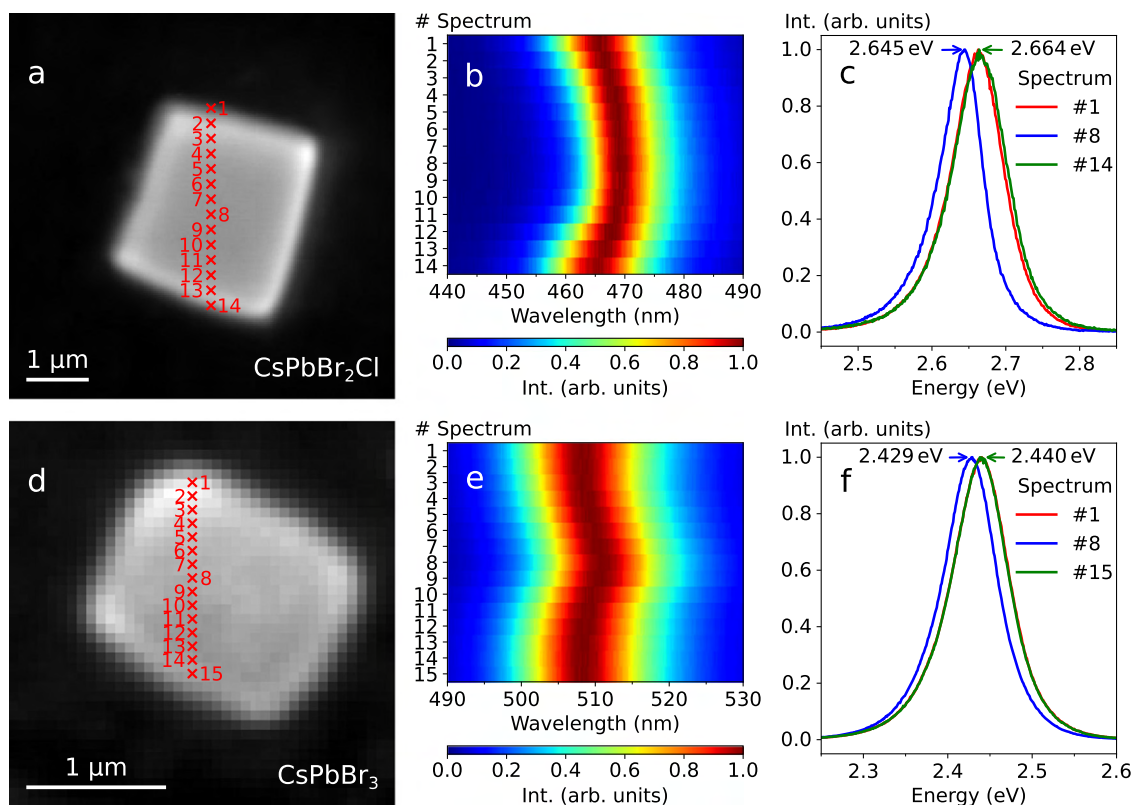


Fig. 1 Spatially resolved fluorescence. **a** Optical micrograph of a CsPbBr₂Cl NC supercrystal. Positions of the measured photoluminescence spectra are indicated. **b** The corresponding normalized spectra. **c** Selected normalized spectra, acquired at the edges and the center of the supercrystal. **d-f** Corresponding data for a CsPbBr₃ supercrystal.

(*d*) and lattice distortion (*g*) using the Williamson–Hall method with $d = 6.8 \pm 0.1$ nm and $g = 2.3 \pm 0.1\%$ (see Supplementary Note 4). The obtained NC size is in good agreement with the scanning electron microscopy (SEM) results.

The SAXS pattern in Fig. 3c represents the typical 4-fold pattern of a simple cubic lattice oriented along the [001]_{SC} axis with four visible orders of Bragg peaks that can be attributed to 100_{SC}, 110_{SC}, 200_{SC} and 210_{SC} reflections of the supercrystal of NCs. We determine an average unit cell parameter of $a_{SC} = 9.9 \pm 0.4$ nm. Considering the NC size obtained by SEM, we obtain an interparticle distance of 2.6 ± 0.4 nm, which is in good agreement with the SEM result (2.5 ± 0.5 nm). All crystallographic axes of the NCs are aligned with the corresponding axes of the supercrystal (e.g. [100]_{AL} || [100]_{SC} and [010]_{AL} || [010]_{SC}), which is consistent with ref. 25.

Analyzing individual SAXS patterns from different locations on the supercrystal, we find substantial local deviations from the average structure (see Supplementary Fig. 12 for examples of single diffraction patterns). To illustrate this, from the Bragg peak positions, we extract the basis vectors a_1 and a_2 , the angle γ between them, and the average azimuthal position φ , which are defined in Fig. 4a (see the “Methods” section for details). As depicted in Fig. 4b, the mean unit cell parameter is largest in the center of the supercrystal with 10.7 nm and smallest at the edges with 7.8 nm. Although both unit cell parameters a_1 and a_2 decrease at the edges (see Supplementary Fig. 16, for separate maps of a_1 and a_2 values), we observe that this lattice contraction is anisotropic. The ratio of the in-plane unit cell parameters a_2/a_1 differs from unity by $\pm 20\%$ in such a way that the NC spacing in the directions along the nearest supercrystal boundary is smaller than normal to it, as shown in Fig. 4c. We note that the mean value $\langle a \rangle = 9.4 \pm 0.7$ nm is slightly smaller than the unit cell

parameters extracted from the average diffraction pattern. We attribute this to the low intensity of scattering from the supercrystal edges, which reduces their contribution to the average pattern. We do not observe a clear trend in the size of the SAXS Bragg peaks (see Supplementary Fig. 15, for the maps). The instrumental peak broadening, determined by the incident X-ray beam size is about 0.015 nm⁻¹ (full width at half maximum, FWHM). The observed peak sizes are much larger and vary in the range from 0.05 nm⁻¹ to 0.2 nm⁻¹ and, as such, they depend mainly on the superlattice distortion. The characteristic length scale on which this distortion evolves is, most probably, smaller than the incident beam. Thus, the areas with different lattice parameters simultaneously illuminated by the incident beam lead to the peak broadening.

The angle γ between the [100]_{SC} and [010]_{SC} axes differs from its average value of $\langle \gamma \rangle = 90 \pm 6^\circ$ in a range of 76° to 105° over the whole supercrystal as shown in Fig. 4d. Specifically, we find $\gamma > 90^\circ$ close to the top and bottom corners of the supercrystal and $\gamma < 90^\circ$ close to the left and right corners. Thus, the angle pointing towards the corner of the supercrystal is always obtuse. We further calculate the azimuthal position φ of the mean line **M** between the [100]_{SC} and [010]_{SC} axes. This angle can be interpreted as the azimuthal orientation of the unit cell of the supercrystal. The orientation changes inhomogeneously throughout the superlattice in the range from 72° to 97° as shown in Fig. 4e. There is no obvious correlation between the lattice orientation and the spatial position within the sample. Overall, these results suggest that the supercrystal is simple cubic on average, but it exhibits substantial local monoclinic distortions.

We analyze the Bragg peaks in the WAXS region of individual diffraction patterns at different locations to study the angular orientation of the NCs inside the superlattice. From the WAXS

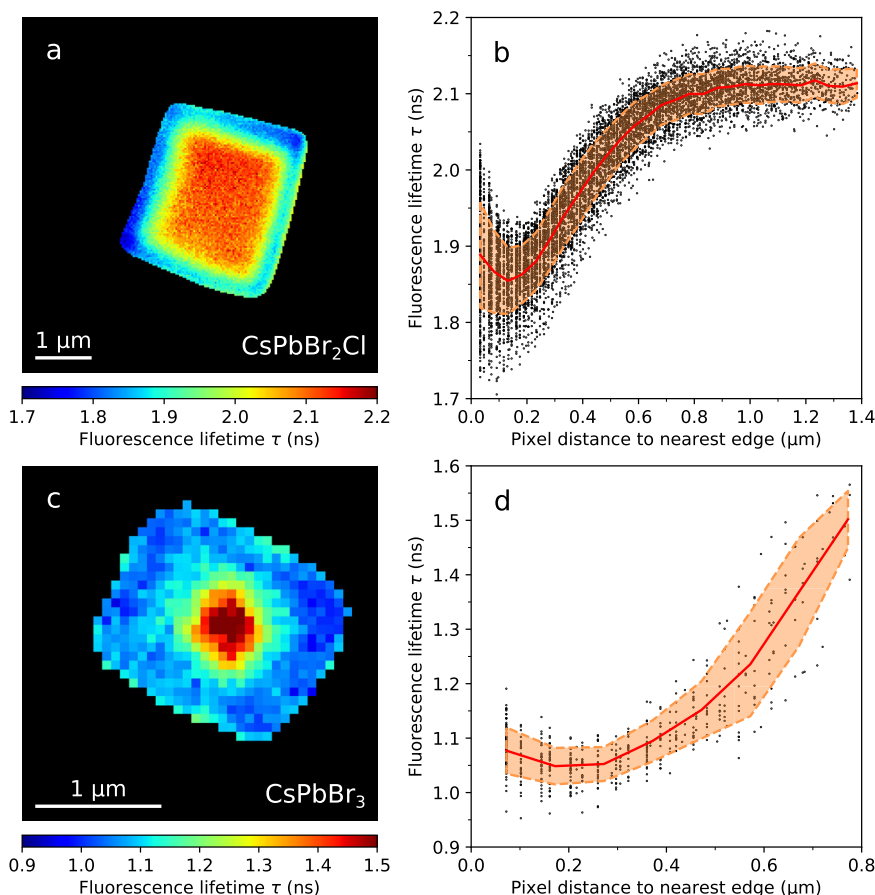


Fig. 2 Spatially resolved fluorescence lifetime imaging. **a** Fluorescence lifetime τ image of a CsPbBr₂Cl NC supercrystal obtained by fitting the experimental time-resolved fluorescence with a monoexponential decay function. **b** Fluorescence lifetime values τ obtained at each pixel inside the supercrystal as a function of the distance to the nearest edge, where the red line shows the mean value, and the dashed lines indicate the confidence interval of $\pm\sigma$. **c**, **d** Analogous results for a CsPbBr₃ NC supercrystal.

Bragg peak analysis, we extract the average WAXS intensity $\langle I_{AL} \rangle$ and the azimuthal position ψ of the $[010]_{AL}$ axis defined in Fig. 5a (see “Methods” section and Supplementary Note 6). In contrast to the intensity of the SAXS Bragg peaks, the WAXS intensity $\langle I_{AL} \rangle$ decreases towards the edges, as shown in Fig. 5b, indicating an out-of-plane rotation of the NCs that shifts the Bragg peaks slightly out of the Ewald sphere²⁸. We find that ψ changes in a wide range from 120° to 142° as shown in Fig. 5c. The map of ψ resembles that of the azimuthal orientation φ of the mean line **M**, shown in Fig. 4e. The 45° offset between the $[010]_{AL}$ axis and the mean line **M** indicates the alignment of the $[110]_{AL}$ axis with the mean line **M** between the $[100]_{SC}$ and $[010]_{SC}$ axes (see Supplementary Fig. 23).

From the azimuthal FWHMs of the WAXS Bragg peaks, we extract the angular disorder $\delta\psi$ of the individual nanocrystals at each spatial point by the Williamson–Hall method as shown in Fig. 5d (see “Methods” for details). The disorder is smallest in the center of a supercrystal (9.9°) and increases to a maximum of 24.0° at the edges. The mean value of the angular disorder is $\langle \delta\psi \rangle = 16.1 \pm 2.8^\circ$, which is consistent with previously observed values for similar superstructures^{25,27–29}.

Despite the fact that the atomic lattice parameter a_{AL} is constant within the error bars throughout the whole supercrystal (see Supplementary Fig. 20, for the map of a_{AL}), we find a difference in the radial width of the Bragg peaks at different locations. By the Williamson–Hall method, we extract the lattice distortion g_q (the ratio $\delta a_{AL}/a_{AL}$, where δa_{AL} is the FWHM of the unit cell parameter distribution around the mean value a_{AL}) at each spatial

point (see “Methods” section for details). We find a clear trend of increasing atomic lattice distortion towards the edges of the supercrystal with a maximum of 2% at the edge, while it is about 1% at a distance $3\ \mu\text{m}$ into the center, as shown in Fig. 6. The trend is even more evident for another supercrystal with particularly good signal-to-noise ratio of the WAXS intensity (see Supplementary Fig. 29).

To rationalize the experimental trend of increased fluorescence energies at the edges of the supercrystal as compared to its center, we carry out density functional modeling of the system. We consider three individual contributions in this regard. First, we recognize that the number of nearest neighbors at the surface of the supercrystal is lower than that in the center, leading to stronger exciton confinement and hence increased fluorescence energies at the edges. Indeed, our DFT calculations confirm this trend in Fig. 7a, which is consistent with the blueshift of the fluorescence spectra observed experimentally for the NCs at the edges. “Nearest neighbors” refers here to adjacent NCs with near-perfect orientational order, that is, a low value of $\delta\psi$ (Fig. 5d). A large orientational misalignment ($\delta\psi$) is likely to have a similar effect on nearest-neighbor coupling as a reduced number of nearest neighbors. Second, we anticipate that the shorter interparticle spacing (Fig. 4b) should facilitate better electronic coupling between the nanocrystals at the edges and, therefore, a decrease in the optical gap at the edges is anticipated. While this expectation is confirmed computationally in Fig. 7b, we note that it is exactly opposite to what is observed experimentally in Fig. 1b, e (see Discussion section for details). Third, the supercrystal is

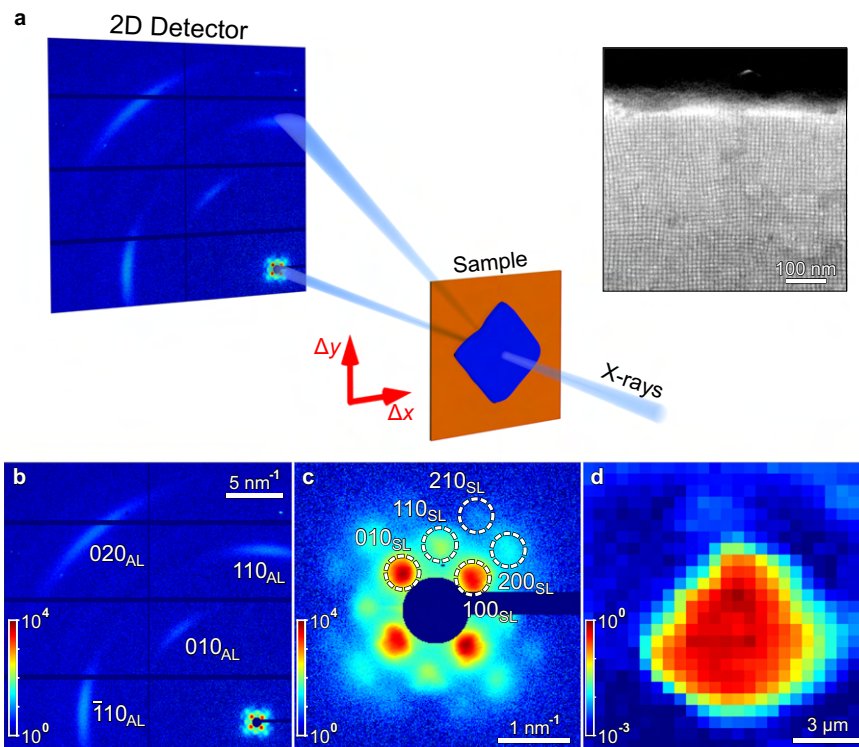


Fig. 3 Spatially resolved X-ray nanodiffraction experiment and average diffraction patterns. **a** Scheme of the X-ray experiment. EIGER X 4 M 2D detector is positioned downstream from the sample. The arrows show the directions Δx and Δy of spatial scanning. Inset (top right): a SEM micrograph of the CsPbBr₂Cl NC supercrystal. **b** Average diffraction pattern for a supercrystal. Several orders of WAXS and SAXS Bragg peaks from the atomic and supercrystal structure, respectively, are well visible. The WAXS Bragg peaks are indexed using pseudocubic notation. **c** Enlarged SAXS region of the averaged diffraction pattern. The Bragg peaks are indexed according to a simple cubic structure. **d** Diffraction map for a scan based on the integrated intensity of the SAXS diffraction patterns at $q < 2 \text{ nm}^{-1}$. The pixel size (the step size) is 500 nm.

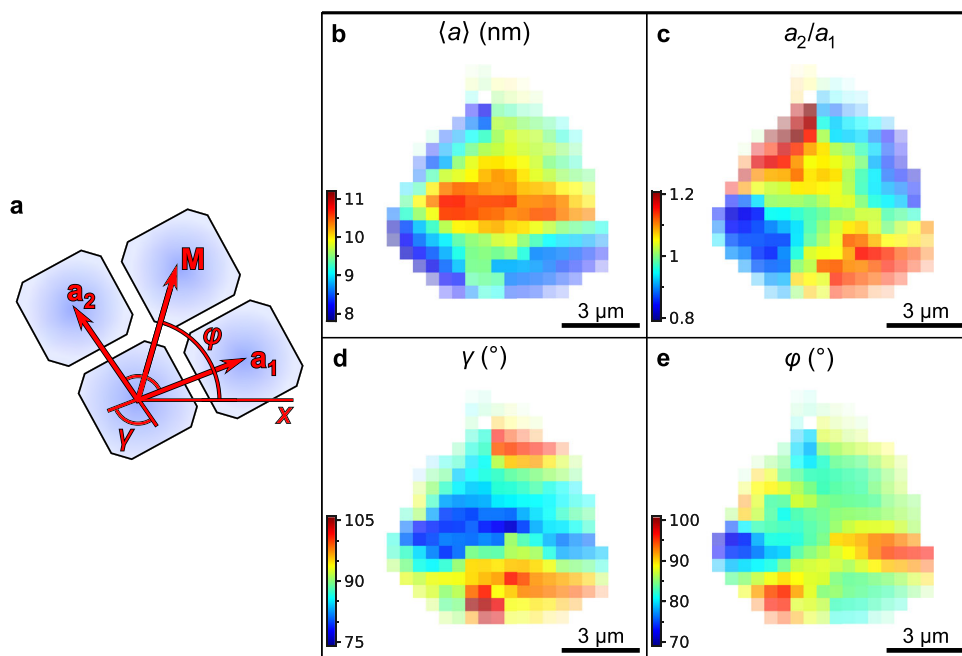


Fig. 4 Spatially resolved SAXS. **a** Definition of the geometrical parameters of a superlattice unit cell: the basis vectors \mathbf{a}_1 and \mathbf{a}_2 with the angle γ between them, and the mean line \mathbf{M} between the basis vectors at the angle φ . **b** Average unit cell parameter $\langle a \rangle = (a_1 + a_2)/2$. **c** Ratio a_2/a_1 of the unit cell parameters along the basis vectors \mathbf{a}_2 and \mathbf{a}_1 . **d** Angle γ between the basis vectors \mathbf{a}_1 and \mathbf{a}_2 . **e** Azimuthal Position φ of the mean line \mathbf{M} between the basis vectors \mathbf{a}_1 and \mathbf{a}_2 . The pixel size in (b-e) is 500 nm.

compressed at the edges, as evident from Fig. 4b. While it is reasonable to assume that the compressive strain will mostly manifest in a denser packing of the soft oleylamine/oleic acid ligand sphere of the NCs, we also consider a partial compression of the hard-inorganic lattice-core. In Fig. 7c we calculate the effect of such compression on the HOMO–LUMO gap (E_{gap}) of the NC. While axial stress applied to the CsCl-terminated surface of the CsPbBr₂Cl particle results in a steady increase of the optical gap consistent with the experiment, similar stress on the CsBr-terminated surfaces of both particles are found to both increase or decrease E_{gap} , depending on the magnitude of the applied stress.

Overall, our computational modeling suggests that the spectral blueshift of the fluorescence from the edges of the supercrystal can be caused mainly due to a reduced NC coordination number

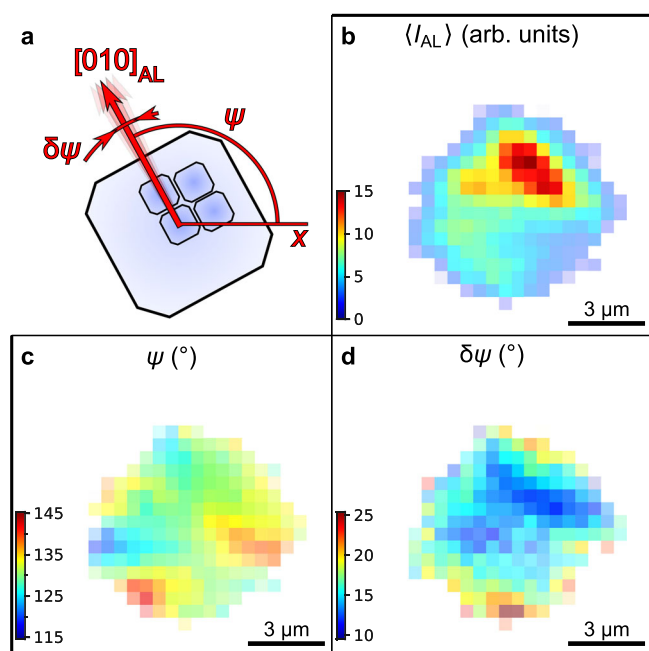


Fig. 5 Spatially resolved WAXS. **a** Definition of the geometrical parameters of the atomic lattice extracted by fitting of the Bragg peaks. **b** Mean intensity of the WAXS Bragg peaks ($\langle I_{\text{AL}} \rangle$). **c** Azimuthal position ψ of the 100_{AL} crystallographic axis of the NCs. **d** FWHM $\delta\psi$ of the angular disorder of the NCs around the mean azimuthal position ψ extracted from the azimuthal FWHMs of the Bragg peaks by the Williamson–Hall method. The pixel size in (**b–d**) is 500 nm.

at the edges as well as the compressive atomic lattice strain in some cases, knowing that the third factor—the shorter interparticle distance—works in the opposite direction, facilitating electronic coupling between adjacent nanocrystals and decreasing the optical gap. However, since the experimentally measured spectral shift is seemingly a combination of all three effects discussed above, a fully quantitative prediction would require more detailed knowledge on their relative contributions as well as the relative orientation and positions of individual nanocrystals, which are currently not available.

Discussion

When NCs are self-assembled into supercrystals from colloidal solution via slow drying, the increasing curvature and surface tension of the evaporating solvent invokes compressive strain on the supercrystal^{33,34}. We hold such a strain responsible for the observed compression of the unit cell parameter by over 20% of the CsPbBr₂Cl NC supercrystals in Fig. 4b. This compression is possible due to the softness of the oleylamine/oleic acid ligand shell of the NCs, enabling a large decrease of the interparticle distance by growing interdigitation of adjacent ligand spheres. We note that the compression occurs gradually over a length scale of many lattice planes ($>1 \mu\text{m}$), meaning that it is not a localized surface reconstruction as commonly observed in atomic crystals¹². The accompanying loss in the angular correlation of the constituting NCs with the superlattice fits a scenario where strain in the supercrystal is partially relieved by forming local structural defects. The comparison of the average (Fig. 3c) vs. the local (Fig. 4) structure of the supercrystal shows that such distortions are indeed frequently present. We note that recent work on CsPbBr₃ NC supercrystals reported perfect structural coherence exclusively in the out-of-plane direction²⁴. Since our experiment is only sensitive to in-plane structural features, the findings here are not contradictory to that report.

Our results in Fig. 4c support the view of Kapuscinsky et al. that strain during the self-assembly is initially isotropic but later becomes increasingly anisotropic³³. In a simple cubic supercrystal, the preferred direction for anisotropic structural changes to manifest is the $\langle 111 \rangle_{\text{SC}}$, which will result in a shear deformation of the ligand spheres³⁵. The expected structure of the supercrystal after this shear deformation is reasonably resembled by the local structure depicted in Fig. 4.

The compression in the supercrystals is not exclusively limited to the soft ligand sphere. With an interparticle distance of $<1 \text{ nm}$ close to the edges of a supercrystal, the space for the two ligand spheres of adjacent NCs is so constrained, that the inorganic

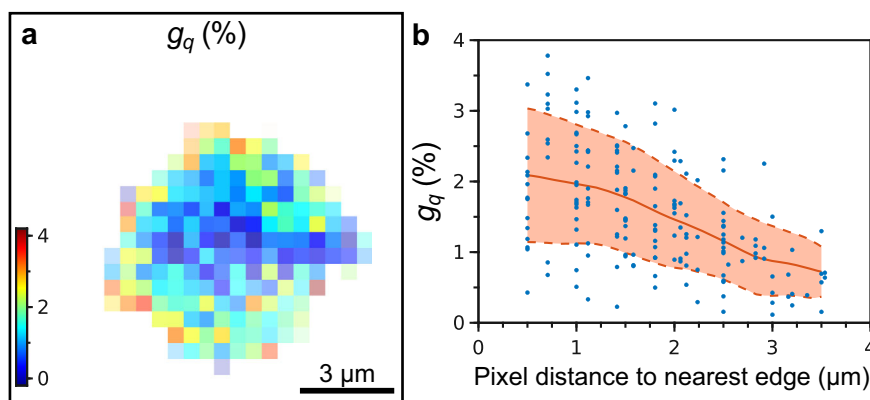


Fig. 6 Spatially resolved atomic lattice distortion. **a** Atomic lattice distortion g_q extracted from the radial FWHMs of the WAXS Bragg peaks by the Williamson–Hall method. The pixel size is 500 nm. **b** The same value g_q for each pixel plotted against the distance from this pixel to the nearest edge of the supercrystal. The red line shows the mean value, the dashed lines indicate the confidence interval of $\pm\sigma$.

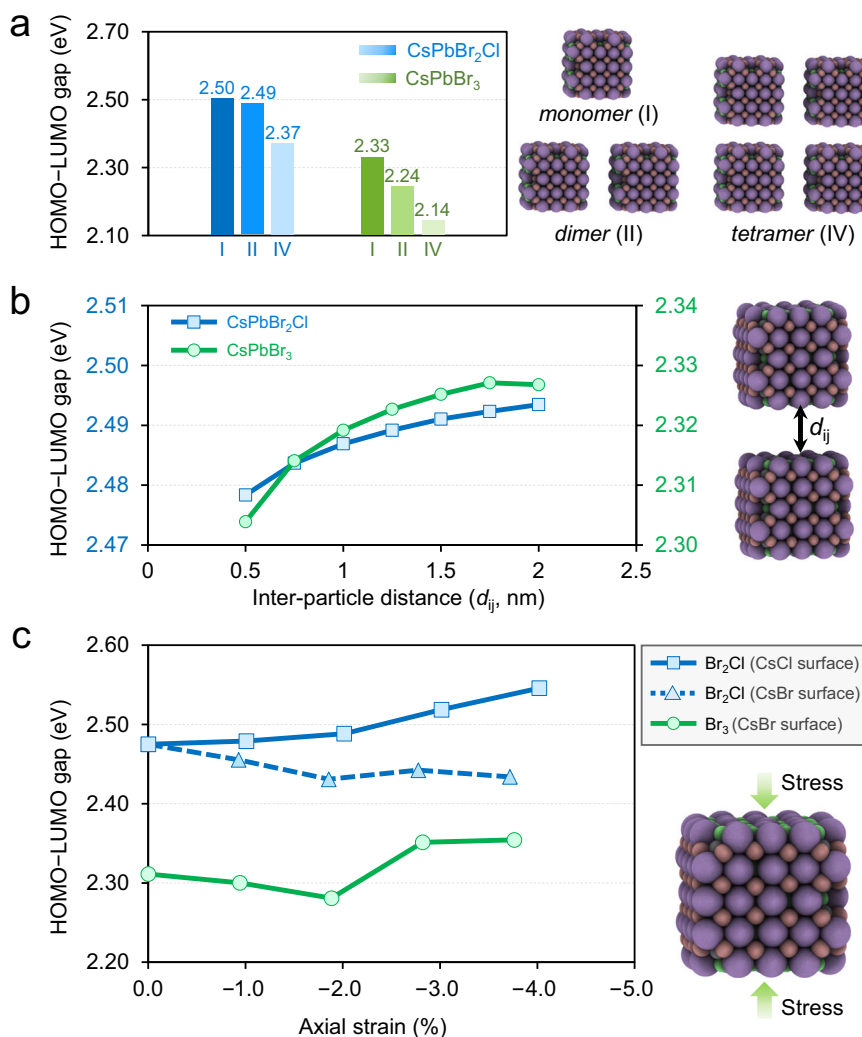


Fig. 7 Density Functional Modeling. Computed HOMO–LUMO gaps as a function of (a) number of neighboring particles considered (dimers and tetramers are 0.5 nm apart), (b) distance d_{ij} between two adjacent particles, and (c) applied axial strain, for both CsPbBr₂Cl and CsPbBr₃ particles. All energies are in eV computed at PBE/DZVP level of theory.

cores of the NCs become compressed as well (Fig. 6). Strain in lead halide perovskite thin films plays an important role for their optoelectronic properties and application in photovoltaic devices³⁶. Our fluorescence and fluorescence lifetime data in Figs. 1, 2 suggest that this is also the case for lead halide NC supercrystals. A comparison of Fig. 1 with Fig. 4b reveals a strong correlation between the gradual blueshift of the fluorescence peak wavelength and the progressive compression of the supercrystal. We suggest that the shift by up to 20 meV is the result of three, partially competing phenomena: (1) a loss in structural coherence as well as isoorientation of NCs (Fig. 5c, d), (2) a decrease of the interparticle distance (Fig. 4b), and (3) the distortion of the atomic lattices of the NCs (Fig. 6). Our DFT calculations in Fig. 7a suggest that the first effect should be associated with a significant blueshift of the fluorescence due to reduced coupling, consistent with a previous report about the importance of structural coherence for electric transport in supercrystals⁶. While the second effect can only lead to a redshift (Fig. 7b), the third effect is also shown to invoke a blueshift for specific facets or magnitudes of strain (Fig. 7c).

With reference to several studies on CsPbBr₃ NCs which reported a redshifted fluorescence after assembly into

supercrystals, we note that the resultant peak wavelength may further be affected by the concomitant changes in the dielectric environment, aging, miniband formation as well as cooperative emission^{8,9,37–39}. However, most of these observations were made under markedly different conditions, such as low temperature, prolonged exposure to air, or self-assembly at the liquid/gas interface, which may be the reason that they are not a dominating factor in our study.

We note a previous report on the spatially resolved fluorescence of CsPb(I_{0.28}Br_{0.72})₃ NC supercrystals with a similar fluorescence blueshift between the center and the edge²⁶. As a main conclusion, gradual release of I₂ gas under intense laser illumination led to the blueshift since lead bromide perovskites exhibit a larger bandgap than the corresponding lead iodide perovskites. The authors argued that the I₂ loss commenced from the edges towards the center, which would explain the spatial fluorescence variations. In CsPbBr₂Cl however, this mechanism is not easily applicable since the reduction potential of Br[−] is much lower than that of I[−]. In line with this, CsPbBr₃ NC supercrystals without a halide mixture show a similar blueshift, indicating that a change in the mixed halide composition is not required to observe the effects reported here.

The decrease of the fluorescence lifetime in Fig. 2 is also strongly correlated with the gradual compression of the supercrystal towards the edges. Moreover, many supercrystals exhibit particularly decreased lifetime values at the corners, which bears similarities with the anisotropic changes in the lattice spacings in Fig. 4c, highlighting again the correlation between structural and optical properties. We speculate that the increased atomic lattice distortion and loss of structural coherence near the edges of the supercrystals result in a reduced stability of the excited state of the emitting NCs. This view is supported by the decreased radiative lifetime values from these locations as well as previous reports on the fluorescence lifetime at grain boundaries of large organic-inorganic perovskites^{40,41}. In view of the currently pursued application of lead halide NC supercrystals as superfluorescent emitters^{8,10}, this would imply that bright and coherent emission originates from the center of the supercrystals as long as they are freshly prepared. Conversely, for aged CsPbBr₂Cl NC supercrystals, the lifetimes are longest at the edges, which points to an increased stability of the excited state, potentially due to the formation of a protective oxide shell⁴².

As an alternative explanation for the spatial differences in the fluorescence (-lifetime) in the supercrystals, we also consider a photon propagation effect, that is, multiple emission and (re-) absorption events, which become more likely with increasing thickness of the emitter material³⁷. Therefore, reabsorption should occur predominantly in the center of the supercrystals but not at the edges. This effect results in an overall redshift of the fluorescence and an increase of the fluorescence lifetime, which would be in line with the observations in this work^{43,44}. Moreover, we would expect the absolute fluorescence intensity per emitter to be lower for an area with frequent reabsorption events and the time-resolved fluorescence decay to be increasingly multiexponential due to the non-radiative losses and multi-step nature of the photon propagation effect. However, we find the fluorescence decay to be monoexponential (Supplementary Figs. 2c, 3c) and the fluorescence intensity to be highest in the center, from where it gradually decreases toward the edges (Supplementary Figs. 6b, 7b). This decrease extends over a much larger distance than the flattening of the edges which we occasionally observe on less faceted supercrystals (Supplementary Fig. 9c), such that the high fluorescence intensity in the center cannot be a mere thickness effect. We note that we would expect a negative correlation between the fluorescence intensity with its corresponding lifetime if reabsorption was dominant in the supercrystals, but we do not find such a correlation in our data (Supplementary Figs. 6f, 7f). In summary, given the relatively high fluorescence quantum yield of lead halide perovskite NCs, reabsorption is likely to partially contribute to the spatially varying optical properties of supercrystals thereof⁴⁵, but our data is inconsistent with it as the dominant cause.

In conclusion, supercrystals of lead halide perovskite NCs self-assembled from solution exhibit a loss in structural coherence, an increasing atomic misalignment between adjacent NCs, and compressive strain near their surfaces. These structural distortions are strongly correlated with a blueshifted fluorescence and decreased radiative lifetimes. We note that structural distortion and surface defects have been shown to strongly affect the fluorescence properties in atomic crystals, such as transition metal dichalcogenides^{13–17}. The structure-fluorescence correlations in supercrystals revealed here are thus another example for the analogy between atoms and NCs as so-called quasi-atoms.

Methods

Chemicals. 1-Octadecene (ODE), technical grade, 90%, Sigma Aldrich; Oleic acid (OA), 97%, Acros Organics; Oleylamine (OAm), 80–90%, Acros Organics; Cesium

carbonate (Cs₂CO₃), 99.99% (trace metal basis), Acros Organics; Lead(II)chloride (PbCl₂), 99.999% (trace metal basis), Sigma Aldrich; Lead(II)bromide (PbBr₂), ≥98%, Sigma Aldrich; Toluene, 99.8%, extra dry, AcroSeal, Acros; Tetrachloroethylene (TCE), ≥99%, Acros Organics; Kapton® polyimide membranes (125 μm thickness) were purchased from DuPont; Si/SiO_x wafers (200 nm SiO_x thickness) were purchased from Siebert Wafer GmbH. All chemicals were used as purchased.

Preparation of Cs-oleate. 203.5 mg Cs₂CO₃ (0.625 mmol) was loaded into a 25 mL three-neck flask along with 10 mL 1-octadecene and 0.625 mL oleic acid, dried for 1 h at 120 °C and then heated to 150 °C under nitrogen atmosphere until all Cs₂CO₃ reacted with oleic acid. The mixture was kept in a glovebox and heated to 110 °C before injection.

Synthesis of CsPbX₃ nanocrystals. CsPbX₃ NCs were made by a hot-injection synthesis using a modified literature method⁴⁶. To synthesize 9 nm CsPbBr₃ or 7 nm CsPbBr₂Cl NCs, 138 mg (0.38 mmol) PbBr₂ or 92 mg (0.25 mmol) PbBr₂ and 35 mg (0.125 mmol) PbCl₂ were degassed in 10 mL ODE in a 25 mL three-neck flask under reduced pressure at 120 °C for 2 h. Then, 1 mL of dried oleylamine (OAm) and 0.5 mL of dried oleic acid (OA) were injected at 120 °C under nitrogen atmosphere with continuous stirring and the reaction mixture was heated to 160 °C. After the solubilization was completed, 0.8 mL of a previously prepared solution of Cs-oleate in ODE (0.125 M) was swiftly injected, and the reaction mixture was cooled to room temperature using an ice-bath.

Isolation and purification of CsPbX₃ nanocrystals. CsPbX₃ NCs were collected by centrifuging the suspension (4650 g, 10 min), decanting the supernatant, and collecting the precipitate. The precipitate was centrifuged again without addition of a solvent (4650 g, 5 min), and the resulting supernatant was removed with a syringe, to separate the traces of residual supernatant. The precipitate was dissolved in 2 mL hexane and centrifuged again (590 g, 5 min) to remove aggregates and larger particles. The resulting supernatant was filtered through a 0.2 μm PTFE syringe filter and stored as stock solution inside of a glovebox with a typically concentration of 16 mM following Maes et al.⁴⁷.

Self-assembly of NC superlattices. For the growth of supercrystals, different substrates (Si wafer, Kapton, glass) were used, depending on the desired experiment. The self-assembly experiment was set up in a glass Petri dish (with a 60 mm diameter), for this purpose three substrates each were placed in such a Petri dish together with a PTFE-lid filled with 1 mL tetrachloroethylene. To each of these substrates, 40 μL of a 1–3 mM solution of the perovskites in TCE was added. The lid of the Petri dish was closed, covered with aluminum foil, and allowed to stand for 24 h. After that, the lid was opened and left for another 5 h to dry completely. All self-assembly preparations were performed under inert atmosphere. The more monodisperse the size distribution of the perovskites, the better the resulting superlattices

Spatially resolved optical measurements. All spatially resolved optical measurements were performed using a home-built inverted confocal laser scanning microscope. The measurements were performed on glass substrates utilizing a high numerical aperture oil immersion objective (NA = 1.4) and a 405 nm pulsed diode laser (Picoquant LDH P-C-405) with variable repetition rates (Picoquant PDL 800-D laser driver) as the excitation source. Under these conditions the lateral resolution of the instrument is approximately 200 nm. A single photon avalanche diode (MPD PDM Series) was used in conjunction with the Picoquant HydraHarp 400 as a time-correlated single photon counting system to detect time-resolved fluorescence. Time-resolved data acquisition and analysis was performed using Picoquants SymPhoTime 64 software package. The spectral data was recorded using an Acton Spectra Pro 2300i spectrometer with a 300 grooves/mm grating. The detector temperature (Princeton PIXIS CCD) was kept steady at –45 °C.

X-ray diffraction experiment. The nanodiffraction experiment was performed at the Coherence Applications beamline P10 of the PETRA III synchrotron source at DESY. An X-ray beam with the wavelength $\lambda = 0.0898$ nm ($E = 13.8$ keV) was focused down to a spot size of approximately 400 × 400 nm² (FWHM) with a focal depth of about 0.5 mm at the GINIX nanodiffraction endstation⁴⁸. The two-dimensional detector EIGER X 4 M (Dectris) with 2070 × 2167 pixels and a pixel size of 75 × 75 μm² was positioned 412 mm downstream from the sample. The detector was aligned ~6 cm off-center in both directions normal to the incident beam to allow simultaneous detection of SAXS and WAXS. We performed a spatially resolved scan of the sample on a Kapton substrate by 25 × 25 spatial points with 500 nm step size and collected 625 diffraction patterns in transmission geometry. The exposure time was set to 0.5 s to prevent radiation damage of the sample. The background scattering pattern from a pure Kapton film was subtracted from every collected pattern.

Bragg peak analysis. Each diffraction pattern was interpolated onto a polar coordinate grid with the origin at the direct beam position. The radial profiles were obtained by averaging along the azimuthal coordinate. To extract parameters of the WAXS and SAXS Bragg peaks separately, we fitted each of them by the 2D Gaussian function

$$I(q, \varphi) = \frac{I_0}{2\pi\sigma_q\sigma_\varphi} \exp\left[-\frac{(q - q_0)^2}{2\sigma_q^2} - \frac{(\varphi - \varphi_0)^2}{2\sigma_\varphi^2}\right],$$

where I_0 is the integrated intensity, q_0 and φ_0 are the radial and azimuthal central positions, and σ_q and σ_φ are the corresponding root mean square (rms) values. The FWHMs of the Bragg peaks were evaluated according to relations: $w_q = 2\sqrt{2\ln 2}\sigma_q$ and $w_\varphi = 2\sqrt{2\ln 2}\sigma_\varphi$. The fitting was done in the appropriate region of the polar coordinates with a single isolated Bragg peak.

For the SAXS peaks, the parameters were pairwise averaged for the corresponding Friedel pairs of the Bragg peaks to improve statistics. The resulting momentum transfer values and angles were used to calculate the real-space parameters of the unit cell: the length of the basis vectors a_1 and a_2 , the angle γ between them and the average azimuthal position φ counted counterclockwise from an arbitrary horizontal axis (see Supplementary Materials for details).

For the WAXS peaks, we calculated an average Bragg peak intensity I_{AL} and the azimuthal position ψ of the $[010]_{AL}$ axis. To obtain the average azimuthal position ψ , we averaged all four azimuthal positions for 010_{AL} , 020_{AL} , 110_{AL} , and $\bar{1}00_{AL}$ Bragg peaks, but corrected the last two values by $+45^\circ$ and -45° , respectively. We used the Williamson–Hall method⁴⁹ to analyze the size of the WAXS Bragg peaks at each spatial point of the supercrystal. The FWHM of the Bragg peak is determined by the NC size and the lattice distortion as follows:

$$w_{q,\varphi}^2(q) = \left(\frac{2\pi K}{L}\right)^2 + (g_{q,\varphi}q)^2, \quad (1)$$

where $w_{q,\varphi}$ is the FWHM of the Bragg peak at q in radial or azimuthal direction, respectively, L is the NC size, $g_{q,\varphi}$ is the radial or angular lattice distortion of the atomic lattice, respectively, K is a dimensionless shape parameter that is about 0.86 for cubic NCs⁵⁰. The radial lattice distortion g_q calculated from the radial FWHM w_q is equal to the ratio $\delta a_{AL}/a_{AL}$, where δa_{AL} is the FWHM of the unit cell parameter distribution around the mean value a_{AL} . The angular lattice distortion g_φ calculated from the azimuthal FWHM w_φ is equal to the FWHM $\delta\psi$ of the angular distribution of the NCs around their average azimuthal position ψ . For the spatially resolved analysis of the FWHMs, the NC size L was fixed at the value, obtained from the average radial profiles. For details of the analysis, see Supplementary materials.

Scanning electron and atomic force microscopy. SEM imaging of supercrystals on Si/SiO_x devices was performed with a HITACHI model SU8030 at 30 kV. To estimate the thickness of micro-crystals, samples were tilted by 45° with respect to the incoming electron beam. AFM investigations were conducted with a Bruker MultiMode 8 HR in contact mode.

Density functional theory calculations. All computations are performed using the CP2K 5.1 program suite using the Quickstep module⁵¹. The PBE exchange correlation functional⁵², a dual basis of localized Gaussians and plane waves (GPW)⁵³ with a 350 Ry plane-wave cutoff, double- ζ basis-set augmented with polarization functions (MOLOPT variant)⁵⁴, and GTH pseudopotentials⁵⁵ for core electrons are used for all calculations. The van der Waals (VDW) interaction was accounted for by employing Grimme's DFT-D3 method⁵⁶. SCF convergence criterion was set at 10^{-6} for all calculations.

Initial geometries of CsPbX₃ ($X = \text{Cl}, \text{Br}$) nanocrystals were obtained by cutting small cubes (~ 2.4 nm) from the bulk, exposing the CsX layer at the surface and maintaining overall charge neutrality of the particle⁵⁷. All structures were then optimized in vacuum using the BFGS optimizer imposing non-periodic boundary conditions with a wavelet Poisson solver⁵⁸, setting a maximum force of $5 \text{ meV} \cdot \text{\AA}^{-1}$ (10^{-4} hartree/bohr) as convergence criteria. For the obtained cartesian coordinates, see Supplementary Data 1. For these non-periodic systems, axial strain was simulated by fixing the length of one side of the cube. If the relaxed cubic nanocrystal has side length $a \times b \times c$, and stress is to be applied along the z -direction, " c " is fixed at some c' by constraining the z coordinates of both the top and bottom surface-atoms along the z -direction, with all other coordinates of all atoms relaxed. % Strain is reported as $(c' - c)/c \times 100\%$. For calculations involving dimers and tetramers, 2/4 monomers were explicitly considered, but periodic boundary condition was imposed with at least 10 \AA vacuum above the surface of the nanocluster to avoid spurious interaction with its periodic image.

Data availability

The X-ray and optical data that support the findings of this study are available in Zenodo.org at <https://zenodo.org/record/5607366>⁵⁹.

Received: 14 September 2021; Accepted: 14 January 2022;

Published online: 16 February 2022

References

- Toso, S. et al. Multilayer diffraction reveals that colloidal superlattices approach the structural perfection of single crystals. *ACS Nano* **15**, 6243–6256 (2021).
- Ye, X. et al. Quasicrystalline nanocrystal superlattice with partial matching rules. *Nat. Mater.* **16**, 214–219 (2017).
- Goubet, N. & Pileni, M. P. Analogy between atoms in a nanocrystal and nanocrystals in a supracrystal: is it real or just a highly probable speculation? *J. Phys. Chem. Lett.* **2**, 1024–1031 (2011).
- Cargnello, M. et al. Substitutional doping in nanocrystal superlattices. *Nature* **524**, 450–453 (2015).
- Dreyer, A. et al. Organically linked iron oxide nanoparticle supercrystals with exceptional isotropic mechanical properties. *Nat. Mater.* **15**, 522–528 (2016).
- Fetzer, F. et al. Structural order enhances charge carrier transport in self-assembled Au-nanoclusters. *Nat. Commun.* **11**, 6188 (2020).
- Yazdani, N. et al. Nanocrystal superlattices as phonon-engineered solids and acoustic metamaterials. *Nat. Commun.* **10**, 4236 (2019).
- Rainò, G. et al. Superfluorescence from lead halide perovskite quantum dot superlattices. *Nature* **563**, 671–675 (2018).
- Tong, Y. et al. Spontaneous self-assembly of perovskite nanocrystals into electronically coupled supercrystals: toward filling the green gap. *Adv. Mater.* **30**, 1801117 (2018).
- Cherniukh, I. et al. Perovskite-type superlattices from lead halide perovskite nanocubes. *Nature* **593**, 535–542 (2021).
- Hoffmann, R. Small but strong lessons from chemistry for nanoscience. *Angew. Chem. Int. Ed.* **52**, 93–103 (2013).
- Somorjai, G. A. & Li, Y. *Introduction to Surface Chemistry and Catalysis*. 2nd edn. (Wiley, 2010).
- Kastl, C. et al. Effects of defects on band structure and excitons in WS₂ revealed by nanoscale photoemission spectroscopy. *ACS Nano* **13**, 1284–1291 (2019).
- Jeong, H. Y. et al. Heterogeneous defect domains in single-crystalline hexagonal WS₂. *Adv. Mater.* **29**, 1605043 (2017).
- Gutiérrez, H. R. et al. Extraordinary room-temperature photoluminescence in triangular WS₂ monolayers. *Nano. Lett.* **13**, 3447–3454 (2013).
- Kim, M. S. et al. Biexciton emission from edges and grain boundaries of triangular WS₂ monolayers. *ACS Nano* **10**, 2399–2405 (2016).
- Rosenberger, M. R., Chuang, H.-J., McCreary, K. M., Li, C. H. & Jonker, B. T. Electrical characterization of discrete defects and impact of defect density on photoluminescence in monolayer WS₂. *ACS Nano* **12**, 1793–1800 (2018).
- Ding, H., Dong, Y., Li, S., Pan, N. & Wang, X. Edge optical scattering of two-dimensional materials. *Opt. Express* **26**, 7797–7810 (2018).
- Ren, D.-D. et al. Photoluminescence inhomogeneity and excitons in CVD-grown monolayer WS₂. *Opt. Mater.* **80**, 203–208 (2018).
- Bohnet, J. G. et al. A steady-state superradiant laser with less than one intracavity photon. *Nature* **484**, 78–81 (2012).
- Higgins, K. D. B. et al. Superabsorption of light via quantum engineering. *Nat. Commun.* **5**, 4705 (2014).
- Mattiotti, F., Kuno, M., Borgonovi, F., Jankó, B. & Celardo, G. L. Thermal decoherence of superradiance in lead halide perovskite nanocrystal superlattices. *Nano Lett.* **20**, 7382–7388 (2020).
- Krieg, F. et al. Monodisperse long-chain sulfobetaine-capped CsPbBr₃ nanocrystals and their superfluorescent assemblies. *ACS Cent. Sci.* **7**, 135–144 (2021).
- Toso, S., Baranov, D., Giannini, C., Marras, S. & Manna, L. Wide-angle x-ray diffraction evidence of structural coherence in CsPbBr₃ nanocrystal superlattices. *ACS Mater. Lett.* **1**, 272–276 (2019).
- van der Burgt, J. S. et al. Cuboidal supraparticles self-assembled from cubic CsPbBr₃ perovskite nanocrystals. *J. Phys. Chem. C* **122**, 15706–15712 (2018).
- Brennan, M. C. et al. Superlattices are greener on the other side: how light transforms self-assembled mixed halide perovskite nanocrystals. *ACS Energy Lett.* **5**, 1465–1473 (2020).
- Zaluzhnyy, I. A. et al. Quantifying angular correlations between the atomic lattice and the superlattice of nanocrystals assembled with directional linking. *Nano Lett.* **17**, 3511–3517 (2017).
- Mukharamova, N. et al. Revealing grain boundaries and defect formation in nanocrystal superlattices by nanodiffraction. *Small* **15**, 1904954 (2019).
- Maier, A. et al. Structure-transport correlation reveals anisotropic charge transport in coupled PbS nanocrystal superlattices. *Adv. Mater.* **32**, 200225 (2020).
- Zhang, M. et al. Growth and characterization of all-inorganic lead halide perovskite semiconductor CsPbBr₃ single crystals. *CrystEngComm* **19**, 6797–6803 (2017).
- Swarnkar, A. et al. Colloidal CsPbBr₃ perovskite nanocrystals: luminescence beyond traditional quantum dots. *Angew. Chem.* **127**, 15644–15648 (2015).
- Liashenko, T. G. et al. Electronic structure of CsPbBr_{3-x}Cl_x perovskites: synthesis, experimental characterization, and DFT simulations. *Phys. Chem. Chem. Phys.* **21**, 18930–18938 (2019).

33. Kapuscinski, M. et al. Temporal evolution of superlattice contraction and defect-induced strain anisotropy in mesocrystals during nanocube self-assembly. *ACS Nano* **14**, 5337–5347 (2020).
34. van der Kooij, H. M., van de Kerkhof, G. T. & Sprakel, J. A mechanistic view of drying suspension droplets. *Soft Matter* **12**, 2858–2867 (2016).
35. Leineweber, A. Understanding anisotropic microstrain broadening in Rietveld refinement. *Z. Kristallogr. Cryst. Mater.* **226**, 905–923 (2011).
36. Xue, D.-J. et al. Regulating strain in perovskite thin films through charge-transport layers. *Nat. Commun.* **11**, 1514 (2020).
37. Baranov, D., Toso, S., Imran, M. & Manna, L. Investigation into the photoluminescence red shift in cesium lead bromide nanocrystal superlattices. *J. Phys. Chem. Lett.* **10**, 655–660 (2019).
38. Baranov, D. et al. Aging of self-assembled lead halide perovskite nanocrystal superlattices: effects on photoluminescence and energy transfer. *ACS Nano* **15**, 650–664 (2021).
39. Tang, Y. et al. Highly stable perovskite supercrystals via oil-in-oil templating. *Nano Lett.* **20**, 5997–6004 (2020).
40. Stavrakas, C. et al. Probing buried recombination pathways in perovskite structures using 3D photoluminescence tomography. *Energy Environ. Sci.* **11**, 2846–2852 (2018). [10.1039](https://doi.org/10.1039/c8ee01039a).
41. de Quilletes Dane, W. et al. Impact of microstructure on local carrier lifetime in perovskite solar cells. *Science* **348**, 683–686 (2015).
42. Wang, Y. et al. Mechanism of strong luminescence photoactivation of citrate-stabilized water-soluble nanoparticles with CdSe cores. *J. Phys. Chem. B* **108**, 15461–15469 (2004).
43. Asbeck, P. Self-absorption effects on the radiative lifetime in GaAs-GaAlAs double heterostructures. *J. Appl. Phys.* **48**, 820–822 (1977).
44. Fang, Y., Wei, H., Dong, Q. & Huang, J. Quantification of re-absorption and re-emission processes to determine photon recycling efficiency in perovskite single crystals. *Nat. Commun.* **8**, 14417 (2017).
45. Pazos-Outón, L. M. et al. Photon recycling in lead iodide perovskite solar cells. *Science* **351**, 1430–1433 (2016).
46. Protesescu, L. et al. Nanocrystals of cesium lead halide perovskites (CsPbX₃, X = Cl, Br, and I): Novel optoelectronic materials showing bright emission with wide color gamut. *Nano Lett.* **15**, 3692–3696 (2015).
47. Maes, J. et al. Light absorption coefficient of CsPbBr₃ perovskite nanocrystals. *J. Phys. Chem. Lett.* **9**, 3093–3097 (2018).
48. Kalbfleisch, S. et al. The Göttingen holography endstation of beamline P10 at PETRA III/DESY. *AIP Conf. Proc.* **1365**, 96–99 (2011).
49. Williamson, G. K. & Hall, W. H. X-ray line broadening from filed aluminium and wolfram. *Acta Metall. Mater.* **1**, 22–31 (1953).
50. Langford, J. I. & Wilson, A. J. C. Scherrer after sixty years: a survey and some new results in the determination of crystallite size. *J. Appl. Cryst.* **11**, 102–113 (1978).
51. Kühne, T. D. et al. CP2K: An electronic structure and molecular dynamics software package—Quickstep: Efficient and accurate electronic structure calculations. *J. Chem. Phys.* **152**, 194103 (2020).
52. Perdew, J. P., Burke, K. & Ernzerhof, M. Generalized gradient approximation made simple. *Phys. Rev. Lett.* **77**, 3865–3868 (1996).
53. Lippert, B., Hutter, J. & Parrinello, M. A hybrid Gaussian and plane wave density functional scheme. *Mol. Phys.* **92**, 477–488 (1997).
54. VandeVondele, J. & Hutter, J. Gaussian basis sets for accurate calculations on molecular systems in gas and condensed phases. *J. Chem. Phys.* **127**, 114105 (2007).
55. Krack, M. Pseudopotentials for H to Kr optimized for gradient-corrected exchange-correlation functionals. *Theor. Chem. Acc.* **114**, 145–152 (2005).
56. Grimme, S., Antony, J., Ehrlich, S. & Krieg, H. A consistent and accurate ab initio parametrization of density functional dispersion correction (DFT-D) for the 94 elements H-Pu. *J. Chem. Phys.* **132**, 154104 (2010).
57. ten Brinck, S. & Infante, I. Surface termination, morphology, and bright photoluminescence of cesium lead halide perovskite nanocrystals. *ACS Energy Lett.* **1**, 1266–1272 (2016).
58. Genovese, L., Deutsch, T., Neelov, A., Goedecker, S. & Beylkin, G. Efficient solution of Poisson's equation with free boundary conditions. *J. Chem. Phys.* **125**, 74105 (2006).
59. Lapkin, D. et al. Spatially resolved fluorescence of caesium lead halide perovskite supercrystals reveals quasi-atomic behavior of nanocrystals. Zenodo repository. <https://doi.org/10.5281/zenodo.5607366> (2021).

Acknowledgements

The authors acknowledge DESY (Hamburg, Germany) for the provision of experimental facilities. Parts of this research were carried out at PETRA III synchrotron facility and we would like to thank the beamline staff for assistance in using the Coherence Application P10 beamline. This work was supported by the DFG under grants SCHE1905/8-1(M.S.), SCHE1905/9-1(M.S.), AN680/6-1(D.A.) and SCHR700/38-1(F.S.) as well as the Carl Zeiss Stiftung (Forschungsstrukturkonzept “Interdisziplinäres nanoBCP-Lab”). D.L., D.As., N.M., Y.Y.K. and I.A.V. acknowledge the support of the Helmholtz Associations Initiative Networking Fund (grant No. HRSF-0002) and the Russian Science Foundation (grant No. 18-41-06001). I.A.V. acknowledges the financial support of the Russian Federation represented by the Ministry of Science and Higher Education of the Russian Federation (Agreement No. 075-15-2021-1352). D.L., N.M., D.As., Y.Y.K., M.Sp., and I.A.V. acknowledge support of the project by Edgar Weckert.

Author contributions

D.L., C.K., and J.H. contributed equally to this work. D.L., D.As., J.C., Y.Y.K., N.M., I.Z., and M.Sp. performed the X-ray scattering experiments. C.K., S.W., and J.W. synthesized the NCs, conducted optical absorption and fluorescence measurements in solution and prepared all samples. J.H. carried out the confocal fluorescence (lifetime) measurements. M.M. performed DFT calculations and A.M. undertook the SEM and AFM measurements. F.S., A.J.M., K.B., D.A., I.A.V., and M.S. conceived and supervised the project. D.L., J.H., M.M., I.A.V., and M.S. wrote the manuscript with input from all authors. All authors have given approval to the final version of the manuscript.

Competing interests

The authors declare no competing interests.

Additional information

Supplementary information The online version contains supplementary material available at <https://doi.org/10.1038/s41467-022-28486-3>.

Correspondence and requests for materials should be addressed to Marcus Scheele or Ivan A. Vartanyants.

Peer review information *Nature Communications* thanks Stefano Bellucci, Ou Chen and the other, anonymous, reviewer(s) for their contribution to the peer review of this work.

Reprints and permission information is available at <http://www.nature.com/reprints>

Publisher's note Springer Nature remains neutral with regard to jurisdictional claims in published maps and institutional affiliations.



Open Access This article is licensed under a Creative Commons Attribution 4.0 International License, which permits use, sharing, adaptation, distribution and reproduction in any medium or format, as long as you give appropriate credit to the original author(s) and the source, provide a link to the Creative Commons license, and indicate if changes were made. The images or other third party material in this article are included in the article's Creative Commons license, unless indicated otherwise in a credit line to the material. If material is not included in the article's Creative Commons license and your intended use is not permitted by statutory regulation or exceeds the permitted use, you will need to obtain permission directly from the copyright holder. To view a copy of this license, visit <http://creativecommons.org/licenses/by/4.0/>.

© The Author(s) 2022

3.2 Angular X-ray cross-correlation analysis applied to the scattering data in 3D reciprocal space

In the fourth paper, the theoretical generalization of the AXCCA technique for application to the intensity distribution measured in 3D reciprocal space from a single crystalline sample is given. The application of the technique is demonstrated on an example of the intensity distribution measured for a colloidal crystal composed of silica spheres.

I personally proposed the idea of such generalization, implemented it in practice and applied it to a dataset measured before. Most of the manuscript was written by me with the contributions of other co-authors.

The fifth paper is focused on a structural study of a single mesocrystalline grain consisting of gold nanocubes. The electron density inside the grain was reconstructed by phase retrieval algorithms from the measured scattered X-ray intensity distribution in 3D reciprocal space. The average SL structure was revealed by means of AXCCA that showed the structure to be different from the expected simple cubic. The combination of these techniques allowed extraction of the strain tensor at different spatial points of the sample with high resolution. Analysis of the anisotropic form factor of the nanocubes allowed the determination of the angular orientation of the nanocubes inside the SL.

I personally analysed the measured intensities in 3D reciprocal space by AXCCA and interpreted the results. Felizitas Kiener prepared the sample. Jerome Carnis took part in the X-ray experiment and performed the CDI reconstruction of the measured dataset. Sebastian Sturm analyzed the strain distribution in the structure revealed by the CDI reconstruction. The part of the manuscript on the results of AXCCA and the form factor analysis was written by me with the contributions of other co-authors.

The Supplementary Materials for this paper can be found at: <https://doi.org/10.1039/d1nr01806j>

The sixth paper represents a systematic structural study of mesocrystals consisting of gold nanocubes with different sizes self-assembled from different solvents. A part of this work included structural investigation of single mesocrystalline grains formed from different solvents. Using AXCCA, the structure was found to deviate from the expected face-centered cubic one to varying degrees depending on the type of solvent.

I personally analysed the measured intensities in 3D reciprocal space by AXCCA and interpreted the results. The part of the manuscript on the results of AXCCA was written by me with the contributions from other co-authors.

The Supplementary Materials for this paper can be found at: <https://doi.org/10.1021/acs.chemmater.1c01941>



Angular X-ray cross-correlation analysis applied to the scattering data in 3D reciprocal space from a single crystal

Dmitry Lapkin,^a Anatoly Shabalin,^a Janne-Mieke Meijer,^b Ruslan Kurta,^c Michael Sprung,^a Andrei V. Petukhov^{d,e} and Ivan A. Vartanyants^{a*}

Received 22 February 2022

Accepted 20 April 2022

Edited by M. Takata, SPring-8, Japan

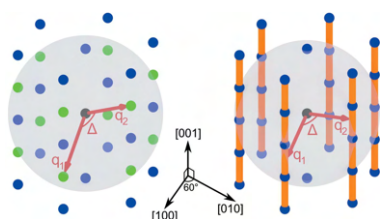
Keywords: X-ray scattering; X-ray cross-correlation analysis; structure determination; crystalline defects.

^aDeutsches Elektronen-Synchrotron (DESY), Notkestrasse 85, 22607 Hamburg, Germany, ^bDepartment of Applied Physics and Institute for Complex Molecular Systems, Eindhoven University of Technology, Eindhoven 5600 MB, The Netherlands, ^cEuropean XFEL, Holzkoppel 4, 22869 Schenefeld, Germany, ^dDebye Institute for Nanomaterials Science, Utrecht University, Utrecht 3584 CS, The Netherlands, and ^eLaboratory of Physical Chemistry, Eindhoven University of Technology, Eindhoven 5612 AZ, The Netherlands. *Correspondence e-mail: ivan.vartanyants@desy.de

An application of angular X-ray cross-correlation analysis (AXCCA) to the scattered intensity distribution measured in 3D reciprocal space from a single-crystalline sample is proposed in this work. Contrary to the conventional application of AXCCA, when averaging over many 2D diffraction patterns collected from different randomly oriented samples is required, the proposed approach provides an insight into the structure of a single specimen. This is particularly useful in studies of defect-rich samples that are unlikely to have the same structure. The application of the method is shown on an example of a qualitative structure determination of a colloidal crystal from simulated as well as experimentally measured 3D scattered intensity distributions.

1. Introduction

The first approaches to study the structure of materials by means of angular correlations in the scattered intensities go back to the late 70s to early 80s (Kam, 1977, 1980; Clark *et al.*, 1983). It was proposed by Kam (1977) to reveal the structure of macromolecules by analyzing the angular correlations in the scattering patterns from randomly oriented molecules in solution. In other research, correlations of scattered laser intensities from colloidal glass were found to be related to its local structure (Clark *et al.*, 1983). At that time, the method did not undergo further development due to the lack of suitable instrumentation (Kam *et al.*, 1981). Recently, however, it has become of great interest after the work of Wochner *et al.* (2009), where angular X-ray cross-correlation analysis (AXCCA) was applied to study the structure of colloidal glasses by means of X-ray scattering. The renewed interest to AXCCA was triggered by the development of modern X-ray sources such as third- and fourth-generation synchrotrons (Schroer, 2019) and novel X-ray free-electron lasers (XFELs) (Emma *et al.*, 2010; Ishikawa *et al.*, 2012; Kang *et al.*, 2017; Decking *et al.*, 2020) that provide an X-ray beam with outstanding characteristics including high brilliance, ultimate coherence and femtosecond pulse durations. These characteristics allow the measure of fluctuations in the scattering patterns containing information about the local structure that could be revealed by AXCCA. The emergence of suitable equipment has led, among practical applications, to the development of the underlying theory (Saldin *et al.*, 2010,



OPEN ACCESS

Published under a CC BY 4.0 licence

2011; Altarelli *et al.*, 2010; Kirian, 2012; Kurta *et al.*, 2016; Martin, 2017).

The practical applications of AXCCA are defined by the investigated sample and geometry of a typical X-ray scattering experiment. In such experiments, the scattered intensities are measured by a 2D detector that represents a cut of reciprocal space by the Ewald sphere. AXCCA applied to such 2D patterns reveals symmetries of the sample in the plane orthogonal to the incident beam. This is particularly suitable in studies of (quasi-)2D samples such as 2D nanostructures (Kurta *et al.*, 2013, 2012; Pedrini *et al.*, 2013), thin polymer films (Kurta *et al.*, 2015; Lehmkuhler *et al.*, 2018; Schulz *et al.*, 2020) and liquid crystals (Zaluzhnyy *et al.*, 2015, 2019; Zaluzhnyy, Kurta, Sulyanova *et al.*, 2017). In some cases, it is possible to refine the unit-cell parameters of 3D superlattices of nanocrystals (Zaluzhnyy, Kurta, André *et al.*, 2017; Mukharamova *et al.*, 2019; Lokteva *et al.*, 2019; Maier *et al.*, 2020).

To explore the symmetries of a 3D sample, one typically collects many 2D patterns from randomly oriented identical samples, for example, injected bioparticles (Kurta *et al.*, 2017; Pande *et al.*, 2018) or nanocrystals (Mendez *et al.*, 2016; Niozu *et al.*, 2020; Ayyer *et al.*, 2021) as shown in Fig. 1(a). To achieve reasonable scattered intensities from a small single sample, extremely high flux of the incident X-ray beam is required that can be provided by modern XFELs. The diffraction patterns collected in such an experiment represent random cuts of reciprocal space as shown in Fig. 1(b) that can be assembled into the intensity distribution in 3D reciprocal space. The main assumption of this approach is the reproducibility of the measured samples. If the measured samples are different, the revealed structure is averaged over many realizations.

At modern third-generation synchrotron sources, we can exploit their high coherence to study the sample structure by

coherent diffraction imaging (CDI). In this technique, the 3D electron density of the sample in real space is reconstructed by a phase retrieval algorithm from the scattered intensity distribution measured in whole reciprocal space (Shabalin *et al.*, 2016; Carnis *et al.*, 2021). This may be achieved by the angular scan of the sample with a large unit cell in small-angle X-ray scattering (SAXS) geometry as shown in Figs. 1(c)–1(e). Although such a reconstruction provides full information about the structure, the method is highly demanding in terms of experimental requirements and data quality. AXCCA is based on the analysis of angular correlations of scattered intensities in reciprocal space and can be applied to datasets of much lower quality, for which the phase retrieval algorithms fail, to reveal the structural features averaged over the sample without the need to perform a reconstruction (Schlotheuber né Brunner *et al.*, 2021).

In this work, we propose employment of AXCCA to study symmetries of the intensity distribution in 3D reciprocal space from a single-crystalline sample. We apply this method to simulated datasets for model colloidal structures and propose a geometrical model to interpret the results. As an example of practical application, we employ the dataset collected for a CDI reconstruction of a colloidal crystal grain (Shabalin *et al.*, 2016; Meijer *et al.*, 2014). We show that the developed method provides qualitative information about the real space structure without performing a complex iterative phase retrieval.

2. Theory

2.1. AXCCA applied to the intensity distribution in 3D reciprocal space

Here, we consider the scattered intensity distribution measured by a 2D detector. The conventional AXCCA is based on the analysis of a two-point cross-correlation function (CCF) defined as (Niozu *et al.*, 2020)

$$C(q_1, q_2, \Delta) = \left\langle \tilde{I}(\mathbf{q}_1) \tilde{I}(\mathbf{q}_2) \delta \left(\frac{\mathbf{q}_1 \mathbf{q}_2}{\|\mathbf{q}_1\| \|\mathbf{q}_2\|} - \cos \Delta \right) \right\rangle, \quad (1)$$

where $\tilde{I}(\mathbf{q}_1)$ and $\tilde{I}(\mathbf{q}_2)$ are the scattered intensities measured by the detector at the points corresponding to the momentum transfer vectors \mathbf{q}_1 and \mathbf{q}_2 with the relative angle Δ between them. The averaging is performed over all positions corresponding to \mathbf{q}_1 and \mathbf{q}_2 with the lengths $q_1 = \|\mathbf{q}_1\|$ and $q_2 = \|\mathbf{q}_2\|$, respectively. The intensities can be scaled to their mean values, for example, as

$$\tilde{I}(\mathbf{q}_i) = \frac{I(\mathbf{q}_i) - \langle I(\mathbf{q}_i) \rangle}{\langle I(\mathbf{q}_i) \rangle}, \quad i = 1, 2, \quad (2)$$

where averaging is performed over all measured intensities corresponding to the momentum transfer vectors \mathbf{q}_i with a certain length $q_i = \|\mathbf{q}_i\|$.

When the measurements are performed in the SAXS geometry corresponding to small momentum transfer vectors, one can neglect the curvature of the Ewald sphere. Then, the definition in equation (1) simplifies to

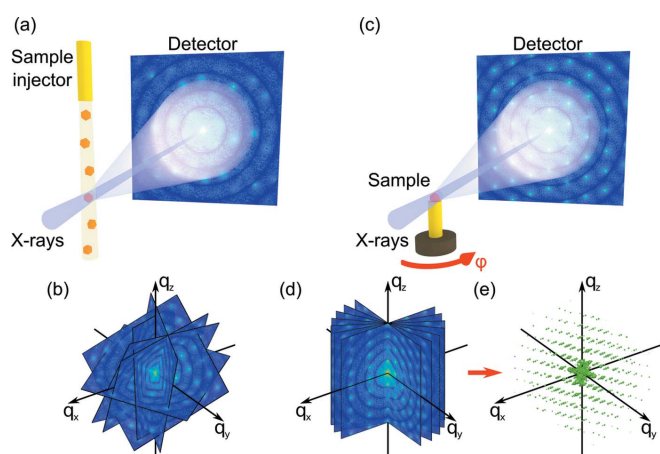


Figure 1
(a) Scheme of the experimental setup for measuring 2D diffraction patterns from different randomly oriented samples injected into the incident X-ray beam. The patterns collected represent random cuts of 3D reciprocal space as shown in (b). (c) Scheme of the experimental setup for measuring 2D diffraction patterns from a single sample rotated around an axis normal to the incident beam. (d) 2D patterns of known orientation can be further interpolated into 3D intensity distribution (e).

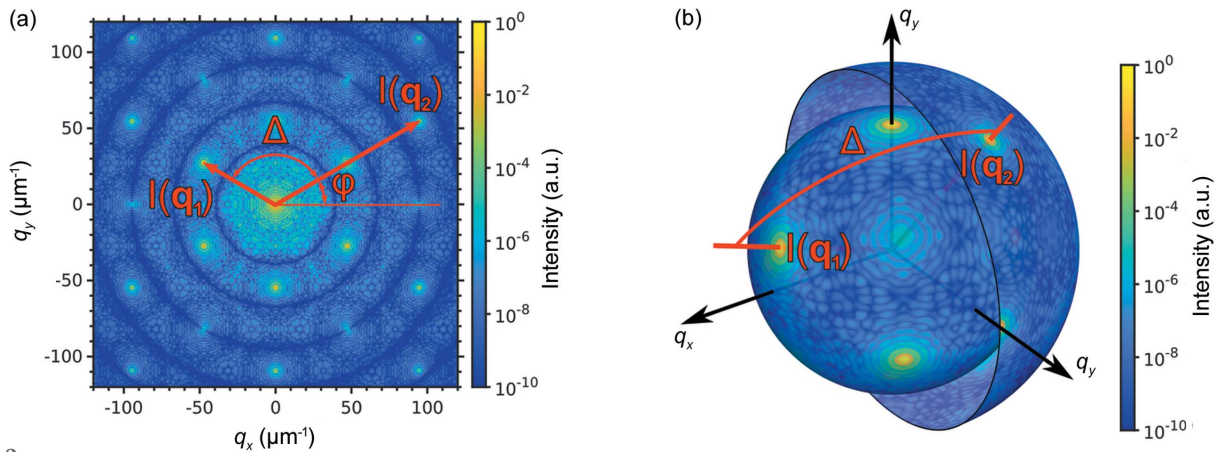


Figure 2

Scheme of the CCF calculation in the case of 2D (a) and 3D (b) intensity distributions. The product of intensities at two points \mathbf{q}_1 and \mathbf{q}_2 in reciprocal space, separated by the angle Δ , contribute into the CCF value at this Δ value. The final CCF is obtained by averaging over all points on the rings/spheres of the corresponding radii. The color code exemplarily represents the simulated intensities for a colloidal crystal with an f.c.c. structure: (a) 2D diffraction pattern from the colloidal crystal oriented along the $[001]_{f.c.c.}$ axis with respect to the incident X-ray beam and (b) intensities at the spheres in 3D reciprocal space of the colloidal crystal with the radii q_1 and q_2 , corresponding to the 111 and 220 reflections, respectively.

$$C(q_1, q_2, \Delta) = \langle \tilde{I}(q_1, \varphi) \tilde{I}(q_2, \varphi + \Delta) \rangle_{\varphi}, \quad (3)$$

where $\tilde{I}(q, \varphi)$ is the scattered intensity measured by a detector at the position $\mathbf{q} = (q, \varphi)$, here q, φ are the polar coordinates, and $\langle \dots \rangle_{\varphi}$ denotes averaging over all angles of φ . The variables used in the definition of CCF in equation (3) are shown in Fig. 2(a).

Typically, the CCFs are averaged over many 2D diffraction patterns collected from different realizations of the system (at different positions of the sample, at different times or from different randomly oriented injected particles). Averaging over many different system realizations allows suppression of random correlations in the scattered intensities specific to a certain realization of the system. The averaged CCFs represent systematic correlations that correspond specifically to the internal structure of the samples and not to the certain realization of the system. Moreover, averaging over many orientations of the samples allows assessment of the correlations in different cuts of 3D reciprocal space. Thus, the resulting CCFs represent all correlations in 3D reciprocal space and not only in certain planes.

In this work, we propose to apply equation (1) to the scattered intensity distribution in 3D reciprocal space measured for a single sample. In 3D reciprocal space, both momentum transfer vectors \mathbf{q}_1 and \mathbf{q}_2 can take any angular position. The averaging in equation (1) is then performed over spheres in reciprocal space with the radii $q_1 = \|\mathbf{q}_1\|$ and $q_2 = \|\mathbf{q}_2\|$, respectively, as shown in Fig. 2(b). The resulting CCFs in this case contain all present correlations from a single sample without a need to perform averaging over many realizations.

We note that a similar result would originate from averaging over many randomly oriented 2D scattering patterns collected from the same sample (or identical samples). Indeed, each pair of momentum transfer vectors taken in 3D reciprocal space lay in a certain 2D hyperplane that can be thought of as a 2D diffraction pattern. If the number of the randomly oriented 2D patterns is big enough, they cover the whole 3D space and the

CCFs averaged over such a set of 2D patterns are identical to the CCFs calculated for the 3D pattern (Niozu *et al.*, 2020). The number of randomly oriented 2D scattering patterns required to obtain the same information as from the 3D scattered intensity distribution is discussed in Section 3.3.

2.2. CCFs in the case of a crystalline sample

AXCCA was shown to be useful to extract additional information from the scattering patterns of crystalline samples (Mendez *et al.*, 2016; Niozu *et al.*, 2020). In this case, the scattered intensity contains well defined Bragg peaks originating from the crystallographic planes of the sample. When the CCF $C(q_1, q_2, \Delta)$ is calculated at the momentum transfer values q_1 and q_2 corresponding to the Bragg peak positions, it contains correlation peaks at the characteristic relative angles Δ between the Bragg peaks, *i.e.* the reciprocal lattice vectors \mathbf{g}_1 and \mathbf{g}_2 with the lengths $q_1 = \|\mathbf{g}_1\|$ and $q_2 = \|\mathbf{g}_2\|$.

Given a model of a unit cell with the lattice basis vectors $\mathbf{a}_1, \mathbf{a}_2$ and \mathbf{a}_3 , we can calculate the reciprocal basis vectors $\mathbf{b}_1, \mathbf{b}_2$ and \mathbf{b}_3 and thus any reciprocal lattice vector (Kittel, 2004). For a pair of Bragg peaks corresponding to the reciprocal lattice vectors \mathbf{g}_1 and \mathbf{g}_2 , the angle between them can be calculated using the scalar product

$$\mathbf{g}_1 \cdot \mathbf{g}_2 = \|\mathbf{g}_1\| \|\mathbf{g}_2\| \cos(\Delta), \quad (4)$$

where dot indicates a scalar product between two vectors. These Bragg peaks would contribute to the CCF calculated for the momentum transfer values q_1 and q_2 corresponding to the norms of the vectors $q_1 = \|\mathbf{g}_1\|$ and $q_2 = \|\mathbf{g}_2\|$, respectively, at the angle Δ , as shown in Fig. 3(a). Given the lattice parameters and symmetry, one can calculate all positions of the correlation peaks. Details of the calculation are given in Appendix A. Note that, in the case of high lattice symmetry, several pairs of different reciprocal lattice vectors with the same norms may contribute to the CCF at the same relative angle Δ . For example, for a face-centered cubic (f.c.c.) lattice, the pair of Bragg peaks 111 and $1\bar{1}\bar{1}$ as well as the pair 111 and $1\bar{1}1$

contribute to the CCF at the same angle $\Delta = \arccos(1/3) \approx 70.53^\circ$. In such a case, different peaks in the resulting CCFs can have different degeneracy, which is reflected in their relative magnitudes.

Considering close-packed structures, different stacking motifs of hexagonal layers result in different symmetries of the structures. Two structures of high symmetry are f.c.c. and hexagonal close-packed (h.c.p.) lattices with the following stacking sequences: ABCABC for f.c.c. and ABAB for h.c.p. (Conway & Sloane, 2013). Stacking faults – irregularities in the stacking sequence – are very common defects in close-packed structures due to a low energy difference between the ideal structures (Bolhuis *et al.*, 1997). A single inversion of the f.c.c. stacking sequence ABCABCACBA corresponds to a Σ_3 -twinning boundary and results in two twinned f.c.c. domains. Random stacking of hexagonal layers results in a so-called ‘random h.c.p.’ (r.h.c.p.) structure containing the motifs characteristic for both f.c.c. and h.c.p. structures. In reciprocal space, the stacking faults produce strong diffuse scattering in the stacking direction connecting the Bragg peaks in the form of rods known as Bragg rods, as shown in Fig. 3(b). Such Bragg rods are intensity modulations in reciprocal space along the straight lines connecting the Bragg peaks with fixed h and k indexes for which $h - k \neq 3n, n \in \mathbb{Z}$ and any index $l \in \mathbb{R}$ (in h.c.p. notation). The Bragg peaks with indexes $h - k = 3n, n \in \mathbb{Z}$ and $l \in \mathbb{Z}$ are stacking-independent and are isolated in reciprocal space (Petukhov *et al.*, 2003). The intensity profiles along the Bragg rods depend on the particular stacking sequence as described by Meijer *et al.* (2014). In contrast to the isolated Bragg peaks that contribute to the CCFs at certain q -values, the Bragg rods contribute to the CCFs in a continuous q -range. Their contribution can be evaluated using the scalar product and corresponding reciprocal basis vectors as described in Appendix A.

3. Results

We demonstrate application of the AXCCA technique on simulated and experimentally measured datasets. The simulated datasets represent scattered intensity distributions in 3D reciprocal space calculated for colloidal crystal grains of different structures. The experimentally measured dataset is the scattered intensity distribution from a similar colloidal crystal studied previously (Shabalin *et al.*, 2016; Meijer *et al.*, 2014). Each of the datasets initially consisted of 360 diffraction patterns obtained by rotation of the sample in the range 0 – 180° around the vertical axis with an angular step size of 0.5° . The simulation parameters selected were similar to those used in the experiment: X-ray energy $E = 8$ keV ($\lambda = 1.55$ Å), a 2D detector (512×512 pixels) with the pixel size $55 \times 55 \mu\text{m}^2$ positioned downstream from the sample at the distance $d = 5.1$ m. The experimental dataset was collected at the P10 Coherence Application beamline at PETRA III synchrotron using a MAXIPIX detector. The 2D patterns from each dataset were interpolated onto a 3D orthogonal grid with a voxel size of $0.4375 \mu\text{m}^{-1}$. We used the flat Ewald sphere approximation because of small scattering angles (less than 0.25° , the corresponding q -values less than $200 \mu\text{m}^{-1}$).

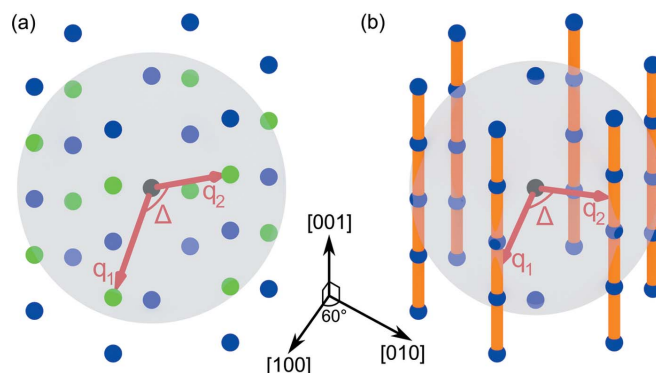


Figure 3 Models of 3D reciprocal space for (a) h.c.p. and (b) r.h.c.p. lattices. The black dot is the origin of reciprocal space, colored dots are the Bragg peaks. The semitransparent sphere shows the sphere S of the radius $q = \|\mathbf{q}_1\| = \|\mathbf{q}_2\|$, at which the CCF is calculated. In (a) the green dots are the Bragg peaks intersecting the sphere S and, thus, contributing to the corresponding CCF at the angle Δ . In (b), the orange rods represent the Bragg rods. They contribute to the corresponding CCF at the angle Δ that is dependent on the radius q of the sphere S .

3.1. Application to the simulated data

For simulations, we considered a spherical colloidal crystal grain with an outer size of $3.6 \mu\text{m}$ consisting of monodisperse silica spheres with a diameter of 230 nm. Different close-packed structures typical for colloidal crystals were simulated: ideal f.c.c. and h.c.p. lattices, two f.c.c. domains with a Σ_3 -twinning boundary, as well as an r.h.c.p. lattice with the stacking sequence ABCABCBCACBCBABAB matching the one observed in the CDI reconstruction (Shabalin *et al.*, 2016) of the experimental data discussed below. The nearest-neighbour distance for all the structures was equal to the diameter of the constituting silica spheres (230 nm). The simulated structures consist of corresponding stacking motifs of the hexagonal layers, as shown in Figs. 4(a), 4(d), 4(g) and 4(j).

The 2D diffraction patterns from the structures were simulated using the *MOLTRANS* software. On the simulated diffraction patterns (see Fig. 4) one can observe concentric rings of intensity due to the form factor of the colloidal spheres and the Bragg peaks that originate from the structure factor of the colloidal crystal lattice. In the diffraction patterns for the structures with stacking faults [see Figs. 4(i) and 4(l)], aside from the isolated Bragg peaks, the Bragg rods along the q_z direction that connect Bragg peaks can be clearly observed.

The azimuthally averaged intensities of the 3D scattered intensity distributions for these structures are shown in Fig. 5(a). The intensity profiles for the ideal f.c.c. and h.c.p. lattices are quite different as they contain the characteristic Bragg peaks for these structures. In contrast, the profile for two twinned f.c.c. domains with a Σ_3 -boundary between them is almost identical to the one for the perfect f.c.c. lattice. This is an expected result because the major contribution to the scattered intensity originates from the domains with the same f.c.c. structure, whereas the contribution from the boundary is negligible. The radial profile for the r.h.c.p. structure is smoothed and contains mostly the peaks common for the f.c.c.

and h.c.p. structures, making it hard to identify the exact stacking sequence. It is even harder in the case of the experimentally measured profile [shown in Fig. 5(a) for comparison] due to lower contrast.

We calculated the CCFs for the pairs of points with the same q -value $q = \|\mathbf{q}_1\| = \|\mathbf{q}_2\|$ in the simulated 3D intensity distributions for all four different structures (see Appendix B for details of the calculation). We considered the CCFs for

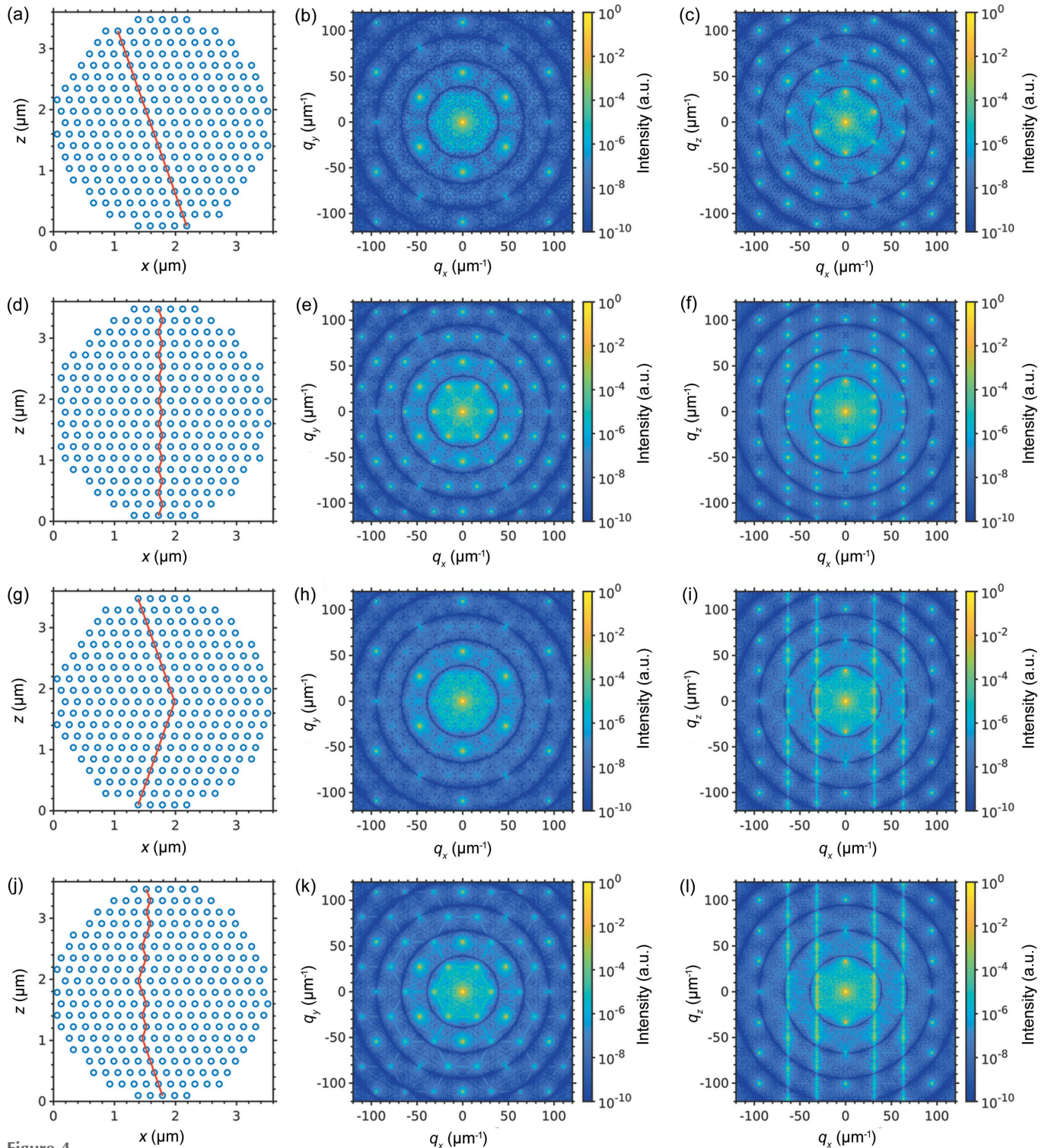


Figure 4 Simulation of 2D diffraction patterns from the structures: (a)–(c) f.c.c., (d)–(f) h.c.p. (g)–(i) twinned f.c.c. domains and (j)–(l) r.h.c.p. The first column contains the simulated structures viewed along $[1\bar{1}0]_{\text{f.c.c.}}/[100]_{\text{h.c.p.}}$, the stacking direction $[111]_{\text{f.c.c.}}/[001]_{\text{h.c.p.}}$ is along the z -axis. The red lines denote the stacking sequence. The second column contains diffraction patterns simulated for an incident beam along the stacking direction $[111]_{\text{f.c.c.}}/[001]_{\text{h.c.p.}}$. The third column contains diffraction patterns simulated for an incident beam along the direction $[110]_{\text{f.c.c.}}/[110]_{\text{h.c.p.}}$.

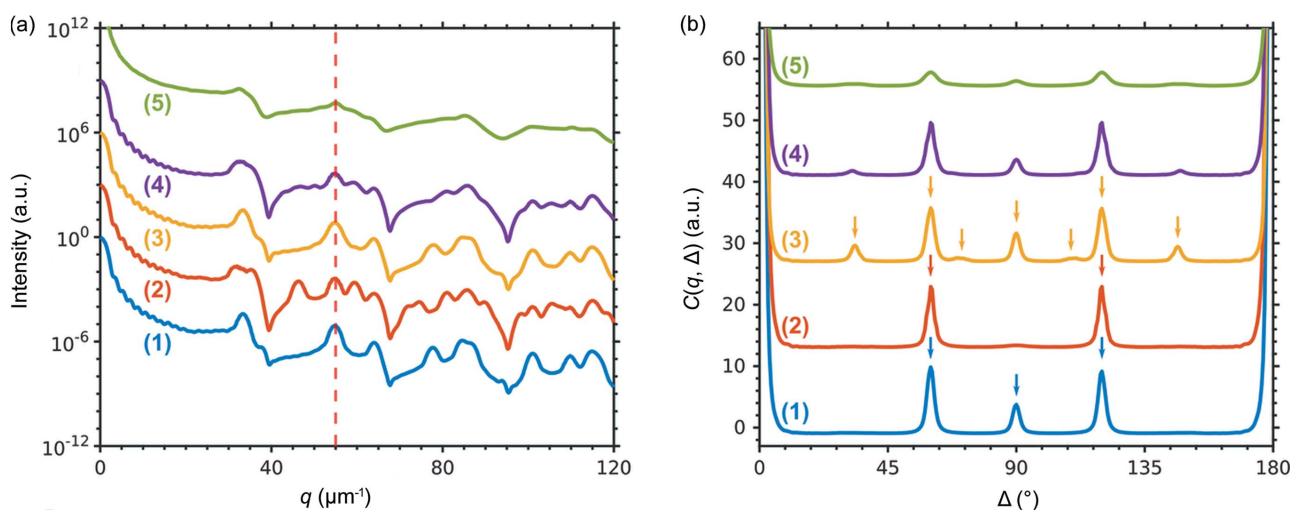


Figure 5 (a) Azimuthally averaged values of the 3D intensity distributions simulated for the following structures: (1) f.c.c. (2) h.c.p. (3) twinned f.c.c. domains and (4) r.h.c.p. and from the experimentally measured sample (5), for comparison. The vertical red dashed line is at $q = 55 \mu\text{m}^{-1}$ corresponding to $220_{\text{f.c.c.}}/110_{\text{h.c.p.}}$ Bragg peaks, for which the CCFs shown in (b) were calculated. (b) CCFs $C(q, \Delta)$ calculated at $q = 55 \mu\text{m}^{-1}$ for the simulated 3D diffraction patterns for the following structures: (1) f.c.c. (2) h.c.p. (3) two twinned f.c.c. domains and (4) r.h.c.p., and from the experimentally measured sample (5), for comparison. The arrows show the peak positions calculated for the corresponding structures by a geometrical model.

intensities at $q = 55 \mu\text{m}^{-1}$ that correspond to stacking independent reflections present for all structures [see Fig. 5(a)]. This q -value corresponds to the 220 reflections from the f.c.c. structure and to the 110 reflections from the h.c.p. structure. Even though these reflections correspond to the same d -spacing, the angles between the equivalent planes are different for these structures. Therefore, the peaks in the CCFs appear at different positions for different structures, as shown in Fig. 5(b). The peak positions from the geometrical model (see Appendix A) coincide with the peak positions in the calculated CCFs for the simulated structures as shown in Fig. 5(b). The peak positions for an f.c.c. structure are clearly distinct from those for an h.c.p. structure because of different symmetry. The CCF for the twinned f.c.c. structure contains additional peaks that are correlations between the peaks originating from different domains. The position of additional peaks is defined by the twinning transformation described in Appendix A. This approach can be extended to other types of twinning (e.g. Σ_5 or Σ_9). The CCF for the r.h.c.p. structure is similar to the one for the twinned f.c.c. domains, but the relative intensity of the peaks is different. This probably indicates the presence of both h.c.p. and f.c.c. stacking motifs, but more general conclusions can be made only analyzing the CCFs calculated for different q -values as described below.

Additional information can be accessed if we review a set of CCFs calculated for various q -values. We calculated the CCFs in the range $q = 25\text{--}115 \mu\text{m}^{-1}$ with a step size of $1 \mu\text{m}^{-1}$ (see Fig. 6). As shown in this figure, the peaks for the simulated structures have different positions in both radial and angular directions, since they originate from different sets of equivalent planes defined by the lattice symmetry. The peak positions for these structures can be calculated from the geometrical model of the reciprocal lattice as described in Appendix A. We note that the peak positions were determined for the structures with the unit-cell parameters corresponding to the

nearest neighbor distance of 230 nm (the size of the silica spheres). In an arbitrary experiment, the unit-cell parameters can be used as the fitting parameters to fit the peak positions in the experimental CCFs (Carnis *et al.*, 2021; Schlottheuber *né* Brunner *et al.*, 2021).

For the ideal f.c.c. and h.c.p. structures, the positions of all brightest peaks in the CCFs coincide with the positions obtained from the geometrical model [see Figs. 6(a) and 6(b)]. Additionally, there are low-intensity peaks at the q -values between the bright peaks that are not explained with this model [see, for example, additional peaks at $q = 36 \mu\text{m}^{-1}$ in Fig. 6(a)]. They originate from the correlations between the Bragg peaks of different orders. Basically, different orders contribute to the scattered intensities at different q -values, but due to the broadening of the Bragg peaks and the absence of noise in the simulated data, their tails contribute to the CCFs. These are not observed in the experimental data due to noise and other artifacts, but can also be considered in the simple geometrical model.

For the twinned f.c.c. structure, the map contains many additional peaks that reflect correlations between the Bragg peaks that originate from different domains. As discussed above, the peak positions are defined by the twinning transformation and can be taken into account as described in Appendix A. For the r.h.c.p. structure, the map contains peaks characteristic for both h.c.p. and f.c.c. structures. It is rather an expected result as soon as the r.h.c.p. structure contains stacking sequences that can be attributed to both h.c.p. and f.c.c. structures. Besides the isolated peaks, the CCFs for the r.h.c.p. and twinned-f.c.c. structures contain also intensity in the form of ‘arcs’ connecting the peaks. They originate from the Bragg rods characteristic for stacking disordered structures with planar defects. Their contribution to the CCFs can be calculated following the procedure described in Appendix A and shown in Fig. 6(d).

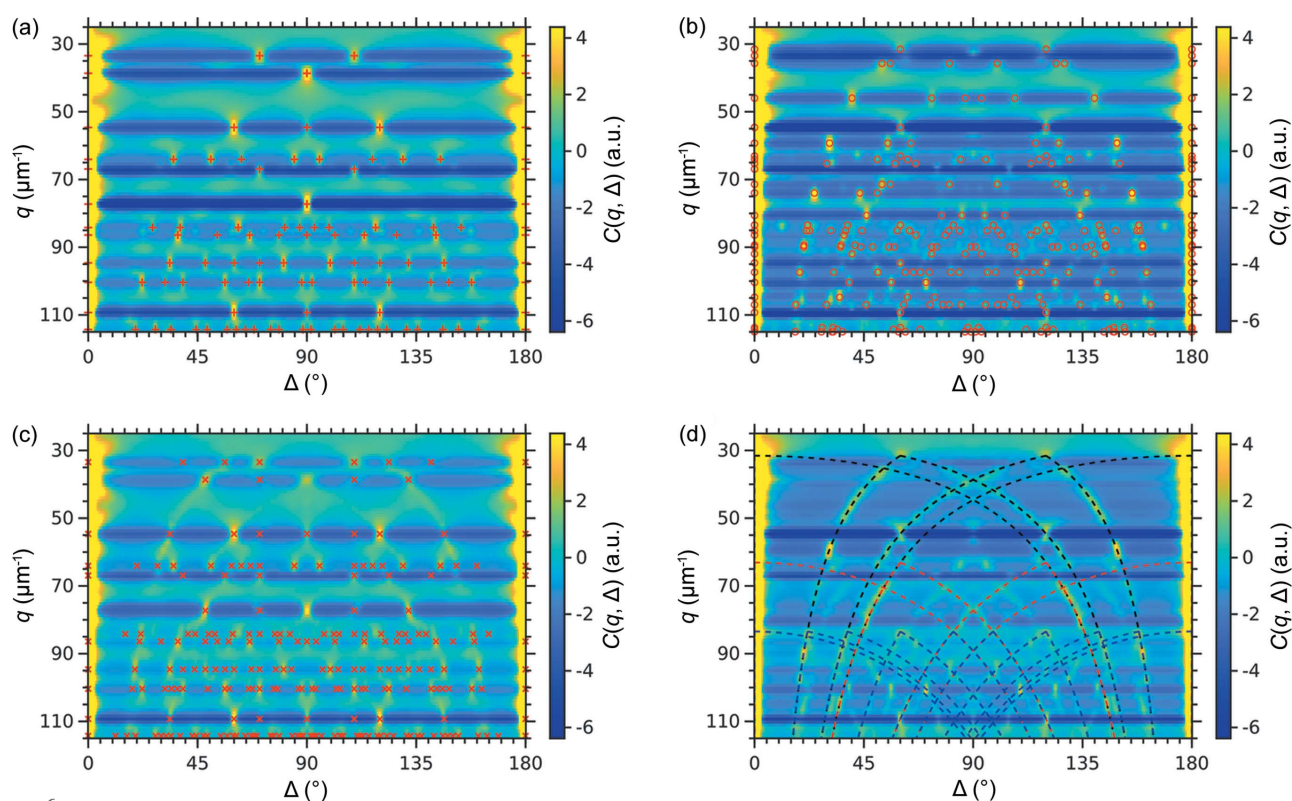


Figure 6
 2D correlation maps $C(q, \Delta)$ calculated in the q -range from 25 to 115 nm^{-1} for the simulated scattered intensities in 3D from (a) f.c.c. (b) h.c.p. (c) twinned f.c.c. and (d) r.h.c.p. structures. The CCFs are stacked together along the vertical axis q . The markers in (a)–(c) indicate the peak positions for the corresponding structures calculated from the geometrical model (see Appendix A). Note that in (c) there are only the peaks corresponding to the inter-domain correlations between the twin domains. The intra-domain correlations from each domain also produce peaks corresponding to an f.c.c. structure shown in (a). In (d) the dashed lines indicate the correlations between the Bragg rods. Only correlations within $10l$ (black lines), $20l$ (red lines) and $21l$ (blue lines) Bragg rod families are shown. Correlations between the Bragg rods from different families as well as for higher order families have been omitted for clarity.

Despite similar intensity profiles, different structures result in different angular distribution of the Bragg peaks. The AXCCA technique allows us to reveal the angular correlations between the Bragg peaks and to determine qualitatively the sample structure even when the azimuthally integrated intensity profiles are almost identical.

3.2. Application to the experimental data

The experimentally measured sample was a colloidal crystal grain with an outer size of about $2 \times 3 \times 4 \text{ μm}^3$ consisting of silica spheres with a diameter of about 230 nm prepared as described by Shabalin *et al.* (2016) and Meijer *et al.* (2014). The collected scattered intensity distribution in 3D reciprocal space contains several orders of Bragg peaks and Bragg rods [see Fig. 7(a)]. An in-plane cut through the origin of reciprocal space [see Fig. 7(b)] reveals the sixfold symmetry characteristic for hexagonal layers of close-packed nanoparticles. Two out-of-plane cuts shown in Figs. 7(c) and 7(d) contain the Bragg rods connecting the Bragg peaks indicating the stacking disorder of the nanoparticle layers. Note that the experimentally measured diffraction patterns have significantly lower contrast compared with the simulated ones. This can be attributed to the polydispersity of the colloidal particles, the

partial coherence of the incident X-rays and other experimental artifacts that are not taken into account in the simulations.

The experimental CCFs calculated in the range $q = 25$ – 115 μm^{-1} with a step size of 1 μm^{-1} are shown in Fig. 8(a). Owing to the lower contrast of the diffraction patterns, these correlation maps also have lower contrast compared with the simulated ones. Moreover, the measured intensity in the locations of form factor minima does not contain any structural information leading to the absence of peaks in the CCFs at the corresponding q -values (e.g. at $q = 38 \text{ μm}^{-1}$). We assumed the colloidal crystal has a close-packed structure and calculated the peak positions in the CCFs according to the geometrical model for the same structures as for the simulated data: ideal f.c.c., h.c.p. and twinned f.c.c. Also, we calculated the positions of the ‘arcs’ corresponding to the correlations between the Bragg rods. The experimental CCFs with the indicated peak positions are shown in Figs. 8(b)–8(d).

Most of the peaks present in the experimental CCFs have the peak positions characteristic for an h.c.p. structure [see Fig. 8(c)], indicating that this stacking motif is a predominant one. Several peaks do not match the positions for the h.c.p. structure, but their positions are characteristic of an f.c.c. structure [see Fig. 8(b)], suggesting the presence of such

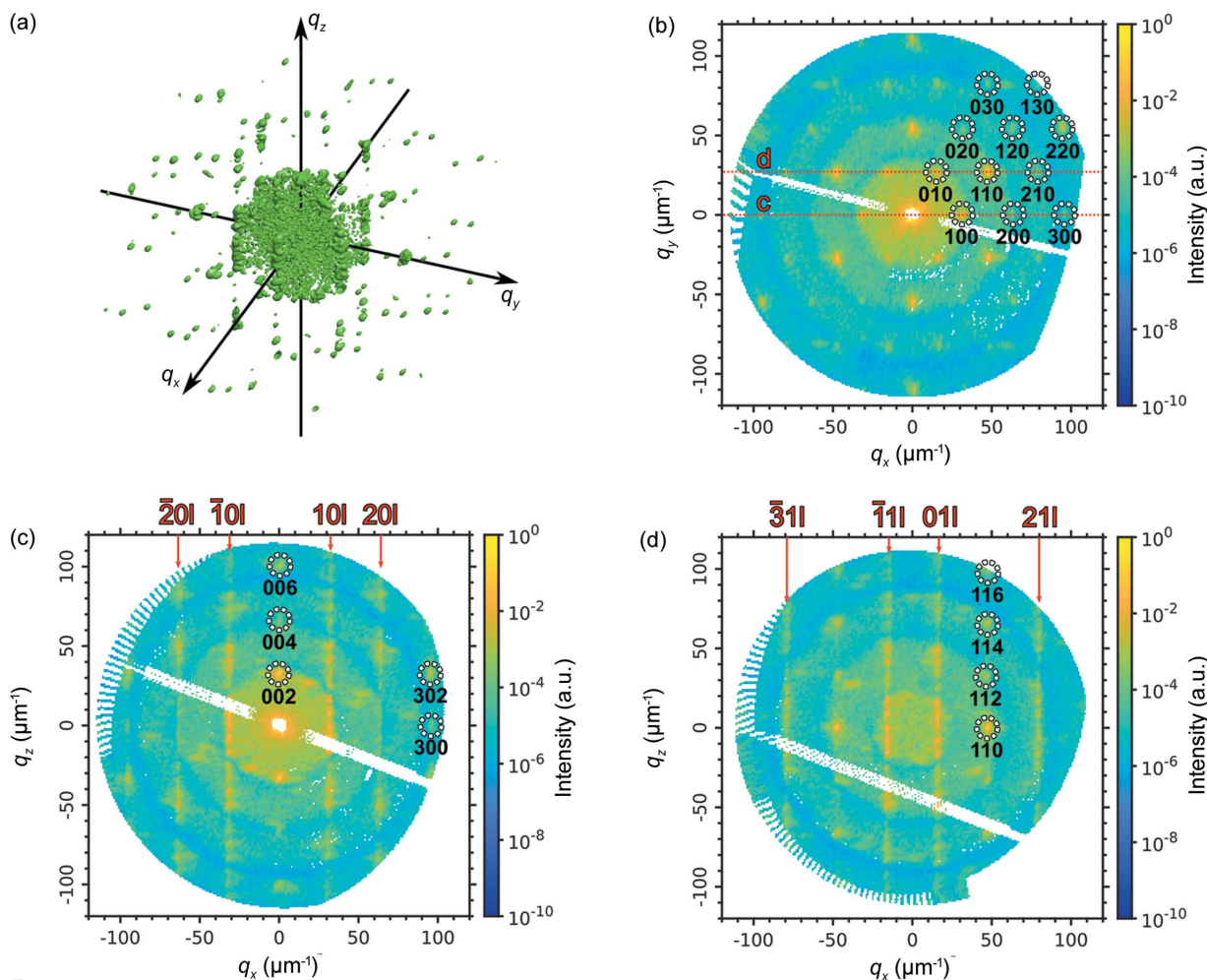


Figure 7
 (a) Isosurface of the measured intensities in 3D reciprocal space. (b) Horizontal cut through the origin of reciprocal space. The Bragg peaks are attributed to an h.c.p. lattice. The red lines show the cuts in the panels (c) and (d). (c) Vertical cut through the 100 and $\bar{1}00$ reflections, and the origin of reciprocal space. (d) Vertical cut through the 010 and $\bar{1}10$ reflections with an offset of 30.5 nm^{-1} along q_y from the origin of reciprocal space. The Bragg rods connecting the Bragg peaks of the $10l$, $20l$ and $21l$ families are indicated with red arrows.

stacking motif in the sample as well. The peaks characteristic for twinned f.c.c. domains are not present in the experimental CCFs [compare with Fig. 6(c)], indicating the absence of such motifs in the sample. In addition, there are ‘arcs’ characteristic for correlations between the Bragg rods similar to those for the simulated r.h.c.p. structure.

Indeed, the stacking sequence revealed in the reconstructed real space structure is ABCABCBCACBCBABAB (Shabalin *et al.*, 2016). This sequence, in general, can be described as a random h.c.p. structure with many stacking faults. However, we can distinguish h.c.p. and f.c.c. motifs in the sequence that produces the corresponding peaks in the CCFs.

3.3. Comparison of AXCCA applied to the intensity distribution in 3D reciprocal space and with the randomly oriented 2D diffraction patterns

As mentioned in Section 2.1, the CCFs calculated for the intensity distribution in 3D reciprocal space should be similar

to the many averaged 2D diffraction patterns obtained from different random angular orientations of the same sample. Such a dataset of 2D diffraction patterns could be collected in an XFEL experiment performed in the single-particle imaging (SPI) experiment, if the same crystalline structure was injected into the X-ray beam many times with random orientations. To prove the similarity of the CCFs obtained from the 3D intensity distribution and the averaged 2D diffraction patterns in random orientations, we simulated 5×10^4 diffraction patterns from the randomly oriented colloidal crystal with the f.c.c. structure using the *MOLTRANS* software as described in Section 3.1. The angular orientations were uniformly distributed in 3D. The CCFs were calculated for q -values in the range $q = 25\text{--}115 \text{ nm}^{-1}$ using equation (3) for each diffraction pattern separately and then averaged over all patterns.

The resulting CCFs averaged over all 5×10^4 patterns are shown in Fig. 9(b) and can be compared to those calculated for the intensity distribution in 3D reciprocal space as described in Section 3.1 and shown in Fig. 9(a). As we can see from these figures, the CCF maps are almost identical and contain peaks

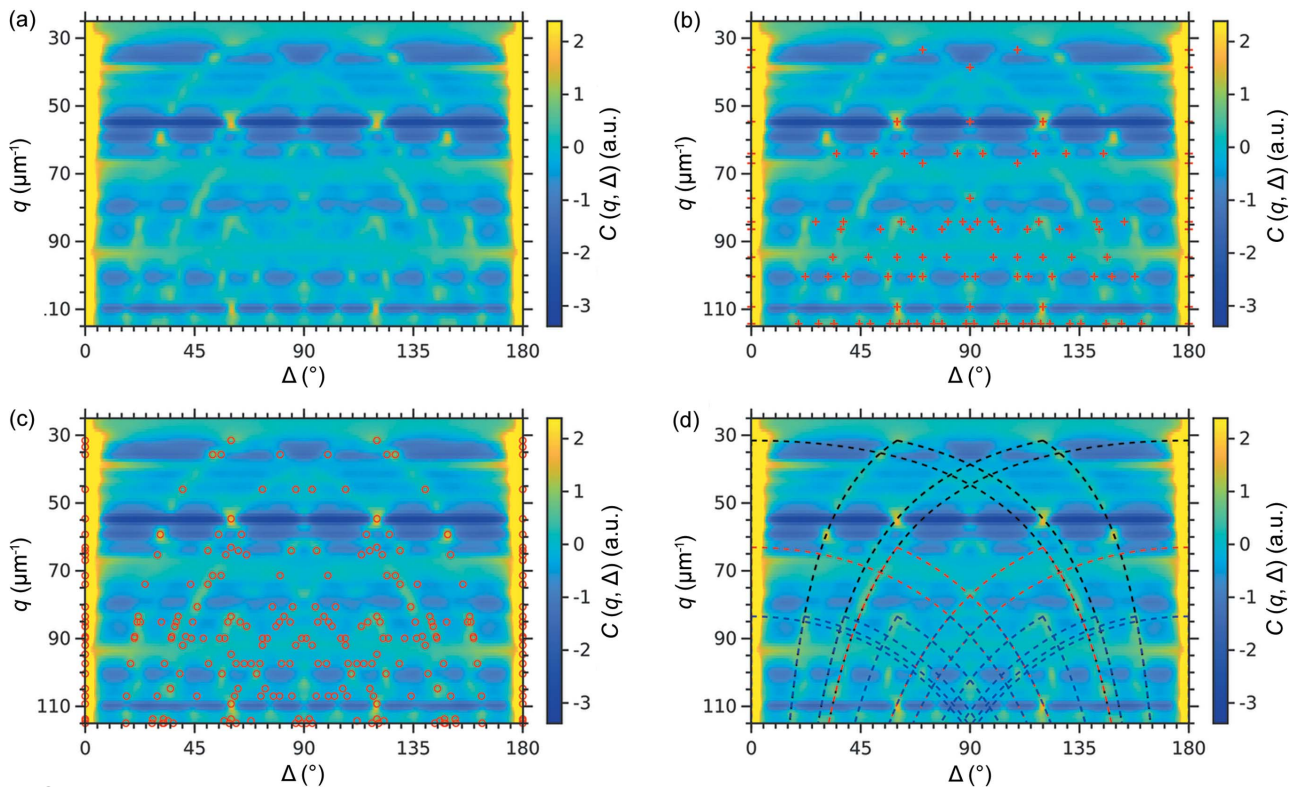


Figure 8 2D correlation maps $C(q, \Delta)$ for the experimentally measured intensity distribution in 3D reciprocal space. (a) Initial correlation map. The markers in (b)–(c) indicate the peak positions for (b) f.c.c. and (c) h.c.p. structures calculated from the geometrical model. In (d) the dashed lines indicate the correlations between the Bragg rods simulated for the r.h.c.p. structure. Only correlations within $10l$ (black lines), $20l$ (red lines) and $21l$ (blue lines) Bragg rod families are shown. Correlations between the Bragg rods from different families as well as for higher order families have been omitted for clarity.

at the same positions. Small deviations probably originate from interpolation of the scattered intensities onto the 3D grid in the second case.

In contrast, the CCF maps averaged over 5×10^2 2D patterns, shown in Fig. 9(c), contain only a fraction of the peaks present in the CCF map calculated for the 3D intensity distribution. This is because such a small number of patterns does not fully cover all possible orientations. Indeed, to contribute to the CCF, a pair of Bragg peaks should be present in a single 2D diffraction pattern. Thus, it requires a certain number of randomly oriented diffraction patterns to catch all possible pairs of the Bragg peaks.

To estimate the number of 2D diffraction patterns in random orientations required to obtain a CCF map similar to the one calculated from the 3D scattered intensity distribution, we calculated the Pearson correlation coefficient (Kendall & Stuart, 1973) $r(N)$ between the CCF maps averaged over different numbers of 2D patterns and the one from the 3D intensity distribution defined as

$$r(N) = \frac{\langle C_{3D}(q, \Delta) C_N(q, \Delta) \rangle}{\sqrt{\langle C_{3D}^2(q, \Delta) \rangle} \sqrt{\langle C_N^2(q, \Delta) \rangle}}, \quad (5)$$

where $C_{3D}(q, \Delta)$ are the CCFs calculated for the intensity distribution in 3D reciprocal space, and $C_N(q, \Delta)$ are the CCFs calculated for the randomly oriented 2D diffraction patterns

and averaged over N patterns. The averaging was performed over all q -values in the range $q = 25\text{--}115 \mu\text{m}^{-1}$ and angles $\Delta = 0\text{--}180^\circ$ for which the CCFs were calculated. We note that the calculated CCFs have zero mean value with averaging over angle Δ at the fixed q -value that allows direct application of the Pearson correlation coefficient.

The evolution of the correlation coefficient with the number of diffraction patterns is shown in Fig. 9(d). When the number of patterns used is below 10^2 , the correlation coefficient is close to zero, indicating that the CCFs do not contain any features corresponding to the structural information. With further increase in the number of patterns used, the correlation coefficient grows indicating the successive appearance of the structured features in the CCF map. At about 3×10^3 patterns it reaches a plateau, while with further increase in the number of patterns it grows only a little bit to the value of 0.95 for 5×10^4 patterns. We suggest that all features in the CCF map appear already at 3×10^3 patterns, while further increase in the number of patterns leads to only minor changes in the relative intensities of the correlation peaks.

Thus, the CCFs calculated from the 2D diffraction patterns obtained for different random orientations of the sample are similar to the CCFs calculated from the scattered intensity distribution in 3D reciprocal space measured for the sample, when the number of 2D patterns is high enough. In the particular case under consideration, the number of required

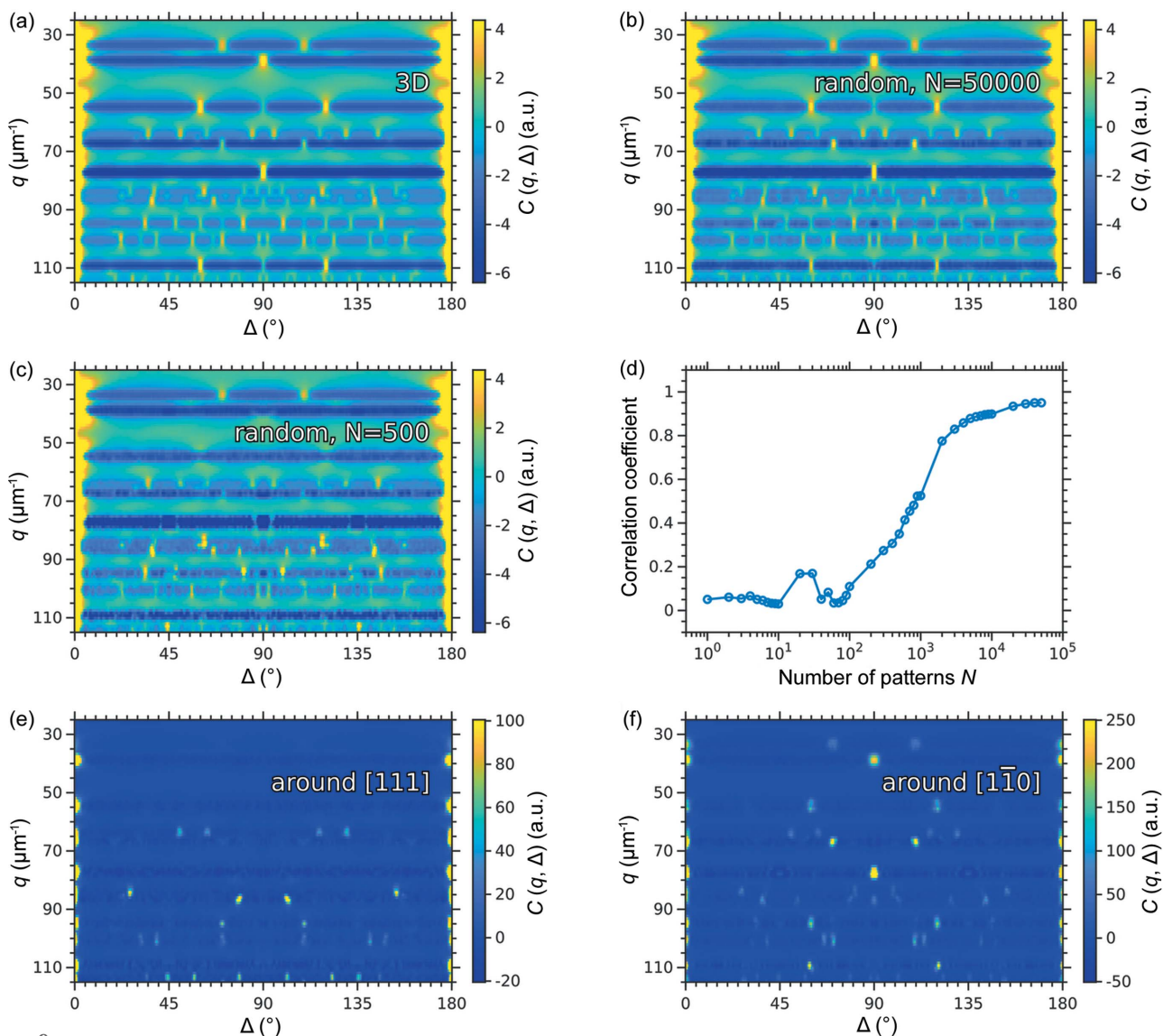


Figure 9 2D correlation maps $C(q, \Delta)$ calculated for (a) the simulated scattered intensities in 3D reciprocal space and (b)–(e) 2D diffraction patterns from a randomly oriented sample averaged over (b) 5×10^4 and (c) 5×10^2 patterns. The scattered intensity distribution in 3D reciprocal space and the 2D diffraction patterns were simulated for the same colloidal crystal with an f.c.c. structure. (d) Pearson correlation coefficient $r(N)$ between the CCF maps averaged over different numbers of 2D diffraction patterns and the CCF map calculated for the intensity distribution in 3D reciprocal space for the same sample. (e)–(f) 2D correlation maps $C(q, \Delta)$ calculated for 2D diffraction patterns obtained by rotation of the sample with an f.c.c. structure around the (e) $[111]_{\text{f.c.c.}}$ and (f) $[1\bar{1}0]_{\text{f.c.c.}}$ axes.

randomly oriented 2D diffraction patterns is about two orders of magnitude higher than the number of systematically measured 2D patterns (e.g. by rotation of the sample) required for reconstruction of the intensity distribution in 3D reciprocal space.

Note that the number of randomly oriented 2D diffraction patterns required to obtain the CCF map similar to the one calculated from the 3D intensity distribution is individual for each sample under study. The number of required patterns depends on the probability to catch at least a pair of the Bragg peaks into a single 2D pattern that, in turn, depends on the angular size and separation of the Bragg peaks in 3D reciprocal space. Therefore, for bulk crystals with many scatterers

and small periodicity, the required number of 2D patterns may be sufficiently higher.

The important point here is the distribution of the angular orientations of the sample, for which 2D diffraction patterns are obtained. Only uniform angular distribution allows us to obtain CCFs similar to those from the 3D intensity distribution, because the 2D patterns in this case cover all pairs of the points in reciprocal space with equal probability. If the angular distribution is not uniform, some correlations will be enhanced while others will be weakened.

To show this, we simulated 2D diffraction patterns from a colloidal crystal with the f.c.c. structure using the *MOLTRANS* software. We simulated two datasets, obtained

by rotation of the sample around the $[111]_{\text{f.c.c.}}$ and $[\bar{1}\bar{1}0]_{\text{f.c.c.}}$ axes in the range $0\text{--}180^\circ$ with an angular step size of 0.5° . The CCFs were calculated for the 2D diffraction patterns in the q -range $25\text{--}115\ \mu\text{m}^{-1}$ with the step size of $1\ \mu\text{m}^{-1}$ and then averaged over all angular positions of the sample. The resulting CCFs calculated for these two datasets are shown in Figs. 9(e) and 9(f). They are different from each other and from the CCF map obtained for the 3D intensity distribution shown in Fig. 9(a). The difference can be explained as follows. A pair of the Bragg peaks gives rise to a peak in the CCFs only if both Bragg peaks are present in the same 2D diffraction pattern. When the diffraction patterns are collected by rotation of the sample around one of its crystallographic axes, each diffraction pattern contains different pairs of the Bragg peaks. The exact set of the Bragg peak pairs present in the dataset is defined by the selected crystallographic axis. Thus, the datasets collected by rotation around different crystallographic axes contain different pairs of the Bragg peaks that give rise to the peaks in the CCF maps. The present peaks in the CCF maps in this case have higher intensity compared with those in the CCF maps obtained for the randomly distributed 2D patterns. This is because, in the latter case, the CCFs are averaged over many patterns, most of which do not contain any correlations at a certain q -value. The diffraction patterns obtained by the rotation around one crystallographic axis are an extreme case, but any other distribution with a preferred direction would result in similar deviations.

4. Conclusions

We proposed to apply the AXCCA technique to the scattered intensity distribution in 3D reciprocal space. Here, we demonstrated an application of the AXCCA for qualitative determination of the crystalline structure of a colloidal crystal, including the present planar defects. AXCCA provides a complementary view on the structure when CDI reconstruction does not work (Schlotheuber né Brunner *et al.*, 2021). The results can be interpreted by means of a simple geometrical model of the crystalline lattice and defects. Direct sensitivity to the angles in reciprocal space provides additional information about the structure compared with the conventional radial intensity profile analysis.

The application of AXCCA to the 3D scattered intensity distribution measured from a single sample by its rotation made it possible to avoid averaging of the revealed structure over many realizations with possibly different defects present. Moreover, the systematic measurement allowed us to significantly reduce the number of measurements needed to obtain orientationally averaged CCFs, compared with measurements from random orientations. We also showed that averaging over 2D diffraction patterns measured during rotation around the fixed axis does not provide the same CCFs as the assembly of intensity distributions in 3D reciprocal space. We think that it is an essential part of the proposed method.

The method described here works well for the colloidal samples with the large unit cell. For such samples, a single rotation around one axis is sufficient to collect scattered

intensities in whole reciprocal space. The same method can be applied as well for the crystal grains with the unit cell of a few Ångströms. In this case, due to the Ewald sphere curvature, one will need to apply two rotations around two orthogonal axes to cover full reciprocal space of the crystal grain. The described formalism will be applicable also in this case.

This approach was already successfully applied for the analysis of the averaged structures and defects in single colloidal grains of gold and magnetite nanocrystals (Carnis *et al.*, 2021; Schlotheuber né Brunner *et al.*, 2021). We expect that it will find applications for understanding the structure of colloidal grains and single crystals in future.

APPENDIX A Geometrical interpretation of the CCFs

Here, we follow the discussion provided by Niozu *et al.* (2020) and apply it to our structures. Any reciprocal lattice vector can be represented as a linear combination of the basis vectors $\mathbf{g}_{hkl} = h\mathbf{b}_1 + k\mathbf{b}_2 + l\mathbf{b}_3$. Let us denote a family of equivalent crystallographic directions as G_{hkl} . Each crystallographic direction that fulfills the diffraction selection rules for a given lattice symmetry corresponds to the position of a Bragg peak in reciprocal space. Using the coordinates of the reciprocal lattice vectors \mathbf{g}_{hkl} and $\mathbf{g}_{h'k'l'}$ we can calculate the angle Δ between a certain pair of the Bragg peaks corresponding to these vectors. This Bragg peaks pair would contribute at the angle Δ to the CCF $C(q_1, q_2, \Delta)$ calculated for $q_1 = \|\mathbf{g}_{hkl}\|$ and $q_2 = \|\mathbf{g}_{h'k'l'}\|$. To evaluate all contributions for a certain fixed q_1 and q_2 , we should consider all Bragg peaks that appear in reciprocal space at these q -values. Then, all angles Δ can be calculated using the scalar product

$$\mathbf{g}_{hkl} \cdot \mathbf{g}_{h'k'l'} = \|\mathbf{g}_{hkl}\| \|\mathbf{g}_{h'k'l'}\| \cos(\Delta), \quad (6)$$

if one considers all possible pairs of the vectors \mathbf{g}_{hkl} and $\mathbf{g}_{h'k'l'}$ from certain families of equivalent crystallographic directions G_{hkl} and $G_{h'k'l'}$, respectively, corresponding to the q -values q_1 and q_2 . Note, in some cases, several families $G_{h_i k_i l_i}$ may contribute at the same q -value. Then, an extended set of the vectors $\cup_i G_{h_i k_i l_i}$ should be considered.

Several crystalline domains in the sample would result in two types of correlation: intra-domain correlations between the Bragg peaks originating from a single domain and inter-domain correlations between the Bragg peaks originating from different domains. The intra-domain correlation contribution to the CCFs can be evaluated as described above. To evaluate the contribution of the inter-domain correlations, one should consider the relative orientation of the domains. The orientation can be taken into account by introducing an orthogonal transformation matrix \mathbf{T} that transforms the basis vectors of one domain into the basis vectors of another. Then, the inter-domain correlations contribute to the CCF $C(q_1, q_2, \Delta)$ at the angles Δ that can be found using the scalar product

$$\mathbf{g}_{hkl} \cdot \mathbf{T}\mathbf{g}_{h'k'l'} = \|\mathbf{g}_{hkl}\| \|\mathbf{g}_{h'k'l'}\| \cos(\Delta), \quad (7)$$

if one considers all possible pairs of the vectors \mathbf{g}_{hkl} and $\mathbf{g}_{h'k'l'}$ from certain families of equivalent crystallographic directions G_{hkl} and $G_{h'k'l'}$ corresponding to the q -values q_1 and q_2 .

For example, for f.c.c. and h.c.p. lattices discussed in this paper, the reciprocal basis vectors can be defined as follows:

$$\begin{cases} \mathbf{b}_1^{\text{f.c.c.}} = \frac{2\pi}{a_{\text{f.c.c.}}} \left(\frac{1}{\sqrt{2}}, -\frac{1}{\sqrt{6}}, \frac{1}{\sqrt{3}} \right) \\ \mathbf{b}_2^{\text{f.c.c.}} = \frac{2\pi}{a_{\text{f.c.c.}}} \left(-\frac{1}{\sqrt{2}}, -\frac{1}{\sqrt{6}}, \frac{1}{\sqrt{3}} \right) \\ \mathbf{b}_3^{\text{f.c.c.}} = \frac{2\pi}{a_{\text{f.c.c.}}} \left(0, \frac{2}{\sqrt{6}}, \frac{1}{\sqrt{3}} \right) \end{cases} \text{ and } \begin{cases} \mathbf{b}_1^{\text{h.c.p.}} = \frac{2\pi}{a_{\text{h.c.p.}}} \left(\frac{2}{\sqrt{3}}, 0, 0 \right) \\ \mathbf{b}_2^{\text{h.c.p.}} = \frac{2\pi}{a_{\text{h.c.p.}}} \left(\frac{1}{\sqrt{3}}, 1, 0 \right) \\ \mathbf{b}_3^{\text{h.c.p.}} = \frac{2\pi}{a_{\text{h.c.p.}}} \left(0, 0, \frac{\sqrt{3}}{2} \right) \end{cases} \quad (8)$$

where $a_{\text{f.c.c.}} = \sqrt{2}d$ and $a_{\text{h.c.p.}} = d$ are the f.c.c. and h.c.p. lattice parameters corresponding to the same nearest-neighbor distance d . The orientation of the f.c.c. basis is selected in such a way that the stacking directions $[001]_{\text{h.c.p.}}/[111]_{\text{f.c.c.}}$ coincide as well as the angular orientation of the hexagonal planes $(001)_{\text{h.c.p.}}/(111)_{\text{f.c.c.}}$ (*i.e.* $[100]_{\text{h.c.p.}}/[1\bar{1}1]_{\text{f.c.c.}}$).

For the simplest f.c.c. twinning with a Σ_3 -boundary discussed in this paper, the transformation matrix \mathbf{T} corresponds to a reflection of the f.c.c. lattice across the $(111)_{\text{f.c.c.}}$ plane and can be written in the following form:

$$\mathbf{T} = \begin{pmatrix} 1 & 0 & 0 \\ 0 & 1 & 0 \\ 0 & 0 & -1 \end{pmatrix}. \quad (9)$$

The Bragg rods originating from the stacking disorder of the hexagonal layers in close-packed structures are intensity modulations along the straight lines normal to the hexagonal layers and along the stacking direction. Their positions are defined by the reciprocal lattice and, using the h.c.p. reciprocal basis vectors from equation (8), can be described by $\mathbf{g}_{hk}(l) = \mathbf{g}_{hk0} + \mathbf{g}_{\perp}(l)$, where \mathbf{g}_{hk0} is a vector from a certain in-plane Bragg peaks family $G_{hk0}^{\text{h.c.p.}}$ and $\mathbf{g}_{\perp}(l) = l\mathbf{b}_3^{\text{h.c.p.}}$, $l \in (-\infty, \infty)$ is a vector along the Bragg rod, normal to the planes. Note the Bragg rods are present only for stacking-dependent families $G_{hk0}^{\text{h.c.p.}}$ for which $h - k \neq 3n$, $n \in \mathbb{Z}$ (Petukhov *et al.*, 2003).

The parameter l corresponding to a certain q -value can be easily calculated for any Bragg rod corresponding to a certain in-plane reciprocal lattice vector \mathbf{g}_{hk0} as

$$l = \frac{(q^2 - \|\mathbf{g}_{hk0}\|^2)^{1/2}}{\|\mathbf{b}_3\|}. \quad (10)$$

Then, a pair of Bragg rods, corresponding to different in-plane vectors \mathbf{g}_{hk0} and $\mathbf{g}_{h'k'0}$ contributes to the CCF $C(q_1, q_2, \Delta)$ at the angle Δ that can be calculated using the scalar product

$$\mathbf{g}_{hk}(l_1) \cdot \mathbf{g}_{h'k'}(l_2) = \|\mathbf{g}_{hk}(l_1)\| \|\mathbf{g}_{h'k'}(l_2)\| \cos(\Delta), \quad (11)$$

where $\mathbf{g}_{hk}(l_i) = \mathbf{g}_{hk0} + \mathbf{g}_{\perp}(l_i)$, \mathbf{g}_{hk0} is a vector of a certain family $G_{hk0}^{\text{h.c.p.}}$, $\mathbf{g}_{\perp}(l_i) = l_i\mathbf{b}_3^{\text{h.c.p.}}$ and parameter l_i corresponding to the q -value q_i is defined by equation (10).

APPENDIX B

Definition of the cross-correlation function for the intensities defined on a grid

Taking into account that the experimental data are typically defined on a grid in reciprocal space, equation (2) can be represented as

$$C(q_1, q_2, \Delta) = \frac{\sum_{\mathbf{q}_i, \mathbf{q}_j \in G} \tilde{I}(\mathbf{q}_i) \tilde{I}(\mathbf{q}_j)}{\sum_{\mathbf{q}_i, \mathbf{q}_j \in G} 1}, \quad (12)$$

where

$$G = \{ \|\mathbf{q}_i\| - q_1 < \varepsilon \} \cap \{ \|\mathbf{q}_j\| - q_2 < \varepsilon \} \cap \{ |\Delta_{ij} - \Delta| < d\Delta \},$$

\mathbf{q}_i and \mathbf{q}_j are the points close to the spheres of the radii q_1, q_2 in reciprocal space, respectively; Δ_{ij} is the relative angle between these points. Parameters ε and $d\Delta$ define the radial and angular averaging windows, respectively. The sum is calculated over all pairs of points $\mathbf{q}_i, \mathbf{q}_j$ with the corresponding relative angle Δ . The average intensity used for the intensity correction in this case is

$$\langle I(q) \rangle = \frac{\sum_{\|\mathbf{q}_i\| - q < \varepsilon} I(\mathbf{q}_i)}{\sum_{\|\mathbf{q}_i\| - q < \varepsilon} 1}. \quad (13)$$

Given the desired resolution of $1 \mu\text{m}^{-1}$, in this work the radial averaging window ε was selected to be $0.5 \mu\text{m}^{-1}$. The angular resolution of Δ was experimentally set to 0.5° that allows us to resolve all peaks in the resulting CCFs. The angular averaging window $d\Delta$ was correspondingly set to 0.25° .

Acknowledgements

The authors are thankful to E. Weckert for supporting the project and providing the *MOLTRANS* software for simulating the scattering patterns. We acknowledge DESY (Hamburg, Germany), a member of the Helmholtz Association HGF, for the provision of experimental facilities. Parts of this research were carried out at PETRAIII synchrotron facility and we would like to thank all the beamline staff for assistance in using Coherence Application beamline P10.

References

- Altarelli, M., Kurta, R. P. & Vartanyants, I. A. (2010). *Phys. Rev. B*, **82**, 104207.
- Ayyer, K., Xavier, P. L., Bielecki, J., Shen, Z., Daurer, B. J., Samanta, A. K., Awel, S., Bean, R., Barty, A., Bergemann, M., Ekeberg, T., Estillore, A. D., Fangohr, H., Giewekemeyer, K., Hunter, M. S., Karnevskiy, M., Kirian, R. A., Kirkwood, H., Kim, Y., Koliyadu, J., Lange, H., Letrun, R., Lübke, J., Michelat, T., Morgan, A. J., Roth, N., Sato, T., Sikorski, M., Schulz, F., Spence, J. C. H., Vagovic, P., Wollweber, T., Worbs, L., Yefanov, O., Zhuang, Y., Maia, F. R. N. C., Horke, D. A., Küpper, J., Loh, N. D., Mancuso, A. P. & Chapman, H. N. (2021). *Optica*, **8**, 15–23.
- Bolhuis, P. G., Frenkel, D., Mau, S.-C. & Huse, D. A. (1997). *Nature*, **388**, 235–236.
- Carnis, J., Kirner, F., Lapkin, D., Sturm, S., Kim, Y. Y., Baburin, I. A., Khubbutdinov, R., Ignatenko, A., Iashina, E., Mistonov, A., Steegmans, T., Wieck, T., Gemming, T., Lubk, A., Lazarev, S.,

- Sprung, M., Vartanyants, I. A. & Sturm, E. V. (2021). *Nanoscale*, **13**, 10425–10435.
- Clark, N. A., Ackerson, B. J. & Hurd, A. J. (1983). *Phys. Rev. Lett.* **50**, 1459–1462.
- Conway, J. H. & Sloane, N. J. A. (2013). *Sphere Packings, Lattices and Groups*. New York: Springer.
- Decking, W., Abeghyan, S., Abramian, P., Abramsky, A., Aguirre, A., Albrecht, C., Alou, P., Altarelli, M., Altmann, P., Amyan, K., Anashin, V., Apostolov, E., Appel, K., Auguste, D., Ayvazyan, V., Baark, S., Babies, F., Baboi, N., Bak, P., Balandin, V., Baldinger, R., Baranasic, B., Barbanotti, S., Belikov, O., Belokurov, V., Belova, L., Belyakov, V., Berry, S., Bertucci, M., Beutner, B., Block, A., Blöcher, M., Böckmann, T., Bohm, C., Böhnert, M., Bondar, V., Bondarchuk, E., Bonezzi, M., Borowiec, P., Bösch, C., Bösenberg, U., Bosotti, A., Böspflug, R., Bousonville, M., Boyd, E., Bozhko, Y., Brand, A., Branlard, J., Briechle, S., Brinker, F., Brinker, S., Brinkmann, R., Brockhauser, S., Brovko, O., Brück, H., Brüdgam, A., Butkowski, L., Büttner, T., Calero, J., Castro-Carballo, E., Cattalanotto, G., Charrier, J., Chen, J., Cherepenko, A., Cheskidov, V., Chiodini, M., Chong, A., Choroba, S., Chorowski, M., Churanov, D., Cichalewski, W., Clausen, M., Clement, W., Cloué, C., Cobos, J. A., Coppola, N., Cunis, S., Czuba, K., Czwalińska, M., D'Almagne, B., Dammann, J., Danared, H., de Zubiaurre Wagner, A., Delfs, A., Delfs, T., Dietrich, F., Dietrich, T., Dohlus, M., Dommach, M., Donat, A., Dong, X., Doynikov, N., Dressel, M., Duda, M., Duda, P., Eckoldt, H., Ehsan, W., Eidam, J., Eints, F., Engling, C., Englisch, U., Ermakov, A., Escherich, K., Eschke, J., Saldin, E., Faesing, M., Fallou, A., Felber, M., Fenner, M., Fernandes, B., Fernández, J. M., Feuker, S., Filippakopoulos, K., Floettmann, K., Fogel, V., Fontaine, M., Francés, A., Martin, I. F., Freund, W., Freyermuth, T., Friedland, M., Fröhlich, L., Fusetti, M., Fydrych, J., Gallas, A., García, O., García-Tabares, L., Geloni, G., Gerasimova, N., Gerth, C., Geßler, P., Gharibyan, V., Gloor, M., Głowinkowski, J., Goessel, A., Gołębiowski, Z., Golubeva, N., Grabowski, W., Graeff, W., Grebentsov, A., Grecki, M., Grevsmuehl, T., Gross, M., Grosse-Wortmann, U., Grünert, J., Grunewald, S., Grzegory, P., Feng, G., Guler, H., Gusev, G., Gutierrez, J. L., Hagge, L., Hamberg, M., Hanneken, R., Harms, E., Hartl, I., Hauberg, A., Hauf, S., Hauschildt, J., Hauser, J., Havlicek, J., Hedqvist, A., Heidbrook, N., Hellberg, F., Henning, D., Hensler, O., Hermann, T., Hidvégi, A., Hierholzer, M., Hintz, H., Hoffmann, F., Hoffmann, M., Hoffmann, M., Holler, Y., Hüning, M., Ignatenko, A., Ilchen, M., Iluk, A., Iversen, J., Iversen, J., Izquierdo, M., Jachmann, L., Jardon, N., Jastrow, U., Jensch, K., Jensen, J., Jezabek, M., Jidda, M., Jin, H., Johansson, N., Jonas, R., Kaabi, W., Kaefer, D., Kammering, R., Kapitza, H., Karabekyan, S., Karstensen, S., Kasprzak, K., Katalev, V., Keese, D., Keil, B., Kholopov, M., Killenberger, M., Kitaev, B., Klimchenko, Y., Klos, R., Knebel, L., Koch, A., Koepke, M., Köhler, S., Köhler, W., Kohlstrunk, N., Konopkova, Z., Konstantinov, A., Kook, W., Koprek, W., Körfer, M., Korth, O., Kosarev, A., Kosiński, K., Kostin, D., Kot, Y., Kotarba, A., Kozak, T., Kozak, V., Kramert, R., Krasilnikov, M., Krasnov, A., Krause, B., Kravchuk, L., Krebs, O., Kretschmer, R., Kreutzkamp, J., Kröplin, O., Krzysik, K., Kube, G., Kuehn, H., Kujala, N., Kulikov, V., Kuzminych, V., La Civita, D., Lacroix, M., Lamb, T., Lancetov, A., Larsson, M., Le Pinvidic, D., Lederer, S., Lensch, T., Lenz, D., Leuschner, A., Levenhagen, F., Li, Y., Liebing, J., Lilje, L., Limberg, T., Lipka, D., List, B., Liu, J., Liu, S., Lorbeer, B., Lorkiewicz, J., Lu, H. H., Ludwig, F., Machau, K., Maciocha, W., Madec, C., Magueur, C., Maiano, C., Maksimova, I., Malcher, K., Maltezopoulos, T., Mamoshkina, E., Manschwet, B., Marcellini, F., Marinkovic, G., Martinez, T., Martirosyan, H., Maschmann, W., Maslov, M., Matheisen, A., Mavric, U., Meißner, J., Meißner, K., Messerschmidt, M., Meyners, N., Michalski, G., Michelato, P., Mildner, N., Moe, M., Moglia, F., Mohr, C., Mohr, S., Möller, W., Mommerz, M., Monaco, L., Montiel, C., Moretti, M., Morozov, I., Morozov, P., Mross, D., Mueller, J., Müller, C., Müller, J., Müller, K., Munilla, J., Münnich, A., Muratov, V., Napoly, O., Näser, B., Nefedov, N., Neumann, R., Neumann, R., Ngada, N., Noelle, D., Obier, F., Okunev, I., Oliver, J. A., Omet, M., Oppelt, A., Ottmar, A., Oublaïd, M., Pagani, C., Paparella, R., Paramonov, V., Peitzmann, C., Penning, J., Perus, A., Peters, F., Petersen, B., Petrov, A., Petrov, I., Pfeiffer, S., Pflüger, J., Philipp, S., Pienaud, Y., Pierini, P., Pivovarov, S., Planas, M., Plawski, E., Pohl, M., Polinski, J., Popov, V., Prat, S., Prenting, J., Priebe, G., Pryscheński, H., Przygoda, K., Pyata, E., Racky, B., Rathjen, A., Ratuschni, W., Regnaud-Campderros, S., Rehlich, K., Reschke, D., Robson, C., Roeber, J., Roggli, M., Rothenburg, J., Rusiński, E., Rybaniec, R., Sahling, H., Salmani, M., Samoylova, L., Sanzone, D., Saretzki, F., Sawlanski, O., Schaffran, J., Schlarb, H., Schlösser, M., Schlott, V., Schmidt, C., Schmidt-Foehre, F., Schmitz, M., Schmökel, M., Schnautz, T., Schneidmiller, E., Scholz, M., Schöneburg, B., Schultze, J., Schulz, C., Schwarz, A., Sekutowicz, J., Sellmann, D., Semenov, E., Serkez, S., Sertore, D., Shehzad, N., Shemarykin, P., Shi, L., Sienkiewicz, M., Sikora, D., Sikorski, M., Silenzi, A., Simon, C., Singer, W., Singer, X., Sinn, H., Sinram, K., Skvorodnev, N., Smirnov, P., Sommer, T., Sorokin, A., Stadler, M., Steckel, M., Steffen, B., Steinhau-Kühl, N., Stephan, F., Stodulski, M., Stolper, M., Sulimov, A., Susen, R., Świerblewski, J., Sydło, C., Syresin, E., Sytchev, V., Szuba, J., Tesch, N., Thie, J., Thiebault, A., Tiedtke, K., Tischhauser, D., Tolkiehn, J., Tomin, S., Tonisch, F., Toral, F., Torbin, I., Trapp, A., Treyer, D., Trowitzsch, G., Trublet, T., Tschentscher, T., Ullrich, F., Vannoni, M., Varela, P., Varghese, G., Vashchenko, G., Vasic, M., Vazquez-Velez, C., Verguet, A., Vilcins-Czvitkovits, S., Villanueva, R., Visentin, B., Viti, M., Vogel, E., Volobuev, E., Wagner, R., Walker, N., Wamsat, T., Weddig, H., Weichert, G., Weise, H., Wenddorf, R., Werner, M., Wichmann, R., Wiebers, C., Wienczek, M., Wilksen, T., Will, I., Winkelmann, L., Winkowski, M., Wittenburg, K., Witzig, A., Wlk, P., Wohlenberg, T., Wojciechowski, M., Wolff-Fabris, F., Wrochna, G., Wrona, K., Yakopov, M., Yang, B., Yang, F., Yurkov, M., Zagorodnov, I., Zalden, P., Zavadtsev, A., Zavadtsev, D., Zhirnov, A., Zhukov, A., Ziemann, V., Zolotov, A., Zolotukhina, N., Zummack, F. & Zybin, D. (2020). *Nat. Photonics*, **14**, 391–397.
- Emma, P., Akre, R., Arthur, J., Bionta, R., Bostedt, C., Bozek, J., Brachmann, A., Bucksbaum, P., Coffee, R., Decker, F.-J., Ding, Y., Dowell, D., Edstrom, S., Fisher, A., Frisch, J., Gilevich, S., Hastings, J., Hays, G., Hering, P., Huang, Z., Iverson, R., Loos, H., Messerschmidt, M., Miahnahri, A., Moeller, S., Nuhn, H.-D., Pile, G., Ratner, D., Rzepiela, J., Schultz, D., Smith, T., Stefan, P., Tompkins, H., Turner, J., Welch, J., White, W., Wu, J., Yocky, G. & Gallayda, J. (2010). *Nat. Photon.* **4**, 641–647.
- Ishikawa, T., Aoyagi, H., Asaka, T., Asano, Y., Azumi, N., Bizen, T., Ego, H., Fukami, K., Fukui, T., Furukawa, Y., Goto, S., Hanaki, H., Hara, T., Hasegawa, T., Hatsui, T., Higashiyama, A., Hirono, T., Hosoda, N., Ishii, M., Inagaki, T., Inubushi, Y., Itoga, T., Joti, Y., Kago, M., Kameshima, T., Kimura, H., Kirihara, Y., Kiyomichi, A., Kobayashi, T., Kondo, C., Kudo, T., Maesaka, H., Maréchal, X. M., Masuda, T., Matsubara, S., Matsumoto, T., Matsushita, T., Matsui, S., Nagasono, M., Nariyama, N., Ohashi, H., Ohata, T., Ohshima, T., Ono, S., Otake, Y., Saji, C., Sakurai, T., Sato, T., Sawada, K., Seike, T., Shirasawa, K., Sugimoto, T., Suzuki, S., Takahashi, S., Takebe, H., Takeshita, K., Tamasaku, K., Tanaka, H., Tanaka, R., Tanaka, T., Togashi, T., Togawa, K., Tokuhisa, A., Tomizawa, H., Tono, K., Wu, S., Yabashi, M., Yamaga, M., Yamashita, A., Yanagida, K., Zhang, C., Shintake, T., Kitamura, H. & Kumagai, N. (2012). *Nat. Photon.* **6**, 540–544.
- Kam, Z. (1977). *Macromolecules*, **10**, 927–934.
- Kam, Z. (1980). *J. Theor. Biol.* **82**, 15–39.
- Kam, Z., Koch, M. H. & Bordas, J. (1981). *Proc. Natl Acad. Sci. USA*, **78**, 3559–3562.
- Kang, H.-S., Min, C.-K., Heo, H., Kim, C., Yang, H., Kim, G., Nam, I., Baek, S. Y., Choi, H.-J., Mun, G., Park, B. R., Suh, Y. J., Shin, D. C., Hu, J., Hong, J., Jung, S., Kim, S.-H., Kim, K., Na, D., Park, S. S., Park, Y. J., Han, J.-H., Jung, Y. G., Jeong, S. H., Lee, H. G., Lee, S., Lee, S., Lee, W.-W., Oh, B., Suh, H. S., Parc, Y. W., Park, S.-J., Kim, M. H., Jung, N.-S., Kim, Y.-C., Lee, M.-S., Lee, B.-H., Sung, C.-W.,

- Mok, I.-S., Yang, J.-M., Lee, C.-S., Shin, H., Kim, J. H., Kim, Y., Lee, J. H., Park, S.-Y., Kim, J., Park, J., Eom, I., Rah, S., Kim, S., Nam, K. H., Park, J., Park, J., Kim, S., Kwon, S., Park, S. H., Kim, K. S., Hyun, H., Kim, S. N., Kim, S., Hwang, S., Kim, M. J., Lim, C., Yu, C.-J., Kim, B.-S., Kang, T.-H., Kim, K.-W., Kim, S.-H., Lee, H.-S., Lee, H.-S., Park, K.-H., Koo, T.-Y., Kim, D.-E. & Ko, I. S. (2017). *Nat. Photon.* **11**, 708–713.
- Kendall, M. G. & Stuart, A. (1973). *The Advanced Theory of Statistics*. Vol. 2, New York: Hafner Publishing Company.
- Kirian, R. A. (2012). *J. Phys. B At. Mol. Opt. Phys.* **45**, 223001.
- Kittel, C. (2004). *Introduction to Solid State Physics*. Hoboken, NJ: Wiley.
- Kurta, R. P., Altarelli, M. & Vartanyants, I. A. (2016). *Advances in Chemical Physics*, Volume 161 edited by S. A. Rice and A. R. Dinner, pp. 1–40. New York: John Wiley.
- Kurta, R. P., Altarelli, M., Weckert, E. & Vartanyants, I. A. (2012). *Phys. Rev. B*, **85**, 184204.
- Kurta, R. P., Donatelli, J. J., Yoon, C. H., Berntsen, P., Bielecki, J., Daurer, B. J., DeMirci, H., Fromme, P., Hantke, M. F., Maia, F. R. N. C., Munke, A., Nettelblad, C., Pande, K., Reddy, H. K. N., Sellberg, J. A., Sierra, R. G., Svenda, M., van der Schot, G., Vartanyants, I. A., Williams, G. J., Xavier, P. L., Aquila, A., Zwart, P. H. & Mancuso, A. P. (2017). *Phys. Rev. Lett.* **119**, 158102.
- Kurta, R. P., Dronyak, R., Altarelli, M., Weckert, E. & Vartanyants, I. A. (2013). *New J. Phys.* **15**, 013059.
- Kurta, R. P., Grodd, L., Mikayelyan, E., Gorobtsov, O. Y., Zaluzhnyy, I. A., Fratoddi, I., Venditti, I., Russo, M. V., Sprung, M., Vartanyants, I. A. & Grigorian, S. (2015). *Phys. Chem. Chem. Phys.* **17**, 7404–7410.
- Lehmkühler, F., Schulz, F., Schroer, M. A., Frenzel, L., Lange, H. & Grübel, G. (2018). *IUCrJ*, **5**, 354–360.
- Lokteva, I., Koof, M., Walther, M., Grübel, G. & Lehmkühler, F. (2019). *Small*, **15**, 1900438.
- Maier, A., Lapkin, D., Mukharamova, N., Frech, P., Assalauova, D., Ignatenko, A., Khubbutdinov, R., Lazarev, S., Sprung, M., Laible, F., Löffler, R., Previdi, N., Bräuer, A., Günkel, T., Fleischer, M., Schreiber, F., Vartanyants, I. A. & Scheele, M. (2020). *Adv. Mater.* **32**, 2002254.
- Martin, A. V. (2017). *IUCrJ*, **4**, 24–36.
- Meijer, J.-M., Shabalin, A., Dronyak, R., Yefanov, O. M., Singer, A., Kurta, R. P., Lorenz, U., Gorobtsov, O., Dzhigayev, D., Gulden, J., Byelov, D. V., Zozulya, A. V., Sprung, M., Vartanyants, I. A. & Petukhov, A. V. (2014). *J. Appl. Cryst.* **47**, 1199–1204.
- Mendez, D., Watkins, H., Qiao, S., Raines, K. S., Lane, T. J., Schenk, G., Nelson, G., Subramanian, G., Tono, K., Joti, Y., Yabashi, M., Ratner, D. & Doniach, S. (2016). *IUCrJ*, **3**, 420–429.
- Mukharamova, N., Lapkin, D., Zaluzhnyy, I. A., André, A., Lazarev, S., Kim, Y. Y., Sprung, M., Kurta, R. P., Schreiber, F., Vartanyants, I. A. & Scheele, M. (2019). *Small*, **15**, 1904954.
- Niozu, A., Kumagai, Y., Nishiyama, T., Fukuzawa, H., Motomura, K., Bucher, M., Asa, K., Sato, Y., Ito, Y., Takahashi, T., You, D., Ono, T., Li, Y., Kuk, E., Miron, C., Neagu, L., Callegari, C., Di Fraia, M., Rossi, G., Galli, D. E., Pincelli, T., Colombo, A., Owada, S., Tono, K., Kameshima, T., Joti, Y., Katayama, T., Togashi, T., Yabashi, M., Matsuda, K., Nagaya, K., Bostedt, C. & Ueda, K. (2020). *IUCrJ*, **7**, 276–286.
- Pande, K., Donatelli, J. J., Malmerberg, E., Foucar, L., Bostedt, C., Schlichting, I. & Zwart, P. H. (2018). *Proc. Natl Acad. Sci. USA*, **115**, 11772–11777.
- Pedrini, B., Menzel, A., Guizar-Sicairos, M., Guzenko, V. A., Gorelick, S., David, C., Patterson, B. D. & Abela, R. (2013). *Nat. Commun.* **4**, 1647.
- Petukhov, A. V., Dolbnya, I. P., Aarts, D. G. A. L., Vroege, G. J. & Lekkerkerker, H. N. W. (2003). *Phys. Rev. Lett.* **90**, 028304.
- Saldin, D. K., Poon, H. C., Bogan, M. J., Marchesini, S., Shapiro, D. A., Kirian, R. A., Weierstall, U. & Spence, J. C. H. (2011). *Phys. Rev. Lett.* **106**, 115501.
- Saldin, D. K., Poon, H. C., Shneerson, V. L., Howells, M., Chapman, H. N., Kirian, R. A., Schmidt, K. E. & Spence, J. C. H. (2010). *Phys. Rev. B*, **81**, 174105.
- Schlothuber né Brunner, J., Maier, B., Thomä, S. L. J., Kirner, F., Baburin, I. A., Lapkin, D., Rosenberg, R., Sturm, S., Assalauova, D., Carnis, J., Kim, Y. Y., Ren, Z., Westermeier, F., Theiss, S., Borrmann, H., Polarz, S., Eychmüller, A., Lubk, A., Vartanyants, I. A., Cölfen, H., Zobel, M. & Sturm, E. V. (2021). *Chem. Mater.* **33**, 9119–9130.
- Schroer, C. G., Agapov, I., Roehlsberger, R., Wanzenberg, R., Brinkmann, R., Weckert, E. & Leemans, W. (2019). *PETRA IV: upgrade of PETRA III to the Ultimate 3DX-ray microscope. Conceptual Design Report (CDR)*. Hamburg: Deutsches Elektronen-Synchrotron DESY.
- Schulz, F., Westermeier, F., Dallari, F., Markmann, V., Lange, H., Grübel, G. & Lehmkühler, F. (2020). *Adv. Mater. Interfaces*, **7**, 2000919.
- Shabalin, A. G., Meijer, J.-M., Dronyak, R., Yefanov, O. M., Singer, A., Kurta, R. P., Lorenz, U., Gorobtsov, O. Y., Dzhigayev, D., Kalbfleisch, S., Gulden, J., Zozulya, A. V., Sprung, M., Petukhov, A. V. & Vartanyants, I. A. (2016). *Phys. Rev. Lett.* **117**, 138002.
- Wochner, P., Gutt, C., Autenrieth, T., Demmer, T., Bugaev, V., Ortiz, A. D., Duri, A., Zontone, F., Grübel, G. & Dosch, H. (2009). *Proc. Natl Acad. Sci. USA*, **106**, 11511–11514.
- Zaluzhnyy, I. A., Kurta, R. P., André, A., Gorobtsov, O. Y., Rose, M., Skopintsev, P., Besedin, I., Zozulya, A. V., Sprung, M., Schreiber, F., Vartanyants, I. A. & Scheele, M. (2017a). *Nano Lett.* **17**, 3511–3517.
- Zaluzhnyy, I. A., Kurta, R. P., Scheele, M., Schreiber, F., Ostrovskii, B. I. & Vartanyants, I. A. (2019). *Materials*, **12**, 3464.
- Zaluzhnyy, I. A., Kurta, R. P., Sulyanova, E. A., Gorobtsov, O. Y., Shabalin, A. G., Zozulya, A. V., Menushenkov, A. P., Sprung, M., Ostrovskii, B. I. & Vartanyants, I. A. (2015). *Phys. Rev. E*, **91**, 042506.
- Zaluzhnyy, I. A., Kurta, R. P., Sulyanova, E. A., Gorobtsov, O. Y., Shabalin, A. G., Zozulya, A. V. P., Menushenkov, A., Sprung, M., Krówczyński, A., Górecka, E., Ostrovskii, B. I. & Vartanyants, I. A. (2017b). *Soft Matter*, **13**, 3240–3252.



Cite this: *Nanoscale*, 2021, **13**, 10425

Exploring the 3D structure and defects of a self-assembled gold mesocrystal by coherent X-ray diffraction imaging†

Jerome Carnis,^{†a} Felizitas Kirner,^{†b} Dmitry Lapkin,^{†a} Sebastian Sturm,^{†c} Young Yong Kim,^{†a} Igor A. Baburin,^d Ruslan Khubbutdinov,^{a,e} Alexandr Ignatenko,^a Ekaterina Iashina,^f Alexander Mistonov,^f Tristan Steegemans,^b Thomas Wieck,^c Thomas Gemming,^{†c} Axel Lubk,^c Sergey Lazarev,^{†a,g} Michael Sprung,^a Ivan A. Vartanyants^{†a,e} and Elena V. Sturm^{†b}

Mesocrystals are nanostructured materials consisting of individual nanocrystals having a preferred crystallographic orientation. On mesoscopic length scales, the properties of mesocrystals are strongly affected by structural heterogeneity. Here, we report the detailed structural characterization of a faceted mesocrystal grain self-assembled from 60 nm sized gold nanocubes. Using coherent X-ray diffraction imaging, we determined the structure of the mesocrystal with the resolution sufficient to resolve each gold nanoparticle. The reconstructed electron density of the gold mesocrystal reveals its intrinsic structural heterogeneity, including local deviations of lattice parameters, and the presence of internal defects. The strain distribution shows that the average superlattice obtained by angular X-ray cross-correlation analysis and the real, "multidomain" structure of a mesocrystal are very close to each other, with a deviation less than 10%. These results will provide an important impact to understanding the fundamental principles of structuring and self-assembly including ensuing properties of mesocrystals.

Received 22nd March 2021,
Accepted 18th May 2021

DOI: 10.1039/d1nr01806j

rsc.li/nanoscale

1. Introduction

Assembling of individual nanocrystals (NCs) in an organized superstructure offers the possibility of combining the physical properties of the individual NCs, like surface plasmon reso-

nances or superparamagnetism, with other physical properties provided by the superstructure, such as mechanical stiffness or geometric coordination.^{1,2} NCs can be self-assembled into a superstructure, which is also known as a mesocrystal, where the separate NCs share a common crystallographic orientation.^{3–5} Among suitable building blocks for mesocrystals, gold nanoparticles have attracted special attention due to the prospect of utilizing their surface plasmon resonance properties. For example, a cancer-selective amplification of chemoradiation with plasmonic nanobubbles has been reported for clusters of gold nanoparticles.^{6,7} Similarly, gold mesocrystals show high potential in the detection of traces of chemical species using surface-enhanced Raman scattering (SERS).^{8–13}

In these applications, both the shape and size of the NCs as well as their mutual arrangement are highly influential on the plasmonic properties.¹⁴ In particular, the crystallographic structure of the assemblies (mesocrystals) determines the coupling strength and coherent superposition of the NCs plasmon polariton modes, which leads to the measured enhancement of the electromagnetic field^{13,15} and the emergence of hybridized plasmon bands.¹⁶ Moreover, when anisotropic NCs are arranged in a mesocrystalline structure, coupling and amplification of directional physical properties can be expected.⁴

While the plasmonic properties of individual nanoparticles or two-dimensional (2D) assemblies can be easily character-

^aDeutsches Elektronen-Synchrotron DESY, Notkestrasse 85, D-22607 Hamburg, Germany. E-mail: ivan.vartanyants@desy.de

^bUniversity of Konstanz, Universitätsstraße 10, 78457 Konstanz, Germany. E-mail: elena.sturm@uni-konstanz.de

^cLeibniz Institute for Solid State and Materials Research, Helmholtzstraße 20, 01069 Dresden, Germany

^dTU Dresden, Bergstraße 66b, 01062 Dresden, Germany

^eNational Research Nuclear University MEPhI (Moscow Engineering Physics Institute), Kashirskoe shosse 31, 115409 Moscow, Russia

^fSaint-Petersburg State University, University Embankment 7/9, 199034 St Petersburg, Russia

^gNational Research Tomsk Polytechnic University (TPU), pr. Lenina 30, 634050 Tomsk, Russia

†Electronic supplementary information (ESI) available: Experimental methods (chemicals and materials, synthesis of gold seeds, synthesis of gold spheres), phase retrieval (data preprocessing, iterative phasing parameters, resolution estimation), structural analysis of mesocrystal base on reconstructed electron density (dilatation maps, strain tensor component maps, model of an ideal crystal strained by the measured superlattice strain). Movies S1–S6. See DOI: 10.1039/d1nr01806j

‡These authors contributed equally to this work.

ized and related to the particle shape and size, the evaluation of optical responses from three-dimensional (3D) superstructures is not straight forward and requires exact knowledge not only of the internal symmetry, translational, and orientational order of the building blocks within the superlattice, but also structural heterogeneity (*e.g.* presence of defects). This knowledge is also important for the fundamental understanding of the phase behavior of nanocubes during the self-assembly process as well as the stability of superstructures.^{17–19}

Previously, we presented a detailed structural characterization of PbS and iron oxide mesocrystalline superstructures using the combination of different transmission electron microscopy (TEM) techniques (including imaging, electron diffraction, high resolution TEM, electron tomography and electron holography).^{20–24} TEM is capable to resolve very small structures, but quickly reaches an application limit for multi-layered superstructures and larger mesocrystals, in particular if composed of more than 20 nm sized gold particles due to their strong electron scattering and absorption. In the few micrometers thick 2D layers of mesocrystals, the structural relationship between the atomic lattice and superlattice of nanocrystals can be studied by X-ray nanodiffraction and angular X-ray cross-correlation analysis (AXCCA) techniques.^{25–29} Also recent developments in application of synchrotron-based small and wide angle X-ray scattering (SAXS and WAXS) techniques allow to resolve bulk structure of self-assembled mesocrystals in terms of symmetry of superlattice and orientational order of nanoparticles,^{30–32} as well as track in real time the self-assembly process.^{33–35} However, to fully understand the mesocrystal formation process and to get insight into the fundamental principles of structure–property relationship of such complex material, detailed high resolution characterization of local structure is crucial. To study the structure of mesocrystals in a non-destructive way and resolve potential defects, we use here coherent X-ray diffraction imaging (CXDI).^{36–38}

The CXDI is a lens-less imaging technique that makes use of the coherence properties of the X-ray beam. When a finite object is illuminated by a coherent X-ray beam, interferences between the incoming wavefront and the scattered beams generate a diffraction pattern, which can be recorded in the far-field by a 2D detector with proper sampling.³⁹ By stepwise rotating the sample and recording 2D diffraction patterns, one can measure a full 3D diffraction pattern and then use iterative algorithms to determine the 3D electron density of a sample.^{40,41} A complex amplitude object is reconstructed, whose modulus is directly related to the object's electron density in the forward scattering geometry.³⁹ To classify the shape of individual nano-particles composing mesocrystals experiments at X-ray free-electron lasers (XFEL) may be performed.^{42,43} CXDI technique has already been applied successfully to a colloidal grain of silica nanospheres (diameter 230 nm), where the accuracy of the determined positions of each colloidal sphere in the lattice was ~ 9 nm.⁴⁴ Here, we push forward this approach to solve the structure of a gold mesocrystal grain self-assembled from 60 nm sized gold nanocubes.

2. Results and discussion

The gold NCs stabilized by cetyltrimethylammonium chloride (CTAC) were synthesized in a three-step seed-mediated method (Fig. S1–S4†),²¹ purified by centrifugation and assembled (Fig. S5†) to faceted mesocrystals (slightly distorted tetragonal prisms, see Fig. 1 and Fig. S6 in ESI†) using depletion forces (see Methods and ESI† for details).

To perform a detailed structural characterization of the superstructure by CXDI, a rectangular cuboid with dimensions about $1.25 \mu\text{m} \times 1.25 \mu\text{m} \times 1.5 \mu\text{m}$ was cut from the central part of one of the grown mesocrystals using a focused ion beam (FIB) and was mounted on a tungsten micromanipulator tip (see Fig. 2).

The CXDI measurements were performed at the Coherence Applications Beamline P10, at the PETRA III (DESY, Germany) storage ring. A sketch of the experimental setup is shown in Fig. 2 (see Methods for details). The stack of 2D diffraction patterns measured in our experiment was interpolated into an orthonormal frame, resulting in a 3D reciprocal space map of our grain (see for details ESI, Movie S1†).

An isosurface of this 3D diffraction pattern is shown in Fig. 3a. One can distinguish streaks with interference fringes at low scattering angles in Fig. 3b, which is due to interference of coherent X-rays on the opposite facets of the mesocrystal. In addition, several orders of superlattice reflections at larger wave vector transfer values can be observed. Between the Bragg peaks, we measured a complex speckle pattern, which encodes the local information about the relative positions of scatterers in the mesocrystal. The direct beam was masked, corresponding to the white area in the center of diffraction pattern as shown in Fig. 3b. In Fig. 3c, an angular average of the diffraction intensities is shown. Although we are dealing with a single-domain mesocrystal, Bragg peaks are broadened due to the highly defective structure of the ensemble. Near $q_z \sim \pm 0.1 \text{ nm}^{-1}$, in Fig. 3b, Bragg peaks are split, which suggests the presence of defects in the superlattice.⁴⁵ The first evaluation of

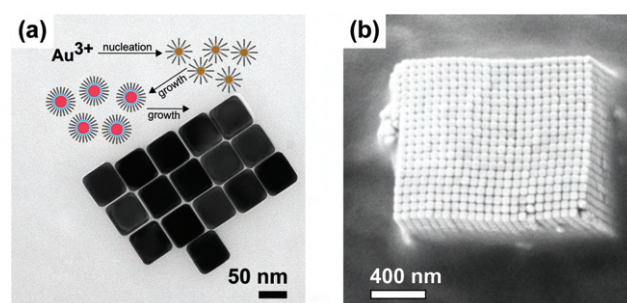


Fig. 1 Synthesis of gold nanoparticles and mesocrystals. (a) TEM image of gold nanocubes stabilized by CTAC and synthesized using a seed-mediated approach. (b) SEM image of the self-assembled gold mesocrystal prior to FIB preparation for the CXDI measurements.

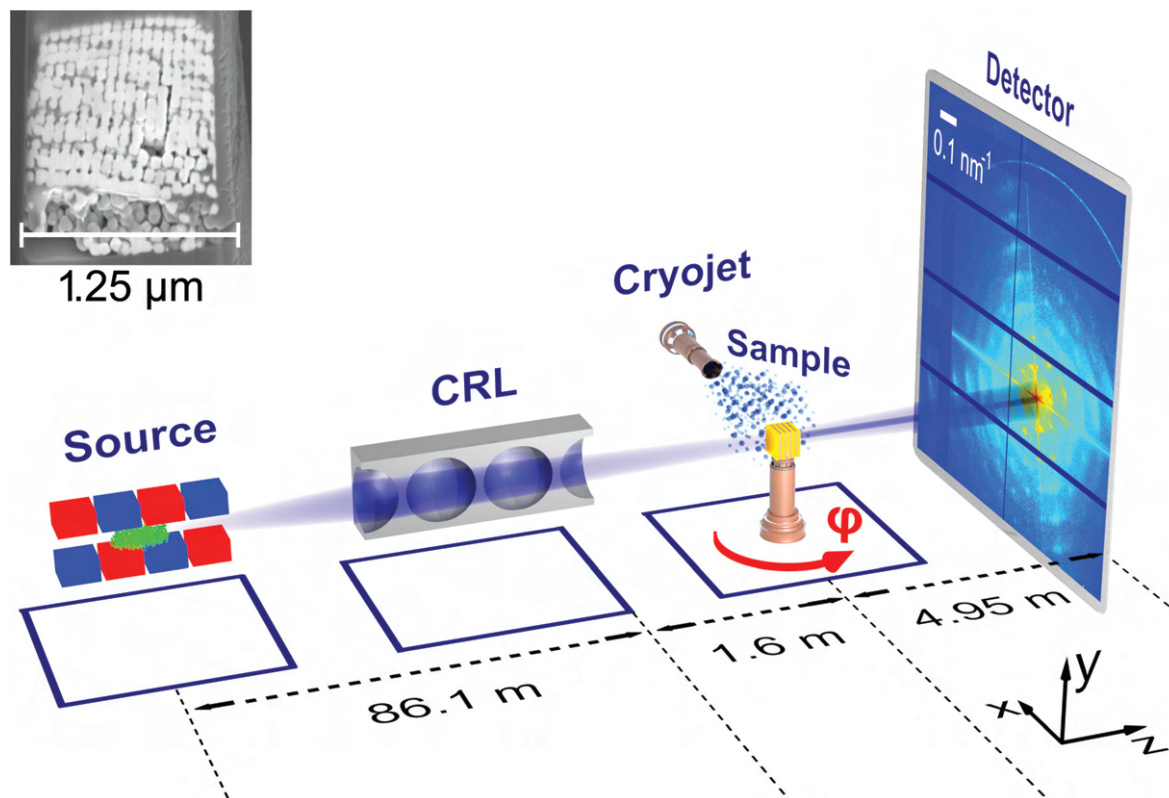


Fig. 2 Schematic layout of the experiment. A monochromatic X-ray beam of 8.7 keV from the undulator source is focused by the Compound Refractive Lenses (CRL) to a spot larger than the mesocrystal grain. The sample was cooled using a liquid nitrogen cryostat. The far field diffraction patterns were measured by a photon counting EIGER X 4M detector positioned downstream the sample. The 3D diffraction map is obtained by rotating the sample around the vertical axis. In the inset, an SEM image of the mesocrystal grain is shown. The laboratory frame convention for the coordinate system is shown in the figure.

the angular averaged X-ray diffraction profile shown in Fig. 3c suggests a simple cubic symmetry (space group $Pm\bar{3}m$) of the superlattice with a lattice parameter $a \sim 62$ nm.

We further analyzed the 3D reciprocal space data by means of the AXCCA technique,^{25–29} which can provide more information about the superlattice structure. This method was specifically modified to perform analysis in 3D reciprocal space (see for details ESI†). We calculated the cross-correlation functions (CCFs) $C(q_1, q_2, \Delta)$ (see ESI† for definition) between the most prominent peaks in the reciprocal space radial profile of Fig. 3c, at momentum transfer values $q_1 = 0.104 \text{ nm}^{-1}$, $q_2 = 0.144 \text{ nm}^{-1}$, $q_3 = 0.172 \text{ nm}^{-1}$, and $q_4 = 0.208 \text{ nm}^{-1}$. The most representative CCFs are shown in Fig. 4a–c (see ESI† for the full set of CCFs). The CCFs reflect angular correlations between the Bragg peaks from the mesocrystalline lattice. The observed peaks in the CCFs do not perfectly fit the initially expected simple cubic lattice model of the mesocrystalline structure. Simulating peak positions for a primitive lattice (space group $P1$) shown in Fig. 4d, we found the optimal angles between the lattice basis vectors. Combining these data with the intensity profiles along the main crystallographic directions ($[100]$, $[010]$ and $[001]$) we obtain the following unit cell parameters in real space: $a = b = 63.2 \pm 0.1$ nm, $c = 62.2 \pm 0.1$ nm, $\alpha = \beta = 75 \pm 1^\circ$, $\gamma = 90 \pm 1^\circ$.

This average primitive cell can actually be identified to have a higher symmetry and corresponds to a primitive cell of a centred monoclinic lattice that has the following parameters in the conventional setting $I2/m$: $a = 62.2$ nm, $b = 89.38$ nm, $c = 88.25$ nm, $\beta = 109.52^\circ$ (see Fig. S12a in ESI†). For convenience, however, we prefer to use the original primitive setting (see Fig. 4d) in the whole manuscript.

The anisotropy of the form-factor of the cubic NCs provides an additional information about the angular orientation of the NCs inside the superlattice. The form-factor maxima are located along the normal to the facets of the NCs. Thus, one can study the angular position of the NCs form-factor maxima with respect to the Bragg peaks and further determine the NC orientation with respect to the superlattice crystallographic axes in real space. The angular position of corresponding maxima was obtained by correlating the simulated form-factor for a cubic NC of the size of 59 ± 1 nm with the experimental intensities at $q = 0.477 \text{ nm}^{-1}$ (see ESI† for details). This q value is the most suitable one to calculate correlations, since it corresponds to one of the maxima of the form-factor, and does not contain any structure factor features. As a result, we obtained an averaged real space model of the entire unit cell including the oriented NCs that is shown in Fig. 4d. The facets of the NCs are aligned neither with the (001) plane, which is

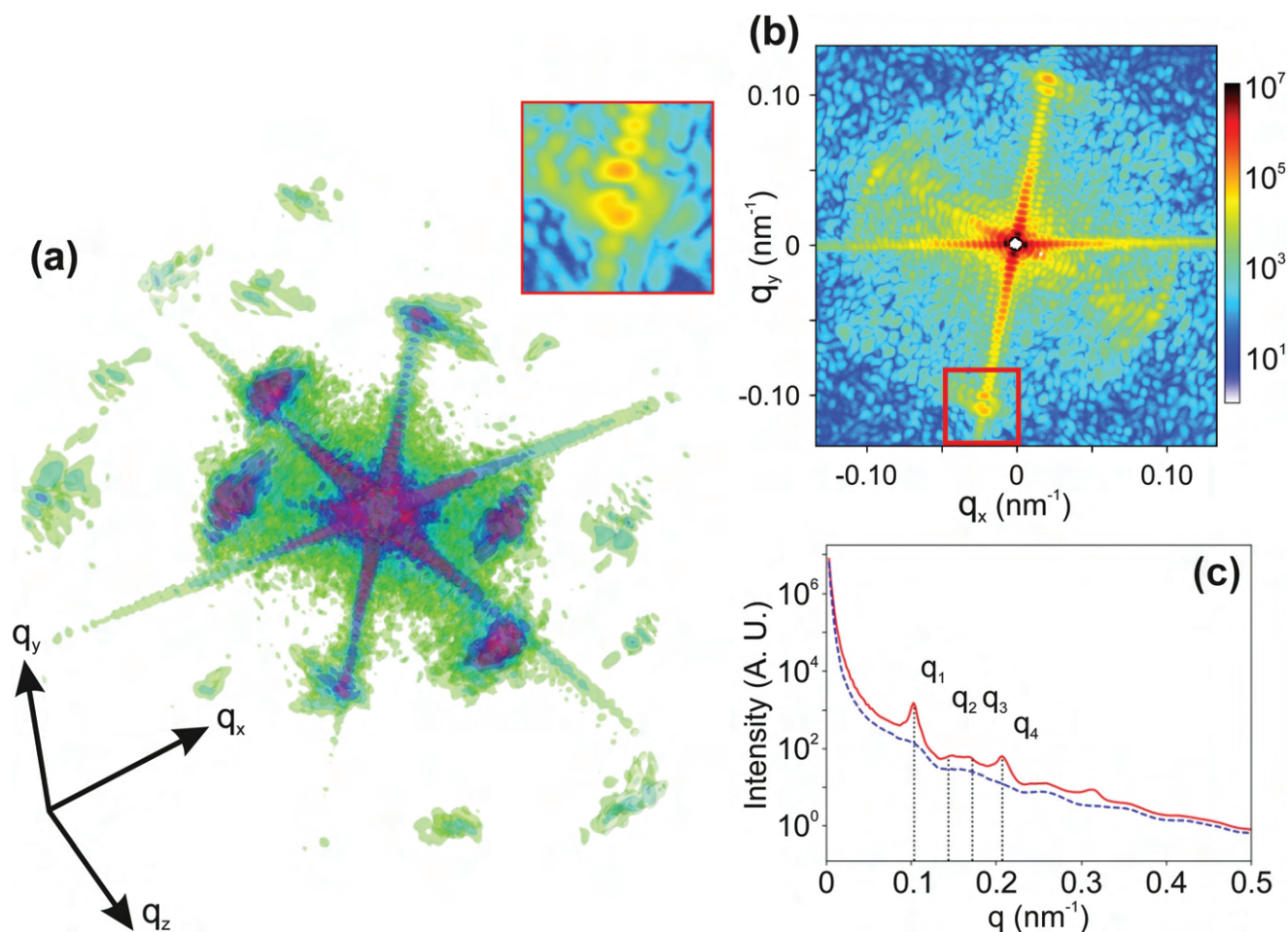


Fig. 3 Diffraction patterns measured in the CXDI experiment. (a) Isosurface view (from 54% to 72% level) of the 3D diffraction pattern from the mesocrystalline grain shown in SEM image in the inset of Fig. 2. The data has been gridded onto the orthonormal laboratory frame. The length of coordinate arrows corresponds to 0.1 nm^{-1} . (b) Slice at the center of the interpolated diffraction pattern in the q_x, q_y plane, showing the low-angle scattering region up to the first superlattice Bragg peaks. An enlarged view of the area outlined by a red box is shown in panel (a). (c) Intensity distribution as a function of the momentum transfer value q obtained by angular averaging of the 3D diffraction pattern (red line). The blue dashed line corresponds to the median value at momentum transfer q determined from the angular averaged values. The AXCCA was performed on the data obtained by subtracting these median values from the 3D diffraction pattern shown in (a). The vertical dotted lines correspond to the momentum transfer values used in the AXCCA: $q_1 = 0.104 \text{ nm}^{-1}$, $q_2 = 0.144 \text{ nm}^{-1}$, $q_3 = 0.172 \text{ nm}^{-1}$, and $q_4 = 0.208 \text{ nm}^{-1}$. Note, that intensities in all panels are given in logarithmic scale.

parallel to the substrate surface, nor with the $[001]$ axis, but are tilted by an angle $\delta \approx 7^\circ$ with respect to this axis. We would like to note here that reciprocal space analysis provides information about the average structure over the whole mesocrystalline grain only. Local structural features are resolved only by employing phase retrieval to reconstruct the electron density of the whole grain.

The 3D diffraction pattern was inverted to a real space 3D electron density map using iterative phase retrieval reconstruction algorithms,^{40,41} providing a full overview of the internal structure of the mesocrystal (see for details Methods and ESI Movie S2†). An isosurface of the reconstructed mesocrystal together with 2D slices parallel to (100) , (010) and (001) planes of the superlattice is shown in Fig. 5 and ESI Fig. S13 and Movies S3 and S4.† The first striking observation is that CXDI

can fully resolve individual nanocubes. The voxel size of the reconstruction is $9.4 \text{ nm} \times 9.4 \text{ nm} \times 9.4 \text{ nm}$, while the resolution estimated by the phase-retrieval transfer function⁴⁶ (PRTF) is $\sim 21 \text{ nm}$ (see ESI and Fig. S7†), which is smaller than the 60 nm size of the individual NCs. The reconstructed structure is tilted in the vertical direction, in agreement with the unit cell parameters of the superlattice obtained by the AXCCA.

The 2D slices of the electron density of the mesocrystalline grain (see Fig. 5b–d) show the presence of several type of defects including point defects, lattice bending, crack, and voids. One could argue that the structure was damaged during sample preparation by the FIB. Indeed, it has been shown that FIB milling can induce a dislocation network in the outer layers of gold NCs.⁴⁷ However, this effect is expected to be limited to the first few tens of nanometers at the surface of the

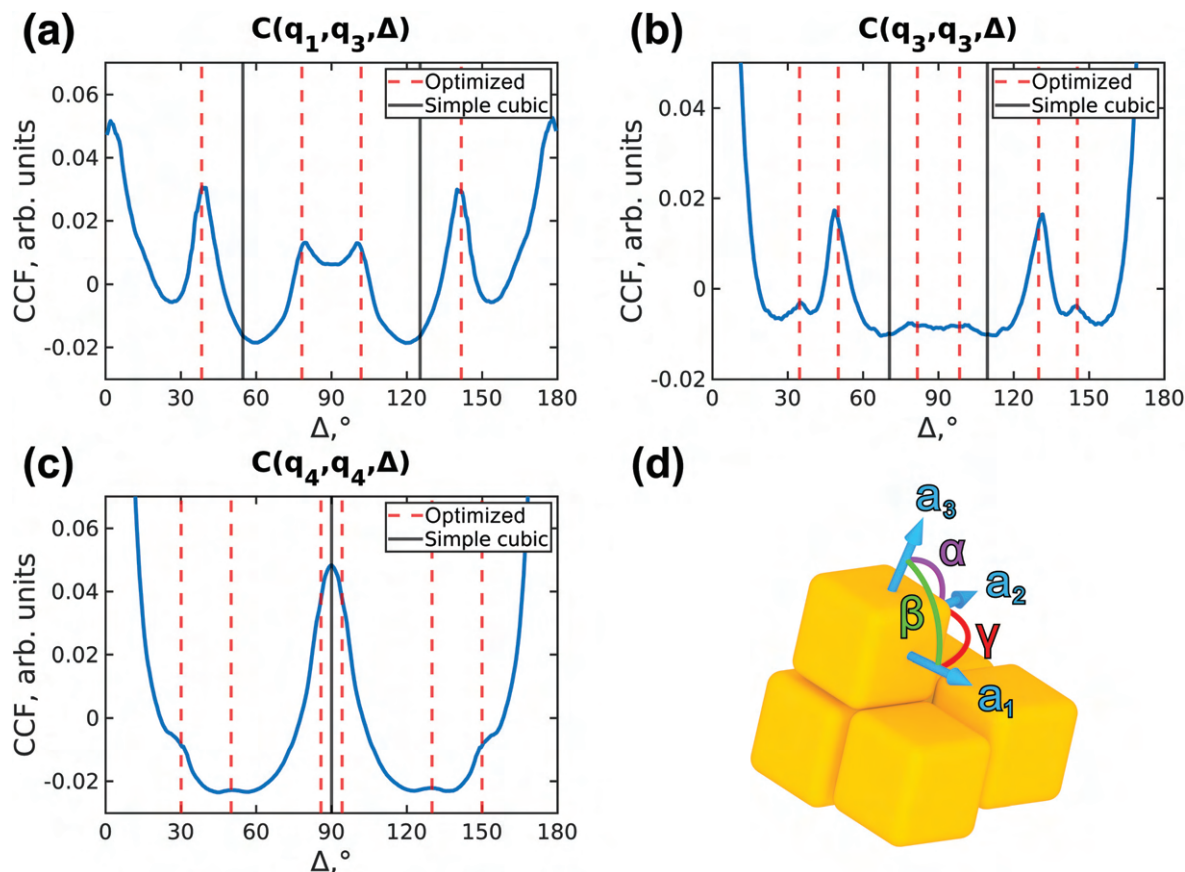


Fig. 4 Angular X-ray cross-correlation functions (CCFs) $C(q_1, q_2, \Delta)$. The CCFs were calculated at the following momentum transfer values (a) $q_1 = 0.104 \text{ nm}^{-1}$ and $q_3 = 0.172 \text{ nm}^{-1}$, (b) $q_3 = 0.172 \text{ nm}^{-1}$, and (c) $q_4 = 0.208 \text{ nm}^{-1}$. The corresponding peak positions for the optimized unit cell are shown with red dashed lines. The peak positions for a simple cubic unit cell are shown with black lines. (d) A real space model of the average optimized unit cell, with $a = b = 63.2 \pm 0.1 \text{ nm}$, $c = 62.2 \pm 0.1 \text{ nm}$, $\alpha = \beta = 75 \pm 1^\circ$, $\gamma = 90 \pm 1^\circ$. The orientation of the nanocubes within the superlattice is revealed by analysis of the anisotropic form-factor.

object, which does not explain the high inhomogeneity of the mesocrystal structure. Consequently, the defects are likely formed during the crystal growth or the post-growth deformation processes (including the crystal contraction during the drying processes and solvent evaporation or by further propagation of existing internal cracks during FIB sample preparation). Defects of both origins are important since application of mesocrystals often requires the material in a dry state.

It is also evident from the reconstructed electron density (see Fig. 5 and Fig. S13 in ESI†), that the packing order of nanoparticles within (001) planes increases substantially in the first three layers from the substrate (ESI Movies S3b and S4b†). We would like to note, that these (001) planes are parallel to the substrate and basal plane of mesocrystals and are perpendicular to the growth direction. In general, the ordering within (001) planes is also much higher than within (100) and (010) planes (see Fig. 5 and Fig. S13e–g in ESI†). These findings are consistent with the layer growth mechanism of mesocrystals, proceeding by particle-by-particle attachment to the facet grown parallel to the substrate. In addition, during the drying process (e.g. solvent evaporation) the nonhomogeneous contraction of the mesocrystal occurs mainly perpendicular to

the basal plane and additional shear stress induces the formation of additional cracks and voids, which mainly propagate perpendicular to substrate (see Fig. 5 and Fig. S13 in ESI†). The most prominent here is a large crack through the entire mesocrystal, visible on the right side of Fig. 5b and c, following the (010) plane, where its zigzag nature suggests a post-growth deformation during the drying process as origin of the crack formation.

To perform a more detailed analysis of the crystal's intrinsic heterogeneity, the 3D reconstructed electron density map was analyzed with a blob detection algorithm to extract the position of the individual NCs within the superlattice (see ESI, section S5†). The assigned position of individual NCs was further used to determine the local variations of packing order with respect to the average superlattice determined by the AXCCA. To do so, we aligned the averaged superlattice positions with the particle positions detected by the algorithm at the middle of the mesocrystal grain. The obtained displacement map clearly visualizes the lattice distortion across the entire 3D volume of the mesocrystal (Fig. 6a). The shift of nanoparticle positions from their averaged value within the superlattice is most significant close to the structural defects

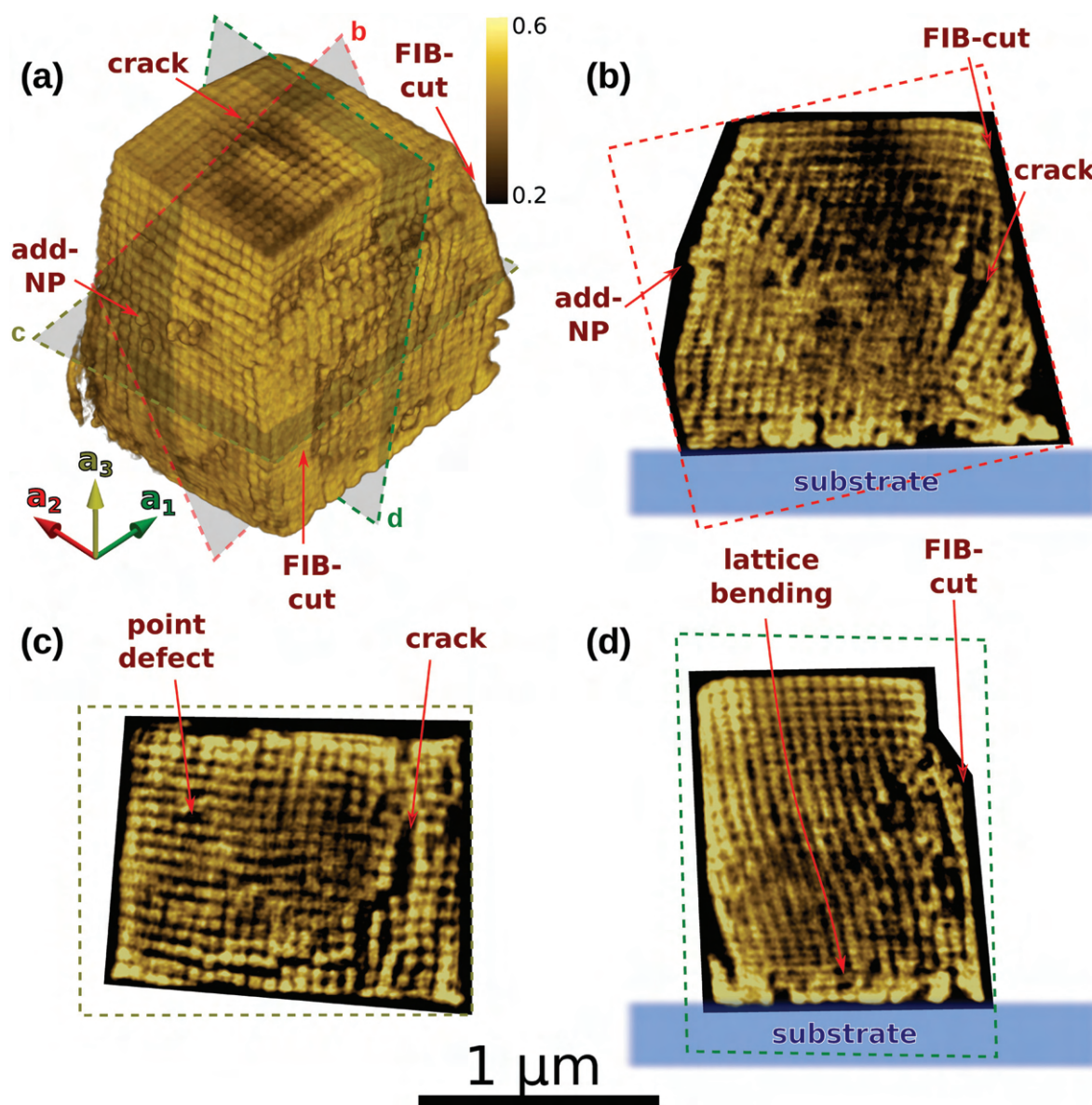


Fig. 5 Reconstructed 3D electron density of the Au mesocrystal grain. (a) Volume rendering of the reconstructed 3D electron density with the position of 2D slices used further to analyze the structure. (b–d) 2D slices parallel to (010) (b), (001) (c) and (100) (d) crystallographic planes through the center of the reconstructed mesocrystal with highlighted superlattice defects.

(see Fig. 5, for comparison). For example, the crack is again clearly visible at the right side of the mesocrystal grain. Furthermore, one can see that for the first three layers from the substrate, the whole lattice plane is still significantly displaced in comparison to the average lattice. The upper left part of the crystal appears to be sheared approximately half a unit cell in a diagonal direction.

In Fig. 6b, examples of extracted local primitive unit cells together with corresponding Voronoi–Dirichlet polyhedron (VDP), also known as the Wigner–Seitz cell for a 3D periodic lattice, at different positions within the mesocrystal are shown. The parameters and geometry of VDP constructed around the “central particle” of each selected cell illustrate the changes of

the local symmetry in the arrangement of nearest neighbours (*e.g.* coordination shell) and coordination number (CN) equal to the number of facets.^{48,49} The magnitude of the dimensionless second moment of inertia of the VDP, normalized to its volume (so-called G_3 -factor) can be used to estimate the degree of distortion of the coordination shell (*e.g.* for cubes G_3 is equal to $1/12 \approx 0.0833$, for cuboctahedra $19/[192(2)^{1/3}] \approx 0.0785$, and for spheres $(1/5)(3/4\pi)^{2/3} \approx 0.0770$).^{48,50} In comparison to cubic VDP of the simple cubic cell (CN is 6; number of vertices is 8, see Fig. 6c), the more complex VDP of the averaged unit cell determined by AXCCA has 12 facets (CN = 12) and 18 vertices with $G_3 = 0.0810$ (Fig. 6c). Interestingly, although the VDPs constructed for the several selected primitive cells (Fig. 6b) have 14 facets

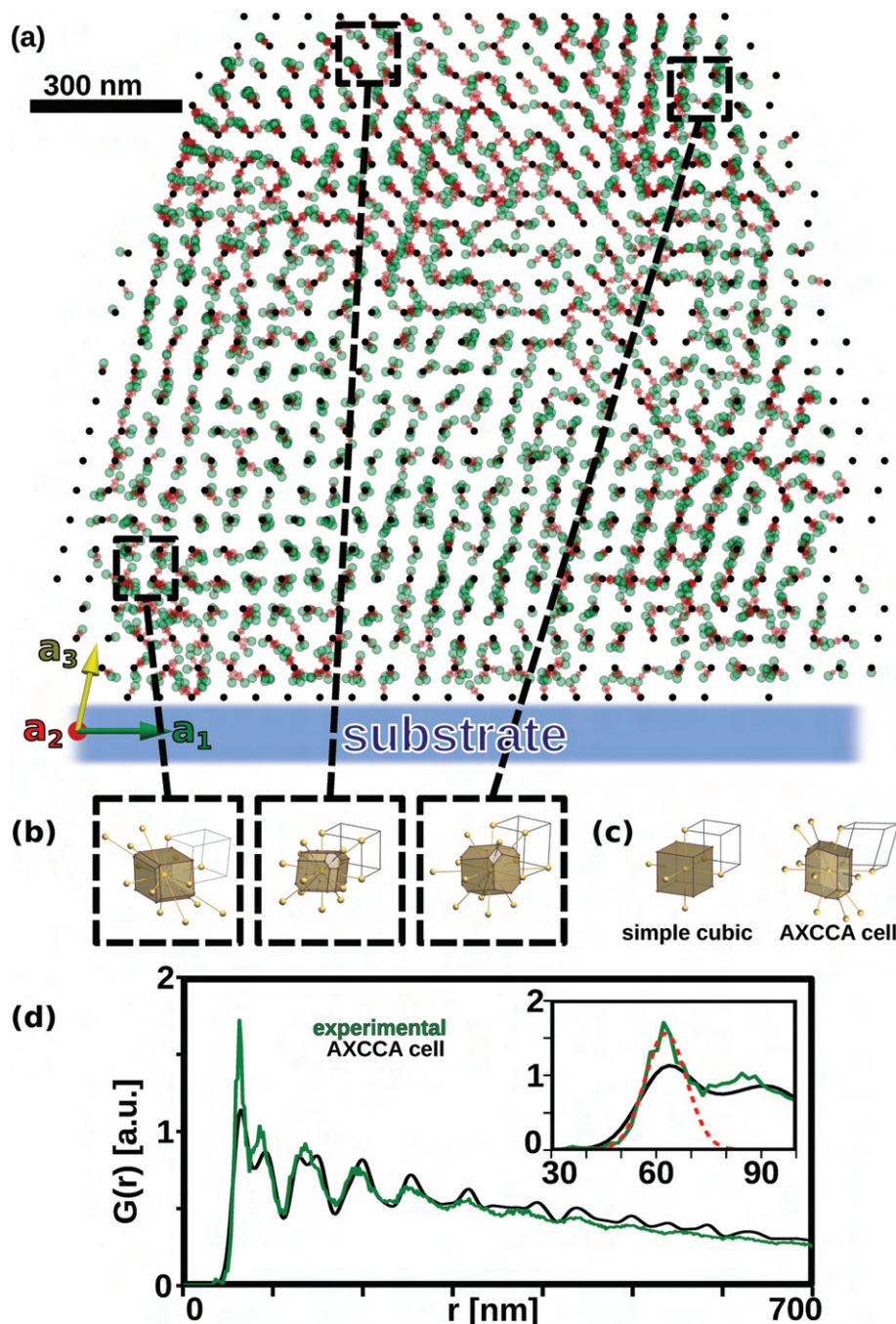


Fig. 6 Structure analysis of the Au mesocrystal grain. (a) Displacement map (red arrows) of the 3D superlattice, obtained based on positions of detected nanoparticles (green dots) with respect to an average superlattice (black dots) with unit cell parameters determined by the AXCCA. The two lattices were aligned at the center of the grain (b) Selected Voronoi–Dirichlet polyhedrons illustrating the change of local symmetry of the arrangement and the number of coordinating particles (G_3 from left to right: 0.0831, 0.0820, 0.0813). (c) Constructed Voronoi–Dirichlet polyhedrons of simple cubic lattice ($G_3 = 0.0833$) and the average superlattice unit cell determined by the AXCCA ($G_3 = 0.0811$). (d) Pair-distribution functions (PDF) obtained for two datasets. First, based on the positions of the detected nanoparticles shown in panel (a) by green dots (green line) and, second, based on an average superlattice unit cell determined by the AXCCA shown by black dots in panel (a) (black line). In the inset an enlarged part of the first two peaks of the PDF-function is shown. The first peak of the experimental curve was fitted by a Gaussian function (red line) which has its maximum position at 62.7 nm and standard deviation 5.9 nm.

(CN = 14), the G_3 parameter varies only from 0.0812 to 0.0831 (just between the values of an ideal simple cubic and experimental cells determined by the AXCCA).

It is worth to note, that the averaged AXCCA lattice can be seen as a distorted primitive cubic arrangement of the particles where each particle has 6 nearest neighbours and

additionally 6 next-nearest neighbours, as evidenced by the faces of the VDP (see Fig. S12a and b in ESI†). The distortion can be understood as follows: the square layers of a simple cubic lattice with the parameters $a = b = 62.2$ nm, $\gamma = 90^\circ$ are sheared against each other (see Fig. S12b in ESI†). The distortions can be attributed both to the smoothed polyhedral shape of the particles that drives the whole arrangement in the direction of a close packing, and to the defects of the structure. Thus, it is not surprising, that the G_3 values calculated from experimental data are very close to the G_3 of the VDP in the simple cubic cell, showing that although the real symmetry of the superlattice cell is lower, its topology deviates only slightly from the simple cubic arrangement. This deviation might be also a result of the tilting of our slightly truncated gold NCs within the superlattice as indicated by the AXCCA (Fig. 4d). This allows to achieve a more efficient space-filling arrangement in accordance with the so-called “bump-to-hollow” packing principle known for molecular crystals⁵¹ and also reported for other mesocrystalline self-assembled structures.^{18,22}

In addition, we also calculated the pair distribution function (PDF) based on the detected positions of individual nanocrystals within the superlattice (see Fig. 6d). The PDF confirmed that the short-range order of the nanoparticles is close to an arrangement with the average cell, while the long-range order (at higher distances r) is significantly disturbed due to the presence of defects and lattice deformations in the real structure of the mesocrystal. The first peak of the PDF curve was fitted by a Gaussian function (see Fig. 6d, inset), revealing that the average distance to the neighbouring particles of the first coordination shell is around 62.7 nm and that the precision of the detected particle positions (given by the standard deviation) is better than 5.9 nm, since the spread includes also the particle displacements due to lattice deformations.

Although the displacement map already gives a good understanding of the large lattice deformation across the whole mesocrystal volume, we additionally extracted a complete superlattice strain map. As a tool to describe the deformation of the superlattice, we defined the superlattice strain tensor as the deviation of the actually observed structure of a mesocrystal compared to the defect free lattice model (determined by the AXCCA) in analogy to the linear elasticity theory for atomic lattices⁵² (see ESI† for details). This linear model, which neglects higher order derivatives, is of course only valid for small deformations. Although formally analogous to the strain as defined in linear elasticity theory (Hooke's law), herein it is merely used as a tool to describe the deviation of the observed experimental structure from the average model. Here, we are not aiming to distinguish an elastic and plastic deformation, nor can we say anything about the stress of the system. In addition, the superlattice dilatation (that is a sum of diagonal elements of the strain tensor) can easily be retrieved, giving a direct visualization of local lattice contractions and expansions (see Fig. 7 and ESI Fig. S14–S23 and Movie S5†). Fig. 7a and b illustrates the highly mosaic structure of the mesocrystal. Even though there are many local fluctuations in the crystal structure, there certainly seems to be a tendency of positive dilatation (lattice expansion) in the vicinity of the huge crack.

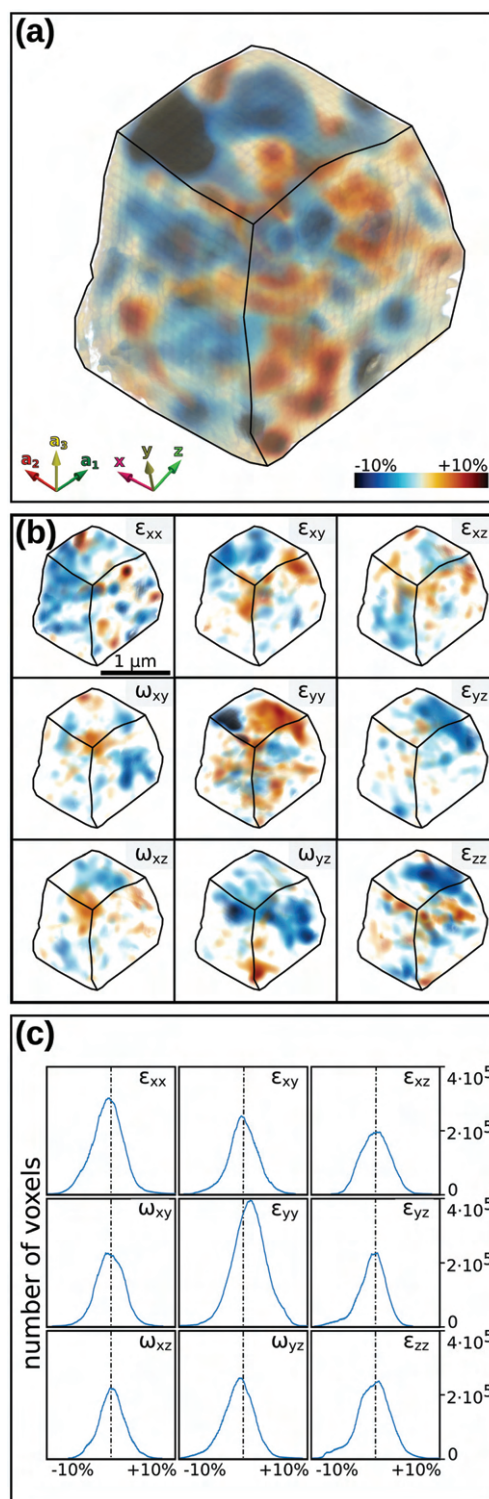


Fig. 7 Structural heterogeneity of the Au mesocrystal grain. (a) Volume rendering of a 3D dilatation map of the superlattice. (b) Volume rendering of 3D maps of the strain tensor components ($\epsilon_{xx} - \epsilon_{zz}$) and rotations ($\omega_{xy} - \omega_{yz}$). The magnitude of strain is illustrated by the color scale in panel (a). (c) Histograms of the strain tensor components and rotations.

The individual strain ε_{ij} and rotation ω_{ij} components can be found in Fig. 7b and Fig. S15–S23 in ESI.† The most obvious feature is the “bipolar” structure, for example, in ε_{xy} and ω_{yz} , which is consistent with the lattice bending, and can be observed in the slices in Fig. 5 and Fig. S16, S23 in ESI.† The calculated strain tensor and rotation components are quantitatively summarized in the histograms (Fig. 7c). The measured strain in all components is in a reasonable range of $\pm 10\%$. The sharpest distribution is shown by the ε_{yy} tensor component, which is closest to the a_3 growth direction of the mesocrystal. In order to verify the fidelity of our calculated superlattice strain, we reapplied the strain to an ideal crystal lattice (*i.e.* averaged superlattice determined by the AXCCA) and were able to reproduce most structural features of the experimentally measured mesocrystal (see ESI Fig. S24 and Movie S6†).

3. Conclusions

In conclusion, we have used a combination of the angular X-ray cross-correlation analysis and coherent X-ray diffractive imaging, to study the 3D structure of a gold mesocrystal. The achieved resolution of 21 nm allowed imaging of individual nanocubes in the mesocrystal grain. Importantly, the precision of the detected particle positions was better than 6 nm. The results reveal a strongly defective structure of the mesocrystal with overall monoclinic symmetry. This technique shows a strong potential in systems that cannot be studied by classical optical or electron microscopy methods and contributes to a better understanding of structural features of self-assembled mesocrystals and especially intrinsic structural heterogeneity (including deviation of crystal symmetry, variation of lattice parameter, distribution of defects and strains). Importantly, the real mesocrystal structure was analyzed with unprecedented detail, calculating a displacement map and the entire strain tensor of the whole specimen.

The unexplored deformation behavior and related changes in structure and functional properties of nanoparticles superlattices limit their promising implementation into devices.⁵³ Therefore, the precise determination of their crystal structure and especially intrinsic structural heterogeneity is crucial for understanding this complex behavior. The proposed methodological approach could be used not only to perform such non-destructive structural characterization of nanostructured materials, but also to build more adequate structural models which in turn could serve as a basis for the precise prediction of the physical properties of nanoparticles self-assemblies using the computational methods.

4. Experimental Section

4.1. Synthesis of gold nanocubes

The synthesis of gold nanocubes was performed by a three-step seed-mediated growth method based on a previously described procedure.²¹ First, small gold seeds are synthesized

which are grown to spheres in a second step (see section S1 of ESI†). These spheres are then processed for the synthesis of cubic particles. An aqueous solution of HAuCl_4 (1.00 mL, 0.01 M) and an aqueous solution of hexadecylpyridinium chloride (CPC) (50.00 mL, 0.10 M) were mixed in a glass vial (100 mL) and tempered to 27 °C. An aqueous solution of ascorbic acid (0.75 mL, 0.10 M) was added, followed by a rapid injection of 400 μL of washed spheres. The solution turned pinkish red and was kept at 27 °C for 3 h. The gold nanocubes are collected by centrifugation at 9000 rpm for 5 min and redispersed in 0.02 M CPC solution. The cubes were characterized by TEM and UV/Vis (Fig. S2†), the single crystalline nature of the particles was proven using electron diffraction (Fig. S3†).

4.2. Preparation of gold mesocrystals

An aqueous solution having approximately 10^{11} particles per mL and a CPC concentration of 0.02 M was prepared. 400 μL of this solution were filled in a 1 mL shell vial with a silicon wafer ($7 \times 5 \text{ mm}^2$). The solution was carefully overlaid with 400 μL of 25 wt% cetyltrimethylammonium chloride (CTAC) in H_2O . An exemplary setup can be found in Fig. S5.† After 12 h, the solution was carefully removed, and the silicon wafer was washed with acetone to yield mesocrystals (Fig. S6†).

4.3. X-ray experiment

Monochromatic X-rays of 8.7 keV were focused down to ~ 2.4 (H) \times 2.0 (V) μm^2 at the sample position completely covering the mesocrystal grain. An electron microscopy image of the sample mounted on the tip is shown in the inset in Fig. 2. The polymer tip was fixed on a rotation stage around the vertical axis. At each angular position, the 2D far-field diffraction pattern was recorded by the EIGER X 4M detector positioned 4.95 m downstream from the sample. The sample was rotated by steps of 0.5° over a range of 180° and, by that, the full 3D diffraction pattern was measured. At each angular position, a series of 10 frames of 0.2 s exposure each were measured, corresponding to 2 s accumulated exposure to the non-attenuated X-ray beam, giving in total 18 min of measurements per sample. The sample was cooled using a liquid nitrogen cryostat, in order to avoid radiation damage of the organic ligands stabilizing NCs which could induce the NCs coalescence and destroy the superlattice ordering.

4.4. Iterative phasing

Phase retrieval was carried out on the interpolated diffracted intensity data using PyNX package,⁵⁴ imposing at each iteration that the calculated Fourier intensity of the current object agrees with the measured 3D data. The metric used to estimate the goodness of the fit during phasing was the free log-likelihood,⁵⁵ available in PyNX. Defective pixels for experimental data and gaps in the detector were not used for imposing the reciprocal space constraint mentioned above and thus were evolving freely during phasing.

The initial support was estimated from the autocorrelation function of the 3D diffraction intensity that included only the first superlattice Bragg peaks. For larger reciprocal space this

support was correspondingly rescaled. While the iterative phase retrieval this support was evolved by application of the “shrink-wrap algorithm”.⁵⁶ A series of 3600 relaxed averaged alternating reflections⁵⁷ plus 200 Error-Reduction⁴⁰ (ER) steps, including “shrink-wrap” algorithm⁵⁶ every 20 iterations were used. The phasing process included implementation of the Lucy–Richardson deconvolution that takes into account partial coherence effects.⁵⁸ The resulting point spread function is shown in Fig. S7a–c of ESI.† To ensure the best reconstruction possible, we kept only the best 10 reconstructions from 1000 with random phase start and performed the mode decomposition.⁵⁵ The weight of the most prominent mode which was considered as a final result was 69%.

Author contributions

I.A.V., E.V.S. designed the study. The samples were synthesized by F.K. The FIB cut preparation were performed by T.W., S.S., T. G. Scanning electron microscopy measurements were realized by F.K., S.S. Data acquisition was performed by J.C., Y.Y.K., R.K., A.I., E.I., A.M., S.L., M.S., I.A.V. The CXDI data analysis was performed by J.C. The AXCCA was performed by D.L. The structural analysis of reconstructed electron density was performed by S. S., I.A.B., A.L., E.V.S. The manuscript was written by J.C., F.K., D.L., S.S., A.L., I.A.B., I.A.V., E.V.S. All authors have given approval to the final version of the manuscript.

Conflicts of interest

There are no conflicts to declare.

Acknowledgements

We acknowledge DESY (Hamburg, Germany), a member of the Helmholtz Association HGF, for the provision of experimental facilities. Parts of this research were carried out at PETRA III synchrotron facility and we would like to thank the beamline staff for assistance in using Coherence Application P10 beamline. This work was supported by the Helmholtz Associations Initiative Networking Fund (grant no. HRSF-0002) and the Russian Science Foundation (grant no. 18-41-06001); DFG (Deutsche Forschungsgemeinschaft) within the SFB 1214 (TP: B1). J. C. would like to thank Vincent Favre-Nicolin for his continuous improvement of the PyNX package used here for phase retrieval. S. S. and A. L. acknowledge funding from the European Research Council (ERC) under the Horizon 2020 research and innovation program of the European Union (grant agreement number 715620). S. L. acknowledges Competitiveness Enhancement Program Grant of Tomsk Polytechnic University and the Governmental program “Science,” project no. FSWW-2020-0014. E. S. thanks Res. Prof. Alexander Shtukenberg for the fruitful discussion and the Zukunftskolleg at the University of Konstanz and “Konstanzia Transition” program of Equal Opportunity Council for finan-

cial support. The authors acknowledge support of the project by Prof. Edgar Weckert and careful reading of the manuscript by Dr Thomas Keller.

References

- 1 L. Zhou and P. O'Brien, *J. Phys. Chem. Lett.*, 2012, **3**, 620–628.
- 2 D. V. Talapin, J. S. Lee, M. V. Kovalenko and E. V. Shevchenko, *Chem. Rev.*, 2010, **110**, 389–458.
- 3 H. Cölfen and S. Mann, *Angew. Chem., Int. Ed.*, 2003, **42**, 2350–2365.
- 4 E. V. Sturm and H. Cölfen, *Chem. Soc. Rev.*, 2016, **45**, 5821–5833.
- 5 E. V. Sturm and H. Cölfen, *Crystals*, 2017, **7**, 207.
- 6 E. Y. Lukianova-Hleb, X. Ren, R. R. Sawant, X. Wu, V. P. Torchilin and D. O. Lapotko, *Nat. Med.*, 2014, **20**, 778–784.
- 7 E. Y. Lukianova-Hleb, X. Ren, J. A. Zasadzinski, X. Wu and D. O. Lapotko, *Adv. Mater.*, 2012, **24**, 3831–3837.
- 8 B. Kim, S. L. Tripp and A. Wei, *J. Am. Chem. Soc.*, 2001, **123**, 7955–7956.
- 9 A. Wei, B. Kim, B. Sadtler and S. L. Tripp, *ChemPhysChem*, 2001, **2**, 743–745.
- 10 Z. Zhu, H. Meng, W. Liu, X. Liu, J. Gong, X. Qiu, L. Jiang, D. Wang and Z. Tang, *Angew. Chem., Int. Ed.*, 2011, **50**, 1593–1596.
- 11 R. A. Alvarez-Puebla, A. Agarwal, P. Manna, B. P. Khanal, P. Aldeanueva-Potel, E. Carbo-Argibay, N. Pazos-Perez, L. Vigderman, E. R. Zubarev, N. A. Kotov and L. M. Liz-Marzan, *Proc. Natl. Acad. Sci. U. S. A.*, 2011, **108**, 8157–8161.
- 12 C. Matricardi, C. Hanske, J. L. Garcia-Pomar, J. Langer, A. Mihi and L. M. Liz-Marzan, *ACS Nano*, 2018, **12**, 8531–8539.
- 13 K. Bian, H. Schunk, D. Ye, A. Hwang, T. S. Luk, R. Li, Z. Wang and H. Fan, *Nat. Commun.*, 2018, **9**, 2365.
- 14 Y. Ma, W. Li, E. C. Cho, Z. Li, T. Yu, J. Zeng, Z. Xie and Y. Xia, *ACS Nano*, 2010, **4**, 6725–6734.
- 15 C. Hamon, M. N. Sanz-Ortiz, E. Modin, E. H. Hill, L. Scarabelli, A. Chuvilin and L. M. Liz-Marzan, *Nanoscale*, 2016, **8**, 7914–7922.
- 16 L. Sun, H. Lin, K. L. Kohlstedt, G. C. Schatz and C. A. Mirkin, *Proc. Natl. Acad. Sci. U. S. A.*, 2018, **115**, 7242–7247.
- 17 F. Smalenburg, L. Filion, M. Marechal and M. Dijkstra, *Proc. Natl. Acad. Sci. U. S. A.*, 2012, **109**, 17886–17890.
- 18 L. Rossi, V. Soni, D. J. Ashton, D. J. Pine, A. P. Philipse, P. M. Chaikin, M. Dijkstra, S. Sacanna and W. T. Irvine, *Proc. Natl. Acad. Sci. U. S. A.*, 2015, **112**, 5286–5290.
- 19 M. Kapuscinski, M. Agthe, Z. P. Lv, Y. Liu, M. Segad and L. Bergström, *ACS Nano*, 2020, **14**, 5337–5347.
- 20 P. Simon, E. Rosseeva, I. A. Baburin, L. Liebscher, S. G. Hickey, R. Cardoso-Gil, A. Eychmuller, R. Kniep and W. Carrillo-Cabrera, *Angew. Chem., Int. Ed.*, 2012, **51**, 10776–10781.

- 21 F. Kirner, P. Potapov, J. Schultz, J. Geppert, M. Müller, G. González-Rubio, S. Sturm, A. Lubk and E. Sturm, *J. Mater. Chem. C*, 2020, **8**, 10844–10851.
- 22 J. Brunner, I. A. Baburin, S. Sturm, K. Kvashnina, A. Rossberg, T. Pietsch, S. Andreev, E. Sturm (née Rosseeva) and H. Cölfen, *Adv. Mater. Interfaces*, 2017, **4**, 1600431.
- 23 J. J. Brunner, M. Krumova, H. Cölfen and E. V. Sturm, *Beilstein J. Nanotechnol.*, 2019, **10**, 894–900.
- 24 P. Simon, L. Bahrig, I. A. Baburin, P. Formanek, F. Roder, J. Sickmann, S. G. Hickey, A. Eyhmüller, H. Lichte, R. Kniep and E. Rosseeva, *Adv. Mater.*, 2014, **26**, 3042–3049.
- 25 I. A. Zaluzhnyy, R. P. Kurta, A. André, O. Y. Gorobtsov, M. Rose, P. Skopintsev, I. Besedin, A. V. Zozulya, M. Sprung and F. Schreiber, *Nano Lett.*, 2017, **17**, 3511–3517.
- 26 N. Mukharamova, D. Lapkin, I. A. Zaluzhnyy, A. Andre, S. Lazarev, Y. Y. Kim, M. Sprung, R. P. Kurta, F. Schreiber, I. A. Vartanyants and M. Scheele, *Small*, 2019, **15**, e1904954.
- 27 A. Maier, D. Lapkin, N. Mukharamova, P. Frech, D. Assalauova, A. Ignatenko, R. Khubbutdinov, S. Lazarev, M. Sprung, F. Laible, R. Löffler, N. Previdi, A. Bräuer, T. Günkel, M. Fleischer, F. Schreiber, I. A. Vartanyants and M. Scheele, *Adv. Mater.*, 2020, **32**, e2002254.
- 28 R. P. Kurta, M. Altarelli and I. A. Vartanyants, *Adv. Chem. Phys.*, 2016, **161**, 1–39.
- 29 I. A. Zaluzhnyy, R. P. Kurta, M. Scheele, F. Schreiber, B. I. Ostrovskii and I. A. Vartanyants, *Materials*, 2019, **12**, 3464.
- 30 B. Lee, K. Littrell, Y. Sha and E. V. Shevchenko, *J. Am. Chem. Soc.*, 2019, **141**, 16651–16662.
- 31 Z.-P. Lv, M. Kapuscinski and L. Bergström, *Nat. Commun.*, 2019, **10**, 4228.
- 32 X. Huang and Z. Wang, *Materials*, 2019, **12**, 3771.
- 33 E. Josten, E. Wetterskog, A. Glavic, P. Boesecke, A. Feoktystov, E. Brauweiler-Reuters, U. Rücker, G. Salazar-Alvarez, T. Brückel and L. Bergström, *Sci. Rep.*, 2017, **7**, 2802.
- 34 M. Agthe, T. S. Plivelic, A. Labrador, L. Bergström and G. Salazar-Alvarez, *Nano Lett.*, 2016, **16**, 6838–6843.
- 35 X. Huang, J. Zhu, B. Ge, F. Gerdes, C. Klinke and Z. Wang, *J. Am. Chem. Soc.*, 2021, **143**, 4234–4243.
- 36 J. W. Miao, P. Charalambous, J. Kirz and D. Sayre, *Nature*, 1999, **400**, 342–344.
- 37 M. A. Pfeifer, G. J. Williams, I. A. Vartanyants, R. Harder and I. K. Robinson, *Nature*, 2006, **442**, 63–66.
- 38 J. Miao, T. Ishikawa, I. K. Robinson and M. M. Murnane, *Science*, 2015, **348**, 530–535.
- 39 I. A. Vartanyants and O. M. Yefanov, in *X-ray Diffraction. Modern Experimental Techniques*, ed. O. H. Seeck and B. M. Murphy, Pan Stanford Publishing, Singapore, 2015, ch. 12, pp. 341–384.
- 40 J. R. Fienup, *Appl. Opt.*, 1982, **21**, 2758–2769.
- 41 S. Marchesini, *Rev. Sci. Instrum.*, 2007, **78**, 011301.
- 42 D. H. Cho, Z. Shen, Y. Ihm, D. H. Wi, C. Jung, D. Nam, S. Kim, S.-Y. Park, K. S. Kim, D. Sung, H. Lee, J.-Y. Shin, J. Hwang, S. Y. Lee, S. Y. Lee, S. W. Han, D. Y. Noh, N. D. Loh and C. Song, *ACS Nano*, 2021, **15**, 4066–4076.
- 43 K. Ayyer, P. L. Xavier, J. Bielecki, Z. Shen, B. J. Daurer, A. K. Samanta, S. Awel, R. Bean, A. Barty, M. Bergemann, T. Ekeberg, A. D. Estillore, H. Fangohr, K. Giewekemeyer, M. S. Hunter, M. Karnevskiy, R. A. Kirian, H. Kirkwood, Y. Kim, J. Koliyadu, H. Lange, R. Letrun, J. Lübke, T. Michelat, A. J. Morgan, N. Roth, T. Sato, M. Sikorski, F. Schulz, J. C. H. Spence, P. Vagovic, T. Wollweber, L. Worbs, O. Yefanov, Y. Zhuang, F. R. N. C. Maia, D. A. Horke, J. Küpper, N. D. Loh, A. P. Mancuso and H. N. Chapman, *Optica*, 2021, **8**, 15–23.
- 44 A. G. Shabalin, J. M. Meijer, R. Dronyak, O. M. Yefanov, A. Singer, R. P. Kurta, U. Lorenz, O. Y. Gorobtsov, D. Dzhigaev, S. Kalbfleisch, J. Gulden, A. V. Zozulya, M. Sprung, A. V. Petukhov and I. A. Vartanyants, *Phys. Rev. Lett.*, 2016, **117**, 138002.
- 45 M. Dupraz, G. Beutier, D. Rodney, D. Mordehai and M. Verdier, *J. Appl. Crystallogr.*, 2015, **48**, 621–644.
- 46 H. N. Chapman, A. Barty, S. Marchesini, A. Noy, S. P. Hau-Riege, C. Cui, M. R. Howells, R. Rosen, H. He, J. C. Spence, U. Weierstall, T. Beetz, C. Jacobsen and D. Shapiro, *J. Opt. Soc. Am. A*, 2006, **23**, 1179–1200.
- 47 F. Hofmann, E. Tarleton, R. J. Harder, N. W. Phillips, P. W. Ma, J. N. Clark, I. K. Robinson, B. Abbey, W. Liu and C. E. Beck, *Sci. Rep.*, 2017, **7**, 45993.
- 48 V. A. Blatov, *Crystallogr. Rev.*, 2007, **10**, 249–318.
- 49 V. A. Blatov, A. P. Shevchenko and D. M. Proserpio, *Cryst. Growth Des.*, 2014, **14**, 3576–3586.
- 50 E. V. Peresyphkina and V. A. Blatov, *Russ. J. Inorg. Chem.*, 2003, **48**, 237–245.
- 51 A. I. Kitaigorodkij, *Organic Chemical Crystallography*, 1961.
- 52 L. D. Landau, L. P. Pitaevskii, A. M. Kosevich and E. M. Lifshitz, *Theory of Elasticity*, Elsevier Science, 3rd edn, 2012.
- 53 D. Giuntini, S. Zhao, T. Krekeler, M. Li, M. Blankenburg, B. Bor, G. Schaan, B. Domènech, M. Müller, I. Scheider, M. Ritter and G. A. Schneider, *Sci. Adv.*, 2021, **7**, eabb6063.
- 54 O. Mandula, M. E. Aizarna, J. Eymery, M. Burghammer and V. Favre-Nicolin, *J. Appl. Crystallogr.*, 2016, **49**, 1842–1848.
- 55 V. Favre-Nicolin, S. Leake and Y. Chushkin, *Sci. Rep.*, 2020, **10**, 1–8.
- 56 S. Marchesini, H. He, H. N. Chapman, S. P. Hau-Riege, A. Noy, M. R. Howells, U. Weierstall and J. C. H. Spence, *Phys. Rev. B: Condens. Matter*, 2003, **68**, 140101.
- 57 D. R. Luke, *Inverse Probl.*, 2004, **21**, 37.
- 58 J. N. Clark, X. Huang, R. Harder and I. K. Robinson, *Nat. Commun.*, 2012, **3**, 993.

Morphogenesis of Magnetite Mesocrystals: Interplay between Nanoparticle Morphology and Solvation Shell

Julian Schlotheuber né Brunner, Britta Maier, Sabrina L. J. Thomä, Felizitas Kirner, Igor A. Baburin, Dmitry Lapkin, Rose Rosenberg, Sebastian Sturm, Dameli Assalauova, Jerome Carnis, Young Yong Kim, Zhe Ren, Fabian Westermeier, Sebastian Theiss, Horst Borrmann, Sebastian Polarz, Alexander Eychmüller, Axel Lubk, Ivan A. Vartanyants, Helmut Cölfen, Mirijam Zobel, and Elena V. Sturm*

Cite This: *Chem. Mater.* 2021, 33, 9119–9130

Read Online

ACCESS |

Metrics & More

Article Recommendations

Supporting Information

ABSTRACT: Nanoparticle assemblies with long-range packing order and preferred crystallographic orientation of building blocks, i.e., *mesocrystals*, are of high interest not only because of their unique physical properties but also due to their complex structure and morphogenesis. In this study, faceted mesocrystals have been assembled from the dispersion of truncated cubic-shaped iron oxide nanoparticles stabilized by oleic acid (OA) molecules using the nonsolvent “gas phase diffusion technique” into an organic solvent. The effects of synthesis conditions as well as of the nanoparticle size and shape on the structure and morphogenesis of mesocrystals were examined. The interactions of OA-capped iron oxide nanoparticles with solvent molecules were probed by analytical ultracentrifugation and double difference pair distribution function analysis. It was shown that the structure of the organic shell significantly depends on the nature and polarity of solvent molecules. For the nonpolar solvents, the interaction of the aliphatic chains of OA molecules with the solvent molecules is favorable and the chains extend into the solvent. The solvation shell around the nanoparticles is more extended in nonpolar and more compact in polar solvents. There is a clear trend for more spherical particles to be assembled into the *fcc* superlattice, whereas less truncated cubes form rhombohedral and tetragonal structures. The observed changes in packing symmetry are reminiscent of structural polymorphism known for “classical” (atomic and molecular) crystals.



INTRODUCTION

The synthesis of nanocrystals and their self-assembly into superstructures is of major importance in current materials science^{1–3} because nanocrystals frequently show exceptional size-dependent properties in comparison to their bulk material.^{4–6} The nanoparticle assemblies not only maintain some of these size-dependent properties but can additionally benefit from collective properties resulting from the interaction of nanoparticles.^{7–12}

Ordered assemblies of nanocrystals have been termed differently in the scientific literature over time, ranging from colloidal crystals, mosaic crystals, supracrystals, supercrystals, and superlattices (SL) to mesocrystals.^{13–18} The latter term is now commonly accepted and used for the assemblies in which orientational (crystallographic) ordering of the crystalline building blocks takes place.^{19–21} Hence, in the most strict sense, mesocrystals (so-called type I) are a special class of colloidal crystals combining a long-range order of particle

packing and their preferable crystallographic orientation (i.e., atomic scale ordering).

In the past few years, many research groups have reported on assembly techniques of micrometer-sized mesocrystals of platinum, magnetite, lead sulfide, and silver, among other materials.^{8,22–30} They have shown remarkable structures of mesocrystals, which are perfectly regular and feature well-defined facets, like “classical” crystals. Commonly, nanocrystals are assembled into mesocrystals either via “drying mediated assembly methods” or via the “gas phase diffusion technique”.^{8,17,26,28,29} Often, the structure of these assemblies is characterized incompletely, with the main emphasis on the

Received: June 7, 2021

Revised: October 24, 2021

Published: November 26, 2021



study of explicit properties or specific applications of mesocrystals.^{10,12,31,32} Nevertheless, investigations with a combination of small- and wide-angle X-ray scattering techniques (SAXS and WAXS) as well as advanced microscopy techniques allow a full structural analysis of self-assembled superstructures based on nanoparticles of different compositions and shapes.^{8,18,23,25,27,29,30} The recently developed angular X-ray cross-correlation analysis (AXCCA) method allows the determination of the superlattice distortion and relative orientation of nanoparticles in mesocrystals with high precision.^{33–37} Similarly, great effort is put on how these crystals nucleate and grow and how the kinetics influence the nonclassical crystallization of mesocrystals.^{16,29,38–43} Furthermore, there are many interesting results on how growth conditions can impact the final structure of mesocrystalline films.^{44–49} Accordingly, different superlattice structures can be obtained by solvent evaporation from dispersions with different dispersion agents as well as from nanoparticles stabilized by different ligands.^{3,24} However, an understanding of the morphogenesis of macroscopic mesocrystals is still essentially lacking. Specifically, the exact parameters which influence the crystal structure and morphology, including packing arrangement and orientational order, remain largely unexplored. Nevertheless, much progress in the influence of medium properties on nanoparticle assembly processes was made by real time tracking of these processes using small-angle X-ray scattering (SAXS).²⁹ It was shown that the assembly process of iron oxide nanoparticles is significantly affected by the evaporation-driven increase of the solvent polarity, particle concentration, and excess of surfactant.²⁹ Furthermore, theoretical considerations for nanocrystals with anisotropic shapes predict the formation of liquid-crystalline and plastic-crystalline phases with orientational and translational order, respectively.⁵⁰ For superparamagnetic iron oxide nanocrystals, within the size range from 5 to 15 nm the magnitude of the magnetic dispersion interactions at zero-field was shown to be negligible in comparison to van der Waals forces between the nanoparticles.⁵¹

In recent years, our work focused on the preparation and structural characterization of self-assembled mesocrystals^{8,13,52–54} prepared from highly monodisperse truncated nanocubes of iron oxide (composed of magnetite with some inclusion of maghemite (up to ~20%)).¹³ Using TEM and SAXS we analyzed the structure of self-assembled mesocrystalline films (formed from toluene dispersion by the drying mediated technique) and showed that the orientational order of nanocrystals within an *fcc* superlattice is in line with the so-called “bump-to-hollow” packing principle¹³ known for molecular crystals (which aims to achieve the most efficient space filling).⁵⁵ We also performed the optimization of crystallization conditions in the gas phase diffusion technique and showed that the appropriate choices of substrate, dispersion, destabilizing agents, concentration of additive (acting as stabilizer and depletion agent), and nanocrystals (the size and shape distribution could be narrowed by multiple recrystallization⁵⁶) allow faceted mesocrystals to grow with sizes from a few micrometers up to the millimeter range.⁵⁷ Furthermore, we confirmed that the external magnetic field could significantly affect the assembly process and change the morphology of aggregates and orientational order of nanoparticles.⁵²

This paper aims to provide a systematic study of morphogenetic aspects of mesocrystals and represents an

important step forward compared to our previous study.^{13,52,53,56,57} Herein, we took advantage of the iron oxide nanocrystals stabilized by oleic acid (OA) as building blocks to create mesocrystalline films and large-scale faceted mesocrystals using “solvent evaporation” and “gas-phase diffusion” techniques, respectively. All experiments on nanoparticle assemblies were carried out without external magnetic field (i.e., in zero-field/the Earth magnetic field is not considered as external). First, herein we study the effect of nanoparticle variables (including size, faceting, habit) on the crystallization process and structuring of mesocrystals. Second, we show that the assembly process can be further influenced by the nature of solvent (tetrahydrofuran, toluene, cyclohexane, and heptane), nonsolvent, and excess of surfactant. For the first time, the formation of the solvation shell around oleic acid capped iron oxide nanoparticles was probed by advanced analytical techniques directly in dispersion, namely, analytical ultracentrifugation (AUC) and double difference pair distribution function (dd-PDF). The solvation shell formed in solvents with different polarities significantly influences the morphogenesis and final structure of the mesocrystals, which is also confirmed by XRD study in combination with AXCCA. A detailed structural characterization of faceted mesocrystals (in terms of packing arrangement and orientational order of nanoparticles) will be discussed in a follow-up article. Finally, we show that mesocrystals exhibit several similarities to “classical” crystals in terms of structural and morphogenetic aspects. The latter also include polymorphism of mesocrystals due to different growth conditions.

RESULTS AND DISCUSSION

The nanocrystals have been synthesized as described by Disch et al.²² Six different nanocrystal batches (batches I–VI) are characterized by different particle sizes and degrees of truncation of cubic nanocrystals (Table S1, Figures S1–S7). In addition to HRTEM images, the relative degree of truncation could be estimated by the ratio between “equivalent edge length of cube” and “minFerret” size (Figures S2–S7). The more this value deviates from 1, the higher is the degree of truncation of the cubic particles: batch I, 0.932, SD = 0.026; batch II, 0.948, SD = 0.022; batch III, 0.938, SD = 0.021; and batch IV, 0.901, SD = 0.044. These nanocrystals were assembled into mesocrystals using either an adapted approach of the “gas phase diffusion technique” (to form faceted 3D mesocrystals) or evaporation induced self-assembly (to form mesocrystalline 2D/3D films).^{13,52,56,58} The shapes of the particles from batches V and VI are best described as quasi-spherical, and they thus assembled into colloidal crystals without preferred crystallographic orientation of nanoparticles. Experimental setups of different techniques are presented in Figure 1. In the case of the gas phase diffusion technique (Figure 1a), the destabilizing diffusion phase infiltrates the nanoparticle dispersion via the gas phase. The destabilizing diffusion phase (so-called nonsolvent or poor solvent) consists of a mixture of ethanol and solvent (1:1), while tetrahydrofuran (THF), toluene, cyclohexane, and heptane were used as solvents, respectively. The mesocrystals are grown on a single-crystalline silicon substrate by destabilization of a nanoparticle dispersion containing an excess of surfactant. In the case of the solvent evaporation technique (Figure 1b), mesocrystals were grown directly on a TEM grid by evaporation of the dispersion agent from the nanocrystal dispersion.

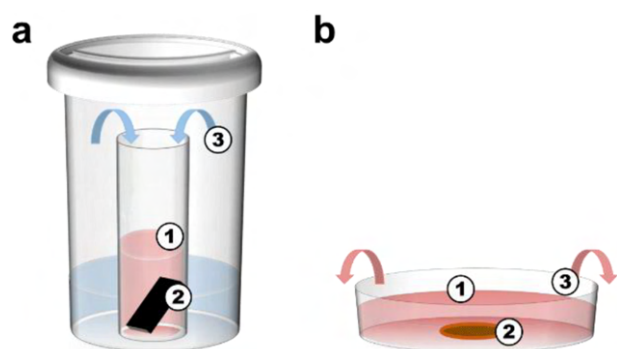


Figure 1. Schematic illustration of experimental setup. (a) Mesocrystal formation by the gas phase diffusion: a glass tube with nanoparticle dispersion (1) with a vertically positioned silicon snippet (2) stored in a glass vial containing the destabilizing diffusion phase (3). The large overall glass vial is sealed. (b) Mesocrystal formation by solvent evaporation: a substrate (2, TEM grid) is placed within the nanocrystal dispersion (1). The dispersion agent then evaporates (3).

By means of electron microscopy (imaging and electron diffraction) and X-ray diffraction (SAXS and WAXS), it was proved that ordered nanoparticle assemblies from batches I–IV could be classified as mesocrystals type I (Supporting Information, Section S2).

Effect of Nanoparticle Shape on the Mesocrystal Morphology. Mesocrystals formed under the same medium conditions but from different nanocrystal batches (batches I–IV) reveal that the habit (i.e., degree of the cube truncation) of the individual building blocks significantly influences the packing symmetry of nanoparticles and mesocrystal morphology. The effect of nanoparticle size (within the investigated range) is less pronounced and mainly depends on the ratio between inorganic core radius and thickness of the organic shell. Figure 2 illustrates faceted mesocrystals prepared by the “gas phase diffusion technique” from a toluene dispersion of magnetite nanocrystals using oleic acid as the surfactant and ethanol as the nonsolvent agent. The building blocks of the mesocrystals from all prepared nanocrystal batches were analyzed using Cs-corrected HRTEM and analytical ultracentrifugation (Table S1 and Figures 2, 3, and S1–S3). All nanoparticle batches show narrow size distributions, with nanocrystals from batch IV being significantly bigger on average than in other batches. While the truncated nanocubes from batches I–IV have a uniform crystal faceting, they differ in their crystal habit. For example, nanocrystals from batch II show the lowest degree of truncation and those from batches I and IV the highest. The shape of the particles from batches V and VI is best described as “quasi-spherical”. Detailed results of TEM investigations of mesocrystalline films prepared from nanocrystals of all six batches by means of the solvent evaporation technique are shown in Figure S5. In case of 3D faceted mesocrystals (batches I–IV) prepared by the “gas phase diffusion technique”, the morphology and the symmetry of the superlattice (i.e., translational order of nanoparticles) clearly changes when changing the crystal habit of the nanocrystals (Figure 2b,e,h,k). Starting with the smallest and highly truncated nanocubes,¹³ these building blocks lead to octahedral mesocrystals consistent with the *fcc* superlattice (Figure 2a–c). The octahedral (111) face shows the *p6mm* symmetry of nanoparticles packing within the surface layer. Nanocrystal batch II presents the least truncated building

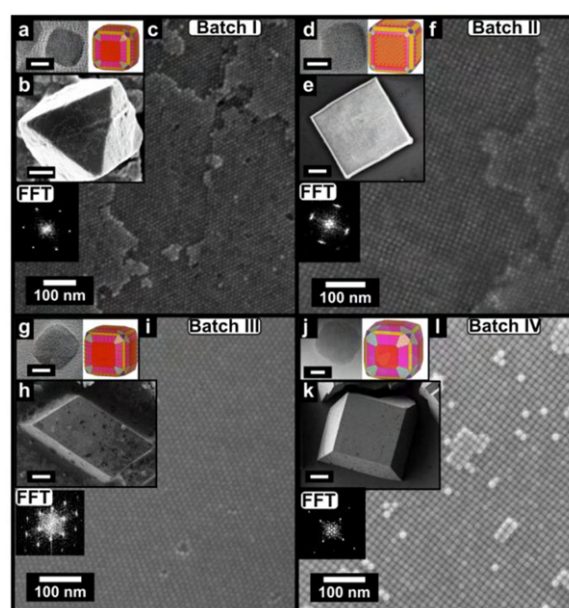


Figure 2. Illustration of mesocrystals crystallized from the toluene dispersion of different nanoparticle batches (I–IV). (a, d, g, j) Cs-corrected HRTEM images (insets, scale bars = 5 nm) of the four nanoparticle batches together with models along [114]. (b, e, h, k) Mesocrystals crystallized under similar conditions in toluene and OA as surfactant. Different morphologies are visualized: (b) An octahedral mesocrystal (*fcc* superlattice; insets, scale bar = 500 nm). (e) A tetragonal prism (*bct* superlattice; inset scale bar = 5 μm). (h) A rhombohedral mesocrystal (inset, scale bar = 10 μm). (k) A truncated tetragonal pyramid (*bct* superlattice; inset, scale bar = 10 μm). (c, f, i, l) HRSEM images and corresponding FFT of the projected mesocrystals faces showing the packing of the nanocubes. (c) For mesocrystals of batch I, a {111} face exhibiting the *p6mm* plane symmetry, (i) the rhombohedral mesocrystals exhibit on its (001) face a *c2mm* planar symmetry, and (f, k) that obtained from batches II and IV have a *p4mm* planar symmetry on its (001) basal face.

blocks, their sizes being slightly bigger than those of the nanocrystals of batch I (Figure S3). Under the given conditions, these slightly truncated nanocrystals form mesocrystals with a morphology of tetragonal prisms (Figure 2d–f, *bct* superlattice). The surface layer of the (001) basal face shows a square arrangement with *p4mm* symmetry. The truncation of nanocrystal batch III (Figure S4) is in between those of nanocrystal batches I and II. These nanocrystals self-assemble to mesocrystals with a rhombohedral morphology (Figure 2h). The symmetry of the surface layer of the basal rhombohedral face is *c2mm* (Figure 2i, FFT). Nanocrystal batch IV at the same time contains the biggest and the most highly truncated cubic building blocks (Figure S5). The morphology of the mesocrystals resulting from these nanocrystals can be described as tetragonal truncated pyramids (Figure 2j). The SEM images of the surface layers of these self-assembled magnetite mesocrystals exhibit the *p4mm* symmetry.

Remarkably, this data (Figure 2) reveals that the morphology of mesocrystals and the related packing symmetry of the nanoparticles (e.g., translational order of nanoparticles within the mesocrystals) changes drastically with an increasing degree of truncation of the cubic building blocks. In the case of self-assembly from toluene dispersion—upon the increase of nanocubes truncation (for particles with similar size)—the symmetry of the superlattice changes from rhombohedral and

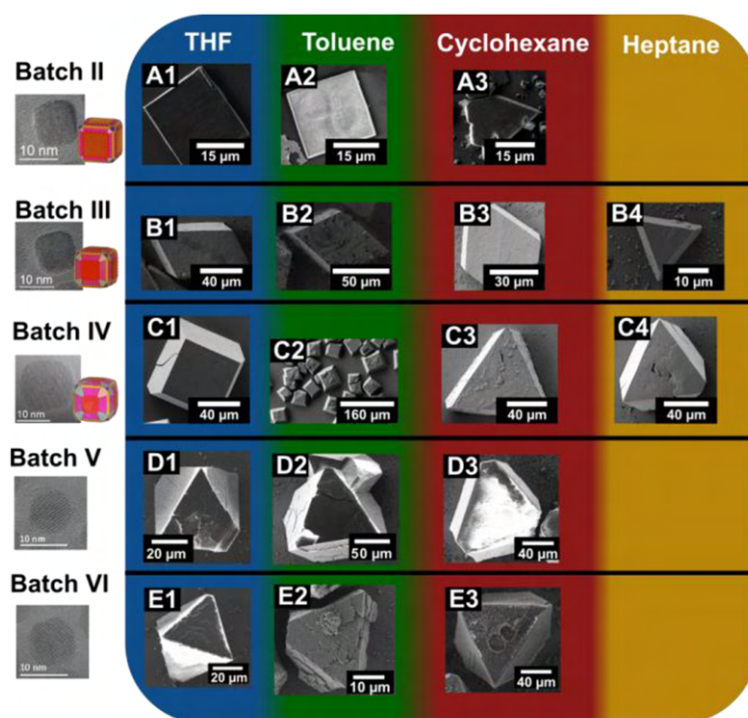


Figure 3. Mesocrystals prepared from nanocrystals dispersed in different solvents (batches II, III, IV, V, VI). Illustration of the changes of morphology of the mesocrystals by changing the solvent (from polar to nonpolar solvents). HRTEM images along [100] of the three nanocrystal batches and its approximated model (along [114]) are given (nanoparticles from batches V and VI show quasi-spherical morphology). The size of the building blocks is presented in Table S1. (A1 and A2) Batch II shows mesocrystals with a morphology of a tetragonal prisms when crystallized from toluene and THF. (A3) The morphology changes to truncated trigonal pyramids when crystallized from cyclohexane. (B1 and B2) Dispersed nanocrystals of batch III in THF and toluene lead to rhombohedral morphologies. (B3 and B4) When crystallized from cyclohexane and heptane, the morphology changes to trigonal truncated pyramids. (C1 and C2) Mesocrystals from nanocrystal batch IV show tetragonal truncated pyramids when crystallized from THF and toluene. (C3 and C4) Trigonal truncated pyramids appear from nanocrystal batch IV when crystallized from cyclohexane and heptane. (D1–E3) Batches V and VI show mesocrystals with a morphology of truncated trigonal pyramids and octahedra crystallized from THF, toluene, and cyclohexane.

bct eventually to *fcc*. The orientational order of the nanocrystals within the mesocrystalline arrays, however, is similar throughout nanocrystal batches I–IV (at least for mesocrystalline films), due to the same faceting of the nanocrystals (Figure S10).

Effect of Dispersion Agent on the Morphology of 3D Colloidal Crystals. Further investigations of nanocrystal batches II–VI show that the morphology of assemblies (namely, mesocrystals for batches II–IV) and translational order of nanoparticles are also significantly affected by the nature of the dispersion agent. SEM and light microscope (LM) images nicely illustrate different morphologies of the aggregates (Figure 3 and Figures S11–S13) crystallized from different media. The self-assembly of the nanoparticles from polar solvents such as THF and toluene (for our purposes solvent polarity is characterized by its dielectric constant and compared to oleic acid, Table S2) can lead to a variety of different morphologies, such as tetragonal prisms (batch II), rhombohedra (batch III), tetragonal truncated pyramids (batch IV), and trigonal truncated pyramids (i.e., could be described as octahedra sliced parallel to (111) basal plane) and octahedra (Figure 3 A1, A2, B1, B2, C1, C2, D1, D2, E1, E2). In addition to these representative “single-like” crystal morphologies, we also observed nearly in all experiments multiply twinned and defective crystals.

The symmetry of the surface layer of the (001) basal face of the mesocrystals from nanocrystal batches II and IV is $p4mm$, while the symmetry of the (001) face for the rhombohedral mesocrystal of nanocrystal batch III is $c2mm$ and those for the octahedral faces of batches V and VI are $p6mm$ (Figure S11d–i, S12g–l, S13g–l). In contrast, the morphology of the colloidal crystals is always a trigonal truncated pyramid (with *fcc* symmetry of the superlattice), when the nanocrystals are aggregating from nonpolar dispersion agents such as cyclohexane and heptane (Figure 3 A3, B3, B4, C3, C4, D3, E3). All these mesocrystals show $p6mm$ plane symmetry of the (111) basal face (Figures S11a–c, S12a–f, and S13a–f). Furthermore, the assembly process of the nanocrystals from nonpolar solvents is slower than for polar solvents.⁵⁷ As an example, with THF as the dispersion agent, the complete self-assembly process occurred within 4 days, but it took 8 days in the case of toluene (keeping all other conditions the same; see the Experimental Section). The complete crystallization time from cyclohexane and heptane solutions may even take up to a month or more. The difference of the morphology and the symmetry of the superlattice (e.g., polymorphism) cannot be exclusively explained by modified kinetics of the self-assembly process. Rather, we need to take into account the specific interaction of iron oxide nanocrystals stabilized by oleic acid molecules with the surrounding medium to explain the observed phenomena.⁵⁹ Similar observations (of solvent

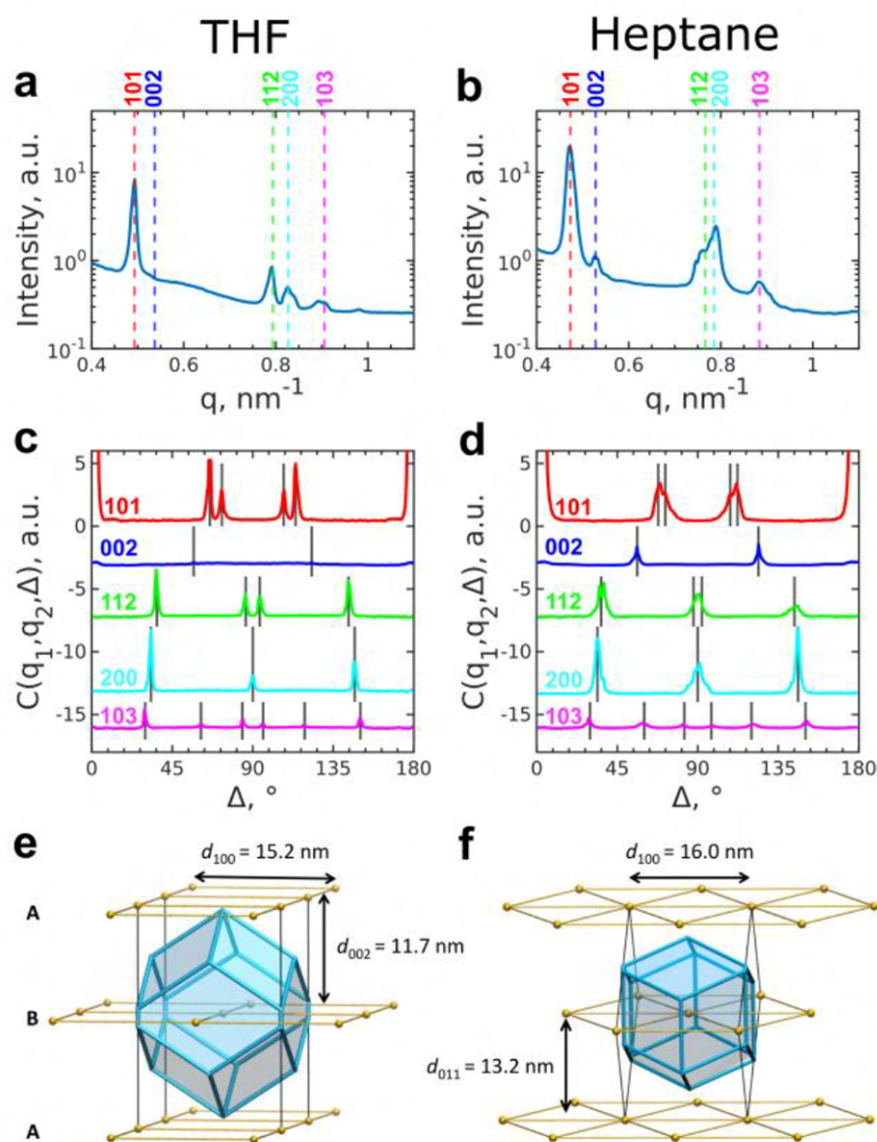


Figure 4. Superlattice structure revealed by AXCCA. (a, b) Angular averaged radial profiles of the scattered intensity from the samples assembled from THF (a) and heptane (b). The dashed vertical lines show the peak positions for the structure with optimized unit cell parameters. (c, d) Cross-correlation functions $C(q_1, q_2, \Delta)$ calculated for the intensities taken at the momentum transfer q_1 corresponding to the 101 Bragg peaks and q_2 corresponding to all peaks shown in panels (a) and (b), respectively. The graphs are offset for clarity. The black vertical lines show the peak position for the structure with optimized unit cell parameters. (e, f) Models of mesocrystals grown from THF and heptane dispersion, illustrating the geometry of the Voronoi polyhedra and interparticle distance. Thin lines outline the bct unit cells.

impact onto the mesocrystal shapes and structures) were also reported for several other nanoparticle self-assemblies.^{29,45,60} Furthermore, molecular crystals can also be prepared with different morphologies and crystal structures (i.e., polymorphs) by crystallization from different solvents.⁵⁸ It was suggested that the polarity and related the dielectric constant of the solvents are crucial for this behavior of molecular and colloidal crystals.²⁹ We suggest that the different morphologies of self-assembled magnetite mesocrystals obtained from different dispersion agents can be correlated to the polarity of the dispersion agents and to the nature of the surfactant stabilizing the nanoparticle (i.e., the organic shell) (Table S2). Here, the interaction between the dispersion agent and the organic shell of the nanocrystals seems to be the most important parameter

influencing the final morphology of the mesocrystals and the symmetry of the superlattice (while we used an excess of surfactant, which is also crucial for the successful formation of the mesocrystals^{13,29}). Cyclohexane and heptane have a significantly lower dielectric constant than toluene and THF. In the case of mesocrystals from batches I–IV with morphologies of tetragonal prisms, rhombohedra, and tetragonal truncated pyramids, the dielectric constant of the solvents is similar to or higher than that of oleic acid and the crystallization time is faster. While for the same batches, the mesocrystals with a shape of a trigonal truncated pyramid crystallize from the less polar solvents (e.g., cyclohexane and heptane). Based on this observation, we can also suggest that the effective shape of the nanoparticles is significantly affected

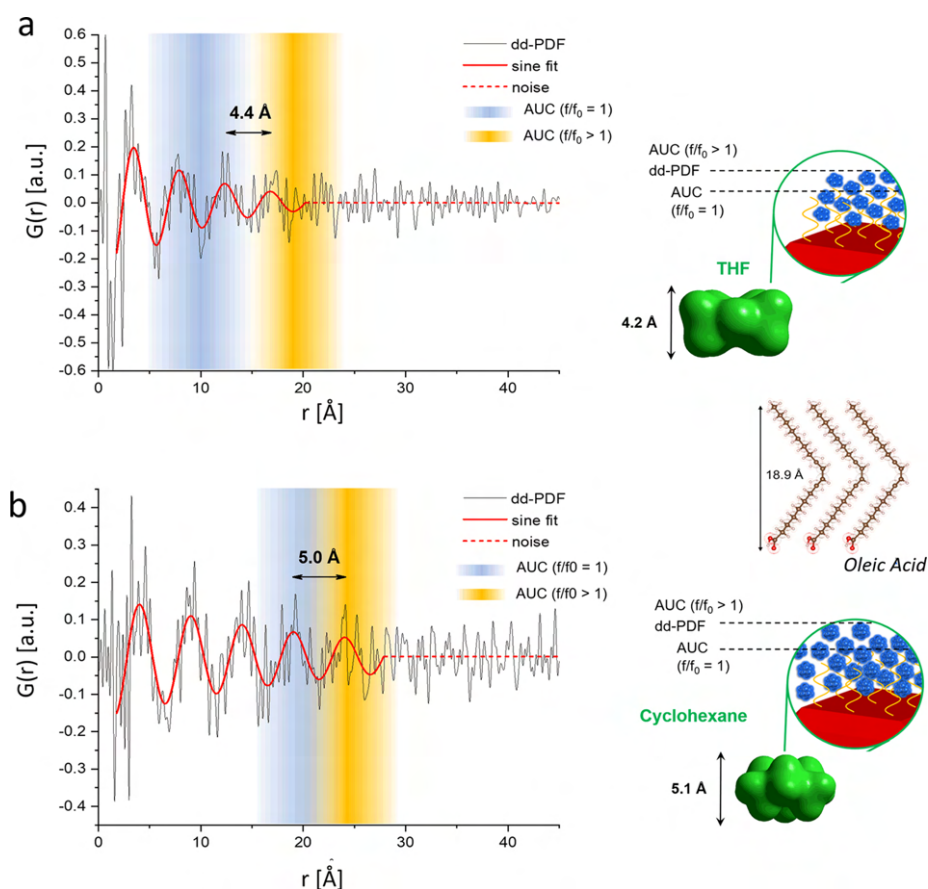


Figure 5. Comparison of solvation shell formed around iron oxide nanocrystals stabilized by oleic acid (Batch VI) in THF (a) and cyclohexane (b) solutions. (Right insets) Schematic illustration of solvation shell around nanoparticles in different solvents and relations between the measured thickness values obtained by dd-PDF and AUC and oleic acid molecules. Fitting of PDF curves shows that, for THF (a), the exponentially decaying sine wave describes the data from 1.8 to 20.2 Å (solid line), while beyond a line function suffices (dashed line; no restructuring beyond 20.2 Å); for cyclohexane (b), the exponentially decaying sine wave extends out to 27.8 Å (solid line). In the insets the side views of the simulated electron density distributions of THF (a) and, respectively, cyclohexane (b) are depicted in green color. Evaluation of AUC data using 2DSA-MC analysis shows that, for THF, the calculated thickness of a dense shell (with $f/f_0 = 1.0$) corresponds to 10.5 Å, while the dynamic one (with $f/f_0 > 1.0$) is 19 Å (close to the value obtained by dd-PDF); for cyclohexane (b), the calculated thickness of the dense shell (with $f/f_0 = 1.0$) corresponds to 22.5 Å, while the dynamic one (with $f/f_0 > 1.0$) is 24 Å (close to the value obtained by dd-PDF).

by the interaction of stabilizing molecules (oleic acid) with the surrounding dispersion agent. It can be hypothesized that in nonpolar solvents the solvation shell changes the effective shape of the nanocrystals toward the spherical shape by smoothing off the edges and vertices of the truncated nanocubes. This smoothing significantly affects the assembly process and the symmetry of the resulting superlattices. These observations are also consistent with the fact that, under the investigated conditions, the colloidal crystals formed from batches V and VI always have the *fcc* structure and the morphology of trigonal truncated pyramids and/or octahedra independent from the dispersion agent.

Effect of Dispersion Agent on the Symmetry of the Superlattice and Interparticle Distance in Mesocrystals.

The mesocrystals grown from dispersions of nanoparticles (batch IV) in heptane and THF were studied by XRD. Intensity distributions in 3D reciprocal space were collected from single grain samples (Figure S14) that allowed the unit cell parameters to be determined not only from the standard radial profile refinement but also from the more precise AXCCA (for details, see Experimental Section and Supporting

Information, Section S5). Both samples could be refined to have *bct* superlattice (Figure 4). The unit cell parameters are $a = 15.2 \pm 0.1$ nm and $c = 23.4 \pm 0.3$ nm for the sample grown from THF and $a = 16.0 \pm 0.2$ nm and $c = 23.5 \pm 0.6$ nm for the sample grown from heptane (Figure 4a–d). The uncertainties refer to the determination of diffraction maxima; therefore, more realistic error estimation could be gained from the broadness of peak profiles (Figure 4a,b) and corresponds to approximately 0.4 and 1 nm (for a and c) for the THF sample and 1.2 and 2 nm (for a and c) for the heptane one. Thus, the former sample has clearly tetragonal symmetry ($c/a = 1.54$), while the latter ($c/a = 1.47$) can be characterized as slightly distorted *fcc* structure (cf. $c/a = \sqrt{2} \approx 1.41$). The difference becomes even better visible from the metric in the unit cell parameter space (see Figure S18) and the geometry of the Voronoi polyhedra⁶¹ (Figure 4e,f). Interestingly, the comparison of lattice parameters of both mesocrystals shows that parameter a is higher for the heptane sample, while c stays nearly the same. This observation might give an impression of anisotropic expansion, if one would consider the same growth scenario of both mesocrystals. However, the SEM images

(Figure 3C1, C4) clearly show that the growth scenarios are indeed different. The layer-by-layer growth of mesocrystals takes place by stacking square nets ($\{001\}$ planes in *bct* structure) in THF (Figure 3C1) and hexagonal nets ($\{011\}$ planes in *bct* = $\{111\}$ planes in *fcc* structure) in heptane (Figure 3C4). Thus, Figure 4e,f shows that heptane molecules lead to an isotropic increase of interparticle distances by ca. 0.8–1.5 nm. Taking into account the size of cubic nanoparticles (“MinFerret” = 14.4 nm, SD = 0.7 nm), the thickness of the organic stabilizer between the particles extends from ca. 0.8 nm in THF to ca. 1.6 nm in heptane. Furthermore, XRD data indicate higher disorder in mesocrystals grown in heptane, by giving broader Bragg peaks in reciprocal space.

Effect of Dispersion Agent on Nanoparticle Solvation Shells.

To investigate the interactions of nanoparticles with solvent molecules directly in liquid dispersion, we employed advanced double difference pair distribution function (dd-PDF) analysis of X-ray total scattering data and analytical ultracentrifugation (AUC). The dd-PDF analysis of nanoparticle dispersions allows the restructuring of solvent molecules to be detected at the nanoparticle interface within the solvation shell.⁶² Due to broken symmetry and additional interactions with the nanoparticle surface, solvent molecules reorganize at interfaces. With increasing distance from the nanoparticles’ surface, the bulk order is regained and the solvation shell signal vanishes. To study the solvation shells around iron oxide nanoparticles capped by oleic acid molecules, high energy X-ray scattering data was collected for nanocube dispersions, as well as for the bulk dispersion media and dried nanopowders as backgrounds. For this dd-PDF analysis, we investigated batches V and VI in cyclohexane and in THF, with and without excess of oleic acid (3 $\mu\text{L}/\text{mL}$). The PDF is obtained by Fourier transformation of the total scattering data after background correction and normalization. In general, the PDF is a histogram of all interatomic distances within a sample. In the case of bulk solvents, both intramolecular distances and intermolecular distance correlations can be detected. The solvation shell signals in the dd-PDFs herein were extracted according to Thomä et al.⁶³ Upon subtraction of the signal from the bulk solvent (pure THF or cyclohexane), all intramolecular distances of the solvent molecules get subtracted as the solvent molecules in the solvation shell do not dissociate or change compared to the bulk. However, their intermolecular arrangement changes, and thus, the medium-range molecular arrangement is affected, which becomes detectable as an electronic density oscillation in the PDF over ca. 30 Å (Figure S20). For all samples, the extracted solvation shell signal contains broad oscillations. The collected signals for THF and cyclohexane were distinctly different. The size of the nanoparticles and the addition of extra oleic acid (in the concentration 3 $\mu\text{L}/\text{mL}$ used for the self-assembly process) did not strongly affect the signal from the solvation shells (Figure S21). The derived solvation shell signals for THF and cyclohexane around nanoparticles from batch VI were exemplarily modeled with exponentially decaying sine waves according to Zobel et al.⁶² and Thomä et al.⁶³ (Figure 5a,b). At the distance where the visible oscillation was decayed, a linear function was chosen for modeling (for more detailed information, see Figure S22). From the sinusoidal fit, we can readily obtain the extent of the restructuring and the overall number of restructured solvent layers (i.e., number of fitted oscillations) as well as the layer spacing (i.e., wavelength of the fitted oscillation). For the

solvation shell formed around nanoparticles in THF, four restructured solvent layers were identified, while it is five layers in cyclohexane. Hence, in cyclohexane, one layer more is affected than in THF. Further, layer spacings of 4.4 and 5.0 Å were obtained for THF and cyclohexane, respectively. These values are in good agreement with the linear sizes of THF and cyclohexane molecules estimated from van der Waals radii, which correlate well with electron density distributions, as known from literature (see insets Figure 5a,b).⁶⁴ Moreover, it can be stated that the extent of restructuring (solvation shell signal before decay) around the investigated iron oxide nanoparticles found with PDF analysis is ca. 8 Å larger for cyclohexane than for THF. Thus, the solvation shell formed around the nanoparticles in cyclohexane could significantly modify the effective shape of the cubic nanoparticles toward the sphere (Figure 5b).

In order to correlate these data with other physicochemical parameters of nanoparticles in different solvents including the effective size, density, and sedimentation behavior, AUC analysis was used. Figures S23 and S24 show the particle size distributions in different solvents as obtained with two different evaluation algorithms. While $g(s)$ yields a distribution, which is not corrected for the diffusion broadening of the sedimenting boundary, the 2 DSA-MC method corrects for this broadening so that individual components in the distribution can be seen and the distribution for each component is much narrower (Figures S23 and S24, left column). In addition, 2 DSA-MC allows for plotting the distribution of the frictional coefficients f/f_0 versus the sedimentation coefficient distribution, while the PCSA-MC method can calculate the partial specific volume of each species in the sedimentation coefficient distribution (Figures S23 and S24, middle and right columns). It is obvious that several populations of nanoparticles exist for most of the samples, but the differences between the most abundant species are small. The hydrodynamic diameter can then be calculated using the

particle density (inverse v_{bar}) using the formula $d_H = \sqrt{\frac{18\eta s f_0}{\rho_p - \rho_s}}$

(where d_H is the hydrodynamic nanoparticle diameter, s is sedimentation coefficient, η is the solvent viscosity, and ρ_p and ρ_s are particle and solvent densities, f/f_0 the frictional coefficient respectively). These values are collected in Table S3. With the known diameter of the inorganic core of the nanoparticles obtained from TEM images, the thickness of the solvated organic shell can be calculated. It can be seen that significant differences exist for different solvents. In THF, the shell thickness is always the smallest, while it is largest for cyclohexane. There are differences between $g(s)$ and 2 DSA-MC, but the general trend is independent of the AUC evaluation method. If compared to the persistence length of an oleic acid molecule (18.9 Å), the oleic acid molecules could fold backward because the interaction of the nonpolar chains with themselves is favored over the interaction with the solvent THF, and they do not have extended solvation shells (evidenced by the PDF analysis). Nevertheless, the molecules still provide steric stabilization. For the nonpolar solvent toluene and to a higher extent cyclohexane, the interaction of the nonpolar chains of oleic acid molecules with the nonpolar solvent is favorable and the chains significantly extend into the solvent. This value varies a bit depending on the batch, but in general the stabilization shell extension in cyclohexane ranges from 17 Å up to 23.5 Å and is close to the values obtained

from dd-PDF analysis. These values further agree well with the persistence length of a stretched oleic acid molecule in an extended solvation shell.

We can now obtain further information looking at the frictional ratios f/f_0 (Table S3). From TEM data, it is known that nanoparticles from both batches V and VI are spherical and therefore have a Perrin friction factor $P = 1$. It is obvious that for particle populations with $f/f_0 = 1$ we can speak of a dense stabilization shell. But there are cases in each sample where f/f_0 can be higher as 1, which indicates a significant amount of “mobile” solvent molecules associated with the particle shell. These are also the cases where a high thickness of the organic shell is observed compared to populations with $f/f_0 = 1$. We can, therefore, treat the solvation shell as dynamic in such a case where the oleic molecules extend into the solvent and also have a significant amount of solvent attached to them due to their favorable interaction. The extension of such a shell is in good agreement with the values obtained by PDF analysis (Figure 5a,b). Upon sedimentation of the particle, the solvent can flow through such a shell, causing increased friction, and also, the oleic acid molecules have more degrees of freedom for movement due to their extension into the solution as those that are folded back on themselves in the dense shell with $f/f_0 = 1$. With the exception of toluene for batch VI, the majority of species in the distribution has $f/f_0 > 1$ for toluene and cyclohexane, while it is 1 for THF, meaning that the shell is dynamic in toluene and cyclohexane, while it is dense in THF.

Based on these findings, we can finally verify the previously proposed hypothesis concerning the effect of solvent on the effective shape of the nanoparticles and changing the structuring and morphogenetic processes of colloidal crystals (incl. mesocrystals). Furthermore, our new findings could be essential for further development of theories describing the aggregation behavior of nanoparticles in solution and potentially could explain the nonadditivity of electrostatic, van der Waals, and other interactions at the nanoscale (and deviations from the classical DLVO theory).⁵⁹

CONCLUSIONS

In summary, we successfully applied different crystallization methods to prepare 3D magnetite mesocrystals (type I) and analyzed the crystallization conditions in detail. The nanocube building blocks were self-assembled either by the solvent evaporation technique or gas phase diffusion technique. We have systematically investigated the effect of different nanoparticle and media parameters on the self-assembly process, morphology, and symmetry of the superlattice of crystallizing mesocrystals. It was shown that the faceting and habit of the nanocrystals is a crucial parameter affecting the symmetry of the superlattice and final morphology of the mesocrystals. However, the translational order of nanocrystals within mesocrystals may be altered by changing the dispersion agent (e.g., THF, toluene, cyclohexane, heptane). As an example, by decreasing the solvent polarity, the shape of the mesocrystals assembled from slightly truncated cubic magnetite nanocrystals can change from tetragonal prisms and rhombohedra to trigonal truncated pyramids and octahedra, reflecting the changes of the superlattice symmetry (tetragonal, rhombohedral, and cubic, respectively). Such changes of nanoparticle packing symmetry are reminiscent of polymorphism known for “classical” crystals. Furthermore, by using dd-PDF and AUC analysis of nanoparticle dispersions, it was shown that extension and density of the solvation shell of

nanoparticles depend on the solvent polarity. For the nonpolar solvents like cyclohexane, the interaction of the nonpolar chains of oleic acid molecules with the solvent molecules is favorable and the chains significantly extend into the solvent. Furthermore, within the solvation shell around the nanoparticle, the extent of restructuring of solvent molecules is by ca. 8 Å larger for cyclohexane than for THF, which significantly modifies the effective shape of the nanoparticles. Thus, in nonpolar solvents, the thick and dynamic solvation shell significantly affects the effective shape of the nanoparticles toward spheres and leads to the formation of colloidal crystals with an *fcc* superlattice and the morphology of octahedra and/or truncated trigonal pyramids. This effect is responsible for the increase of the interparticle distances in mesocrystals grown from polar (e.g., THF) vs nonpolar solvents (e.g., heptane). These findings are consistent with our previously proposed phenomenological model,^{8,21} suggesting that the type of particle packing depends on the effective softness of building blocks, which in turn (along with the nature of a solvent) has impact on the shape of the mesocrystals.

Finally, this fundamental research contributes to the understanding of the basic principles of morphogenesis of self-assembled faceted mesocrystals built up from cubic magnetite nanoparticles with different degrees of truncation. These basic principles can be readily transferred to other nanocrystal systems. They will serve as a proxy system for the optimization of synthesis conditions and synthesis of mesocrystals with defined structure and morphology.

EXPERIMENTAL SECTION

Synthesis of the Nanocubes. The heating-up method was used for the preparation of the iron oxide nanocubes with different sizes and degrees of truncation according to the literature.^{13,65,66}

Synthesis of the Mesocrystals: Evaporation Induced Self-Assembly. The evaporation induced self-assembly was performed according to the literature.¹³ A nanocrystal dispersion (5 mg/mL) containing oleic acid (1 μ L/mL) is dried slowly on top of a carbon-foiled TEM grid.

Synthesis of the Mesocrystals: Gas Phase Diffusion Technique. In a glass vial containing a silicon snippet (orientation (100), CrysTec Kristalltechnologie), 400–500 μ L of the nanoparticle dispersion of a given nanoparticle and surfactant (oleic acid) concentration was injected. A typical experiment is performed with 5 mg/mL nanocrystal concentration and 3 μ L/mL surfactant concentration. This glass vial was put into another glass vial containing the diffusion phase (1.5–2.5 mL). It was then stored until the nanoparticles were destabilized. Finally, the silicon snippet was removed and investigated.

Scanning Electron Microscopy. For the SEM images, a Zeiss CrossBeam 1540XB was used, reaching a resolution of up to 1.1 nm. It is equipped with an InLens detector and SE2 detector.

Transmission Electron Microscopy. The TEM images were recorded using two different microscopes. The Zeiss Libra 120 can reach a point resolution of 0.34 nm with a 120 kV lanthanum hexaboride emitter and a Koehler illumination system. The high resolution TEM imaging of the nanoparticles was performed at 300 kV acceleration voltage using a probe and image aberration corrected FEI TITAN³ transmission electron microscope. TEM images were analyzed with DigitalMicrograph Gatan Microscopy Suite 3 software (Gatan Inc., ver. 3.41.2938.1). To calculate the core diameter of the nanocrystal batches, TEM images were processed using Fiji software. The histograms were fitted using a Gaussian function.

Single-Crystal Small-Angle X-ray Scattering. The SAXS measurements of the selected mesocrystals were performed by means of a Bruker AXS Nanostar diffractometer using Cu $K\alpha$ radiation. The analysis of the SAXS pattern was performed using JEMS software.

Single-Crystal Wide-Angle X-ray Diffraction. A single mesocrystal was mounted on a MicroLoop holder. The XRD images were collected by use of a Rigaku AFC7 diffractometer equipped with Mercury CCD Detector (Mo $K\alpha$ radiation, $\lambda = 0.71073 \text{ \AA}$).

Analytical Ultracentrifugation. The AUC measurements were performed on an Optima XL-A (Beckman Coulter, Palo Alto, CA, United States) using absorbance optics at 7000 rpm at 20 °C. The 12 mm double sector titanium centerpieces (Nanolitics, Potsdam, Germany) were used for all experiments. Sedfit (version 16.1c by Peter Schuck⁶⁷) was used for performing the $g(s)$ distributions with the $ls-g^*(s)$ model and Tikhonov-Phillips regularization.⁶⁸ Ultra-Scan3⁶⁹ (Version 4.0, revision 2783) was used for performing the two-dimensional spectrum analysis (2DSA),⁷⁰ Custom Grid (CG),⁷¹ and parametrically constrained spectrum analysis (PCSA)⁷¹ on the Jewels Supercomputer. The 2DSA-, CG-, and PCSA-Monte Carlo (MC) analyses were performed with 50 iterations. The final fitted densities from PCSA-MC analyses were used for the calculations of the hydrodynamic diameter (d_H) of nanoparticles. In order to evaluate the sole effect of interaction of oleic acid capped nanoparticles with solution molecules and the formation of the solvation shell by excluding the effect of nanocrystal shape anisotropy and faceting (since a friction coefficient significantly affected by particle shape), the quasi-spherical nanoparticles of batches V and VI were used. In another d_H order, the real density of magnetite nanoparticles stabilized by oleic acid was estimated by taking into account that the oleic acid content was around 20 wt % (based on the results of chemical analysis).¹³

X-ray Scattering Experiment on the Single Grains. The X-ray experiment was performed on the cuboidal grains with all dimensions of about 1 μm cut from the mesocrystals of batch IV (with the largest nanoparticles, Figure S5) grown from THF and heptane dispersions by focused ion beam (see Supporting Information S4 for details). The scattered intensity in full 3D reciprocal space of the colloidal crystal grains was measured the same way as described in ref 37. The experiment was performed at P10 Coherence Applications beamline at PETRA III storage ring (DESY, Germany). Monochromatic X-rays of 10.235 keV were focused down to $\sim 2.5 \times 2.0 \mu\text{m}^2$ at the sample position completely covering a slightly smaller colloidal crystal grain. The colloidal crystal grain was fixed on a tungsten tip mounted on a rotation stage and rotated around the vertical axis. At each angular position, the 2D far-field diffraction patterns were recorded by the EIGER X 4 M detector positioned 4.95 m downstream from the sample. The sample was rotated by steps of 0.33° over a range of 180° and, by that, the full 3D diffraction pattern was measured. At each angular position, a series of three frames of 1 s exposure each were measured, corresponding to 3 s accumulated exposure to the nonattenuated X-ray beam. The sample was cooled using a liquid nitrogen cryostat, in order to avoid radiation damage of the organic ligands (stabilizing nanocrystals) which could induce the coalescence of nanoparticles and destroy the superlattice ordering.

Angular X-ray Cross-Correlation Analysis. AXCCA was performed as described in ref 37. Cross-correlation functions were calculated between the intensities taken at the brightest first peak momentum transfer ($q \approx 0.5 \text{ nm}^{-1}$) and at other momentum transfers in the range of $q = 0.4\text{--}1.3 \text{ nm}^{-1}$ with the step of 0.005 nm^{-1} . The resulting cross-correlation map was represented in (q, Δ)-coordinates. The expected peak positions for the selected superlattice model in these coordinates were calculated, and the cross-correlation intensities in these positions were calculated by interpolation of the experimental map. The optimal unit cell parameters of the superlattice were found by maximization of the total intensities at the expected peak positions (see Supporting Information for details).

PDF Data Acquisition and Processing. In order to correlate results of AUC and dd-PDF, particles of batches V and VI were studied. XRD measurements of dispersions of iron oxide nanocubes and pure solvents were carried out at 68 keV (0.1823 Å) at the European Synchrotron Radiation Facility (ESRF) at beamline ID15-A using a PILATUS3 X CdTe 2 M detector ($253.7 \times 288.8 \text{ mm}^2$ sensitive area, $172 \times 172 \mu\text{m}^2$ pixel size). XRD data of a corresponding dry iron oxide nanopowder was acquired at beamline

I15-1 (XPDF) at 65.4 keV (0.18957 Å) at Diamond Light Source equipped with a PerkinElmer detector XRD 4343 CT ($432 \times 432 \text{ mm}^2$ active area, $150 \times 150 \mu\text{m}^2$ pixel size). Each data set at ESRF was collected for a total of 3 min and at Diamond Light Source for 6 min. Thereby, 20 data collections of 9 s (ESRF) and 12 data collections of 30 s (Diamond) each were performed and then averaged. All samples were measured in 1 mm Kapton capillaries. NIST chromium(III) oxide standards (ESRF) and NIST silicon standards (Diamond) were used for distance calibration and instrumental resolution determination. For data processing of ESRF data, the following software packages were used: for masking Fit2D; for calibration pyFAI-calib2; and for radial integration xpdtools. For data from Diamond Light Source calibration, radial integration, masking, and normalization of the data were done in the DAWN software package.⁷² PDF processing was carried out with xPDFsuite⁷³ and fitting in IgorPro by WaveMetrics. All data was treated in the same way during data analysis. The powder PDF of the iron oxide nanopowder was scaled to the experimental d-PDFs each with an individual scale factor y_1 in the distance range $>20 \text{ \AA}$. The iron oxide nanopowder data was collected on nanoparticles of batch IV, while the dispersions measured contained nanoparticles of batches V and VI, as no powder of the latter cubes was available. The difference between the PDFs of 8–100 and 150 Å cubes, in particular over the interesting distance range of 30 Å, is negligible as the shape functions of the cubes are pretty similar in this range. Moreover, the shape functions are constantly decaying over r , while the solvent restructuring features a sinusoidal structural fingerprint. Therefore, for means of this data analysis, where the PDFs are subtracted in real space, any errors which are of importance to the interpretations drawn due to the subtraction of the PDF of a slightly offset iron oxide powder size can be ruled out. According to Thomä et al.⁶³ the dd-PDFs of the different dispersions can be compared by mutual scaling of the powder PDF contribution to the overall PDF. For this, we again use the scale factor y_2 and in this case the intensity of the IONP PDF peak at 28.52 Å. All samples were scaled to an intensity of 0.3 at this point, since this value was the average value for all samples. The description of the solvation layers is based on an exponentially decaying sine wave according to Thomä et al.⁶³ The high frequency ripples visible in the dd-PDFs are high-frequency noise due to the low concentration of the dispersions and do not contain any structural signal.

■ ASSOCIATED CONTENT

Supporting Information

The Supporting Information is available free of charge at <https://pubs.acs.org/doi/10.1021/acs.chemmater.1c01941>.

Additional data including SEM and TEM images, dd-PDF and AUC evaluation, and details of AXCCA (PDF)

■ AUTHOR INFORMATION

Corresponding Author

Elena V. Sturm – Department of Chemistry, Universität Konstanz, 78467 Konstanz, Germany; orcid.org/0000-0002-9470-3684; Email: elena.sturm@uni-konstanz.de

Authors

Julian Schlotheuber né Brunner – Department of Chemistry, Universität Konstanz, 78467 Konstanz, Germany

Britta Maier – Department of Chemistry, Universität Konstanz, 78467 Konstanz, Germany

Sabrina L. J. Thomä – Department of Chemistry, University of Bayreuth, 95447 Bayreuth, Germany; Institute of Crystallography, RWTH Aachen University, 52066 Aachen, Germany

Felizitas Kirner – Department of Chemistry, Universität Konstanz, 78467 Konstanz, Germany

- Igor A. Baburin** – Department of Chemistry, TU Dresden, 01062 Dresden, Germany
- Dmitry Lapkin** – Deutsches Elektronen-Synchrotron DESY, D-22607 Hamburg, Germany
- Rose Rosenberg** – Department of Chemistry, Universität Konstanz, 78467 Konstanz, Germany
- Sebastian Sturm** – Advanced Methods of Electron Microscopy (AMEM), Leibniz Institute for Solid State and Materials Research (IFW) Dresden, 01069 Dresden, Germany
- Dameli Assalauova** – Deutsches Elektronen-Synchrotron DESY, D-22607 Hamburg, Germany
- Jerome Carnis** – Deutsches Elektronen-Synchrotron DESY, D-22607 Hamburg, Germany
- Young Yong Kim** – Deutsches Elektronen-Synchrotron DESY, D-22607 Hamburg, Germany; orcid.org/0000-0001-6102-9518
- Zhe Ren** – Deutsches Elektronen-Synchrotron DESY, D-22607 Hamburg, Germany
- Fabian Westermeier** – Deutsches Elektronen-Synchrotron DESY, D-22607 Hamburg, Germany
- Sebastian Theiss** – Department of Chemistry, Universität Konstanz, 78467 Konstanz, Germany; Institute of Inorganic Chemistry, Leibniz-University Hannover, 30167 Hannover, Germany
- Horst Borrmann** – Max-Planck-Institute for Chemical Physics of Solids, 01187 Dresden, Germany
- Sebastian Polarz** – Department of Chemistry, Universität Konstanz, 78467 Konstanz, Germany; Institute of Inorganic Chemistry, Leibniz-University Hannover, 30167 Hannover, Germany; orcid.org/0000-0003-1651-4906
- Alexander Eychmüller** – Department of Chemistry, TU Dresden, 01062 Dresden, Germany; orcid.org/0000-0001-9926-6279
- Axel Lubk** – Advanced Methods of Electron Microscopy (AMEM), Leibniz Institute for Solid State and Materials Research (IFW) Dresden, 01069 Dresden, Germany
- Ivan A. Vartanyants** – Deutsches Elektronen-Synchrotron DESY, D-22607 Hamburg, Germany; National Research Nuclear University MEPHI (Moscow Engineering Physics Institute), Moscow 115409, Russian Federation; orcid.org/0000-0002-0340-8234
- Helmut Cölfen** – Department of Chemistry, Universität Konstanz, 78467 Konstanz, Germany; orcid.org/0000-0002-1148-0308
- Mirijam Zobel** – Department of Chemistry, University of Bayreuth, 95447 Bayreuth, Germany; Institute of Crystallography, RWTH Aachen University, 52066 Aachen, Germany; orcid.org/0000-0002-8207-8316

Complete contact information is available at:
<https://pubs.acs.org/10.1021/acs.chemmater.1c01941>

Author Contributions

The manuscript was written through contributions of all authors. All authors have given approval to the final version of the manuscript.

Notes

The authors declare no competing financial interest.

ACKNOWLEDGMENTS

We hereby acknowledge the DFG (Deutsche Forschungsgemeinschaft) for financial support (SFB1214 Project B1). We thank Clara Schlotheuber for editorial help and fruitful

discussions. We also thank Dr. Danny Haubold and Ramon Zimmermanns for being a great help in laboratory work. S.S. and A.L. acknowledge funding from the European Research Council (ERC) under the Horizon 2020 research and innovation program of the European Union (Grant Agreement Number 715620). M.Z. acknowledges support by the Bavarian Academy for Sciences and Humanities. M.Z. and S.T. acknowledge beamtime at ID15-ERH at European Synchrotron Radiation Facility and I15-1 at Diamond Lightsource, as well as support from the respective beamline scientists Gavin Vaughan and Phil Chater. We acknowledge DESY (Hamburg, Germany), a member of the Helmholtz Association HGF, for the provision of experimental facilities. Parts of this research were carried out at PETRA III synchrotron facility, and we would like to thank the beamline staff and especially Michael Sprung for assistance in using Coherence Application P10 beamline. This work was supported by the Helmholtz Associations Initiative Networking Fund (Grant No. HRSF-0002) and the Russian Science Foundation (Grant No. 18-41-06001). We also gratefully acknowledge the Gauss Center for Supercomputing e.V. (www.gauss-centre.eu) for providing computing time through the John von Neumann Institute for Computing (NIC) on the GCS Supercomputer JUWELS at the Jülich Supercomputing Center (JSC), which was used to receive the models in ULRSCAN for AUC data. E.V.S. thanks the Zukunftscolleg at the University of Konstanz and “Konstanz Transition” programme of equal opportunity council for financial support. Last but not least, we thank the Bio Imaging Center Constance and Stefan Helfrich to help us to evaluate light microscope images, quantitatively.

REFERENCES

- (1) Talapin, D. V. Nanocrystal solids: A modular approach to materials design. *MRS Bull.* **2012**, *37* (1), 63–71.
- (2) Talapin, D. V.; Lee, J. S.; Kovalenko, M.; Shevchenko, E. Prospects of Colloidal Nanocrystals for Electronic and Optoelectronic Applications. *Chem. Rev.* **2010**, *110*, 389–458.
- (3) Reichhelm, A.; Haubold, D.; Eychmüller, A. Ligand Versatility in Supercrystal Formation. *Adv. Funct. Mater.* **2017**, *27* (39), 1700361.
- (4) Polarz, S. Shape Matters: Anisotropy of the Morphology of Inorganic Colloidal Particles – Synthesis and Function. *Adv. Funct. Mater.* **2011**, *21* (17), 3214–3230.
- (5) Talapin, D. V.; Shevchenko, E. V. Introduction: Nanoparticle Chemistry. *Chem. Rev.* **2016**, *116* (18), 10343–10345.
- (6) Trepka, B.; Erler, P.; Selzer, S.; Kollek, T.; Boldt, K.; Fonin, M.; Nowak, U.; Wolf, D.; Lubk, A.; Polarz, S., Nanomorphology Effects in Semiconductors with Native Ferromagnetism: Hierarchical Europium (II) Oxide Tubes Prepared via a Topotactic Nanostructure Transition. *Adv. Mater.* **2018**, *30* (1), 1703612.
- (7) Kagan, C. R.; Lifshitz, E.; Sargent, E. H.; Talapin, D. V., Building devices from colloidal quantum dots. *Science* **2016**, *353* (6302), aac5523.
- (8) Simon, P.; Rosseeva, E.; Baburin, I. A.; Liebscher, L.; Hickey, S. G.; Cardoso-Gil, R.; Eychmüller, A.; Kniep, R.; Carrillo-Cabrera, W. PbS-organic mesocrystals: the relationship between nanocrystal orientation and superlattice array. *Angew. Chem., Int. Ed.* **2012**, *51* (43), 10776–81.
- (9) Boles, M. A.; Ling, D.; Hyeon, T.; Talapin, D. V. The surface science of nanocrystals. *Nat. Mater.* **2016**, *15* (2), 141–53.
- (10) Dreyer, A.; Feld, A.; Kornowski, A.; Yilmaz, E. D.; Noei, H.; Meyer, A.; Krekeler, T.; Jiao, C.; Stierle, A.; Abetz, V.; Weller, H.; Schneider, G. A. Organically linked iron oxide nanoparticle supercrystals with exceptional isotropic mechanical properties. *Nat. Mater.* **2016**, *15* (5), 522–528.
- (11) Abécassis, B. Three-Dimensional Self Assembly of Semiconducting Colloidal Nanocrystals: From Fundamental Forces to

- Collective Optical Properties. *ChemPhysChem* **2016**, *17* (5), 618–631.
- (12) Boles, M. A.; Engel, M.; Talapin, D. V. Self-Assembly of Colloidal Nanocrystals: From Intricate Structures to Functional Materials. *Chem. Rev.* **2016**, *116* (18), 11220–11289.
- (13) Brunner, J.; Baburin, I. A.; Sturm, S.; Kvashnina, K.; Rossberg, A.; Pietsch, T.; Andreev, S.; Sturm née Rosseeva, E.; Cölfen, H. Self-Assembled Magnetite Mesocrystalline Films: Toward Structural Evolution from 2D to 3D Superlattices. *Adv. Mater. Interfaces* **2017**, *4* (1), 1600431.
- (14) Quan, Z. W.; Fang, J. Y. Superlattices with non-spherical building blocks. *Nano Today* **2010**, *5* (5), 390–411.
- (15) Imai, H.; Tochimoto, N.; Nishino, Y.; Takezawa, Y.; Oaki, Y. Oriented Nanocrystal Mosaic in Monodispersed CaCO₃ Microspheres with Functional Organic Molecules. *Cryst. Growth Des.* **2012**, *12* (2), 876–882.
- (16) Haubold, D.; Reichhelm, A.; Weiz, A.; Borchardt, L.; Ziegler, C.; Bahrig, L.; Kaskel, S.; Ruck, M.; Eychemüller, A. The Formation and Morphology of Nanoparticle Supracrystals. *Adv. Funct. Mater.* **2016**, *26* (27), 4890–4895.
- (17) Bergström, L.; Sturm née Rosseeva, E. V.; Salazar-Alvarez, G.; Cölfen, H. Mesocrystals in Biominerals and Colloidal Arrays. *Acc. Chem. Res.* **2015**, *48* (5), 1391–402.
- (18) Zhang, J.; Zhu, J.; Li, R.; Fang, J.; Wang, Z. Entropy-Driven Pt₃Co Nanocube Assembles and Thermally Mediated Electrical Conductivity with Anisotropic Variation of the Rhombohedral Superlattice. *Nano Lett.* **2017**, *17* (1), 362–367.
- (19) Cölfen, H.; Antonietti, M. *Mesocrystals and Nonclassical Crystallization*. John Wiley & Sons: Chichester, 2008.
- (20) De Yoreo, J. J.; Gilbert, P. U. P. A.; Sommerdijk, N. A. J. M.; Penn, R. L.; Whitelam, S.; Joester, D.; Zhang, H.; Rimer, J. D.; Navrotsky, A.; Banfield, J. F.; Wallace, A. F.; Michel, F. M.; Meldrum, F. C.; Cölfen, H.; Dove, P. M. Crystallization by particle attachment in synthetic, biogenic, and geologic environments. *Science* **2015**, *349* (6247), aaa6760.
- (21) Sturm née Rosseeva, E. V.; Cölfen, H. Mesocrystals: structural and morphogenetic aspects. *Chem. Soc. Rev.* **2016**, *45* (21), 5821–5833.
- (22) Disch, S.; Wettterskog, E.; Hermann, R. P.; Salazar-Alvarez, G.; Busch, P.; Bruckel, T.; Bergström, L.; Kamali, S. Shape induced symmetry in self-assembled mesocrystals of iron oxide nanocubes. *Nano Lett.* **2011**, *11* (4), 1651–6.
- (23) Li, R.; Bian, K.; Wang, Y.; Xu, H.; Hollingsworth, J. A.; Hanrath, T.; Fang, J.; Wang, Z. An Obtuse Rhombohedral Superlattice Assembled by Pt Nanocubes. *Nano Lett.* **2015**, *15* (9), 6254–60.
- (24) Wei, J.; Schaeffer, N.; Pileni, M.-P. Solvent-Mediated Crystallization of Nanocrystal 3D Assemblies of Silver Nanocrystals: Unexpected Superlattice Ripening. *Chem. Mater.* **2016**, *28* (1), 293–302.
- (25) Bian, K.; Li, R.; Fan, H. Controlled Self-Assembly and Tuning of Large PbS Nanoparticle Supercrystals. *Chem. Mater.* **2018**, *30* (19), 6788–6793.
- (26) Hanske, C.; Hill, E. H.; Vila-Liarte, D.; González-Rubio, G.; Matricardi, C.; Mihi, A.; Liz-Marzán, L. M. Solvent-Assisted Self-Assembly of Gold Nanorods into Hierarchically Organized Plasmonic Mesostructures. *ACS Appl. Mater. Interfaces* **2019**, *11* (12), 11763–11771.
- (27) Huang, X.; Wang, Z. Supercrystallography-Based Decoding of Structure and Driving Force of Nanocrystal Assembly. *Materials* **2019**, *12* (22), 3771–3771.
- (28) Imai, H.; Matsumoto, R.; Takasaki, M.; Tsukiyama, K.; Sawano, K.; Nakagawa, Y. Evaporation-driven manipulation of nanoscale brickwork structures for the design of 1D, 2D, and 3D microarrays of rectangular building blocks. *CrystEngComm* **2019**, *21* (45), 6905–6914.
- (29) Lv, Z.-P.; Kapuscinski, M.; Bergström, L. Tunable assembly of truncated nanocubes by evaporation-driven poor-solvent enrichment. *Nat. Commun.* **2019**, *10* (1), 4228.
- (30) Zhu, H.; Fan, Z.; Yu, L.; Wilson, M. A.; Nagaoka, Y.; Eggert, D.; Cao, C.; Liu, Y.; Wei, Z.; Wang, X.; He, J.; Zhao, J.; Li, R.; Wang, Z.; Grünwald, M.; Chen, O. Controlling Nanoparticle Orientations in the Self-Assembly of Patchy Quantum Dot-Gold Heterostructural Nanocrystals. *J. Am. Chem. Soc.* **2019**, *141* (14), 6013–6021.
- (31) Andre, A.; Zhrebetsky, D.; Hanifi, D.; He, B.; Samadi Khoshkhou, M.; Jankowski, M.; Chasse, T.; Wang, L.-W.; Schreiber, F.; Salleo, A.; Liu, Y.; Scheele, M. Toward Conductive Mesocrystalline Assemblies: PbS Nanocrystals Cross-Linked with Tetrathiafulvalene Dicarboxylate. *Chem. Mater.* **2015**, *27* (23), 8105–8115.
- (32) Tebbe, M.; Lentz, S.; Guerrini, L.; Fery, A.; Alvarez-Puebla, R. A.; Pazos-Perez, N. Fabrication and optical enhancing properties of discrete supercrystals. *Nanoscale* **2016**, *8* (25), 12702–12709.
- (33) Mukharamova, N.; Lapkin, D.; Zaluzhnyy, I. A.; André, A.; Lazarev, S.; Kim, Y. Y.; Sprung, M.; Kurta, R. P.; Schreiber, F.; Vartanyants, I. A.; Scheele, M. Revealing Grain Boundaries and Defect Formation in Nanocrystal Superlattices by Nanodiffraction. *Small* **2019**, *15* (50), 1904954.
- (34) Zaluzhnyy, I. A.; Kurta, R. P.; André, A.; Gorobtsov, O. Y.; Rose, M.; Skopintsev, P.; Besedin, I.; Zozulya, A. V.; Sprung, M.; Schreiber, F.; Vartanyants, I. A.; Scheele, M. Quantifying Angular Correlations between the Atomic Lattice and the Superlattice of Nanocrystals Assembled with Directional Linking. *Nano Lett.* **2017**, *17* (6), 3511–3517.
- (35) Zaluzhnyy, I. A.; Kurta, R. P.; Scheele, M.; Schreiber, F.; Ostrovskii, B. I.; Vartanyants, I. A. Angular X-ray Cross-Correlation Analysis (AXCCA): Basic Concepts and Recent Applications to Soft Matter and Nanomaterials. *Materials* **2019**, *12* (21), 3464.
- (36) Kurta, R. P.; Altarelli, M.; Vartanyants, I. A., Structural analysis by x-ray intensity angular cross correlations. In *Advances in Chemical Physics*, Rice, S. A.; Dinner, A. R., Eds. John Wiley & Sons, Inc., Hoboken: New Jersey, 2016; Vol. 161, pp 1–39.
- (37) Carnis, J.; Kirner, F.; Lapkin, D.; Sturm, S.; Kim, Y. Y.; Baburin, I. A.; Khubbutdinov, R.; Ignatenko, A.; Iashina, E.; Mistonov, A.; Steegemans, T.; Wieck, T.; Gemming, T.; Lubk, A.; Lazarev, S.; Sprung, M.; Vartanyants, I. A.; Sturm, E. V. Exploring the 3D structure and defects of a self-assembled gold mesocrystal by coherent X-ray diffraction imaging. *Nanoscale* **2021**, *13* (23), 10425–10435.
- (38) de Nijs, B.; Dussi, S.; Smalenburg, F.; Meeldijk, J. D.; Groenendijk, D. J.; Fillion, L.; Imhof, A.; van Blaaderen, A.; Dijkstra, M. Entropy-driven formation of large icosahedral colloidal clusters by spherical confinement. *Nat. Mater.* **2015**, *14* (1), 56–60.
- (39) Agthe, M.; Plivelic, T. S.; Labrador, A.; Bergström, L.; Salazar-Alvarez, G. Following in Real Time the Two-Step Assembly of Nanoparticles into Mesocrystals in Levitating Drops. *Nano Lett.* **2016**, *16* (11), 6838–6843.
- (40) Agthe, M.; Hoydalsvik, K.; Mayence, A.; Karvinen, P.; Liebi, M.; Bergström, L.; Nygard, K. Controlling Orientational and Translational Order of Iron Oxide Nanocubes by Assembly in Nanofluidic Containers. *Langmuir* **2015**, *31* (45), 12537–43.
- (41) Guillaussier, A.; Yu, Y.; Voggu, V. R.; Aigner, W.; Cabezas, C. S.; Houck, D. W.; Shah, T.; Smilgies, D.-M.; Pereira, R. N.; Stutzmann, M.; Korgel, B. A. Silicon Nanocrystal Superlattice Nucleation and Growth. *Langmuir* **2017**, *33* (45), 13068–13076.
- (42) Zanaga, D.; Bleichrodt, F.; Altantzis, T.; Winckelmans, N.; Palenstijn, W. J.; Sijbers, J.; de Nijs, B.; van Huis, M. A.; Sánchez-Iglesias, A.; Liz-Marzán, L. M.; van Blaaderen, A.; Joost Batenburg, K.; Bals, S.; Van Tendeloo, G. Quantitative 3D analysis of huge nanoparticle assemblies. *Nanoscale* **2016**, *8* (1), 292–299.
- (43) Born, P.; Munoz, A.; Cavelius, C.; Kraus, T. Crystallization Mechanisms in Convective Particle Assembly. *Langmuir* **2012**, *28* (22), 8300–8308.
- (44) Choi, J. J.; Bealing, C. R.; Bian, K.; Hughes, K. J.; Zhang, W.; Smilgies, D. M.; Hennig, R. G.; Engstrom, J. R.; Hanrath, T. Controlling nanocrystal superlattice symmetry and shape-anisotropic interactions through variable ligand surface coverage. *J. Am. Chem. Soc.* **2011**, *133* (9), 3131–8.
- (45) Quan, Z.; Xu, H.; Wang, C.; Wen, X.; Wang, Y.; Zhu, J.; Li, R.; Sheehan, C. J.; Wang, Z.; Smilgies, D. M.; Luo, Z.; Fang, J. Solvent-

mediated self-assembly of nanocube superlattices. *J. Am. Chem. Soc.* **2014**, *136* (4), 1352–9.

(46) Wetterskog, E.; Klapper, A.; Disch, S.; Josten, E.; Hermann, R. P.; Rücker, U.; Brückel, T.; Bergström, L.; Salazar-Alvarez, G. Tuning the structure and habit of iron oxide mesocrystals. *Nanoscale* **2016**, *8* (34), 15571–15580.

(47) Lee, B.; Littrell, K.; Sha, Y.; Shevchenko, E. V. Revealing the Effects of the Non-solvent on the Ligand Shell of Nanoparticles and Their Crystallization. *J. Am. Chem. Soc.* **2019**, *141* (42), 16651–16662.

(48) Huang, X.; Zhu, J.; Ge, B.; Deng, K.; Wu, X.; Xiao, T.; Jiang, T.; Quan, Z.; Cao, Y. C.; Wang, Z. Understanding Fe₃O₄ Nanocube Assembly with Reconstruction of a Consistent Superlattice Phase Diagram. *J. Am. Chem. Soc.* **2019**, *141* (7), 3198–3206.

(49) Huang, X.; Wang, Z. Supercrystallography-Based Decoding of Structure and Driving Force of Nanocrystal Assembly. *Materials* **2019**, *12* (22), 3771.

(50) Agarwal, U.; Escobedo, F. A. Mesophase behaviour of polyhedral particles. *Nat. Mater.* **2011**, *10* (3), 230–235.

(51) Faure, B.; Salazar-Alvarez, G.; Bergström, L. Hamaker Constants of Iron Oxide Nanoparticles. *Langmuir* **2011**, *27* (14), 8659–8664.

(52) Brunner, J. J.; Krumova, M.; Colfen, H.; Sturm née Rosseeva, E. V. Magnetic field-assisted assembly of iron oxide mesocrystals: a matter of nanoparticle shape and magnetic anisotropy. *Beilstein J. Nanotechnol.* **2019**, *10*, 894–900.

(53) Opel, J.; Brunner, J.; Zimmermanns, R.; Steegmans, T.; Sturm, E.; Kellermeier, M.; Cölfen, H.; García-Ruiz, J. M. Symbiosis of Silica Biomorphs and Magnetite Mesocrystals. *Adv. Funct. Mater.* **2019**, *29* (37), 1902047–1902047.

(54) Sturm, S.; Sigleitmeier, M.; Wolf, D.; Vogel, K.; Gratz, M.; Faivre, D.; Lubk, A.; Büchner, B.; Sturm née Rosseeva, E. V.; Cölfen, H., Magnetic Nanoparticle Chains in Gelatin Ferrogels: Bioinspiration from Magnetotactic Bacteria. *Adv. Funct. Mater.* **2019**, *29* (45), 1905996.

(55) Kitaigorodskij, A. I. *Organic Chemical Crystallography*. Consultants Bureau 1961; p 541.

(56) Brunner, J.; Maier, B.; Rosenberg, R.; Sturm, S.; Cölfen, H.; Sturm, E. V. Nonclassical Recrystallization. *Chem. - Eur. J.* **2020**, *26* (66), 15242–15248.

(57) Schlotheuber née Brunner, J. J.; Maier, B.; Kirner, F.; Sturm, S.; Cölfen, H.; Sturm, E. V., Self-Assembled Faceted Mesocrystals: Advances in Optimization of Growth Conditions. *Cryst. Growth Des.* **2021**, *21*, 5490.

(58) Spingler, B.; Schnidrig, S.; Todorova, T.; Wild, F. Some thoughts about the single crystal growth of small molecules. *CrystEngComm* **2012**, *14* (3), 751–757.

(59) Silvera Batista, C. A.; Larson, R. G.; Kotov, N. A. Nonadditivity of nanoparticle interactions. *Science* **2015**, *350* (6257), 1242477.

(60) Chan, H.; Demortiere, A.; Vukovic, L.; Kral, P.; Petit, C. Colloidal nanocube supercrystals stabilized by multipolar Coulombic coupling. *ACS Nano* **2012**, *6* (5), 4203–13.

(61) Blatov, V. A. Voronoi–dirichlet polyhedra in crystal chemistry: theory and applications. *Crystallogr. Rev.* **2004**, *10* (4), 249–318.

(62) Zobel, M.; Neder, R. B.; Kimber, S. A. Universal solvent restructuring induced by colloidal nanoparticles. *Science* **2015**, *347* (6219), 292–4.

(63) Thomä, S. L. J.; Krauss, S. W.; Eckardt, M.; Chater, P.; Zobel, M. Atomic insight into hydration shells around faceted nanoparticles. *Nat. Commun.* **2019**, *10* (1), 995.

(64) Tkatchenko, A.; Scheffler, M. Accurate molecular van der Waals interactions from ground-state electron density and free-atom reference data. *Phys. Rev. Lett.* **2009**, *102* (7), No. 073005.

(65) Park, Y. I.; Piao, Y.; Lee, N.; Yoo, B.; Kim, B. H.; Choi, S. H.; Hyeon, T. Transformation of hydrophobic iron oxide nanoparticles to hydrophilic and biocompatible maghemite nanocrystals for use as highly efficient MRI contrast agent. *J. Mater. Chem.* **2011**, *21* (31), 11472–11477.

(66) Agthe, M.; Wetterskog, E.; Mouzon, J.; Salazar-Alvarez, G.; Bergström, L. Dynamic growth modes of ordered arrays and mesocrystals during drop-casting of iron oxide nanocubes. *CrystEngComm* **2014**, *16* (8), 1443–1450.

(67) Schuck, P. P. *SEDFIT version 16.1c*. <http://analyticalultracentrifugation.com/download.htm>.

(68) Schuck, P.; Rossmanith, P. Determination of the sedimentation coefficient distribution by least-squares boundary modeling. *Biopolymers* **2000**, *54* (5), 328–41.

(69) Demeler, B. *UltraScan version 4.0, release 2783. A Comprehensive Data Analysis Software Package for Analytical Ultracentrifugation Experiments. The University of Lethbridge, Department of Chemistry and Biochemistry*. <http://www.ultrascan3.aucsolutions.com/download.php>.

(70) Brookes, E.; Cao, W.; Demeler, B. A two-dimensional spectrum analysis for sedimentation velocity experiments of mixtures with heterogeneity in molecular weight and shape. *Eur. Biophys. J.* **2010**, *39* (3), 405–14.

(71) Demeler, B.; Nguyen, T. L.; Gorbet, G. E.; Schirf, V.; Brookes, E. H.; Mulvaney, P.; El-Ballouli, A. O.; Pan, J.; Bakr, O. M.; Demeler, A. K.; Hernandez Uribe, B. I.; Bhattacharai, N.; Whetten, R. L. Characterization of size, anisotropy, and density heterogeneity of nanoparticles by sedimentation velocity. *Anal. Chem.* **2014**, *86* (15), 7688–95.

(72) Filik, J.; Ashton, A. W.; Chang, P. C. Y.; Chater, P. A.; Day, S. J.; Drakopoulos, M.; Gerring, M. W.; Hart, M. L.; Magdysyuk, O. V.; Michalik, S.; Smith, A.; Tang, C. C.; Terrill, N. J.; Wharmby, M. T.; Wilhelm, H. Processing two-dimensional X-ray diffraction and small-angle scattering data in DAWN 2. *J. Appl. Crystallogr.* **2017**, *50* (3), 959–966.

(73) Yang, X.; Juhas, P.; Farrow, C. L.; Billinge, S. J. L. xPDFsuite: an end-to-end software solution for high throughput pair distribution function transformation, visualization and analysis. *arXiv:1402.3163v3*, 2014.

Chapter 4

Summary

This work deals with structural studies of colloidal crystals and mesocrystals by novel X-rays methods. The work consists of two major parts.

In the first part, the structures were revealed by analysis of 2D scattering patterns with the form factor fitting, Bragg peak fitting, and AXCCA.

Firstly, a colloid consisting of thermoresponsive gold-PNIPAM core-shell nanoparticles was studied during cooling and heating. 2D scattering patterns were measured in USAXS geometry. I analysed the core-shell form factor measured for a diluted sample at different temperatures, extracted the geometrical parameters of the core-shell particles, and found the signs of a volume phase transition when the polymer shell collapses. I analysed the structure factors measured for a concentrated sample at different temperatures and found the phase transition from a fluid state to a crystalline phase. The fluid structure factor was fitted by the Percus-Yevick hard sphere model that gave the sphere radius and volume fraction. The parameters of the Bragg peaks of the crystalline structure factor were extracted by the separate fitting of each Bragg peak with the Gaussian function. The Bragg peaks were attributed to an rhcp lattice, and the lattice parameters were found to evolve during the crystallization and melting. Moreover, during the melting, a splitting of the Bragg peaks was observed which implies the cracking of a crystallite into several smaller crystallites. The extracted FWHMs of the Bragg peaks were converted into the strain values by the Williamson-Hall method, and the strain was found to grow during both crystallization and melting. Signs of in-plane as well as out-of-plane plane defects (stacking faults) were found by analysis of the FWHMs. These findings shed light on the structural features of crystallization and melting of thermoresponsive colloidal crystals that are believed to be fully reversible and repeatable.

Secondly, mesocrystalline microchannels consisting of lead sulfide PbS nanoparticles functionalized with Cu₄APc self-assembled on a Kapton substrate with preliminary deposited gold contacts were investigated. 2D scattering patterns were measured

in complementary SAXS/WAXS geometry that allowed registration of the Bragg peaks from both SL and ALs of the nanoparticles. I extracted the unit cell parameters of both SL and AL by fitting the Bragg peaks with the Gaussian functions. The microchannels were found to be characterized by two different structures (bcc and hcp) with different distances between the adjacent nanocrystals. I exploited AXCCA to determine the angular orientation of the nanocrystals inside the SL. The results of the structural investigations were compared with the results of transport measurements of the same channels performed before the X-ray experiment. There was found a correlation between the structure and the distance between the adjacent nanocrystals inside the mesocrystalline microchannels. Moreover, signs of transport anisotropy were revealed by correlating the angular orientation of the SL inside the microchannels and their conductivity.

Thirdly, mesocrystals consisting of cesium lead halide nanoparticles stabilized with OA and OAm were investigated. 2D scattering patterns were measured in the same complementary SAXS/WAXS geometry as in the previous case at different points with high spatial resolution. I analysed the Bragg peaks from both SL and AL of the nanocrystals by fitting them with the Gaussian functions. Extracted unit cell parameters indicated that the local structure of the SL is different from the average one and tends to distort on the mesocrystal boundaries. The nanocrystals were found to be angularly disordered and closer to the adjacent ones on the mesocrystal edges. These results were compared with the results of fluorescence spectroscopy and lifetime measurements. The optical properties on the edges were found to differ from the bulk properties as well. A similar characteristic length from the mesocrystal edge on which the deviations in structure and optical properties happen suggested that the structural heterogeneity is one of the reasons for the differences in optical properties.

In the second part, the structures were revealed by analysis of the intensity distribution measured in 3D reciprocal space with AXCCA.

Firstly, I revised the theoretical background of AXCCA for application to 3D scattered intensity distributions instead of 2D scattering patterns. I proposed a geometrical model for interpretation of the AXCCA results from the scattered intensities measured for single crystalline grains. I successfully demonstrated the application of the developed technique on an exemplifying dataset. For a colloidal crystal consisting of silica spheres, it allowed to quantitatively reveal the stacking sequence in a close-packed structure and indicated the presence of plane defects in the sample.

Secondly, for a mesocrystalline grain consisting of gold nanocubes, I exploited AXCCA to reveal the average SL structure that was found to be triclinic. This result was used in combination with the electron density reconstruction by the phase retrieval methods to extract the strain tensor. I analysed the anisotropic form factor features of the nanocubes to extract the angular orientation of the nanocubes inside the SL.

Together, the obtained results allowed the full structural characterization of a gold mesocrystalline grain.

Thirdly, for mesocrystalline grains consisting of gold nanocubes self-assembled from different solvents (tetrahydrofuran and heptane), I exploited AXCCA to reveal the average SL structure. It was found to be body-center tetragonal in both cases with the tetragonal distortion close to that characteristic for an fcc lattice. The degree of difference from the fcc structure was found to be depended on the solvent used. This fact shed light on the fundamental question of the mesocrystal self-assembly from a solvent.

To summarize, this work contributes to the development of novel X-ray methods available for structural investigations of colloidal crystals and mesocrystals. The results obtained by the developed techniques on colloidal and mesocrystalline samples are of high interest to the materials science community and potentially lead to improvement in the application of the studied materials.

List of publications

Publications directly related to this thesis

1. **D. Lapkin**, A. Shabalin, R. P. Kurta, J.-M. Meijer, M. Sprung, A. V. Petukhov, and I. A. Vartanyants. Angular X-ray cross-correlation analysis applied to the scattering data in 3D reciprocal space from a single crystal. *IUCrJ* **9** (2022).
2. **D. Lapkin**, C. Kirsch, J. Hiller, D. Andrienko, D. Assalauova, K. Braun, J. Carnis, Y. Y. Kim, M. Mandal, A. Maier, A. J. Meixner, N. Mukharamova, M. Scheele, F. Schreiber, M. Sprung, J. Wahl, S. Westendorf, I. A. Zaluzhnyy, and I. A. Vartanyants. Spatially resolved fluorescence of caesium lead halide perovskite supercrystals reveals quasi-atomic behavior of nanocrystals. *Nat. Commun.* **13**, 892 (2022).
3. **D. Lapkin**, N. Mukharamova, D. Assalauova, S. Dubinina, J. Stellhorn, F. Westermeier, S. Lazarev, M. Sprung, M. Karg, I. A. Vartanyants, and J.-M. Meijer. In situ characterization of crystallization and melting of soft, thermoresponsive microgels by small-angle X-ray scattering. *Soft Matter* **18**, 1591 (2022).
4. J. Carnis, F. Kirner, **D. Lapkin**, S. Sturm, Y. Y. Kim, I. A. Baburin, R. Khubbutdinov, A. Ignatenko, E. Iashina, A. Mistonov, T. Steegemans, T. Wieck, T. Gemming, A. Lubk, S. Lazarev, M. Sprung, I. A. Vartanyants, and E. V. Sturm. Exploring the 3D structure and defects of a self-assembled gold mesocrystal by coherent X-ray diffraction imaging” *Nanoscale* **13**, 10425 (2021).
5. J. Schlotheuber né Brunner, B. Maier, S. L. Thomä, F. Kirner, I. A. Baburin, **D. Lapkin**, R. Rosenberg, S. Sturm, D. Assalauova, J. Carnis, Y. Y. Kim, Z. Ren, F. Westermeier, S. Theiss, H. Borrmann, S. Polarz, A. Eychmüller, A. Lubk, I. A. Vartanyants, H. Cölfen, M. Zobel, and E. V. Sturm. Morphogenesis of magnetite mesocrystals: Interplay between nanoparticle morphology and solvation shell. *Chem. Mater.* **33**, 9119 (2021).
6. A. Maier, **D. Lapkin**, N. Mukharamova, P. Frech, D. Assalauova, A. Ignatenko, R. Khubbutdinov, S. Lazarev, M. Sprung, F. Laible, R. Löffler, N. Previdi, A. Bräuer, T. Günkel, M. Fleischer, F. Schreiber, I. A. Vartanyants, and M. Scheele. Structure–transport correlation reveals anisotropic charge transport in coupled PbS

nanocrystal superlattices. *Adv. Mater.* **32**, 2002254 (2020).

Other publications

1. R. Khubbutdinov, N. Gerasimova, G. Mercurio, D. Assalauova, J. Carnis, L. Gelisio, L. Le Guyader, A. Ignatenko, Y. Y. Kim, B. E. Van Kuiken, R. P. Kurta, **D. Lapkin**, M. Teichmann, A. Yaroslavtsev, O. Gorobtsov, A. P. Menushenkov, M. Scholz, A. Scherz, and I. A. Vartanyants. High spatial coherence and short pulse duration revealed by the Hanbury Brown and Twiss interferometry at the European XFEL. *Struct. Dyn.* **8**, 044305 (2021).
2. **D. A. Lapkin**, A. N. Korovin, S. N. Malakhov, A. V. Emelyanov, V. A. Demin, and V. V. Erokhin. Optical Monitoring of the Resistive States of a Polyaniline-Based Memristive Device. *Adv. Electron. Mater.* **6**, 2000511 (2020).
3. N. V. Prudnikov, **D. A. Lapkin**, A. V. Emelyanov, A. A. Minnekhanov, Yu. N. Malakhova, S. N. Chvalun, V. A. Demin, and V. V. Erokhin. Associative STDP-like learning of neuromorphic circuits based on polyaniline memristive microdevices. *J. Phys. D Appl. Phys.* **53**, 414001 (2020).
4. N. Mukharamova, **D. Lapkin**, I. A. Zaluzhnyy, A. André, S. Lazarev, Y. Y. Kim, M. Sprung, R. P. Kurta, F. Schreiber, I. A. Vartanyants, and M. Scheele. Revealing Grain Boundaries and Defect Formation in Nanocrystal Superlattices by Nanodiffraction. *Small* **15**, 1904954 (2019).
5. B. S. Shvetsov, A. N. Matsukatova, A. A. Minnekhanov, A. A. Nesmelov, B. V. Goncharov, **D. A. Lapkin**, M. N. Martyshov, P. A. Forsh, V. V. Rylkov, V. A. Demin, and A. V. Emelyanov. Poly-para-xylylene-Based Memristors on Flexible Substrates. *Tech. Phys. Lett.* **45**, 1103 (2019).
6. **D. A. Lapkin**, S. N. Malakhov, V. A. Demin, S. N. Chvalun, and L. A. Feigin. Hybrid polyaniline/polyamide-6 fibers and nonwoven materials for assembling organic memristive elements. *Synthetic Met.* **254**, 63 (2019).
7. A. A. Minnekhanov, A. V. Emelyanov, **D. A. Lapkin**, K. E. Nikiruy, B. S. Shvetsov, A. A. Nesmelov, V. V. Rylkov, V. A. Demin, and V. V. Erokhin. Parylene Based Memristive Devices with Multilevel Resistive Switching for Neuromorphic Applications. *Sci. Rep.* **9**, 10800 (2019).
8. **D. A. Lapkin**, A. V. Emelyanov, V. A. Demin, V. V. Erokhin, L. A. Feigin, P. K. Kashkarov, and M. V. Kovalchuk. Polyaniline-based memristive microdevice with high switching rate and endurance. *Appl. Phys. Lett.* **112**, 043302 (2018).
9. **D. A. Lapkin**, A. V. Emelyanov, V. A. Demin, T. S. Berzina, and V. V. Erokhin. Spike-timing-dependent plasticity of polyaniline-based memristive element. *Microelectron. Eng.* **185**, 43 (2018).

10. **D. A. Lapkin**, S. N. Malakhov, V. A. Demin, and S. N. Chvalun. An organic memristive element based on single polyaniline/polyamide-6 fiber. *Tech. Phys. Lett.* **43**, 1102 (2017).
11. Yu. N. Malakhova, A. N. Korovin, **D. A. Lapkin**, S. N. Malakhov, V. V. Shcherban, E. B. Pichkur, S. N. Yakunin, V. A. Demin, S. N. Chvalun, and V. Erokhin. Planar and 3D fibrous polyaniline-based materials for memristive elements. *Soft Matter* **13**, 7300 (2017).
12. A. V. Emelyanov, **D. A. Lapkin**, V. A. Demin, V. V. Erokhin, S. Battistoni, G. Baldi, and M. V. Kovalchuk. First steps towards the realization of a double layer perceptron based on organic memristive devices. *AIP Adv.* **6**, 111301 (2016).
13. V. A. Demin, A. V. Emelyanov, **D. A. Lapkin**, V. V. Erokhin, P. K. Kashkarov, and M. V. Kovalchuk. Neuromorphic elements and systems as the basis for the physical implementation of artificial intelligence technologies. *Crystallogr. Rep.* **61**, 992 (2016).
14. **D. A. Lapkin**, A. N. Korovin, V. A. Demin, A. V. Emelyanov. and S. N. Chvalun. Organic memristive device based on polyaniline film prepared by spin coating. *BioNanoScience* **5**, 181 (2015).

List of abbreviations

2D two-dimensional

3D three-dimensional

AL atomic lattice

AXCCA Angular X-ray Cross-Correlation Analysis

AXRS Anomalous X-ray Scattering

bcc body-centered cubic

CCF Cross-Correlation Function

CDI Coherent Diffraction Imaging

CT Computed Tomography

CTR Crystal Truncation Rod

Cu4APc copper 4,4',4'',4'''-tetraaminophthalocyanine

DLS Dynamic Light Scattering

DLVO Derjaguin-Landau-Verwey-Overbeek

EXAFS Extended X-ray Absorption Fine Structure

fcc face-centered cubic

FEL Free-Electron Laser

FWHM full-width-at-half-maximum

GISAXS Grazing-Incidence Small-Angle X-ray Scattering

GIWAXS Grazing-Incidence Wide-Angle X-ray Scattering

hcp hexagonal close-packed

HRTEM High Resolution Transmission Electron Microscopy

LCLS Linac Coherent Light Source

LCST Lower Critical Solution Temperature

OA oleic acid

OAm oleylamine

PMMA poly(methyl methacrylate)

PNIPAM poly(N-isopropylacrylamide)

rhcp random hexagonal closed-packed

SASE Self-Amplified Spontaneous Emission

SAXS Small-Angle X-ray Scattering

SL superlattice

TEM Transmission Electron Microscopy

USAXS Ultra-Small-Angle X-ray Scattering

UV Ultraviolet

VPT Volume Phase Transition

WAXS Wide-Angle X-ray Scattering

XAES X-ray induced Auger Electron Spectroscopy

XAS X-ray Absorption Spectroscopy

XFEL X-ray Free-Electron Laser

XPCS X-ray Photon Correlation Spectroscopy

XPS X-ray Photoemission Spectroscopy

XRF X-ray Fluorescence

Bibliography

- ¹C. H. Gerould, “Comments on the use of latex spheres as size standards in electron microscopy”, *J. Appl. Phys.* **21**, 183–184 (1950).
- ²T. Alfrey, E. Bradford, J. Vanderhoff, and G. Oster, “Optical properties of uniform particle-size latexes”, *J. Opt. Soc. Am.* **44**, 603–609 (1954).
- ³Z. Cheng, P. Chaikin, W. Russel, W. Meyer, J. Zhu, R. Rogers, and R. Ottewill, “Phase diagram of hard spheres”, *Mater. Design* **22**, 529–534 (2001).
- ⁴J.-M. Meijer, A. Shabalin, R. Dronyak, O. Yefanov, A. Singer, R. Kurta, U. Lorenz, O. Gorobstov, D. Dzhigaev, J. Gulden, et al., “Double hexagonal close-packed structure revealed in a single colloidal crystal grain by Bragg rod analysis”, *J. Appl. Crystallogr.* **47**, 1199–1204 (2014).
- ⁵D. Giuntini, S. Zhao, T. Krekeler, M. Li, M. Blankenburg, B. Bor, G. Schaan, B. Domènech, M. Müller, I. Scheider, et al., “Defects and plasticity in ultrastrong supercrystalline nanocomposites”, *Sci. Adv.* **7**, eabb6063 (2021).
- ⁶Y. Sun and Y. Xia, “Shape-controlled synthesis of gold and silver nanoparticles”, *Science* **298**, 2176–2179 (2002).
- ⁷J. D. Forster, J.-G. Park, M. Mittal, H. Noh, C. F. Schreck, C. S. O’Hern, H. Cao, E. M. Furst, and E. R. Dufresne, “Assembly of optical-scale dumbbells into dense photonic crystals”, *ACS Nano* **5**, 6695–6700 (2011).
- ⁸K. Miszta, J. De Graaf, G. Bertoni, D. Dorfs, R. Brescia, S. Marras, L. Ceseracciu, R. Cingolani, R. Van Roij, M. Dijkstra, et al., “Hierarchical self-assembly of suspended branched colloidal nanocrystals into superlattice structures”, *Nat. Mater.* **10**, 872–876 (2011).
- ⁹H. Cölfen and M. Antonietti, “Mesocrystals: inorganic superstructures made by highly parallel crystallization and controlled alignment”, *Angew. Chem. Int. Edit.* **44**, 5576–5591 (2005).
- ¹⁰F. Scotognella, D. P. Puzzo, A. Monguzzi, D. S. Wiersma, D. Maschke, R. Tubino, and G. A. Ozin, “Nanoparticle one-dimensional photonic-crystal dye laser”, *Small* **5**, 2048–2052 (2009).

- ¹¹S. Furumi, H. Fudouzi, and T. Sawada, "Self-organized colloidal crystals for photonics and laser applications", *Laser Photonics Rev.* **4**, 205–220 (2010).
- ¹²S. John, "Strong localization of photons in certain disordered dielectric superlattices", *Phys. Rev. Lett.* **58**, 2486 (1987).
- ¹³S. A. Asher, J. M. Weissman, A. Tikhonov, R. D. Coalson, and R. Kesavamoorthy, "Diffraction in crystalline colloidal-array photonic crystals", *Phys. Rev. E* **69**, 066619 (2004).
- ¹⁴Y. Bai, W. Yang, Y. Sun, and C. Sun, "Enzyme-free glucose sensor based on a three-dimensional gold film electrode", *Sensor. Actuat. B - Chem.* **134**, 471–476 (2008).
- ¹⁵F. Su, X. Zhao, Y. Wang, J. Zeng, Z. Zhou, and J. Y. Lee, "Synthesis of graphitic ordered macroporous carbon with a three-dimensional interconnected pore structure for electrochemical applications", *J. Phys. Chem. B* **109**, 20200–20206 (2005).
- ¹⁶O.-H. Kim, Y.-H. Cho, S. H. Kang, H.-Y. Park, M. Kim, J. W. Lim, D. Y. Chung, M. J. Lee, H. Choe, and Y.-E. Sung, "Ordered macroporous platinum electrode and enhanced mass transfer in fuel cells using inverse opal structure", *Nat. Comm.* **4**, 1–9 (2013).
- ¹⁷J.-S. Lee, M. V. Kovalenko, J. Huang, D. S. Chung, and D. V. Talapin, "Band-like transport, high electron mobility and high photoconductivity in all-inorganic nanocrystal arrays", *Nat. Nanotechnol.* **6**, 348–352 (2011).
- ¹⁸T.-H. Kim, K.-S. Cho, E. K. Lee, S. J. Lee, J. Chae, J. W. Kim, D. H. Kim, J.-Y. Kwon, G. Amaratunga, S. Y. Lee, et al., "Full-colour quantum dot displays fabricated by transfer printing", *Nat. Photonics* **5**, 176–182 (2011).
- ¹⁹T. Harman, P. Taylor, M. Walsh, and B. LaForge, "Quantum dot superlattice thermoelectric materials and devices", *Science* **297**, 2229–2232 (2002).
- ²⁰G. Rainò, M. A. Becker, M. I. Bodnarchuk, R. F. Mahrt, M. V. Kovalenko, and T. Stöferle, "Superfluorescence from lead halide perovskite quantum dot superlattices", *Nature* **563**, 671–675 (2018).
- ²¹J.-M. Meijer, *Colloidal crystals of spheres and cubes in real and reciprocal space* (Springer, 2015).
- ²²J.-M. Meijer, V. W. de Villeneuve, and A. V. Petukhov, "In-plane stacking disorder in polydisperse hard sphere crystals", *Langmuir* **23**, 3554–3560 (2007).
- ²³D. V. Byelov, J. Hilhorst, A. B. Leferink op Reinink, I. Snigireva, A. Snigirev, G. B. Vaughan, G. Portale, and A. V. Petukhov, "Diffuse scattering in random-stacking hexagonal close-packed crystals of colloidal hard spheres", *Phase Transit.* **83**, 107–114 (2010).

- ²⁴D. Dunphy, H. Fan, X. Li, J. Wang, and C. J. Brinker, “Dynamic investigation of gold nanocrystal assembly using in situ grazing-incidence small-angle X-ray scattering”, *Langmuir* **24**, 10575–10578 (2008).
- ²⁵M. C. Weidman, D.-M. Smilgies, and W. A. Tisdale, “Kinetics of the self-assembly of nanocrystal superlattices measured by real-time in situ X-ray scattering”, *Nat. Mater.* **15**, 775–781 (2016).
- ²⁶A. Shabalin, J.-M. Meijer, R. Dronyak, O. Yefanov, A. Singer, R. Kurta, U. Lorenz, O. Gorobtsov, D. Dzhigaev, S. Kalbfleisch, et al., “Revealing three-dimensional structure of an individual colloidal crystal grain by coherent X-ray diffractive imaging”, *Phys. Rev. Lett.* **117**, 138002 (2016).
- ²⁷N. Goubet, P. Albouy, A. Thompson, and M. Pileni, “Polymorphism in nanoparticle-based crystals depending upon their single or polycrystalline character”, *CrystEngComm* **18**, 6166–6175 (2016).
- ²⁸I. A. Zaluzhnyy, R. P. Kurta, A. André, O. Y. Gorobtsov, M. Rose, P. Skopintsev, I. Besedin, A. V. Zozulya, M. Sprung, F. Schreiber, et al., “Quantifying angular correlations between the atomic lattice and the superlattice of nanocrystals assembled with directional linking”, *Nano Lett.* **17**, 3511–3517 (2017).
- ²⁹I. Lokteva, M. Koof, M. Walther, G. Grübel, and F. Lehmkuhler, “Monitoring nanocrystal self-assembly in real time using in situ small-angle X-ray scattering”, *Small* **15**, 1900438 (2019).
- ³⁰J. D. Jackson, *Classical electrodynamics* (Wiley, New York, 1975).
- ³¹L. D. Landau and E. M. Lifshitz, *The classical theory of fields*, Course of theoretical physics (Butterworth-Heinemann, 1975).
- ³²J. Als-Nielsen and D. McMorrow, *Elements of modern X-ray physics* (Wiley, 2011).
- ³³D. Attwood, A. Sakdinawat, and L. Geniesse, *X-rays and extreme ultraviolet radiation: principles and applications* (Cambridge University Press, 2017).
- ³⁴J. Goodman, *Statistical optics*, Wiley Series in Pure and Applied Optics (Wiley, 2015).
- ³⁵W. C. Röntgen, “Über eine neue Art von Strahlen”, *Sitzungsber. Phys. Med. Ges. Würtzburg* **9**, 132–141 (1895).
- ³⁶P. Bouguer, *Essai d’optique sur la gradation de la lumière* (Claude Jombert, 1729).
- ³⁷A. Beer, *Grundriss des photometrischen Calculs: mit in den Text eingedruckten Holzschnitten* (Vieweg, 1854).
- ³⁸T. M. Buzug, “Computed tomography”, in *Springer handbook of medical technology* (Springer, 2011), pp. 311–342.
- ³⁹L. De Chiffre, S. Carmignato, J.-P. Kruth, R. Schmitt, and A. Weckenmann, “Industrial applications of computed tomography”, *CIRP Annals* **63**, 655–677 (2014).

- ⁴⁰E. Maire and P. J. Withers, “Quantitative X-ray tomography”, *Int. Mat. Rev.* **59**, 1–43 (2014).
- ⁴¹A. Einstein, “Über einen die Erzeugung und Verwandlung des Lichtes betreffenden heuristischen Gesichtspunkt”, *Ann. Phys.* **322**, 132–148 (1905).
- ⁴²M. Newville, “Fundamentals of XAFS”, *Rev. Mineral. Geochem.* **78**, 33–74 (2014).
- ⁴³I. Lindau, P. Pianetta, S. Doniach, and W. Spicer, “X-ray photoemission spectroscopy”, *Nature* **250**, 214–215 (1974).
- ⁴⁴D. C. Koningsberger and R. Prins, *X-ray absorption: principles, applications, techniques of EXAFS, SEXAFS and XANES* (John Wiley and Sons Inc., New York, NY, 1987).
- ⁴⁵B. Beckhoff, B. Kanngießer, N. Langhoff, R. Wedell, and H. Wolff, *Handbook of practical X-ray fluorescence analysis* (Springer Science & Business Media, 2007).
- ⁴⁶N. H. Turner and J. A. Schreifels, “Surface analysis: X-ray photoelectron spectroscopy and Auger electron spectroscopy”, *Anal. Chem.* **64**, 302–320 (1992).
- ⁴⁷N. Wiener, “Generalized harmonic analysis”, *Acta Math.* **55**, 117–258 (1930).
- ⁴⁸A. Khintchine, “Korrelationstheorie der stationären stochastischen Prozesse”, *Math. Ann.* **109**, 604–615 (1934).
- ⁴⁹P. H. van Cittert, “Die wahrscheinliche Schwingungsverteilung in einer von einer Lichtquelle direkt oder mittels einer Linse beleuchteten Ebene”, *Physica* **1**, 201–210 (1934).
- ⁵⁰F. Zernike, “The concept of degree of coherence and its application to optical problems”, *Physica* **5**, 785–795 (1938).
- ⁵¹K. Balewski, W. Brefeld, W. Decking, H. Franz, R. Röhlberger, and E. E. Weckert, *PETRA III: a low emittance synchrotron radiation source. Technical design report*, tech. rep. (DESY, Hamburg, Germany, Feb. 2004).
- ⁵²J. Thomson, *Conduction of electricity through gases* (Cambridge University Press, 1928).
- ⁵³A. H. Compton, “A quantum theory of the scattering of X-rays by light elements”, *Phys. Rev.* **21**, 483 (1923).
- ⁵⁴A. H. Compton, “The spectrum of scattered X-rays”, *Phys. Rev.* **22**, 409 (1923).
- ⁵⁵G. A. Carlsson, C. A. Carlsson, K.-F. Berggren, and R. Ribberfors, “Calculation of scattering cross sections for increased accuracy in diagnostic radiology. I. Energy broadening of Compton-scattered photons”, *Med. Phys.* **9**, 868–879 (1982).
- ⁵⁶G. Matscheko, G. A. Carlsson, and R. Ribberfors, “Compton spectroscopy in the diagnostic X-ray energy range: II. Effects of scattering material and energy resolution”, *Phys. Med. Biol.* **34**, 199 (1989).
- ⁵⁷M. Cooper, P. Mijnen, N. Shiotani, N. Sakai, and A. Bansil, *X-ray Compton scattering*, Vol. 5 (OUP Oxford, 2004).

- ⁵⁸R. N. Bracewell and R. N. Bracewell, *The Fourier transform and its applications*, Vol. 31999 (McGraw-hill New York, 1986).
- ⁵⁹Y. Waseda, *Anomalous X-ray scattering for materials characterization: Atomic-scale structure determination*, Springer Tracts in Modern Physics (Springer Berlin Heidelberg, 2003).
- ⁶⁰P. J. Brown, A. G. Fox, E. N. Maslen, M. A. O’Keefe, and B. T. M. Willis, “Intensity of diffracted intensities”, in *International Tables for Crystallography*, Vol. C, edited by H. Fuess, T. Hahn, H. Wondratschek, U. Müller, U. Shmueli, E. Prince, A. Authier, V. Kopský, D. B. Litvin, M. G. Rossmann, E. Arnold, S. Hall, B. McMahon, and E. Prince, 1st ed., Series Title: International Tables for Crystallography (International Union of Crystallography, Chester, England, Oct. 2006), pp. 554–595.
- ⁶¹L. Feigin and D. Svergun, *Structure analysis by small-angle X-ray and neutron scattering* (Springer US, 2013).
- ⁶²T. Li, A. J. Senesi, and B. Lee, “Small angle X-ray scattering for nanoparticle research”, *Chem. Rev.* **116**, 11128–11180 (2016).
- ⁶³D. I. Svergun and M. H. Koch, “Small-angle scattering studies of biological macromolecules in solution”, *Rep. Prog. Phys.* **66**, 1735 (2003).
- ⁶⁴L. Landau and E. Lifshits, *Statistical physics, part 1*, Course of theoretical physics (1958).
- ⁶⁵M. Glazer and G. Burns, *Space groups for solid state scientists* (Elsevier Science, 2013).
- ⁶⁶T. C. Hales, “A proof of the kepler conjecture”, *Ann. Math.* **162**, 1065–1185 (2005).
- ⁶⁷P. G. Bolhuis, D. Frenkel, S.-C. Mau, and D. A. Huse, “Entropy difference between crystal phases”, *Nature* **388**, 235–236 (1997).
- ⁶⁸G. Stout, L. Jensen, and L. Jensen, *X-ray structure determination: a practical guide*, A Wiley-Interscience publication (Wiley, 1989).
- ⁶⁹G. Girolami, *X-ray crystallography* (University Science Books, 2015).
- ⁷⁰I. K. Robinson, “Crystal truncation rods and surface roughness”, *Phys. Rev. B* **33**, 3830 (1986).
- ⁷¹A. Petukhov, I. Dolbnya, D. Aarts, G. Vroege, and H. Lekkerkerker, “Bragg rods and multiple X-ray scattering in random-stacking colloidal crystals”, *Phys. Rev. Lett.* **90**, 028304 (2003).
- ⁷²J. Langford and A. Wilson, “Scherrer after sixty years: a survey and some new results in the determination of crystallite size”, *J. Appl. Crystallogr.* **11**, 102–113 (1978).
- ⁷³A. Stokes and A. Wilson, “The diffraction of X-rays by distorted crystal aggregates-I”, *P. Phys. Soc.* **56**, 174 (1944).

- ⁷⁴G. Williamson and W. Hall, "X-ray line broadening from filed aluminium and wolfram", *Acta Metall. Mater.* **1**, 22–31 (1953).
- ⁷⁵P. Chaikin and T. Lubensky, *Principles of condensed matter physics* (Cambridge University Press, 2000).
- ⁷⁶L. S. Ornstein and F. Zernike, "Accidental deviations of density and opalescence at the critical point of a single substance", *Proc. Akad. Sci. Amsterdam* **17**, 793 (1914).
- ⁷⁷J. K. Percus and G. J. Yevick, "Analysis of classical statistical mechanics by means of collective coordinates", *Phys. Rev.* **110**, 1 (1958).
- ⁷⁸M. Wertheim, "Exact solution of the Percus-Yevick integral equation for hard spheres", *Phys. Rev. Lett.* **10**, 321 (1963).
- ⁷⁹D. J. Kinning and E. L. Thomas, "Hard-sphere interactions between spherical domains in diblock copolymers", *Macromolecules* **17**, 1712–1718 (1984).
- ⁸⁰N. W. Ashcroft and J. Lekner, "Structure and resistivity of liquid metals", *Phys. Rev.* **145**, 83 (1966).
- ⁸¹H. Chen, Y. Waseda, and K. Aust, "Structure of $Pt_{75}P_{25}$ glass", *Phys. Status Solidi A* **65**, 695–700 (1981).
- ⁸²E. W. Kaler, K. E. Bennett, H. T. Davis, and L. Scriven, "Toward understanding microemulsion microstructure: a small-angle X-ray scattering study", *J. Chem. Phys.* **79**, 5673–5684 (1983).
- ⁸³S. Menon, C. Manohar, and K. S. Rao, "A new interpretation of the sticky hard sphere model", *J. Chem. Phys.* **95**, 9186–9190 (1991).
- ⁸⁴J. B. Hayter and J. Penfold, "An analytic structure factor for macroion solutions", *Mol. Phys.* **42**, 109–118 (1981).
- ⁸⁵R. Kurta, M. Altarelli, E. Weckert, and I. Vartanyants, "X-ray cross-correlation analysis applied to disordered two-dimensional systems", *Phys. Rev. B* **85**, 184204 (2012).
- ⁸⁶R. Kurta, R. Dronyak, M. Altarelli, E. Weckert, and I. Vartanyants, "Solution of the phase problem for coherent scattering from a disordered system of identical particles", *New J. Phys.* **15**, 013059 (2013).
- ⁸⁷Z. Kam, "Determination of macromolecular structure in solution by spatial correlation of scattering fluctuations", *Macromolecules* **10**, 927–934 (1977).
- ⁸⁸Z. Kam, "The reconstruction of structure from electron micrographs of randomly oriented particles", *J. Theor. Biol.* **82**, 15–39 (1980).
- ⁸⁹P. Wochner, C. Gutt, T. Autenrieth, T. Demmer, V. Bugaev, A. D. Ortiz, A. Duri, F. Zontone, G. Grübel, and H. Dosch, "X-ray cross correlation analysis uncovers hidden local symmetries in disordered matter", *P. Natl. Acad. Sci.* **106**, 11511–11514 (2009).

- ⁹⁰D. Saldin, V. Shneerson, M. R. Howells, S. Marchesini, H. N. Chapman, M. Bogan, D. Shapiro, R. Kirian, U. Weierstall, K. Schmidt, et al., “Structure of a single particle from scattering by many particles randomly oriented about an axis: toward structure solution without crystallization?”, *New J. Phys.* **12**, 035014 (2010).
- ⁹¹D. Saldin, H. Poon, V. Shneerson, M. Howells, H. Chapman, R. Kirian, K. Schmidt, and J. Spence, “Beyond small-angle X-ray scattering: exploiting angular correlations”, *Phys. Rev. B* **81**, 174105 (2010).
- ⁹²M. Altarelli, R. Kurta, and I. Vartanyants, “X-ray cross-correlation analysis and local symmetries of disordered systems: general theory”, *Phys. Rev. B* **82**, 104207 (2010).
- ⁹³B. Pedrini, A. Menzel, M. Guizar-Sicairos, V. A. Guzenko, S. Gorelick, C. David, B. D. Patterson, and R. Abela, “Two-dimensional structure from random multiparticle X-ray scattering images using cross-correlations”, *Nat. Commun.* **4**, 1–9 (2013).
- ⁹⁴J. J. Donatelli, P. H. Zwart, and J. A. Sethian, “Iterative phasing for fluctuation X-ray scattering”, *P. Natl. Acad. Sci.* **112**, 10286–10291 (2015).
- ⁹⁵D. Saldin, H. Poon, M. Bogan, S. Marchesini, D. Shapiro, R. Kirian, U. Weierstall, and J. Spence, “New light on disordered ensembles: ab initio structure determination of one particle from scattering fluctuations of many copies”, *Phys. Rev. Lett.* **106**, 115501 (2011).
- ⁹⁶R. A. Kirian, “Structure determination through correlated fluctuations in X-ray scattering”, *J. Phys. B - At. Mol. Opt.* **45**, 223001 (2012).
- ⁹⁷D. Starodub, A. Aquila, S. Bajt, M. Barthelmess, A. Barty, C. Bostedt, J. D. Bozek, N. Coppola, R. B. Doak, S. W. Epp, et al., “Single-particle structure determination by correlations of snapshot X-ray diffraction patterns”, *Nat. Commun.* **3**, 1–7 (2012).
- ⁹⁸K. Pande, J. J. Donatelli, E. Malmerberg, L. Foucar, C. Bostedt, I. Schlichting, and P. H. Zwart, “Ab initio structure determination from experimental fluctuation X-ray scattering data”, *P. Natl. Acad. Sci.* **115**, 11772–11777 (2018).
- ⁹⁹N. A. Clark, B. J. Ackerson, and A. J. Hurd, “Multidetector scattering as a probe of local structure in disordered phases”, *Phys. Rev. Lett.* **50**, 1459 (1983).
- ¹⁰⁰J. Rodenburg and I. Rauf, “A cross-correlation measure of order in “amorphous” indium oxide”, in *Inst. Phys. Conf. Ser. Vol. 98*, 5 (1989), pp. 119–122.
- ¹⁰¹J. Gibson, M. Treacy, T. Sun, and N. Zaluzec, “Substantial crystalline topology in amorphous silicon”, *Phys. Rev. Lett.* **105**, 125504 (2010).
- ¹⁰²A. C. Y. Liu, M. J. Neish, G. Stokol, G. Buckley, L. Smillie, M. D. de Jonge, R. Ott, M. Kramer, and L. Bourgeois, “Systematic mapping of icosahedral short-range order in a melt-spun $Zr_{36}Cu_{64}$ metallic glass”, *Phys. Rev. Lett.* **110**, 205505 (2013).

- ¹⁰³R. P. Kurta, L. Wiegart, A. Flueraşu, and A. Madsen, “Fluctuation X-ray scattering from nanorods in solution reveals weak temperature-dependent orientational ordering”, *IUCrJ* **6**, 635–648 (2019).
- ¹⁰⁴R. Kurta, Y. Chesnokov, E. Weckert, and I. Vartanyants, “Cross-correlation analysis of X-ray scattering from oxygen clusters”, in *J. Phys. Conf. Ser. Vol. 463, 1* (IOP Publishing, 2013), p. 012046.
- ¹⁰⁵P. Vester, I. A. Zaluzhnyy, R. P. Kurta, K. B. Möller, E. Biasin, K. Haldrup, M. M. Nielsen, and I. A. Vartanyants, “Ultrafast structural dynamics of photo-reactions observed by time-resolved X-ray cross-correlation analysis”, *Struct. Dynam.* **6**, 024301 (2019).
- ¹⁰⁶I. Zaluzhnyy, R. Kurta, E. Sulyanova, O. Gorobtsov, A. Shabalin, A. Zozulya, A. Menushenkov, M. Sprung, B. Ostrovskii, and I. Vartanyants, “Spatially resolved X-ray studies of liquid crystals with strongly developed bond-orientational order”, *Phys. Rev. E* **91**, 042506 (2015).
- ¹⁰⁷I. Zaluzhnyy, R. Kurta, E. Sulyanova, O. Y. Gorobtsov, A. Shabalin, A. Zozulya, A. Menushenkov, M. Sprung, A. Krówczyński, E. Górecka, et al., “Structural studies of the bond-orientational order and hexatic–smectic transition in liquid crystals of various compositions”, *Soft Matter* **13**, 3240–3252 (2017).
- ¹⁰⁸I. Zaluzhnyy, R. Kurta, A. Menushenkov, B. Ostrovskii, and I. Vartanyants, “Direct reconstruction of the two-dimensional pair distribution function in partially ordered systems with angular correlations”, *Phys. Rev. E* **94**, 030701 (2016).
- ¹⁰⁹D. Mendez, T. J. Lane, J. Sung, J. Sellberg, C. Levard, H. Watkins, A. E. Cohen, M. Soltis, S. Sutton, J. Spudich, et al., “Observation of correlated X-ray scattering at atomic resolution”, *Philos. T. R. Soc. B* **369**, 20130315 (2014).
- ¹¹⁰D. Mendez, H. Watkins, S. Qiao, K. S. Raines, T. J. Lane, G. Schenk, G. Nelson, G. Subramanian, K. Tono, Y. Joti, et al., “Angular correlations of photons from solution diffraction at a free-electron laser encode molecular structure”, *IUCrJ* **3**, 420–429 (2016).
- ¹¹¹A. Niozu, Y. Kumagai, T. Nishiyama, H. Fukuzawa, K. Motomura, M. Bucher, K. Asa, Y. Sato, Y. Ito, T. Takanashi, et al., “Characterizing crystalline defects in single nanoparticles from angular correlations of single-shot diffracted X-rays”, *IUCrJ* **7**, 276–286 (2020).
- ¹¹²F. Lehmkuhler, B. Fischer, L. Müller, B. Ruta, and G. Grübel, “Structure beyond pair correlations: X-ray cross-correlation from colloidal crystals”, *J. Appl. Crystallogr.* **49**, 2046–2052 (2016).

- ¹¹³F. Lehmkuhler, F. Schulz, M. A. Schroer, L. Frenzel, H. Lange, and G. Grübel, “Heterogeneous local order in self-assembled nanoparticle films revealed by X-ray cross-correlations”, *IUCrJ* **5**, 354–360 (2018).
- ¹¹⁴F. Lehmkuhler, F. Schulz, M. A. Schroer, L. Frenzel, H. Lange, and G. Grübel, “Local orientational order in self-assembled nanoparticle films: the role of ligand composition and salt”, *J. Appl. Crystallogr.* **52**, 777–782 (2019).
- ¹¹⁵F. Schulz, F. Westermeier, F. Dallari, V. Markmann, H. Lange, G. Grübel, and F. Lehmkuhler, “Plasmonic supercrystals with a layered structure studied by a combined TEM-SAXS-XCCA approach”, *Adv. Mater. Interfaces* **7**, 2000919 (2020).
- ¹¹⁶G. F. Mancini, T. Latychevskaia, F. Pennacchio, J. Reguera, F. Stellacci, and F. Carbone, “Order/disorder dynamics in a dodecanethiol-capped gold nanoparticles supracrystal by small-angle ultrafast electron diffraction”, *Nano Lett.* **16**, 2705–2713 (2016).
- ¹¹⁷W. Crookes, “I. On the illumination of lines of molecular pressure, and the trajectory of molecules”, *P. R. Soc. Lond.* **28**, 102–111 (1879).
- ¹¹⁸J. J. Thomson, “XL. Cathode rays”, *Lond. Edinb. Dublin Philos. Mag. J. Sci.* **44**, 293–316 (1897).
- ¹¹⁹R. Bujila, A. Omar, and G. Poludniowski, “A validation of spekpy: a software toolkit for modelling x-ray tube spectra”, *Phys. Medica* **75**, 44–54 (2020).
- ¹²⁰J. Stöhr, “Two-photon X-ray diffraction”, *Phys. Rev. Lett.* **118**, 024801 (2017).
- ¹²¹A. Liénard, “Champ électrique et magnétique produit par une charge électrique concentrée en un point et animée d’un mouvement quelconque”, *L’Éclairage Électrique* **16**, 5 (1898).
- ¹²²D. W. Kerst, “The acceleration of electrons by magnetic induction”, *Phys. Rev.* **60**, 47 (1941).
- ¹²³D. Iwanenko and I. Pomeranchuk, “On the maximal energy attainable in a betatron”, *Phys. Rev.* **65**, 343 (1944).
- ¹²⁴L. Arzimovitch and I. Pomeranchuk, “The radiation of fast electrons in the magnetic field”, *J. Phys. (USSR)* **9**, 267 (1945).
- ¹²⁵H. C. Pollock, “The discovery of synchrotron radiation”, *Am. J. Phys.* **51**, 278–280 (1983).
- ¹²⁶D. H. Tomboulia and P. Hartman, “Spectral and angular distribution of ultraviolet radiation from the 300-MeV Cornell synchrotron”, *Phys. Rev.* **102**, 1423 (1956).
- ¹²⁷I. M. Ado and P. Cherenkov, “Energy distribution of incoherent radiation from synchrotron electrons”, in *Sov. Phys. Dokl. Vol. 1* (1957), pp. 517–517.
- ¹²⁸F. Korolev, O. Kulikov, and A. Yarov, “Polarization properties of synchrotron radiation from high-energy electrons”, *Sov. Phys. JETP* **16** (1963).

- ¹²⁹G. Bathow, E. Freytag, and R. Haensel, “Measurement of synchrotron radiation in the X-ray region”, *J. Appl. Phys.* **37**, 3449–3454 (1966).
- ¹³⁰A. Hofmann, *The physics of synchrotron radiation*, Cambridge Monographs on Particle Physics, Nuclear Physics and Cosmology (Cambridge University Press, 2004).
- ¹³¹J. Schwinger, “On the classical radiation of accelerated electrons”, *Phys. Rev.* **75**, 1912 (1949).
- ¹³²H. Kitamura, “Present status of SPring-8 insertion devices”, *J. Synchrotron Radiat.* **5**, 184–188 (1998).
- ¹³³I. K. Robinson, I. A. Vartanyants, G. J. Williams, M. A. Pfeifer, and J. A. Pitney, “Reconstruction of the shapes of gold nanocrystals using coherent X-ray diffraction”, *Phys. Rev. Lett.* **87**, 195505 (2001).
- ¹³⁴F. Pfeiffer, “X-ray ptychography”, *Nat. Photonics* **12**, 9–17 (2018).
- ¹³⁵G. Grübel and F. Zontone, “Correlation spectroscopy with coherent X-rays”, *J. Alloy. Compd.* **362**, 3–11 (2004).
- ¹³⁶O. G. Shpyrko, “X-ray photon correlation spectroscopy”, *J. Synchrotron Radiat.* **21**, 1057–1064 (2014).
- ¹³⁷S Kalbfleisch, H Neubauer, S. Krüger, M Bartels, M Osterhoff, D. Mai, K Giewekemeyer, B Hartmann, M Sprung, and T Salditt, “The Göttingen holography endstation of beamline P10 at PETRA III/DESY”, in *Aip conf. proc. Vol. 1365, 1* (American Institute of Physics, 2011), pp. 96–99.
- ¹³⁸D. Einfeld, J Schaper, and M Plesko, “Design of a diffraction limited light source (DIFL)”, in *Proceedings particle accelerator conference, Vol. 1* (IEEE, 1995), pp. 177–179.
- ¹³⁹A. L. Schawlow and C. H. Townes, “Infrared and optical masers”, *Phys. Rev.* **112**, 1940 (1958).
- ¹⁴⁰J. M. Madey, “Stimulated emission of bremsstrahlung in a periodic magnetic field”, *J. Appl. Phys.* **42**, 1906–1913 (1971).
- ¹⁴¹D. A. Deacon, L. Elias, J. M. Madey, G. Ramian, H. Schwettman, and T. I. Smith, “First operation of a free-electron laser”, *Phys. Rev. Lett.* **38**, 892 (1977).
- ¹⁴²A. Kondratenko and E. Saldin, “Generating of coherent radiation by a relativistic electron beam in an undulator”, *Part. Accel.* **10**, 207–216 (1980).
- ¹⁴³S. Milton, E. Gluskin, N. Arnold, C. Benson, W. Berg, S. Biedron, M. Borland, Y.-C. Chae, R. Dejus, P. Den Hartog, et al., “Exponential gain and saturation of a self-amplified spontaneous emission free-electron laser”, *Science* **292**, 2037–2041 (2001).

- ¹⁴⁴A. Tremaine, X. Wang, M. Babzien, I. Ben-Zvi, M. Cornacchia, H.-D. Nuhn, R. Malone, A. Murokh, C. Pellegrini, S. Reiche, et al., “Experimental characterization of nonlinear harmonic radiation from a visible self-amplified spontaneous emission free-electron laser at saturation”, *Phys. Rev. Lett.* **88**, 204801 (2002).
- ¹⁴⁵V. Ayvazyan, N. Baboi, I. Bohnet, R. Brinkmann, M. Castellano, P. Castro, L. Catani, S. Choroba, A. Cianchi, M. Dohlus, et al., “Generation of GW radiation pulses from a VUV free-electron laser operating in the femtosecond regime”, *Phys. Rev. Lett.* **88**, 104802 (2002).
- ¹⁴⁶V. Ayvazyan, N. Baboi, J. Bähr, V. Balandin, B. Beutner, A. Brandt, I. Bohnet, A. Bolzmann, R. Brinkmann, O. I. Brovko, J. P. Carneiro, S. Casalbuoni, M. Castellano, P. Castro, L. Catani, et al., “First operation of a free-electron laser generating GW power radiation at 32 nm wavelength”, *Eur. Phys. J. D* **37**, 297–303 (2006).
- ¹⁴⁷P. Emma, R. Akre, J. Arthur, R. Bionta, C. Bostedt, J. Bozek, A. Brachmann, P. Bucksbaum, R. Coffee, F.-J. Decker, et al., “First lasing and operation of an ångstrom-wavelength free-electron laser”, *Nat. Photonics* **4**, 641–647 (2010).
- ¹⁴⁸E. Saldin, E. Schneidmiller, and M. Yurkov, *The physics of free electron lasers*, Advanced Texts in Physics (Springer Berlin Heidelberg, 2013).
- ¹⁴⁹M. J. Bogan, W. H. Benner, S. Boutet, U. Rohner, M. Frank, A. Barty, M. M. Seibert, F. Maia, S. Marchesini, S. Bajt, B. Woods, V. Riot, S. P. Hau-Riege, M. Svenda, E. Marklund, et al., “Single particle X-ray diffractive imaging”, *Nano Lett.* **8**, 310–316 (2008).
- ¹⁵⁰S. Boutet, L. Lomb, G. J. Williams, T. R. M. Barends, A. Aquila, R. B. Doak, U. Weierstall, D. P. DePonte, J. Steinbrener, R. L. Shoeman, M. Messerschmidt, A. Barty, T. A. White, S. Kassemeyer, R. A. Kirian, et al., “High-resolution protein structure determination by serial femtosecond crystallography”, *Science* **337**, 362–364 (2012).
- ¹⁵¹J. M. Glowia, J. Cryan, J. Andreasson, A. Belkacem, N. Berrah, C. I. Blaga, C. Bostedt, J. Bozek, L. F. DiMauro, L. Fang, J. Frisch, O. Gessner, M. Gühr, J. Hajdu, M. P. Hertlein, et al., “Time-resolved pump-probe experiments at the LCLS”, *Opt. Express* **18**, 17620–17630 (2010).
- ¹⁵²D. Shaw and D. Shaw, *Introduction to colloid and surface chemistry*, Chemical, Petrochemical & Process (Elsevier Science, 1992).
- ¹⁵³P. Hiemenz and R. Rajagopalan, *Principles of colloid and surface chemistry, revised and expanded* (CRC Press, 2016).
- ¹⁵⁴I. Freestone, N. Meeks, M. Sax, and C. Higgitt, “The Lycurgus cup – a roman nanotechnology”, *Gold Bull.* **40**, 270–277 (2007).
- ¹⁵⁵M. Faraday, “X. The Bakerian lecture. — Experimental relations of gold (and other metals) to light”, *Philos. T. R. Soc. Lond.*, 145–181 (1857).

- ¹⁵⁶T. Graham, "X. Liquid diffusion applied to analysis", *Philos. T. R. Soc. Lond.*, 183–224 (1861).
- ¹⁵⁷M. A. Hayat, *Colloidal gold: principles, methods, and applications* (Elsevier, 2012).
- ¹⁵⁸J. E. Millstone, S. J. Hurst, G. S. Métraux, J. I. Cutler, and C. A. Mirkin, "Colloidal gold and silver triangular nanoprisms", *Small* **5**, 646–664 (2009).
- ¹⁵⁹I. Pastoriza-Santos and L. M. Liz-Marzán, "Colloidal silver nanoplates. State of the art and future challenges", *J. Mater. Chem.* **18**, 1724–1737 (2008).
- ¹⁶⁰H.-J. Yang, S.-Y. He, H.-L. Chen, and H.-Y. Tuan, "Monodisperse copper nanocubes: synthesis, self-assembly, and large-area dense-packed films", *Chem. Mater.* **26**, 1785–1793 (2014).
- ¹⁶¹W. Li, R. Zamani, M. Ibáñez, D. Cadavid, A. Shavel, J. R. Morante, J. Arbiol, and A. Cabot, "Metal ions to control the morphology of semiconductor nanoparticles: copper selenide nanocubes", *J. Am. Chem. Soc.* **135**, 4664–4667 (2013).
- ¹⁶²V. K. Ravi, P. K. Santra, N. Joshi, J. Chugh, S. K. Singh, H. Rensmo, P. Ghosh, and A. Nag, "Origin of the substitution mechanism for the binding of organic ligands on the surface of $CsPbBr_3$ perovskite nanocubes", *J. Phys. Chem. Lett.* **8**, 4988–4994 (2017).
- ¹⁶³W. Yang, X. Liu, D. Li, L. Fan, and Y. Li, "Aggregation-induced preparation of ultrastable zinc sulfide colloidal nanospheres and their photocatalytic degradation of multiple organic dyes", *Phys. Chem. Chem. Phys.* **17**, 14532–14541 (2015).
- ¹⁶⁴J. Shen, Y. Jung, A. S. Disa, F. J. Walker, C. H. Ahn, and J. J. Cha, "Synthesis of $SnTe$ nanoplates with $\{100\}$ and $\{111\}$ surfaces", *Nano Lett.* **14**, 4183–4188 (2014).
- ¹⁶⁵F. Zhang, C. Chen, S. V. Kershaw, C. Xiao, J. Han, B. Zou, X. Wu, S. Chang, Y. Dong, A. L. Rogach, et al., "Ligand-controlled formation and photoluminescence properties of $CH_3NH_3PbBr_3$ nanocubes and nanowires", *ChemNanoMat* **3**, 303–310 (2017).
- ¹⁶⁶S. Sacanna and A. Philipse, "Preparation and properties of monodisperse latex spheres with controlled magnetic moment for field-induced colloidal crystallization and (dipolar) chain formation", *Langmuir* **22**, 10209–10216 (2006).
- ¹⁶⁷D. J. Kraft, R. Ni, F. Smallenburg, M. Hermes, K. Yoon, D. A. Weitz, A. van Blaaderen, J. Groenewold, M. Dijkstra, and W. K. Kegel, "Surface roughness directed self-assembly of patchy particles into colloidal micelles", *P. Natl. Acad. Sci.* **109**, 10787–10792 (2012).
- ¹⁶⁸K. Margulis, X. Zhang, L.-M. Joubert, K. Bruening, C. J. Tassone, R. N. Zare, and R. M. Waymouth, "Formation of polymeric nanocubes by self-assembly and crystallization of dithiolane-containing triblock copolymers", *Angew. Chem.* **129**, 16575–16580 (2017).

- ¹⁶⁹B. Derjaguin and L. Landau, "Theory of the stability of strongly charged lyophobic sols and of the adhesion of strongly charged particles in solutions of electrolytes", *Acta Physicochim. URSS* **14**, 633 (1941).
- ¹⁷⁰E. J. W. Verwey, "Theory of the stability of lyophobic colloids", *J. Phys. Chem.* **51**, 631–636 (1947).
- ¹⁷¹U. Gasser, E. R. Weeks, A. Schofield, P. Pusey, and D. Weitz, "Real-space imaging of nucleation and growth in colloidal crystallization", *Science* **292**, 258–262 (2001).
- ¹⁷²E. H. de Hoog, W. K. Kegel, A. van Blaaderen, and H. N. Lekkerkerker, "Direct observation of crystallization and aggregation in a phase-separating colloid-polymer suspension", *Phys. Rev. E* **64**, 021407 (2001).
- ¹⁷³J. Savage, D. Blair, A. Levine, R. Guyer, and A. Dinsmore, "Imaging the sublimation dynamics of colloidal crystallites", *Science* **314**, 795–798 (2006).
- ¹⁷⁴S. Schütter, J. Roller, A. Kick, J.-M. Meijer, and A. Zumbusch, "Real-space imaging of translational and rotational dynamics of hard spheres from the fluid to the crystal", *Soft Matter* **13**, 8240–8249 (2017).
- ¹⁷⁵J. M. Grogan, L. Rotkina, and H. H. Bau, "In situ liquid-cell electron microscopy of colloid aggregation and growth dynamics", *Phys. Rev. E* **83**, 061405 (2011).
- ¹⁷⁶J. Park, H. Zheng, W. C. Lee, P. L. Geissler, E. Rabani, and A. P. Alivisatos, "Direct observation of nanoparticle superlattice formation by using liquid cell transmission electron microscopy", *ACS Nano* **6**, 2078–2085 (2012).
- ¹⁷⁷B. Michen, C. Geers, D. Vanhecke, C. Endes, B. Rothen-Rutishauser, S. Balog, and A. Petri-Fink, "Avoiding drying-artifacts in transmission electron microscopy: characterizing the size and colloidal state of nanoparticles", *Sci. Rep.* **5**, 1–7 (2015).
- ¹⁷⁸B. H. Kim, J. Yang, D. Lee, B. K. Choi, T. Hyeon, and J. Park, "Liquid-phase transmission electron microscopy for studying colloidal inorganic nanoparticles", *Adv. Mater.* **30**, 1703316 (2018).
- ¹⁷⁹R. Pecora, *Dynamic light scattering: applications of photon correlation spectroscopy* (Springer US, 2013).
- ¹⁸⁰B. Berne and R. Pecora, *Dynamic light scattering: with applications to chemistry, biology, and physics*, Dover Books on Physics (Dover Publications, 2013).
- ¹⁸¹E. Tomaszewska, K. Soliwoda, K. Kadziola, B. Tkacz-Szczesna, G. Celichowski, M. Cichowski, W. Szmaja, and J. Grobelny, "Detection limits of DLS and UV-Vis spectroscopy in characterization of polydisperse nanoparticles colloids", *J. Nanomater.* **2013**, 313081 (2013).
- ¹⁸²P. A. Hassan, S. Rana, and G. Verma, "Making sense of Brownian motion: colloid characterization by dynamic light scattering", *Langmuir* **31**, 3–12 (2015).

- ¹⁸³D. Pontoni, T. Narayanan, J.-M. Petit, G. Grübel, and D. Beysens, “Microstructure and dynamics near an attractive colloidal glass transition”, *Phys. Rev. Lett.* **90**, 188301 (2003).
- ¹⁸⁴X. Lu, S. Mochrie, S. Narayanan, A. Sandy, and M Sprung, “How a liquid becomes a glass both on cooling and on heating”, *Phys. Rev. Lett.* **100**, 045701 (2008).
- ¹⁸⁵L. Frenzel, M. Dartsch, G. M. Balaguer, F. Westermeier, G. Grübel, and F. Lehmkuhler, “Glass-liquid and glass-gel transitions of soft-shell particles”, *Phys. Rev. E* **104**, L012602 (2021).
- ¹⁸⁶J. Wagner, W. Härtl, and R. Hempelmann, “Characterization of monodisperse colloidal particles: comparison between SAXS and DLS”, *Langmuir* **16**, 4080–4085 (2000).
- ¹⁸⁷D. Pontoni, T. Narayanan, and A. Rennie, “Time-resolved SAXS study of nucleation and growth of silica colloids”, *Langmuir* **18**, 56–59 (2002).
- ¹⁸⁸X. Chen, J. Wang, R. Pan, S. Roth, and S. Förster, “Insights into growth kinetics of colloidal gold nanoparticles: in situ SAXS and UV–Vis evaluation”, *J. Phys. Chem. C* **125**, 1087–1095 (2020).
- ¹⁸⁹Q. Tian, D. Zhang, N. Li, M. J. Henderson, Q. Li, G. Royal, J. Courtois, M. Yan, Z. Zhu, and L. Almásy, “Structural study of polystyrene-b-poly (acrylic acid) micelles complexed with uranyl: a SAXS core–shell model analysis”, *Langmuir* **36**, 4820–4826 (2020).
- ¹⁹⁰M. Hildebrandt, S. Lazarev, J. Pérez, I. A. Vartanyants, J.-M. Meijer, and M. Karg, “SAXS investigation of core–shell microgels with high scattering contrast cores: access to structure factor and volume fraction”, *Macromolecules* **55**, 2959–2969 (2022).
- ¹⁹¹W. M. Stanley, “Isolation of a crystalline protein possessing the properties of tobacco-mosaic virus”, *Science* **81**, 644–645 (1935).
- ¹⁹²L. Onsager, “The effects of shape on the interaction of colloidal particles”, *Ann. NY Acad. Sci.* **51**, 627–659 (1949).
- ¹⁹³W. W. Wood and J. Jacobson, “Preliminary results from a recalculation of the Monte Carlo equation of state of hard spheres”, *J. Chem. Phys.* **27**, 1207–1208 (1957).
- ¹⁹⁴B. J. Alder and T. E. Wainwright, “Phase transition for a hard sphere system”, *J. Chem. Phys.* **27**, 1208–1209 (1957).
- ¹⁹⁵W. G. Hoover and F. H. Ree, “Melting transition and communal entropy for hard spheres”, *J. Chem. Phys.* **49**, 3609–3617 (1968).
- ¹⁹⁶C. De Kruif, P. Rouw, J. Jansen, and A. Vrij, “Hard sphere properties and crystalline packing of lyophilic silica colloids”, *J. Phys. Colloq.* **46**, C3–295 (1985).
- ¹⁹⁷P. N. Pusey and W Van Megen, “Phase behaviour of concentrated suspensions of nearly hard colloidal spheres”, *Nature* **320**, 340–342 (1986).

- ¹⁹⁸J. Zhu, M. Li, R. Rogers, W. Meyer, R. Ottewill, W. Russel, and P. Chaikin, "Crystallization of hard-sphere colloids in microgravity", *Nature* **387**, 883–885 (1997).
- ¹⁹⁹A. Petukhov, I. Dolbnya, D. Aarts, G. Vroege, and H. Lekkerkerker, "Bragg rods and multiple X-ray scattering in random-stacking colloidal crystals", *Phys. Rev. Lett.* **90**, 028304 (2003).
- ²⁰⁰I. Dolbnya, A. Petukhov, D. Aarts, G. Vroege, and H. Lekkerkerker, "Coexistence of rhcp and fcc phases in hard-sphere colloidal crystals", *Europhys. Lett.* **72**, 962 (2005).
- ²⁰¹J. Hilhorst, J. R. Wolters, and A. V. Petukhov, "Slanted stacking faults and persistent face centered cubic crystal growth in sedimentary colloidal hard sphere crystals", *CrystEngComm* **12**, 3820–3826 (2010).
- ²⁰²A. Sinitskii, V. Abramova, N. Grigorieva, S. Grigoriev, A. Snigirev, D. Byelov, and A. Petukhov, "Revealing stacking sequences in inverse opals by microradian X-ray diffraction", *Europhys. Lett.* **89**, 14002 (2010).
- ²⁰³A. Yethiraj and A. van Blaaderen, "A colloidal model system with an interaction tunable from hard sphere to soft and dipolar", *Nature* **421**, 513–517 (2003).
- ²⁰⁴D. Gottwald, C. Likos, G. Kahl, and H. Löwen, "Phase behavior of ionic microgels", *Phys. Rev. Lett.* **92**, 068301 (2004).
- ²⁰⁵J. C. Pàmies, A. Cacciuto, and D. Frenkel, "Phase diagram of Hertzian spheres", *J. Chem. Phys.* **131**, 044514 (2009).
- ²⁰⁶D. Heyes and A. Brańka, "Interactions between microgel particles", *Soft Matter* **5**, 2681–2685 (2009).
- ²⁰⁷M. E. Leunissen, C. G. Christova, A.-P. Hynninen, C. P. Royall, A. I. Campbell, A. Imhof, M. Dijkstra, R. Van Roij, and A. Van Blaaderen, "Ionic colloidal crystals of oppositely charged particles", *Nature* **437**, 235–240 (2005).
- ²⁰⁸R. Ni, A. P. Gantapara, J. De Graaf, R. Van Roij, and M. Dijkstra, "Phase diagram of colloidal hard superballs: from cubes via spheres to octahedra", *Soft Matter* **8**, 8826–8834 (2012).
- ²⁰⁹Y. Zhang, F. Lu, D. Van Der Lelie, and O. Gang, "Continuous phase transformation in nanocube assemblies", *Phys. Rev. Lett.* **107**, 135701 (2011).
- ²¹⁰J.-M. Meijer, F. Hagemans, L. Rossi, D. V. Byelov, S. I. Castillo, A. Snigirev, I. Snigireva, A. P. Philipse, and A. V. Petukhov, "Self-assembly of colloidal cubes via vertical deposition", *Langmuir* **28**, 7631–7638 (2012).
- ²¹¹Y. Jiao, F. H. Stillinger, and S. Torquato, "Optimal packings of superballs", *Phys. Rev. E* **79**, 041309 (2009).
- ²¹²R. D. Batten, F. H. Stillinger, and S. Torquato, "Phase behavior of colloidal superballs: shape interpolation from spheres to cubes", *Phys. Rev. E* **81**, 061105 (2010).

- ²¹³J.-M. Meijer, A. Pal, S. Ouhajji, H. N. Lekkerkerker, A. P. Philipse, and A. V. Petukhov, "Observation of solid–solid transitions in 3D crystals of colloidal superballs", *Nat. Commun.* **8**, 1–8 (2017).
- ²¹⁴P. F. Damasceno, M. Engel, and S. C. Glotzer, "Crystalline assemblies and densest packings of a family of truncated tetrahedra and the role of directional entropic forces", *ACS Nano* **6**, 609–614 (2012).
- ²¹⁵A. P. Gantapara, J. de Graaf, R. van Roij, and M. Dijkstra, "Phase diagram and structural diversity of a family of truncated cubes: degenerate close-packed structures and vacancy-rich states", *Phys. Rev. Lett.* **111**, 015501 (2013).
- ²¹⁶J. Gong, R. S. Newman, M. Engel, M. Zhao, F. Bian, S. C. Glotzer, and Z. Tang, "Shape-dependent ordering of gold nanocrystals into large-scale superlattices", *Nat. Commun.* **8**, 1–9 (2017).
- ²¹⁷Y. H. Lee, C. L. Lay, W. Shi, H. K. Lee, Y. Yang, S. Li, and X. Y. Ling, "Creating two self-assembly micro-environments to achieve supercrystals with dual structures using polyhedral nanoparticles", *Nat. Commun.* **9**, 1–8 (2018).
- ²¹⁸I. D. Hosein, S. H. Lee, and C. M. Liddell, "Dimer-based three-dimensional photonic crystals", *Adv. Funct. Mater.* **20**, 3085–3091 (2010).
- ²¹⁹A. Pal, J.-M. Meijer, J. R. Wolters, W. K. Kegel, and A. V. Petukhov, "Structure and stacking order in crystals of asymmetric dumbbell-like colloids", *J. Appl. Crystallogr.* **48**, 238–243 (2015).
- ²²⁰T. Wang, J. Zhuang, J. Lynch, O. Chen, Z. Wang, X. Wang, D. LaMontagne, H. Wu, Z. Wang, and Y. C. Cao, "Self-assembled colloidal superparticles from nanorods", *Science* **338**, 358–363 (2012).
- ²²¹J. P. Hoogenboom, D. Derks, P. Vergeer, and A. van Blaaderen, "Stacking faults in colloidal crystals grown by sedimentation", *J. Chem. Phys.* **117**, 11320–11328 (2002).
- ²²²K. Jensen, D. Pennachio, D. Recht, D. Weitz, and F. Spaepen, "Rapid growth of large, defect-free colloidal crystals", *Soft Matter* **9**, 320–328 (2013).
- ²²³Y. Suzuki, T. Sawada, and K. Tamura, "Colloidal crystallization by a centrifugation method", *J. Cryst. Growth* **318**, 780–783 (2011).
- ²²⁴P. Jiang and M. J. McFarland, "Large-scale fabrication of wafer-size colloidal crystals, macroporous polymers and nanocomposites by spin-coating", *J. Am. Chem. Soc.* **126**, 13778–13786 (2004).
- ²²⁵M. Pichumani, P. Bagheri, K. M. Poduska, W. González-Viñas, and A. Yethiraj, "Dynamics, crystallization and structures in colloid spin coating", *Soft Matter* **9**, 3220–3229 (2013).
- ²²⁶P. Jiang, J. Bertone, K. S. Hwang, and V. Colvin, "Single-crystal colloidal multilayers of controlled thickness", *Chem. Mater.* **11**, 2132–2140 (1999).

- ²²⁷Z. Cai, J. Teng, Y. Wan, and X. Zhao, "An improved convective self-assembly method for the fabrication of binary colloidal crystals and inverse structures", *J. Colloid Interf. Sci.* **380**, 42–50 (2012).
- ²²⁸H. G. Schild, "Poly (N-isopropylacrylamide): experiment, theory and application", *Prog. Polym. Sci.* **17**, 163–249 (1992).
- ²²⁹R. Pelton, "Temperature-sensitive aqueous microgels", *Adv. Colloid Interfac.* **85**, 1–33 (2000).
- ²³⁰A. M. Alsayed, M. F. Islam, J. Zhang, P. J. Collings, and A. G. Yodh, "Premelting at defects within bulk colloidal crystals", *Science* **309**, 1207–1210 (2005).
- ²³¹Z. Wang, F. Wang, Y. Peng, Z. Zheng, and Y. Han, "Imaging the homogeneous nucleation during the melting of superheated colloidal crystals", *Science* **338**, 87–90 (2012).
- ²³²Z. Wang, F. Wang, Y. Peng, and Y. Han, "Direct observation of liquid nucleus growth in homogeneous melting of colloidal crystals", *Nat. Commun.* **6**, 1–9 (2015).
- ²³³S. Narayanan, J. Wang, and X.-M. Lin, "Dynamical self-assembly of nanocrystal superlattices during colloidal droplet evaporation by in situ small angle X-ray scattering", *Phys. Rev. Lett.* **93**, 135503 (2004).
- ²³⁴P. Siffalovic, E. Majkova, L. Chitu, M. Jergel, S. Luby, A. Satka, and S. Roth, "Self-assembly of iron oxide nanoparticles studied by time-resolved grazing-incidence small-angle X-ray scattering", *Phys. Rev. B* **76**, 195432 (2007).
- ²³⁵P. Siffalovic, E. Majkova, L. Chitu, M. Jergel, S. Luby, I. Capek, A. Satka, A. Timmann, and S. Roth, "Real-time tracking of superparamagnetic nanoparticle self-assembly", *Small* **4**, 2222–2228 (2008).
- ²³⁶S. Xiong, D. R. Dunphy, D. C. Wilkinson, Z. Jiang, J. Strzalka, J. Wang, Y. Su, J. J. de Pablo, and C. J. Brinker, "Revealing the interfacial self-assembly pathway of large-scale, highly-ordered, nanoparticle/polymer monolayer arrays at an air/water interface", *Nano Lett.* **13**, 1041–1046 (2013).
- ²³⁷Y. Dai, B. Lin, M. Meron, K. Kim, B. Leahy, T. A. Witten, and O. G. Shpyrko, "Synchrotron X-ray studies of rapidly evolving morphology of self-assembled nanoparticle films under lateral compression", *Langmuir* **29**, 14050–14056 (2013).
- ²³⁸E. Josten, E. Wetterskog, A. Glavic, P. Boesecke, A. Feoktystov, E. Brauweiler-Reuters, U. Rücker, G. Salazar-Alvarez, T. Brückel, and L. Bergström, "Superlattice growth and rearrangement during evaporation-induced nanoparticle self-assembly", *Sci. Rep.* **7**, 1–9 (2017).
- ²³⁹S. Maiti, A. André, R. Banerjee, J. Hagenlocher, O. Konovalov, F. Schreiber, and M. Scheele, "Monitoring self-assembly and ligand exchange of PbS nanocrystal superlattices at the liquid/air interface in real time", *J. Phys. Chem. Lett.* **9**, 739–744 (2018).

- ²⁴⁰B. Abécassis, F. Testard, and O. Spalla, “Gold nanoparticle superlattice crystallization probed in situ”, *Phys. Rev. Lett.* **100**, 115504 (2008).
- ²⁴¹X. Chen, J. Schröder, S. Hauschild, S. Rosenfeldt, M. Dulle, and S. Förster, “Simultaneous SAXS/WAXS/UV-Vis study of the nucleation and growth of nanoparticles: a test of classical nucleation theory”, *Langmuir* **31**, 11678–11691 (2015).
- ²⁴²I. Lokteva, M. Koof, M. Walther, G. Grübel, and F. Lehmkuhler, “Coexistence of hcp and bct phases during in situ superlattice assembly from faceted colloidal nanocrystals”, *J. Phys. Chem. Lett.* **10**, 6331–6338 (2019).
- ²⁴³M. Kapuscinski, M. Agthe, Z.-P. Lv, Y. Liu, M. Segad, and L. Bergström, “Temporal evolution of superlattice contraction and defect-induced strain anisotropy in mesocrystals during nanocube self-assembly”, *ACS Nano* **14**, 5337–5347 (2020).
- ²⁴⁴L. Frenzel, F. Lehmkuhler, I. Lokteva, S. Narayanan, M. Sprung, and G. Grübel, “Anomalous dynamics of concentrated silica-PNIPAm nanogels”, *J. Phys. Chem. Lett.* **10**, 5231–5236 (2019).
- ²⁴⁵L. Frenzel, F. Lehmkuhler, M. Koof, I. Lokteva, and G. Grübel, “The phase diagram of colloidal silica-PNIPAm core-shell nanogels”, *Soft Matter* **16**, 466–475 (2020).
- ²⁴⁶J. Fang, Y. Xuan, and Q. Li, “Preparation of polystyrene spheres in different particle sizes and assembly of the ps colloidal crystals”, *Sci. China Technol. Sci.* **53**, 3088–3093 (2010).
- ²⁴⁷J. Gulden, O. Yefanov, A. Mancuso, V. Abramova, J. Hilhorst, D. Byelov, I. Snigireva, A. Snigirev, A. Petukhov, and I. Vartanyants, “Coherent X-ray imaging of defects in colloidal crystals”, *Phys. Rev. B* **81**, 224105 (2010).
- ²⁴⁸S. Lazarev, I. Besedin, A. V. Zozulya, J.-M. Meijer, D. Dzhigaev, O. Y. Gorobtsov, R. P. Kurta, M. Rose, A. G. Shabalin, E. A. Sulyanova, et al., “Ptychographic X-ray imaging of colloidal crystals”, *Small* **14**, 1702575 (2018).
- ²⁴⁹A. Zozulya, J.-M. Meijer, A. Shabalin, A. Ricci, F. Westermeier, R. Kurta, U. Lorenz, A. Singer, O. Yefanov, A. Petukhov, et al., “In situ X-ray crystallographic study of the structural evolution of colloidal crystals upon heating”, *J. Appl. Crystallogr.* **46**, 903–907 (2013).
- ²⁵⁰E. A. Sulyanova, A. Shabalin, A. V. Zozulya, J.-M. Meijer, D. Dzhigaev, O. Gorobtsov, R. P. Kurta, S. Lazarev, U. Lorenz, A. Singer, et al., “Structural evolution of colloidal crystal films in the process of melting revealed by Bragg peak analysis”, *Langmuir* **31**, 5274–5283 (2015).
- ²⁵¹A. V. Zozulya, I. A. Zaluzhnyy, N. Mukharamova, S. Lazarev, J.-M. Meijer, R. P. Kurta, A. Shabalin, M. Sprung, A. V. Petukhov, and I. A. Vartanyants, “Unraveling the structural rearrangement of polymer colloidal crystals under dry sintering conditions”, *Soft Matter* **14**, 6849–6856 (2018).

- ²⁵²T. Yasuda, K. Nishikawa, and S. Furukawa, "Structural colors from TiO_2/SiO_2 multilayer flakes prepared by sol-gel process", *Dyes Pigm.* **92**, 1122–1125 (2012).
- ²⁵³J. M. Weissman, H. B. Sunkara, A. S. Tse, and S. A. Asher, "Thermally switchable periodicities and diffraction from mesoscopically ordered materials", *Science* **274**, 959–963 (1996).
- ²⁵⁴J. Martorell and N. Lawandy, "Distributed feedback oscillation in ordered colloidal suspensions of polystyrene microspheres", *Opt. Commun.* **78**, 169–173 (1990).
- ²⁵⁵Y. Nishijima, K. Ueno, S. Juodkazis, V. Mizeikis, H. Misawa, M. Maeda, and M. Minaki, "Tunable single-mode photonic lasing from zirconia inverse opal photonic crystals", *Opt. Express* **16**, 13676–13684 (2008).
- ²⁵⁶H. Cong and B. Yu, "Fabrication of superparamagnetic macroporous Fe_3O_4 and its derivatives using colloidal crystals as templates", *J. Colloid Interf. Sci.* **353**, 131–136 (2011).
- ²⁵⁷Z. Zhou, Q. Yan, F. Su, and X. Zhao, "Replicating novel carbon nanostructures with 3D macroporous silica template", *J. Mater. Chem.* **15**, 2569–2574 (2005).
- ²⁵⁸J. I. Chen, G. von Freymann, S. Y. Choi, V. Kitaev, and G. A. Ozin, "Amplified photochemistry with slow photons", *Adv. Mater.* **18**, 1915–1919 (2006).
- ²⁵⁹A. Stein, B. E. Wilson, and S. G. Rudisill, "Design and functionality of colloidal-crystal-templated materials—chemical applications of inverse opals", *Chem. Soc. Rev.* **42**, 2763–2803 (2013).
- ²⁶⁰J.-Y. Shiu, C.-W. Kuo, P. Chen, and C.-Y. Mou, "Fabrication of tunable superhydrophobic surfaces by nanosphere lithography", *Chem. Mater.* **16**, 561–564 (2004).
- ²⁶¹J. Wang, Y. Wen, J. Hu, Y. Song, and L. Jiang, "Fine control of the wettability transition temperature of colloidal-crystal films: from superhydrophilic to superhydrophobic", *Adv. Funct. Mater.* **17**, 219–225 (2007).
- ²⁶²R. Li, K. Bian, T. Hanrath, W. A. Bassett, and Z. Wang, "Decoding the superlattice and interface structure of truncate PbS nanocrystal-assembled supercrystal and associated interaction forces", *J. Am. Chem. Soc.* **136**, 12047–12055 (2014).
- ²⁶³A. Dreyer, A. Feld, A. Kornowski, E. D. Yilmaz, H. Noei, A. Meyer, T. Krekeler, C. Jiao, A. Stierle, V. Abetz, et al., "Organically linked iron oxide nanoparticle supercrystals with exceptional isotropic mechanical properties", *Nat. Mater.* **15**, 522–528 (2016).
- ²⁶⁴C. Yan, I. Arfaoui, N. Goubet, and M.-P. Pileni, "Soft supracrystals of Au nanocrystals with tunable mechanical properties", *Adv. Funct. Mater.* **23**, 2315–2321 (2013).
- ²⁶⁵X. Ling, S. Roland, and M.-P. Pileni, "Supracrystals of N-heterocyclic carbene-coated Au nanocrystals", *Chem. Mater.* **27**, 414–423 (2015).

- ²⁶⁶P. Tartaj, "Sub-100 nm TiO_2 mesocrystalline assemblies with mesopores: preparation, characterization, enzyme immobilization and photocatalytic properties", *Chem. Commun.* **47**, 256–258 (2011).
- ²⁶⁷S. Toso, D. Baranov, D. Altamura, F. Scattarella, J. Dahl, X. Wang, S. Marras, A. P. Alivisatos, A. Singer, C. Giannini, et al., "Multilayer diffraction reveals that colloidal superlattices approach the structural perfection of single crystals", *ACS Nano* **15**, 6243–6256 (2021).
- ²⁶⁸Z. Fan and M. Grünwald, "Orientational order in self-assembled nanocrystal superlattices", *J. Am. Chem. Soc.* **141**, 1980–1988 (2019).
- ²⁶⁹D. M. Balazs, D. N. Dirin, H.-H. Fang, L. Protesescu, G. H. ten Brink, B. J. Kooi, M. V. Kovalenko, and M. A. Loi, "Counterion-mediated ligand exchange for PbS colloidal quantum dot superlattices", *ACS Nano* **9**, 11951–11959 (2015).
- ²⁷⁰M. C. Weidman, K. G. Yager, and W. A. Tisdale, "Interparticle spacing and structural ordering in superlattice PbS nanocrystal solids undergoing ligand exchange", *Chem. Mater.* **27**, 474–482 (2015).
- ²⁷¹J. S. van der Burgt, J. J. Geuchies, B. van der Meer, H. Vanrompay, D. Zanaga, Y. Zhang, W. Albrecht, A. V. Petukhov, L. Filion, S. Bals, et al., "Cuboidal supraparticles self-assembled from cubic $CsPbBr_3$ perovskite nanocrystals", *J. Phys. Chem. C* **122**, 15706–15712 (2018).
- ²⁷²P. Simon, E. Rosseeva, I. A. Baburin, L. Liebscher, S. G. Hickey, R. Cardoso-Gil, A. Eychmüller, R. Kniep, and W. Carrillo-Cabrera, "PbS–organic mesocrystals: the relationship between nanocrystal orientation and superlattice array", *Angew. Chem.* **124**, 10934–10939 (2012).
- ²⁷³Y. Yu, X. Lu, A. Guillaussier, V. R. Voggu, W. Pinerros, M. De La Mata, J. Arbiol, D.-M. Smilgies, T. M. Truskett, and B. A. Korgel, "Orientationally ordered silicon nanocrystal cuboctahedra in superlattices", *Nano Lett.* **16**, 7814–7821 (2016).
- ²⁷⁴N. Mukharamova, D. Lapkin, I. A. Zaluzhnyy, A. André, S. Lazarev, Y. Y. Kim, M. Sprung, R. P. Kurta, F. Schreiber, I. A. Vartanyants, et al., "Revealing grain boundaries and defect formation in nanocrystal superlattices by nanodiffraction", *Small* **15**, 1904954 (2019).
- ²⁷⁵R. Zheng, H. Gu, B. Xu, K. K. Fung, X. Zhang, and S. P. Ringer, "Self-assembly and self-orientation of truncated octahedral magnetite nanocrystals", *Adv. Mater.* **18**, 2418–2421 (2006).
- ²⁷⁶B. T. Diroll, X. Ma, Y. Wu, and C. B. Murray, "Anisotropic cracking of nanocrystal superlattices", *Nano Lett.* **17**, 6501–6506 (2017).

- ²⁷⁷K. Bian, J. J. Choi, A. Kaushik, P. Clancy, D.-M. Smilgies, and T. Hanrath, "Shape-anisotropy driven symmetry transformations in nanocrystal superlattice polymorphs", *ACS Nano* **5**, 2815–2823 (2011).
- ²⁷⁸S. Toso, D. Baranov, C. Giannini, S. Marras, and L. Manna, "Wide-angle X-ray diffraction evidence of structural coherence in $CsPbBr_3$ nanocrystal superlattices", *ACS Mater. Lett.* **1**, 272–276 (2019).
- ²⁷⁹O. L. Lazarenkova and A. A. Balandin, "Miniband formation in a quantum dot crystal", *J. Appl. Phys.* **89**, 5509–5515 (2001).
- ²⁸⁰C.-W. Jiang and M. A. Green, "Silicon quantum dot superlattices: modeling of energy bands, densities of states, and mobilities for silicon tandem solar cell applications", *J. Appl. Phys.* **99**, 114902 (2006).
- ²⁸¹M. Artemyev, A. Bibik, L. Gurinovich, S. Gaponenko, and U. Woggon, "Evolution from individual to collective electron states in a dense quantum dot ensemble", *Phys. Rev. B* **60**, 1504 (1999).
- ²⁸²A. Zabet-Khosousi, P.-E. Trudeau, Y. Suganuma, A.-A. Dhirani, and B. Statt, "Metal to insulator transition in films of molecularly linked gold nanoparticles", *Phys. Rev. Lett.* **96**, 156403 (2006).

Acknowledgments

First of all, I would like to thank Prof. Dr. Ivan Vartaniants and Prof. Dr. Edgar Weckert for providing me an opportunity to work on this Thesis in the Coherent X-ray Scattering and Imaging group at the DESY Photon Science Division. I also appreciate their scientific advice and tough discussions during the group meetings, which brought this work to an essentially higher level. I thank Prof. Dr. Ivan Vartaniants and Prof. Dr. Christian Schroer for their supervision and reviewing the Thesis.

I would also like to thank the present and former members of the Coherent X-ray Scattering and Imaging group: Ruslan Kurta, Luca Gelisio, Young Yong Kim, Dmitry Dzhigaev, Ivan Zaluzhnyy, Max Rose, Sergey Lazarev, Jerome Carnis, Alexandr Ignatenko, Anatoly Shabalin, Nastasia Mukharamova, Ruslan Khubbutdinov, Dameli Assalauova, Gerard Hinsley, Kuan Hoon Ngoi, Shweta Singh, and Bihan Wang for shaping my closest scientific environment and passing your knowledge (not only scientific) on to me. I would like to express my gratitude to Nastasia Mukharamova for many advice during my first days at DESY that allowed me to settle well in the group and in everyday life in Hamburg. I also appreciate extremely fruitful discussions with Sergey Lazarev supported by his self-explanatory sketches, which had a profound effect on my understanding of the reciprocal space concept. I would like to thank Young Yong Kim for providing many useful scripts that have been widely used during my work in the group and passed on to future generations of the group members. Special thanks go to Gerard Hinsley for proofreading the most important parts of this Thesis.

I am thankful to the groups of Prof. Dr. Frank Schreiber and Prof. Dr. Marcus Scheele from the Eberhard Karl University of Tübingen, the group of Prof. Dr. Janne-Mieke Meijer from the Eindhoven University of Technology, and the group of Prof. Dr. Elena Sturm from the Ludwig Maximilian University of Munich for the deep collaboration in all the projects presented in this Thesis and for the most important step – the sample preparation.

I am especially grateful to the team of the P10 beamline at PETRA III facility, namely, Dr. Michael Sprung, Dr. Fabian Westermeier, Dr. Rustam Rysov, Dr. Zhe Ren, and others. Without their kind support and discussions during all the experiments mentioned in this Thesis, it would have missed most of the results and novelty.

I am specifically thankful to Nastasia Mukharamova, Anatoly Shabalin, Maria Nau-

movia, Sergiu Levcenko, Dameli Assalauova, Ruslan Khubbutdinov, Rustam Rysov, Sergei Riabchuk, Semyon Goncharov, Andrey Fedulin, Ivan Sobolev, Anton Sokolov, Taisiia Cheremnykh, Radik Batraev, and others for filling my PhD time with fun and joy, for tea sessions at DESY, and for traveling together all around Europe.

Last, but not least, I would like to thank my parents, Marina and Alexander Lapkin, for providing me an opportunity to study this world and acceptance of my decisions. And my grandparents, Ludmila and Victor Melikhov, for my primary physical education and inspiration for doing science.